Alma Mater Studiorum – Università di Bologna

DOTTORATO DI RICERCA IN

CHIMICA

Ciclo 31°

Settore Concorsuale: 03/B1

Settore Scientifico Disciplinare: CHIM/03

BIOINSPIRED DESIGN OF INORGANIC ADVANCED FUNCTIONAL MATERIALS

Presentata da: Giulia Magnabosco

Coordinatore Dottorato

Prof. Aldo Roda

Supervisore

Prof. Giuseppe Falini

Cosupervisore

Prof. Joanna Aizenberg

Esame finale anno 2019

Abstract

Nature offers outstanding examples of structures and composite materials which exploit a variety of functions, often combining two or more needs. A great example can be found in sea sponges, silica structures that couple an hydrodynamic shape, allowing the flow of water and symbiotic organisms, with the ability of direct light with optical fiber-like constituents. [1] Butterfly wings are made of chitinous 2D Christmas tree-like nanostructures that allow them to be at the same time non-wettable and intensely colored. [2,3] Biominerals entrap organic molecules in the inorganic matrix to control polymorphism and morphology and enhance their mechanical proprieties. [4,5]

The strategies found in Nature can be exploited to create new materials, optimizing both the fabrication process and the material performances. In this work, I describe the fabrication of new inorganic materials with functional applications, ranging from drug delivery to bio-catalysis.

Calcite single crystal composites are commonly found in biomineralized shells, in which small molecules such as amino acids [6] and macromolecules such as protein [7,8] are embedded within the inorganic matrix and modify the habit and proprieties of the material. We exploited the ability of calcite crystals to entrap molecules [9,10] and nano-objects [11-14] to obtain functional materials, with particular focus on drug delivery. In fact, calcium carbonate dissolves at acidic pHs that are typical of cancer and inflamed tissues, making it an ideal carrier for passive drug delivery systems. At the same time, the study of the additive entrapment and precipitation conditions [15] gives insights on the crystallization mechanism, shedding light on biomineralization processes. Two representative examples are described.

As a representative molecule for this study retinoic acid (RA), a vitamin A precursor used to differentiate stem cells into neurons, has been used. [16] RA/calcite hybrid crystals were prepared by direct mixing of Ca^{2+} and CO_3^{2-} ions in the presence of 200 µM retinoic acid. Even though no significant change in the morphology of the crystals was observed (figure A 1a-b), Rietveld refinement of high resolution X-Ray powder diffraction confirmed the entrapment of RA by showing a strain along the c-axis cell parameter. RA/calcite hybrid crystals were embedded into a fibrin matrix to form a bioresorbable 3D network ideal as a cell support (figure A 1c). The differentiation of NE-4C/SH-SY5Y cells into a densely interconnected neuronal network was first assessed seeding the cells in the presence of the RA/calcite hybrid single crystals (figure A 1d-e). After prolonged time of incubation, neuronal processes are detectable and the active areas are almost completely covered by a dense layer of mature neuronal cells. This demonstrates that RA/calcite hybrid crystals entrapped in a fibrin network can cause the differentiation of the majority of cells and the formation of a dense neuronal network with long and interconnected neuronal filaments.

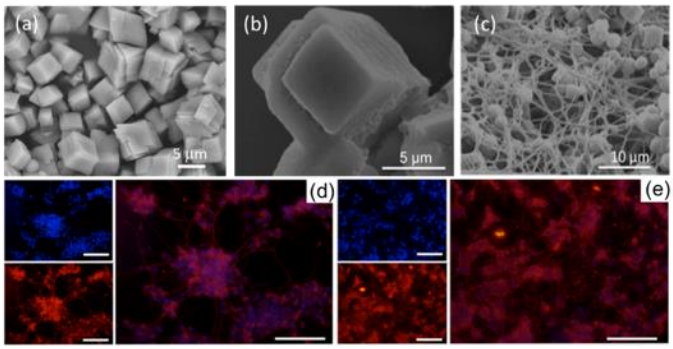

Figure A 1. Calcite crystals grown (a) in the absence and (b) in the presence of 200 µM RA and (c) RA/calcite crystals embedded in the fibrin matrix. Immunofluorence images: cell differentiation day 8 through RA released from the calcite/RA hybrid single crystals. (d) Shows the formation of the neuronal network of Ne4C in astrocytes, (e) show the differentiation of SH-SY5Y cells into neurons. The blue color (DAPI) marks the nuclei of all the cells. The differentiation is visualized by the specific labelling of III β-tubulin, a typical marker of neuronal processes (red).

The mechanism of inclusion of nano-object into calcite single crystals has been widely investigated recently, with a particular focus on the enhancing of the mechanical proprieties rising from the fabrication of a single crystal composite. Despite that, poor attention has been paid to the surface chemistry of the additive. For this reason, we studied the inclusion of fluorescent core-shell silica nanoparticles (PluS-X) carrying different functional groups on their surface into calcite single crystals. Calcite crystals have been grown in the presence of different concentration of amine (PluS-NH_2), carboxyl (PluS-COOH) and hydroxyl (PluS-OH) terminating nanoparticles and their distribution and loading into the crystals has been evaluated exploiting their fluorescence. Hydroxyl nanoparticles are most efficiently entrapped into the crystals without a strong modification of the crystal morphology (figure A 2a-g). Furthermore, high resolution TEM analysis allowed to confirm that the single crystal nature of the crystal is conserved even in the presence of the particles (figure A 2h). In the future, we plan to exploit the ability of including drugs in the PluS-X core and functionalizing their shells with tumor specific targeting agents to couple the passive drug delivery behavior of $CaCO_3$ with the active one of the PluS-X themselves.

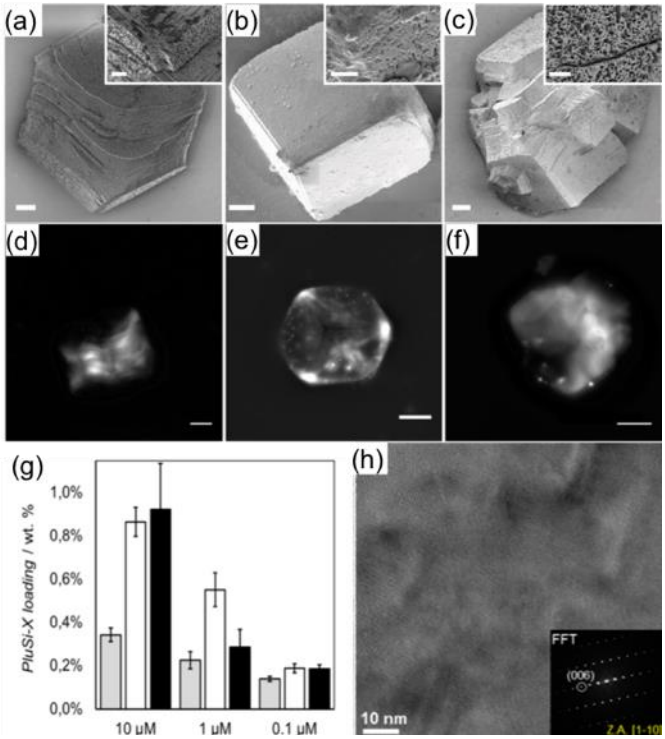

Figure A 2 . SEM and confocal micrographs of calcite crystals grown in the presence of 10 µM (a,d) PluS-COOH, (b,e) PluS-OH and (c,f) PluS-NH_2. Scalebar is 10 µm and 20 µm respectively. (g) PluS-X loading of PluS-COOH (grey), PluS-OH (white), and PluS-NH_2 (black). (h) HRTEM image showing the single crystal nature of the PluS-OH/$CaCO_3$ hybrid crystal and its FFT (inset).

Crystalline order on a bigger length scale gives rise to interesting optical proprieties when materials with appropriate dielectric constants are used. Inverse opals (IO) consist in a periodic array of void spaces in a bulk matrix and, other than being fabricated in the lab, they occur even in Nature in a variety of exoskeletons, feathers and fruits. Nanofabrication allows to use a great variety of constituents that are not available in Nature, creating new materials with greater performances. Here, titania and silica inverse opals structures coupled with plasmonic nanoparticles have been successfully used to obtain laser driven remote and localize enhancement of the activity of the model enzyme lipase. Inverse opals with tailored pore size and refractive index contrast between the two materials show a photonic band gap, meaning that some frequencies cannot propagate in any direction inside the material. The frequencies at the edge of the band gap are allowed to propagate slowly inside the material, giving rise to the slow light effect. According to Fermi's golden rule, the absorption of light by molecules or particles is inversely proportional to its velocity, meaning that the slow light effect will increase the absorption of light by object present in the photonic material. Plasmonic nanoparticles (nPs) can absorb light and convert it into heating (figure A 3a). So, the presence of plasmonic nPs of the surface of the inverse opal will increase the heating rate with respect to the isolated nPs, creating an easy to recover substrate with high surface area and improved heating rate (figure A 3b). The produced heat has been then exploited to enhance the activity of lipase, increasing its activity of almost 6 times (figure A 3c-d). Since most of the catalytic reactions increase their rate by increasing the temperature, such a system can be used as a universal platform for enhanced catalytic efficiency.

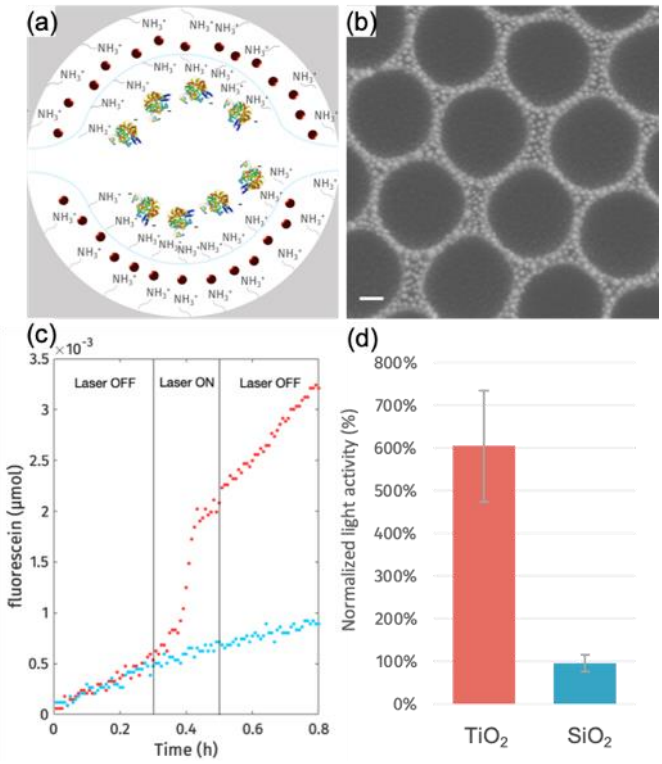

Figure A 3. (a) Schematic of the composition of the platform. Gold nPs are represented in red, titania in gray and silica in light blue. (b) HRSEM image of gold nPs on the IO surface. Scalebar is 100 µm. (c) fluorescein production by lipase upon laser irradiation for titania IO (red) and silica IO (blue). (d) Enhancement of the activity of lipase during irradiation of the TiO_2 substrate-showing the slow light effect- and the SiO_2 substrate-not showing slow light effect.

As stated previously, biominerals present such complex morphologies that is not possible to replicate them *in vitro*. Sea urchin spines are composed of an interconnected network of pores with controlled dimensions and arrangement that give rise to a structure with a high surface area/volume ratio (figure A 4a). Those structures can conveniently be used as a template for the synthesis other materials with different proprieties. Colloidal assembly on the surface of pores increases the surface area while keeping the spaces interconnected to allow the flow of small molecules. Colloidal nanoparticles were successfully assembled onto the sea urchin spine surface obtaining an ordered array (figure A 4b).

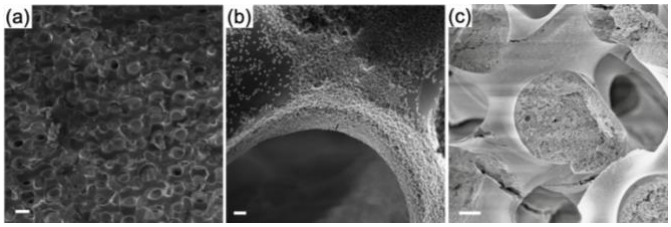

Figure A 4. SEM images of (a) sea urchin spine porous structure, (b) ordered colloid array inside the sea urchin spine pores and (c) colloid/spine structure replica made of silica after $CaCO_3$ dissolution, showing the submicrometric scale porosity given by the colloids. Scalebar is 50 µm in (a), 1 µm in (b) and 2 µm in (c).

The colloid/spine structure can be used as a mold for other inorganic materials, such as silica or titania, to obtain a different length scale porosity scaffold (figure A 4c) with a surface area of around 850 times the one of the pristine spine. Titania is particularly interesting since it catalyzes the photodegradation of small organic molecules when irradiated with UV light. A hybrid silica/titania scaffold replicating the urchin spine was obtained after dissolution of the $CaCO_3$ and polymers template. The catalytic activity of the final platform will be studied.

Conclusions

Nature offers outstanding examples of multifunctional complex structures able to address different needs by changing the composition or the arrangement of the available materials. In this work, a representative selection of bioinspired materials with functional application is presented.

Taking inspiration from biominerals, calcite hybrid crystals including both small molecules and nPs have been synthesized. RA, a small molecule active in cell differentiation, has been included into calcite single crystals and its activity is conserved upon slow dissolution of the matrix. PluS-OH nanoparticles were successfully occluded into calcite without modifying the single crystalline nature of the material. Since different molecules such as drugs or biologically active molecules can be occluded into the PluS-X core, our strategy allows to embed different functions into the additive and make it independent from the nature of the molecule itself.

Inverse opal structures able to slow light coupled with plasmonic nanoparticles and the enzyme lipase have been successfully used to obtain laser driven remote and localized control of the catalytic efficiency of the enzyme, thus obtaining a universal platform for catalytical efficiency enhancement.

Sea urchin spines whose surface area has been amplified by adsorption of colloidal particles have been successfully used as a template to obtain a silica/titania replica with potential application in the photodegradation of small organic molecules.

In conclusion, this thesis shows a selection of functional inorganic materials synthesized using design strategies found in Nature or exploiting natural occurring complex structures as templates, taking advantage of the possibility of using constituents that are not available to biological organisms.

References

1 J. Aizenberg, J. C. Weaver, M. S. Thanawala, V. C. Sundar, D. E. Morse and P. Fratzl, *Science*, 2005, **309**, 275–278.

2 M. Kolle, P. M. Salgard-Cunha, M. R. J. Scherer, F. Huang, P. Vukusic, S. Mahajan, J. J. Baumberg and U. Steiner, *Nature Nanotech*, 2010, **5**, 511–515.

3 P. Vukusic, J. R. Sambles and C. R. Lawrence, *Nature*, 2000, **404**, 457–457.

4 A. Berman, L. Addadi and S. Weiner, *Nature*, 1988, **331**, 546–548.

5 Y.Y. Kim, J. D. Carloni, B. Demarchi, D. Sparks, D. G. Reid, M. E. Kunitake, C. C. Tang, M. J. Duer, C. L. Freeman, B. Pokroy, K. Penkman, J. H. Harding, L. A. Estroff, S. P. Baker and F. C. Meldrum, *Nat Mater*, 2016, **15**, 903–910.

6 S. Borukhin, L. Bloch, T. Radlauer, A. H. Hill, A. N. Fitch and B. Pokroy, *Adv. Funct. Mater.*, **22**, 4216–4224.

7 R. A. Metzler, G. A. Tribello, M. Parrinello and P. U. P. A. Gilbert, *J. Am. Chem. Soc.*, 2010, **132**, 11585–11591.

8 B.A. Gotliv, N. Kessler, J. L. Sumerel, D. E. Morse, N. Tuross, L. Addadi and S. Weiner, *ChemBioChem*, 2005, **6**, 304–314.

9 G. Magnabosco, M. D. Giosia, I. Polishchuk, E. Weber, S. Fermani, A. Bottoni, F. Zerbetto, P. G. Pelicci, B. Pokroy, S. Rapino, G. Falini and M. Calvaresi, *Adv. Healthcare Mater.*, 2015, **4**, 1510–1516.

10 G. Magnabosco, I. Polishchuk, J. Erez, S. Fermani, B. Pokroy and G. Falini, *CrystEngComm*, 2018, **440**, 126–4.

11 Y.Y. Kim, K. Ganesan, P. Yang, A. N. Kulak, S. Borukhin, S. Pechook, L. Ribeiro, R. Kröger, S. J. Eichhorn, S. P. Armes, B. Pokroy and F. C. Meldrum, *Nat Mater*, 2011, **10**, 890–896.

12 Y.-Y. Kim, A. S. Schenk, D. Walsh, A. N. Kulak, O. Cespedes and F. C. Meldrum, *Nanoscale*, 2014, **6**, 852–859.

13 G. Magnabosco, I. Polishchuk, F. Palomba, E. Rampazzo, L. Prodi, J. Aizenberg, B. Pokroy, and G. Falini, *Angewandte chemie, under review*

14 G. Magnabosco, H. Hauzer, S. Fermani, F. Corticelli, M. Christian, V. Morandi, J. Erez and G. Falini, *in preparation*

15 G. Magnabosco, I. Polishchuk, B. Pokroy, R. Rosenberg, H. Coelfen and G. Falini, *Chem. Commun.*, 2017, **53**, 4811–4814.

16 M. Barbalinardo, I. Polishchuk, G. Magnabosco, M. Di Giosia, S. Fermani, F. Biscarini, G. Falini, M. Calvaresi, F. Zerbetto, B. Pokroy, F. Valle, *submitted*

Table of Contents

1 Introduction

1.1 Finding inspiration in Nature

Living organisms are able to find outstanding solutions for their needs by generating high-performing structures [1] and using simple strategies with low energy usage, as the use of resources not leading to the exploitation of a function will be a disadvantage from an evolutive point of view. In fact, looking at Nature, it's almost impossible to find structures that do not serve any purpose. In the design of functional materials, by looking at the strategies adopted by Nature, one will start as close as possible to an optimal solution. [2-5]

Organisms are able to synthesize high performance structures in mild conditions, opposed to how the same materials are fabricated synthetically. The understanding of the underlying biological mechanisms allows scientists to mimic or take inspiration from characteristics of biological systems in non-living systems instead of simply replicating it. Bio-inspiration, a growing field in material science, goes beyond the mere imitation of the biogenic solution taking advantages of the principles governing its design.

The first challenge in the design of a bioinspired material is to understand the principles and mechanisms generating the biogenic system and relate them to their function. The second step consists in engineering the ideal solution using the principles extrapolated by the bio-inspiration source, designing a material which can be, from a chemical and physical point of view, significantly different from the one it is inspired by. In fact, one of the main advantages of the fabrication process is that it can exploit of the great range of materials and procedures that are available to scientists and overcome the limitation that living organisms are subjected to.

Given the complexity of biological systems, what scientists were able to do up-to-now was to abstract simplified versions of organisms' capability and mimic some of their functions using simpler or different mechanisms. Nevertheless, this research effort leads to the development of new processes and to their use to solve problems that a biological solution would not be able to solve. At this point, it becomes clear that the main concept of bio-inspiration relies in the exploitation of strategies derived from Nature to respond to needs which can be really different from the one the organism faces.

This thesis work aims to use strategies found in biomineralization and biogenic materials to address practical challenges, such as drug delivery and catalytic efficiency enhancement, while examining the chemical and physical principles underlying the related phenomena.

1.2 Biogenic functional materials

Living organisms are able to meet their needs by molding the materials they're made of, often producing structures able to exploit more the one function at the same time. There are two main approaches used by the organism to obtain the desired function: (i) the presence of additives during the deposition process can modify the habit of the material as well as its proprieties, for example increasing its toughness or (ii) molding of the material at the micro-nanoscale produces behavior which are independent from the composition of the structure. Often both strategies are employed together.

Well-characterized and representative examples are given below.

1.2.1 Lotus effect

The water-repellence and self-cleaning behavior of lotus leaves are one of the most typical examples of nanostructure related proprieties. By examining different specie leaves, Barthlott and Neinhuis were able to correlate the structure of the surface of a given specie leaf (Figure 1) with its contact angle (Table 1). [6] Interestingly, the hydrophobicity of the surface can be ascribed only to the patterning on the surface (Figure 1e-h), as those microstructures are made by cells or cuticular folds combined with epicuticular wax crystalloids with different geometry and composition.

Table 1.Contact angle of different specie leaves. Contact angle below 110° classifies the surfaces as hydrophilic. Reproduced from [6].

Plant species	Contact Angle
Gnetum gnemon	55.4 ± 2.7
Heliconia densiflora	28.4 ± 4.3
Fagus sylvatica	71.7 ± 8.8
Magnolia denudate	88.9 ± 6.9
Nelumbo nucifera	160.4 ± 0.7
Colocasia esculenta	159.7 ± 1.4
Brassica oleracea	160.3 ± 0.8
Mutisia decurrens	128.4 ± 3.6

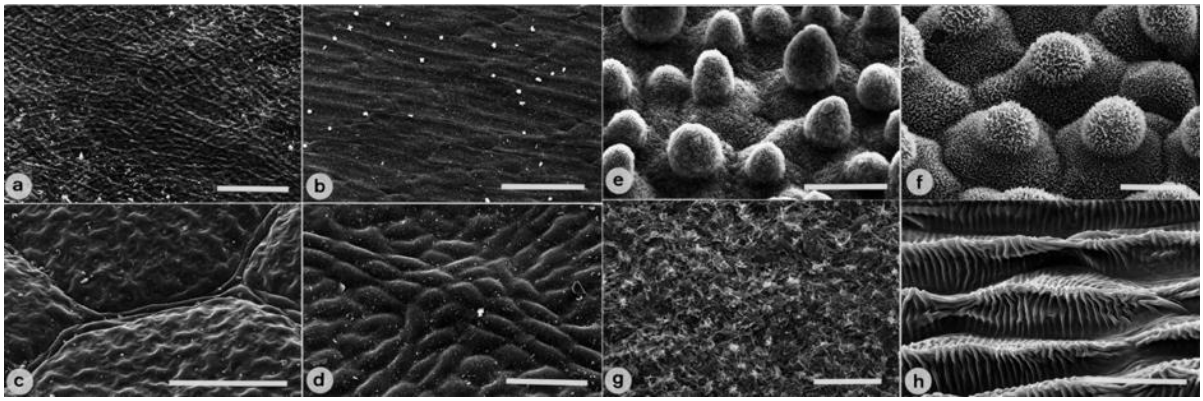

Figure 1. Scanning electron micrographs of the adaxial leaf surface of smooth, wettable (a–d) and rough, water-repellent (e–h) leaf surfaces. The smooth leaves of *Gnetum gnemon* (a) and *Heliconia densiflora* (b) are almost completely lacking microstructures while those of *Fagus sylvatica* (c) and *Magnolia denudata* (d) are characterized by sunken and raised nervature, respectively. The rough surfaces of *Nelumbo nucifera* (e) and *Colocasia esculenta* (f) are characterized by papillose epidermal cells and an additional layer of epicuticular waxes. *Brassica oleracea* leaves (g) are densely covered by wax crystalloids without being papillose, and the petal surfaces of *Mutisia decurrens* (h) are characterized by cuticular folds. Bars 100 µm (a–d) and 20 µm (e–h). Reproduced from [6].

The presence of a microstructure on the surface prevents the water droplets to completely touch the leaf surface and forms a composite between the wax crystalloids and the air enclosed among them, thus disfavoring the wetting from an energetical point of view. The drop will sit on the surface without spreading and will roll off the leaf easily.

The hydrophobicity of the surface is responsible for the self-cleaning proprieties shown by those leaves, known as lotus-effect. In fact, as the drops are rolling off the surface, they embed dust particles and microorganisms they find along their path. The high velocity they can reach, promoted by the low interaction with the surface, prevents the particles from be just displaced by the running droplet, which entraps them and push them out the leaf. The so-called Lotus-effect plays an important role in protecting the organism from the contamination by pathogens such as algae and bacteria by (i) removing them from the surface and (ii) promoting a low-humidity environment in which is difficult for them to survive. Given its interesting proprieties, the design used by leaves has been used as an inspiration to fabricate nanostructures preventing wetting and biofouling which find applications in a great number of fields, ranging from construction to medical devices.

1.2.2 Gecko paws

Gecko paws are another well-characterized example of functions related to nanostructure. In fact, the high adhesion of the paws to surfaces, which allows geckos to climb vertical wall with speeds up to 1 m s^{-1}, is due to the presence of small branched keratin fibers, called setae, on the edge of each digit. Setae are organized in a grid-like geometry and each seta branches to give rise to a great number of fibrils ending with a spatular tip (Figure 2). [7] The shape of the fibril tip, their number and arrangement are responsible for the outstanding adhesive proprieties of the gecko, which has at the same time a high adhesive proprieties and low detachment energy. By combining loading and dragging toward its body, the gecko can adhere to the surface. The great number of fibrils and their slightly different orientation allow it to adhere to rough surfaces. By changing the angle between the fibrils and the surface, the gecko can easily detach from the surface. Adhesion relies on van der Walls forces, meaning that the gecko can walk to surfaces independently from their composition, and that its proprieties are due to the structure and not its chemistry. [8]

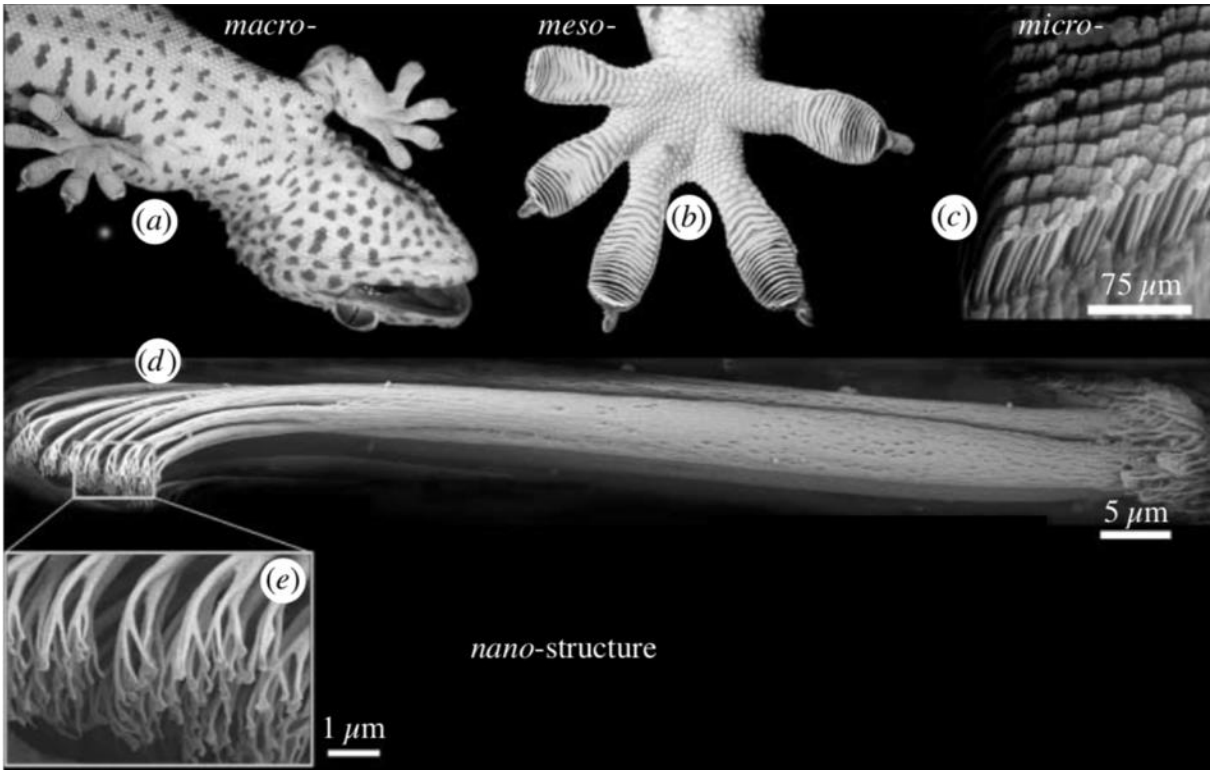

Figure 2. Structural hierarchy of the gecko adhesive system. Images (a,b) provided by Mark Moffett. (a) Ventral view of a tokay gecko (*Gekko gecko*) climbing a vertical glass surface. (b) Ventral view of the foot of a tokay gecko, showing a mesoscale array of seta-bearing scansors (adhesive lamellae). (c) Microscale array of setae are arranged in a nearly grid-like pattern on the ventral surface of each scansor. In this scanning electron micrograph, each diamond-shaped structure is the branched end of a group of four setae clustered together in a tetrad. (d) Cryo-SEM image of a single gecko seta (image by S. Gorb and K. Autumn). Note individual keratin

fibrils comprising the setal shaft. (e) Nanoscale array of hundreds of spatular tips of a single gecko seta. Reproduced from [7].

Interestingly, gecko's paws have self-cleaning proprieties. In fact, when dirty digits adhere to surface, dust particles attach to the latter as the interacting surface is higher. After a few steps on a clean surface, the paws recover enough adhesive proprieties to support the gecko weight (Figure 3). [9]

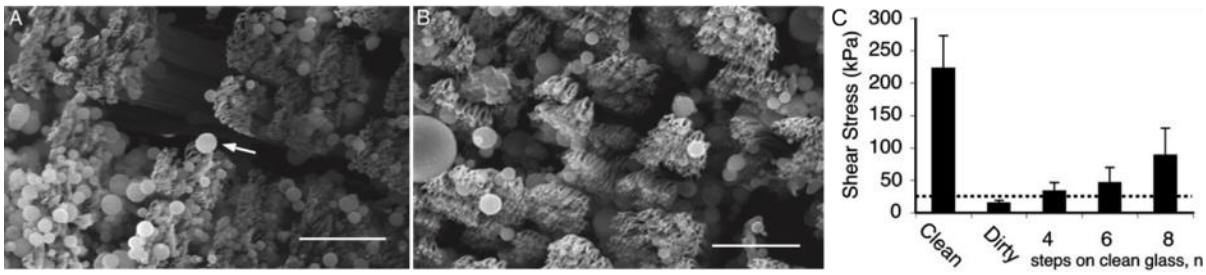

Figure 3. Scanning electron micrographs of arrays. (A) Representative array after dirtying with microspheres. Arrow indicates a microsphere adhering to several spatulae. (B) Array from the same animal after five simulated steps. Microspheres are still present, but spatular surfaces are mostly clean. (Scale bars: 10 µm.) (C) Mean shear stress in clean, dirty, and self-cleaned gecko digits. Dotted line indicates minimum shear stress required to support one gecko's body weight (43 g) by a single toe (area ≅ 0.19 cm^2). After clogging with 2.5-µm- radius microspheres, four steps on clean glass restored setal force to a level sufficient to support the gecko by a single toe. Reproduced from [9]

Similar structures can be found in other organisms such as beetles, flies and spiders (Figure 4). The dimension of the spatular tip, their number and their extension are inversely proportional to the body mass, as splitting up the contact into finer subcontacts increases adhesion. [10]

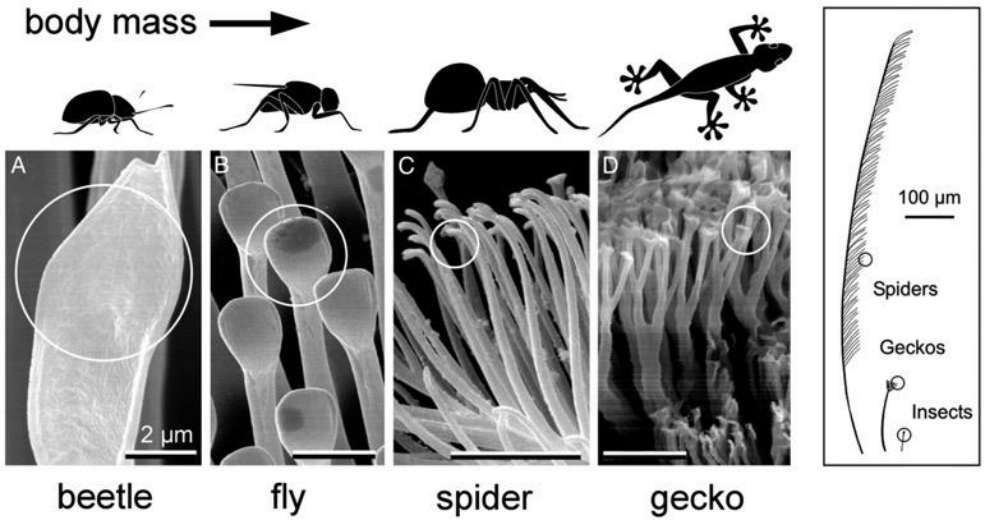

Figure 4. Terminal elements (circles) in animals with hairy design of attachment pads. Note that heavier animals exhibit finer adhesion structures. Reproduced from [10].

The incredible dry adhesive proprieties shown by geckos and caused by the nanostructures present on their digits are a promising source of inspiration for a new generation of adhesive materials which do not rely on the chemical composition of the sticky material and can add further proprieties, e.g. self-cleaning, to the material.

1.2.3 Nacre

Biomineralization is one of the richest sources of inspiration for bioinspired materials. In fact, Nature developed a wide variety of hard materials with unique and diverse proprieties, ranging from lenses to bones, that act as body structures, weapons and sensor. Among biominerals, calcium carbonate is one of the most diffused. Even though $CaCO_3$ is brittle, the organic molecules embedded into the inorganic matrix during the biomineralization process together with the nano-structures organisms are able to fabricate make it the ideal constituent of materials with incredible mechanical proprieties, having their ultimate example in nacre. In fact, nacre is composed of aragonite tablets with thickness around 500 nm separated by a thin organic layer, which both directs crystal nucleation and growth and prevents crack propagation (Figure 5). [11]

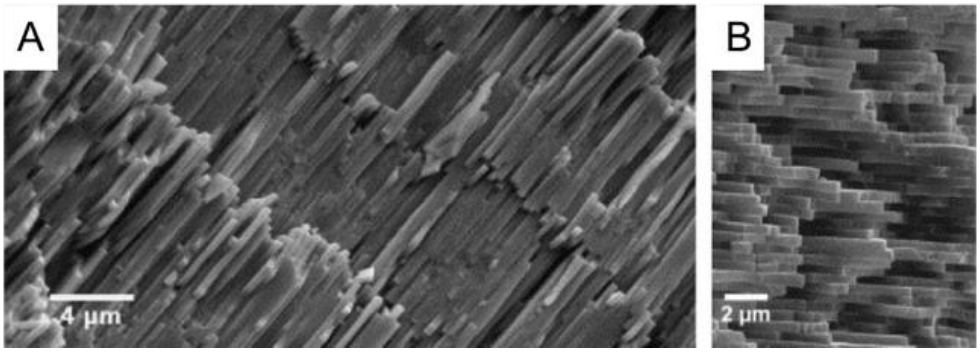

Figure 5. (A) Scanning electron micrograph of the fracture surface of the cross-section of *N. pompilius* septum, showing the layered structure of nacre. The fracture propagated along the borders between the tablets, reveals a flat surface in which stacks of aligned tablets encompassing tens of layers can be observed. (B) Scanning electron micrograph of a fracture surface of the cross-section of *A. rigida* nacre, showing the layered structure of the nacre. Fracture propagated along the border between the tablets, showing the staggered "brick wall" structure of the nacre, where tablets from different layers are not aligned. Reproduced from [11]

Other than being comprise between crystalline tablets, organic molecules are embedded even within them, enhancing the mechanical proprieties of the material by creating spots in which the energy involved in a damage can be dissipated. This mechanism has been observed even in other calcified materials such as sea urchin spines [12] and have been replicated synthetically both by using small molecules (amino acids) [13] and bigger objects (micelles and nanoparticles). [14,15]

Nacre is a good example of how Nature optimizes both the structure and the composition of the material to improve its performances, giving us suggestions on how to improve the proprieties of the material itself and how to design structures with optimal performances.

1.3 Synthetic inorganic functional materials

As shown in 1.2, Nature is able to obtain a wide range of functional materials by changing the composition and the design of the structures it produces. Thus, it is one of the most powerful sources of inspiration for scientists working in nanotechnology, which can observe already optimized structures to use as starting point for designing devices for their needs.

Due to the recent improvement of imaging techniques, many new information on the nanopatterning of biogenic functional materials became available so that, thanks to the advances in fabrication skills, new functional materials have been prepared.

Bottom-up approaches are appealing due to the easiness in scale-up the fabrication process and consistency in synthesis results. These techniques often rely on self-assembly processes, which take advantage from the self-similarity of the components of the system. Two representative examples of inorganic functional materials mimicking biogenic counterparts are given.

1.3.1 Bone inspired hydroxyapatite aerogel

The structure of bones has always been fascinating for scientists due to its mechanical proprieties and the need for new methods for its regeneration pushed researcher to investigate new solutions to prepare similar materials. [16]

The porous structure of trabecular bone inspired ultralight hydroxyapatite (HAP) nanowire aerogels (Figure 6) with three-dimensional interconnected highly porous meshwork structure using a simple, environmentally friendly, low-cost method which can be scaled up for large-scale production. The ultrahigh porous, lightweight, high elastic, and ultralow thermal conductive aerogel can be easily functionalized to change its surface chemistry.

The presence of a great number of interconnected pores allows excellent air permeability and low air flow resistance and has been thus make it an interesting platform for applications in air pollution treatment, such as in air purification, breathing masks, treating automobile and chimney exhausts, and so forth.

The possibility of flowing liquids in the aerogel pores, whose surface functionalization can be tailored, allows the separation of oil−water mixtures, exhibiting high absorption capacities for different oils and organic solvents. The elastic proprieties of the aerogel allow it to be used as a sponge, making possible to squeeze it and make it recover its adsorption proprieties.

In conclusion, this bone-inspired aerogel is a promising example of a multifunctional platform based on inorganic materials.

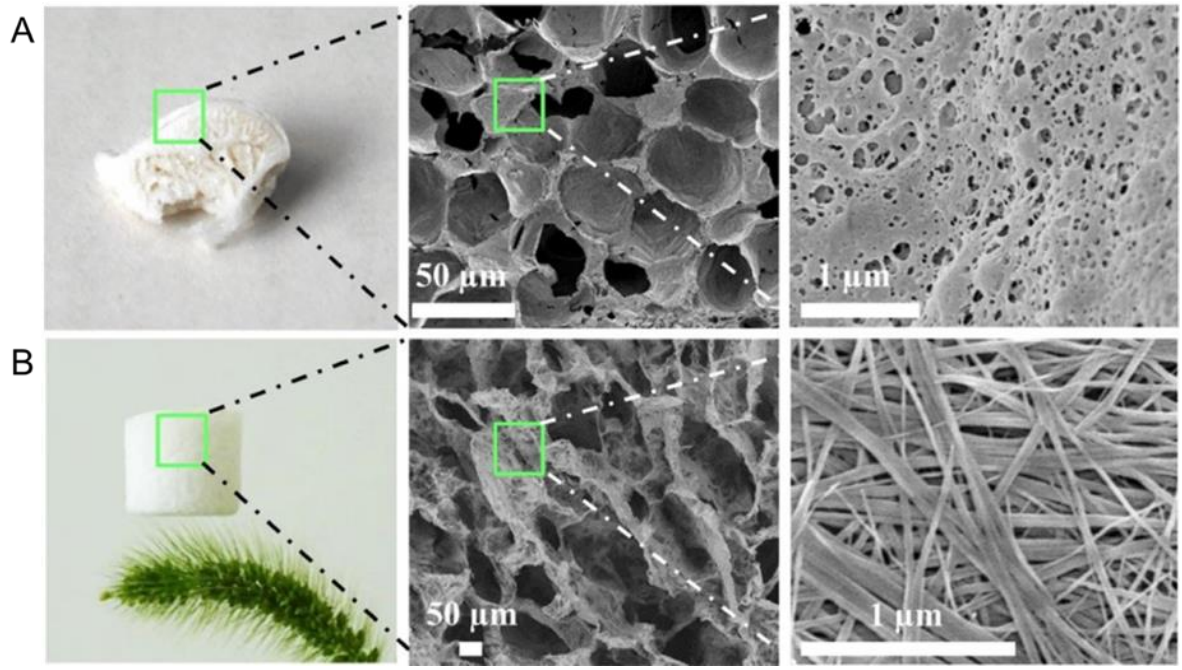

Figure 6. Digital image and SEM micrographs of the cancellous bone. (C) Digital image and SEM micrographs of the as-prepared HAP nanowire aerogel. Reproduced from [16]

1.3.2 Transparent nacre-like material

Nacre, as one of the toughest biogenic materials, is an inspiration source for the fabrication of materials with outstanding mechanical proprieties. The key of nacre fracture resistance is in the organic matrix entrapped among the aragonite tablets. Thus, this structure has been recreated using materials other than calcium carbonate and a wide variety of organic polymers.

Das *et al.* used synthetic clays with different aspect ratio to prepare self-assembled nacre-like multifunctional materials. [17] The mechanical properties are dependent on the size of the nanoclay, ranging from ultrastiff materials for the highest aspect ratio to extremely tough materials with pronounced inelastic deformation for the smallest. This behavior can be ascribed both to the higher ratio of organic component present in the smaller platelets system and to the different fracture mechanism.

The biggest advantage in the use of synthetic nanoclay over natural one is the possibility of obtaining a fully transparent, glass-like nacre-mimetics while at the same time showing among the best gas barrier properties known for nacre-mimetics (Figure 7).

This study designs a bio-inspired multifunctional material obtained by combining advanced and tunable mechanical properties and extends the application prospects of nacre-mimetic materials beyond mechanical properties or the focus on singular functionalities, paving the way for high performance, mechanically robust, transparent barrier coatings and self-standing substrates for organic electronics.

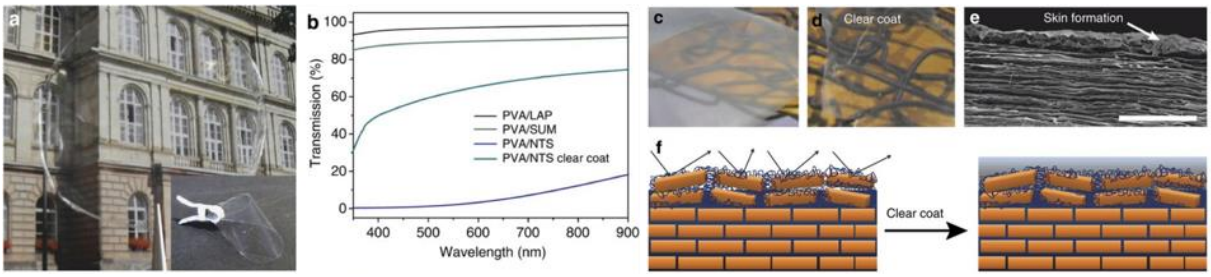

Figure 7. (a) Photographs of an almost fully transparent PVA/LAP film. (b) Transparency by UV-Visible spectroscopy (normalized to 25 µm thickness). (c,d) Nacre-mimetics with larger nanoclay (PVA/NTS) show translucency, but require a clear-coat matching the refractive index of the nacre-mimetics closely to become almost transparent. (e) SEM depicting the skin formed during preparation of a PVA/NTS nacre-mimetic (scale bar, 5 µm). (f) Schematic (not in scale) showing how a clear coat of matching refractive index diminishes surface scattering by providing a smooth top surface layer. Reproduced from [17].

1.4 Aim of the thesis

Nature provides us with countless inspiration sources for the design of functional platforms, allowing us to take advantage of its already optimized materials and strategies. Given the wider range of constituents available for *in vitro* fabrication of such materials compared to the ones which can be found in Nature, there are virtually no limits to the devices that can be produced.

The aim of this thesis is to obtain functional inorganic materials with applications ranging from drug delivery to catalysis while examining the chemical and physical processes underlying the observed phenomena.

In the second chapter, the synthesis and characterization of calcium carbonate-based materials is described. The embedding of functional single-molecules as well as nanoparticles has been explored with the double goal of obtaining hybrid single crystals and understanding crystallization mechanisms. The possibility of obtaining bionic crystals, that is to say functional materials synthesized by living organisms, has been explored by using foraminifera as bioreactors.

In the third chapter is described the design of a photonic platform for enhanced catalytical efficiency based on a titania inverse opal structure. The slow light effect caused by the alternating refractive index medium has been exploited to obtain remote and localized control of the activity of the enzyme lipase.

In the fourth chapter, the possibility of using sea urchin spine as a template for the fabrication of 3-dimensional hybrid silica and titania scaffolds with high surface area and interconnected pores has been explored. Such a platform has ideal characteristics for applications in catalysis and as a scaffold for cells growth.

1.5 References

1 J. W. C. Dunlop and P. Fratzl, *Annu. Rev. Mater. Res.*, 2010, **40**, 1–24.

2 G. M. Whitesides, *Interface Focus*, 2015, **5**, 31.

3 A. E. Rawlings, J. P. Bramble and S. S. Staniland, *Soft Matter*, 2012, **8**, 6675–6679.

4 J. Aizenberg and P. Fratzl, *Adv. Mater.*, 2009, **21**, 387–388.

5 J. Aizenberg and P. Fratzl, *Adv. Funct. Mater.*, 2013, **23**, 4398–4399.

6 W. Barthlott and C. Neinhuis, *Planta*, 1997, **202**, 1–8.

7 K. Autumn and N. Gravish, *Philosophical Transactions of the Royal Society A: Mathematical, Physical and Engineering Sciences*, 2008, **366**, 1575–1590.

8 K. Autumn, M. Sitti, Y. A. Liang, A. M. Peattie, W. R. Hansen, S. Sponberg, T. W. Kenny, R. Fearing, J. N. Israelachvili and R. J. Full, *Proc Natl Acad Sci USA*, 2002, **99**, 12252–12256.

9 W. R. Hansen and K. Autumn, *Proc Natl Acad Sci USA*, 2005, **102**, 385–389.

10 E. Arzt, S. Gorb and R. Spolenak, *Proc Natl Acad Sci USA*, 2003, **100**, 10603–10606.

11 F. Nudelman, B.-A. Gotliv, L. Addadi and S. Weiner, *Journal of Structural Biology*, 2006, **153**, 176–187.

12 J. Aizenberg, J. Aizenberg, J. Hanson and T. F. Koetzle, *J. Am. Chem. Soc.*, 1997, **119**, 881–886.

13 Y.-Y. Kim, J. D. Carloni, B. Demarchi, D. Sparks, D. G. Reid, M. E. Kunitake, C. C. Tang, M. J. Duer, C. L. Freeman, B. Pokroy, K. Penkman, J. H. Harding, L. A. Estroff, S. P. Baker and F. C. Meldrum, *Nat Mater*, 2016, **15**, 903–910.

14 Y.-Y. Kim, K. Ganesan, P. Yang, A. N. Kulak, S. Borukhin, S. Pechook, L. Ribeiro, R. Kröger, S. J. Eichhorn, S. P. Armes, B. Pokroy and F. C. Meldrum, *Nat Mater*, 2011, **10**, 890–896.

15 K. R. Cho, Y.-Y. Kim, P. Yang, W. Cai, H. Pan, A. N. Kulak, J. L. Lau, P. Kulshreshtha, S. P. Armes, F. C. Meldrum and J. J. De Yoreo, *Nature Communications*, 2016, **7**, 10187.

16 Y.-G. Zhang, Y.-J. Zhu, Z.-C. Xiong, J. Wu and F. Chen, *ACS Appl. Mater. Interfaces*, 2018, **10**, 13019–13027.

17 P. Das, J.-M. Malho, K. Rahimi, F. H. Schacher, B. Wang, D. E. Demco and A. Walther, *Nature Communications*, 2015, **6**, 1–14.

2 Calcium carbonate single crystal composites

2.1 Introduction

Crystal growth has always attracted great interest for the fundamental role it covers in fundamental science as well as for technological development. A crystal is defined as an ordered arrangement of objects, thereof it can be made out of molecules, ions or even particles. [1-3] Inorganic ionic crystals, usually made of atomic ions and small inorganic groups, are particularly diffused in Nature as they are one of the major components of rocks and sediments. Furthermore, organisms are able to synthesize those crystals and take advantage of their properties. For example, mammalians use calcium phosphate to build their bones, bacteria use iron oxide to create small magnets they use to orient themselves and sea organisms use calcium carbonate to synthesize their shells. [4,5] The process of precipitation of inorganic crystalline materials performed by living organisms is called biomineralization and it is a widely studied phenomenon for the incredible control that the organism exerts on polymorphism and morphology. [6,7] Calcium carbonate is the most studied bioderived material and it is a great example of the control exerted by living materials on the inorganic phase. [8-10]

The key of organism's control over the precipitation process can be found in the organic matter they excrete to direct nucleation and growth of the crystals. [11,12] One of the most beautiful examples is nacre, a material that can be found in the inner side of many shells. [13] [14,15] Nacre is made of aragonite tablets with controlled thickness, crystallographic orientation and location. Between each of these tablets there is a thin organic layer composed of β-chitin, silk-fibroid like proteins and acidic macromolecules. Carboxylic groups present in the aspartic residues are able to coordinate Ca^{2+} ions and direct the nucleation of aragonite with the c-axis perpendicular to the shell surface. [12,16,17] The growth of the crystals continues along the a and b directions until they connect each other. The final structure exhibit incredible mechanical proprieties compared to geogenic aragonite even if the total organic content is less than 3 % w/w. [18] Thus, we can conclude that organic inclusion into an inorganic matrix can significantly modify the behavior of the starting materials.

By looking at the processes happening in Nature, we can take inspiration to produce new materials with tailored characteristics for our purposes using organic additives that are not available to living organisms. [19-25]

2.1.1 Crystallization mechanism

Due to the important role it covers in biomineralization, great attention has been paid to $CaCO_3$ precipitation mechanism, which is consistent for processes happening both *in vitro* and *in vivo*. Crystallization is a self-assembly process, during which ions come together in different configurations to produce diverse crystalline structures. [1,2,5] $CaCO_3$ is mainly found in an amorphous form (ACC), and in three crystalline anhydrous forms, vaterite, aragonite and calcite, listed in order of increasing thermodynamic stability.

First of all, from a classical point of view, the precipitation of a crystalline phase happens only when supersaturation conditions are meet, that it to say when $\Omega \geq 1$, with Ω defined for $CaCO_3$ as:

$$\Omega = \frac{[Ca^{2+}] * [CO_3^{2-}]}{K_{ps}}$$

It is important to notice that K_{ps} is specific for each polymorph, thus giving rise to a difference in supersaturation conditions for each possible forming phase. Above its Ω a certain phase precipitates, while under this value it dissolves. Given that supersaturation conditions are meet, the most straightforward way to describe a crystallization process is to think at it as a journey along an energy landscape, starting from a solvated state of high free energy towards a low free energy state in the crystal. All the characteristics of the final crystal are due to the shape of this landscape, in particular to the energy barrier that can entrap the material in a non-equilibrium state. When dealing with a crystallization process, it is important to consider both the kinetic and thermodynamic driving forces for precipitation. Kinetic control becomes important increasing when the concentration of starting materials increases up to the point at which classical crystallization principles are not followed anymore (see 2.1.2).

The crystallization process can be divided into nucleation and growth of the crystal. During nucleation, Ca^{2+} and CO_3^{2-} ions associate into clusters, that continuously grow and reduce due to addition and removal of ions. [26] The free energy of the cluster increases since the contribution of the surface is more significant than the one of the bulk. When a cluster is able to grow above the critical dimension (R*) its free energy decreases due to a stronger contribution of the bulk and a stable nucleus forms (see Figure 8). Note that the nucleation process is specific for each polymorph and generally less stable forms are easier to nucleate.

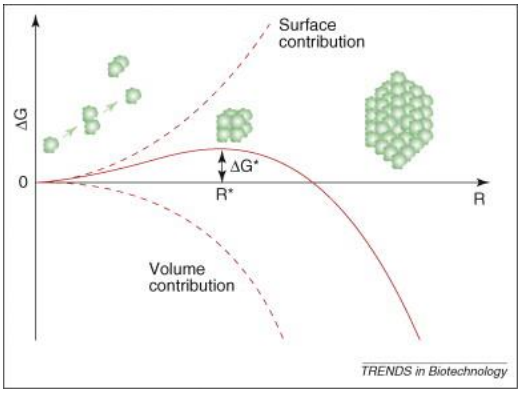

Figure 8. Energy path followed during the nucleation process Reproduced from [27]

After a stable nucleus is formed, the crystal enters the growth phase and it increases its size by addition of ions.

When growing calcite in low supersaturation conditions and in the absence of additives, a classic crystallization mechanism is followed. [28] After the formation of a stable cluster, the crystal continues to grow by addition of ions, which adsorb to the surface of the already formed crystal. Depending on supersaturation conditions, different scenarios are observed (see Figure 9):

A. At low supersaturation conditions, growth proceeds with a spiral mechanism;
B. At intermediate supersaturation conditions, both a spiral growth and a nucleation of island on the surface of the crystal can take place;
C. At high supersaturation, 2D nucleation on the surface prevails.

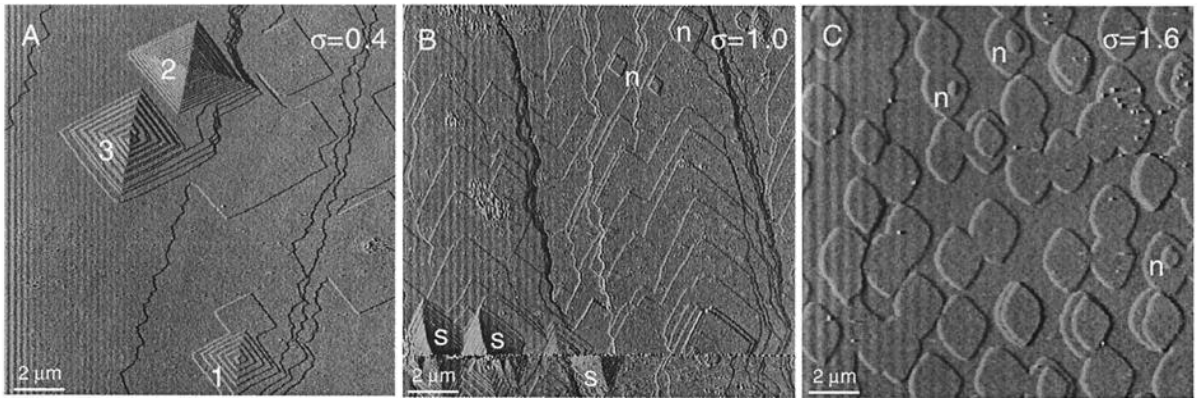

Figure 9. Fluid Cell AFM images showing the growth mechanism on a (101 4) face at different supersaturation states. (A) Observations of spiral growth collected at 0.4 within minutes after the input of solution. Three spirals are observed in the imaging area. Spirals 1 and 3 are single ones, and spiral 2 is a convolution of two double ones. In the area where dislocations are absent, growth occurred by the advancement of existing mono-molecular layers. (B) Co-existence of spiral growth (denoted by s) and homogeneous surface nucleation growth (denoted by n) at 1.0. Spirals occurred in the bottom part of the image where dislocations were linearly distributed. Two-dimensional nuclei appear in the upper right portion of the images. Growth by advancement of existing steps dominated in the rest imaging area. (C) The dominance of growth by two-dimensional surface nucleation was recorded at 1.6 within tens of seconds after the input of solution. Two-dimensional surface nuclei

at 100's nm scale formed randomly on the surface with some of them already coalesced to form bigger nuclei. Continuous surface nucleation is also observed at several locations (denoted by n). Reproduced from [29]

The different pathways followed by the growing crystals are of fundamental importance when studying the interaction of additives with the crystal surface as the change in the final morphology can be related to the adsorption processes happening at the nanoscale. In the recent years, new growth mechanism that do not follow classical thermodynamic rules were proposed and are discussed below.

2.1.2 Alternative precipitation mechanisms

Despite the great knowledge acquired on calcite crystallization, classical growth theory does not explain all experimental evidences. Thus, the possibility of non-classical crystallization mechanisms has been a wide topic of discussion in the recent years. [3,30-35]

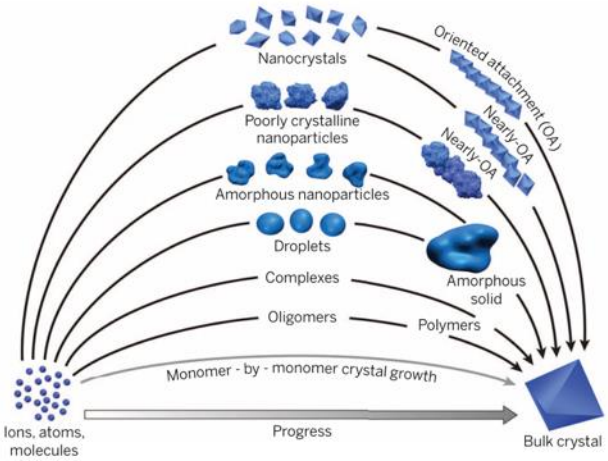

Figure 10. Schematic representation of the possible pathways for a single crystal precipitation. Reproduced from [3]. Reprinted with permission from AAAS.

Three main paths can be followed: (i) formation of cluster or liquid phase precursors, (ii) amorphous intermediate formation or (iii) oriented attachment of nanoparticles (Figure 10). These paths are favored when crystals are grown in high supersaturation conditions or in the presence of additives such as poly(4-styrene sulphonate-co-maleic acid) and poly(styrene-alt-maleic acid).

Great attention was paid to amorphous intermediates since this mechanism seems to be involved in many biomineralization processes. [36,37] The amorphous phase can then crystallize after assembling *in situ* giving rise to complex morphologies.

Stable nanoparticles formation is favored by high supersaturation and stabilizing additives, the nanoparticles can then assemble in an oriented manner and might eventually fuse together along the high-energy crystal faces.

For the aim of this work, only the classical crystallization pathway will be taken into account since recent studies demonstrated that our precipitation conditions promote this precipitation route. [38] [39]

2.1.3 Precipitation techniques

$CaCO_3$ can be prepared with different methodologies that provide Ca^{2+} and CO_3^{2-} sources. They can be divided into two main categories: batch techniques and vapor diffusion methods. A batch precipitation consists in the direct addition of a solution containing Ca^{2+} to one containing CO_3^{2-} or vice versa. A high supersaturation is reached upon the mixing of the two solutions and precipitation takes places immediately, producing kinetic products that eventually evolve into thermodynamically more stable phases by a dissolution and reprecipitation mechanism.

Vapor diffusion methods take advantage of carbonate speciation and use CO_2, that will be in equilibrium with HCO_3^- and CO_3^{2-} in an aqueous solution, as a source of CO_3^{2-} ions. The most diffused vapor diffusion method consists in the use of solid ammonium carbonate ($(NH_4)_2CO_3$), that spontaneously decomposes into gaseous ammonia (NH_3) and carbon dioxide (CO_2), and a Ca^{2+} solution in a closed container. After a first phase during which the equilibrium with the free space of the container is reached, the two gases diffuse into the Ca^{2+} solution. NH_3 increases the pH of the solution, promoting the conversion of CO_2 to CO_3^{2-} (see Figure 11). [40]

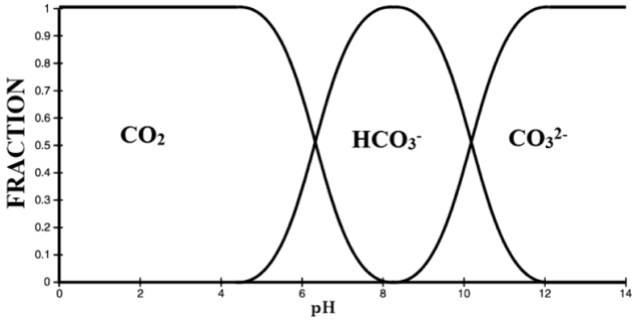

Figure 11. Carbonate speciation in water depending on pH. Reproduced from [41] and [42]

The slow increase of CO_3^{2-} concentration allows a slow increase in supersaturation, so that thermodynamically stable polymorphs can be obtained.

To better understand the precipitation process, Ihli *et al.* investigated the effect of different experimental parameters on the kinetic of precipitation measuring the turbidity of the solution, its pH and free Ca^{2+} concentration. [43] While the quantity of $(NH_4)_2CO_3$ in the solution doesn't affect the precipitation, an increase in Ca^{2+} concentration from 10 mM to 50 mM delays nucleation due to the increase of the time required for conversion of bicarbonate into carbonate. The control of surface area exposed to vapor and diffusion barrier also affect

precipitation by modifying diffusion of the gas phase. In particular, an increase of surface area linearly enhances carbonate concentration, thereof decreasing induction time and increasing pH and nucleation rate. Diffusion barriers are commonly exploited in vapor diffusion protocol and it was proven that they allow a longer induction time and keep supersaturation higher longer. ACC nucleation is hypothesized since a higher supersaturation respect to this phase is reached, but it is not demonstrated.

In conclusion, even if the vapor diffusion method is a powerful tool to investigate the effect of additive at low scales, attention should be paid to the experimental condition as the system is strongly affected by numerous external parameters and can suffer of low reproducibility.

2.1.4 Entrapment of molecules and hybrid crystals for functional applications

Living organisms use insoluble organic molecule as scaffolds and soluble organic molecules as crystal growth modifier to shape calcium carbonate into the complex morphologies that can be found in Nature. [4] The former act as a template over which crystal growth takes place, controlling the nucleation direction and growth of the crystals, while the latter are believed to act on crystal morphology and be incorporated into the growing matrix. The effect of these molecules on the growth of calcium carbonate *in vitro* has been widely examined to relate their structure to the effect on crystalline morphology and polymorphism. In fact, the specific adsorption of molecules onto crystalline face decreases the growth rate of these faces without affecting the one of the others, thus causing a change in the crystalline habit (see Figure 12). Therefore, observing morphology of crystals grown in the presence of additives gives information on the nature of the interaction. [17,44]

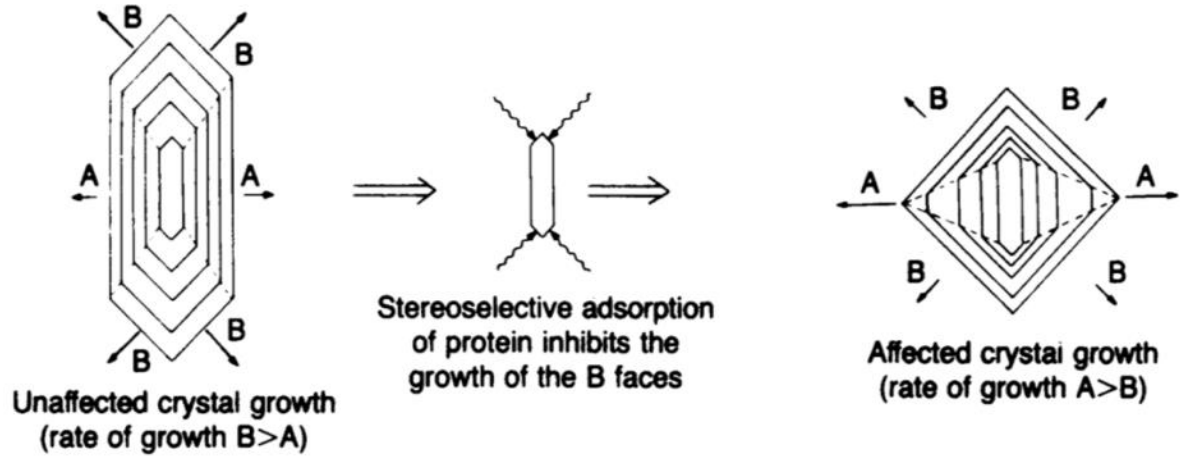

Figure 12. Effect on adsorbed additives on the final crystal morphology. Reproduced from [17]

Calcite crystals grown in the presence of acidic macromolecules extracted from biogenic calcite form (001) planes that are not common in crystals grown in the absence of additives. Furthermore, labelling the adsorbed proteins with antibodies confirms their presence these faces. (001) faces alternate planes exposing calcium to ones exposing carbonate, creating planes with a net charge which favor the interaction with soluble additives. One other important parameter is the distance between the groups able to coordinate calcium or carbonate, which might favor a polymorph over the other. Despite that, is difficult to relate these proprieties of the additives to just one effect and is better to relate their effect to the cooperative effect of different mechanisms.

Other than studying the effect of additives to understand their role during biomineralization processes, calcium carbonate crystals have been grown in the presence of molecules of interest in order to obtain hybrid materials. [45] The molecules to be entrapped have been chosen taking inspiration by functional groups usually found in macromolecules involved in

biomineralization processes, such as carboxylated or sulphonated residues, with the goal of obtaining functional material with improved characteristics compared to pristine crystals. [46] Calcite is often used to prepare single crystal composites for its thermodynamic stability, its mechanical proprieties and the possibility of obtaining it as a single crystal. In the recent years, many groups extensively studied the possibility to include molecules or bigger species such as nanoparticles or micelles into calcite single crystals to obtain functional materials. [22,46,47]

The inclusion of amino acids into calcite crystals and their effect over crystal morphology and polymorphism has been extensively characterized. It was found that the inclusion of amino acids into calcite crystals increases hardness of the crystals themselves. A 2.2 mol% content of aspartate almost doubles the hardness of calcite crystals reaching values typically found in biominerals. This effect can be ascribed to the direct blocking exerted by the molecules onto the crystalline planes, that can break upon dislocation of the lattice to absorb the energy of the fracture. [48]

Calcite single crystals entrapping dyes have been used to obtain an emitting material tunable in the visible spectrum and emitting white light. Crystals were grown in the presence of different organic dyes containing sulphonated groups, believed to increase entrapping, and the distribution of the dye was studied by confocal microscopy. All dyes showed an approximately linear increase in occlusion with the initial [Dye]/[Ca^{2+}]. Incorporation is related to the number and distribution of the sulphonate groups rather than the molecular weight of the dye. Even if the incorporation level is too low to give significant lattice parameter distortion or line broadening from high-resolution synchrotron powder X-ray diffraction analysis, the composite crystals exhibited visible fluorescence under ultraviolet excitation (365 nm). By growing the crystals in the presence of a mixture of dyes of different color, white emitting crystals have been obtained and the approach was extended to nanoparticles synthesis, thus preparing a biocompatible emitting system with promising application *in vivo*. [20]

Many other examples of functional materials obtained by using calcium carbonate single crystals can be found in the recent literature, demonstrating the variety of possibility arising from the synthesis of single crystal composites. [49]

2.1.5 A representative application: doxorubicin entrapment into calcite single crystals

Reproduced with permission from: Magnabosco, G., Di Giosia, M., Polishchuk, I., Weber, E., Fermani, S., Bottoni, A., Zerbetto, F., Pelicci, P. G., Pokroy, B., Rapino, S., Falini, G. and Calvaresi, M. (2015), Calcite Single Crystals as Hosts for Atomic-Scale Entrapment and Slow Release of Drugs. Adv. Healthcare Mater., 4: 1510-1516. doi:10.1002/adhm.201500170

2.1.5.1 Introduction

Nano- and microparticles hold great promise for controlled and targeted drug release and delivery. [50-52]An ideal drug carrier should not exert harmful effects on normal cells. It should also satisfy requirements of stability, in vivo biocompatibility, and ability of targeted on-demand release. [50-52] Inorganic nanomaterials may fulfill most of these requirements. Due to the simplicity of synthesis and modification, it is possible to control the particle size, shape, and surface functionalization. [52] Inorganic nanomaterials are usually made of durable and robust materials, which allow encapsulation and protection of sufficient amounts of cargos, preventing preleakage and damage to normal cells. [53]

Among inorganic carriers, calcium carbonate crystals represent an ideal platform to produce smart carriers for drugs due to their capability to adsorb, and more importantly to entrap drugs. [24,53-72] Organic molecules are commonly found incorporated inside biogenic calcium carbonate ($CaCO_3$) crystals. [73,74] Nature in several organisms uses minerals to store vital ions and structural and functional molecules and macromolecules. [6,75] The use of $CaCO_3$ as a cargo-carrier represents an application of biomineralization inspired principles. [45,76,77] $CaCO_3$forms common biominerals that are intimately associated to biological fluids, which, in turn, makes them highly biocompatible. In the body, it degrades to Ca^{2+} and CO_3^{2-}, which are products that are not toxic. [78,79]

The preparation of $CaCO_3$ crystals is a simple, low cost, and organic solvent-free process (low-level exposure to residual toxic organic solvents may lead to lasting toxic effects). Under highly optimized conditions, crystal formation can control the size of $CaCO_3$ particles from the micro- to the nanometer range, with relatively narrow size distributions. [80] The pH sensitive $CaCO_3$ solubility can release entrapped molecules only when the dissolution of the crystals occurs. [81] Drug/$CaCO_3$ hybrid crystals allow zero-leakage of drugs at the physiological pH of 7.4, and release drugs in acidic conditions. $CaCO_3$ carriers are particularly suitable for selective release of drugs in tissues that are more acidic than normal physiological pH (tumors, inflamed tissues). [82,83]

In biomedical application of $CaCO_3$, besides crystalized $CaCO_3$, amorphous $CaCO_3$(ACC) is also effective in the delivery of drug. The ACC is used as a template for the synthesis of

doxorubicin@silica nanoparticles [83] and directly encapsulate doxorubicin (DOX) for pH-responsive release of ACC-DOX@silica nanoparticles. [84]

In general, development of an effective drug delivery system requires understanding of the chemical and physical properties that affect i) the interaction between the drug and the micro-nanoparticles, and ii) the interaction between the micro-nanocarriers and the biological environment. Often, the structural characterization of the interaction between drug and carrier is missing. Dopant molecules can be either located between individual crystallites of polycrystalline materials or entrapped inside single crystals where they can mimic the stereochemical features of the host.

In the present work, DOX, an anthracycline drug widely used in chemotherapy, [85] is used as a model molecule to study the entrapment in calcite crystals and its release. The use of calcium carbonate nanoparticles as host for DOX and other therapeutic molecules has been already reported in a number of studies. [24,53-72] In most cases, DOX was adsorbed onto preformed calcium carbonate based micro-nanoparticles or mesocrystalline $CaCO_3$ particles. In all cases the distribution of DOX in the mineral host, as well the host crystallography, were not investigated.

The characterization of the drug host from the material point of view has also not been the main goal of previous work that was more concerned with biochemical aspects. The aim of the presented research is to determine how DOX is incorporated inside $CaCO_3$ single crystals, examine the effects of such incorporation on the hosting crystalline lattice and understand the mechanism of incorporation. The biological activity of $CaCO_3$/DOX systems is also assayed.

2.1.5.2 Results and Discussion

Calcium carbonate/DOX hybrid crystal precipitation was conducted at room temperature by controlled diffusion of CO_2 and NH_3 vapors into 10×10^{-3} mM calcium chloride solutions containing different concentrations of DOX. The precipitation process was stopped after 4 days.

1.1.1.1.1. Effect of DOX Doping on the Morphology of Calcite Crystals

In the absence of DOX, only rhombohedral single crystals of calcite are precipitated. In these crystals, characterized by an average size of 50 µm, only the typical {10.4} faces are observable. The presence of DOX influenced the crystallization process as a function of its initial concentration in solution. At low concentrations, 5×10^{-4} and 5×10^{-3} mM, DOX did not affect the precipitation of calcite. At a concentration of 5×10^{-2} mM the crystals became hoppered, showing holes on the {10.4} rhombohedral faces. Increasing the concentration of DOX to 5×10^{-1} mM and 5×10^{-3} mM results both in the observation of the copresence of spherulites with aggregated rhombohedral crystals and in the strong inhibition of the precipitation that is usually associated with the deposition of few aggregates and

submicrometer sized particles. Calcite was the only crystalline phase detected by X-ray powder diffraction in the control experiments and in the experiments where 5×10^{-4} mM, 5×10^{-3} mM or 5×10^{-2} mM DOX was used. When a higher concentration of DOX was used (5×10^{-1} mM and 5×10^{-3} mM), small amounts of vaterite coprecipitated with calcite (Figure 13). The optimal initial concentration of DOX was 5×10^{-2} mM.

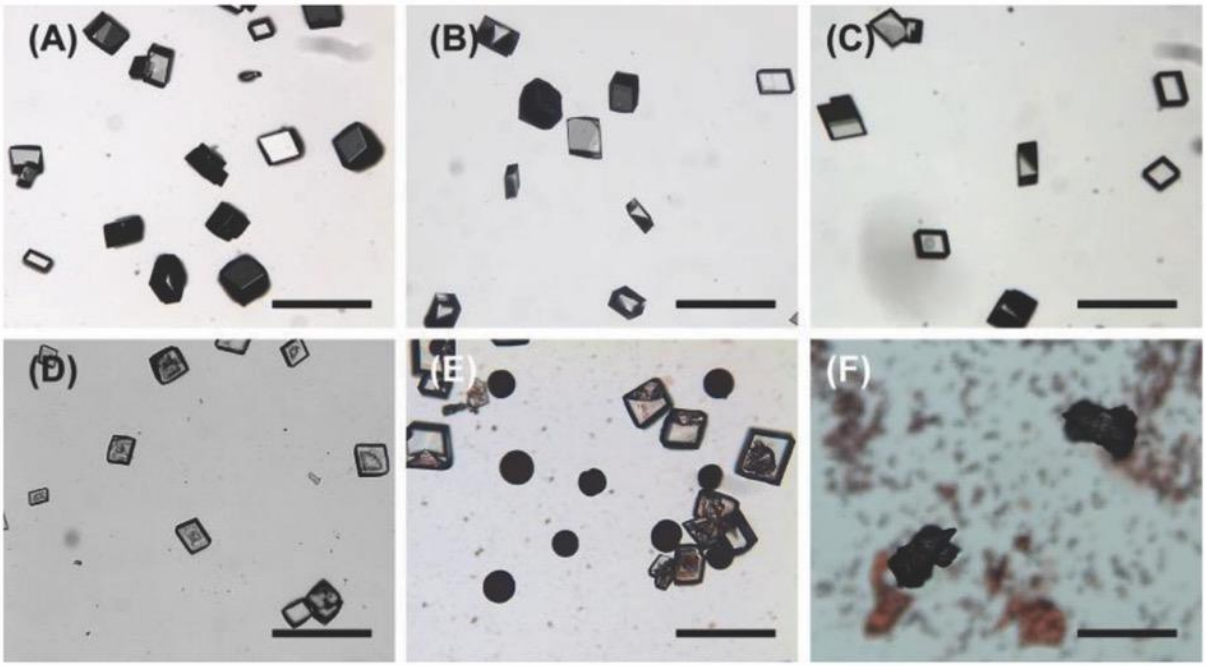

Figure 13. Optical microscope pictures of DOX/calcite hybrid crystals precipitated in the presence of different initial concentrations of DOX. A) No DOX, B) 5×10^{-4} mM, C) 5×10^{-3} mM, D) 5×10^{-2} mM, E) 5×10^{-1} mM, and F) 5 m. Scale bar 100 µm.

The textural features of the DOX/calcite hybrid crystals were further investigated by scanning electron microscopy, as illustrated in Figure 14.

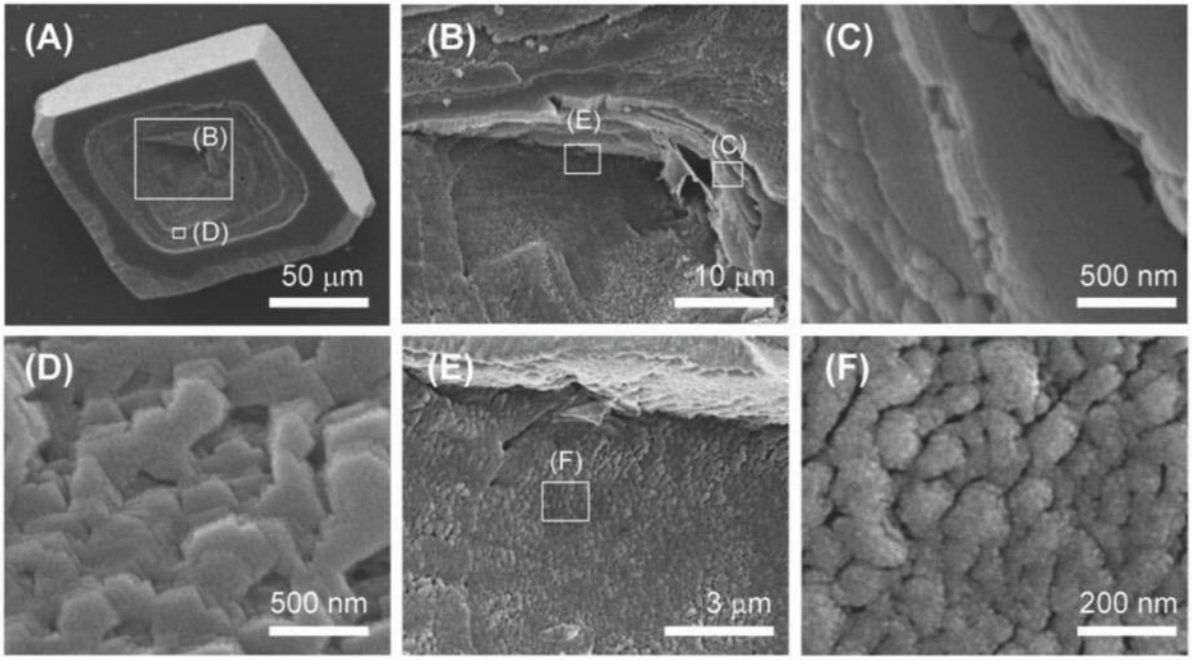

Figure 14. Scanning electron microscope pictures of DOX/calcite hybrid crystals precipitated in the presence of 5×10^{-2} mM DOX. Textural details of different region of the crystal in (A) are illustrated. The rectangle indicates the region of magnification and the subscript the corresponding picture.

Each crystal was characterized by the presence of a rounded cavity at the center of one of the {10.4} faces. The diameter of this cavity increased from inside to outside and changed among crystals. The wall of the cavity was stepped, with each step formed by a flat (10.4) face and some unspecific rough riser. Moving toward the center of the crystal, the thickness of the steps decreases from about 500 to less than 200 nm. The surface of the (*hk.l*) face showed the presence of packed spheroid nanoparticles, of about 100 nm, on which particles of few nanometers were observed. The formation of hoppers was explained by limited diffusion of constituent ions toward the growing crystal face. [86,87]In this case, formation of additional crystalline faces on the hole walls supports a mechanism of thermodynamic control of growth spiraling due to the screw dislocations induced by the DOX–calcite interaction. This aspect was further investigated by X-ray diffraction analysis.

2.1.5.3 Effect of DOX Doping on the Lattice Structure of Calcite Crystals

To examine the influence of DOX on the crystal structure of the hybrid crystals formed in the presence of the optimal concentration 5×10^{-2} mM of DOX, high-resolution synchrotron powder diffraction (HRXRD) measurements were carried out on the 11-BM beamline (Argonne National Laboratory, Argonne, USA). These measurements allowed, by determination of lattice distortion parameters, to ascertain whether DOX indeed is incorporated into the calcite lattice. We have already demonstrated that when organic molecules are incorporated into an inorganic crystalline host they induce lattice distortions [88-90] and lead to unique microstructures. [89,90] This has been shown both in biogenic crystals

as well as in bioinspired calcite [91] and ZnO. [92,93] The procedure of the measurements has been described extensively elsewhere. In short, we applied Rietveld analysis and line profile analysis on the full diffraction patterns.

The measurements were performed on the control calcite sample, DOX/calcite hybrid sample and on the DOX/calcite hybrid sample after a mild thermal annealing at 250 °C for 2 h. Analysis of the diffraction patterns indicates a single calcite phase in all measured samples (see Figure 15 as an example).

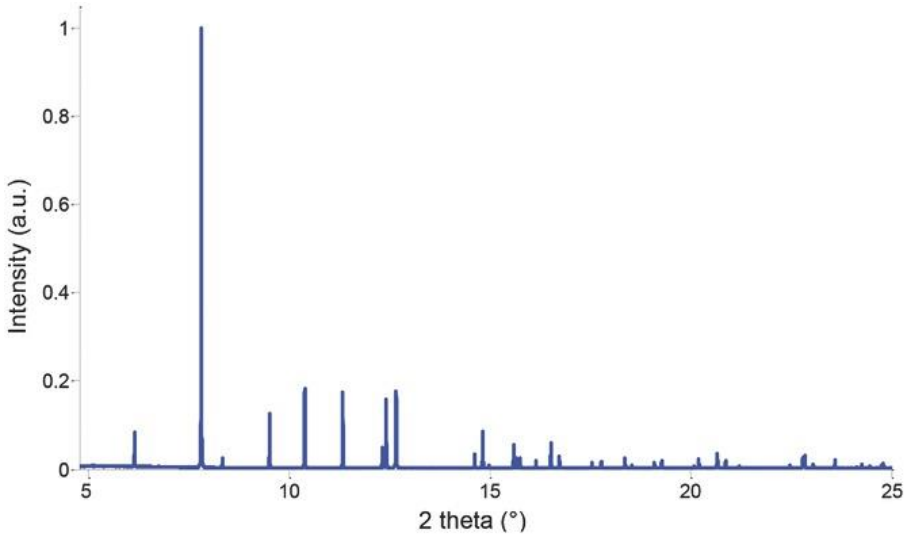

Figure 15. HRXRD diffraction profile of the DOX/calcite hybrid crystals precipitated in the presence of 5 × 10^{-2} mM DOX.

The (104) diffraction peak of DOX/calcite hybrid crystals shifts toward a smaller Bragg angle, which indicates lattice expansion compared to the control sample (Figure 16). This lattice distortion is due to the incorporation of DOX inside the calcite crystal. In Figure 16 the (104) diffraction peak of the hybrid crystal is split. The splitting is due to the fact that the majority of the crystals well incorporate DOX, while some of them do not. After the mild annealing treatment, the diffraction peak shifts back to that of the control sample. The lattice distortion relaxes as the organics are burnt out. The postannealing peak becomes considerably wider, the full width at half maximum (FWHM) doubles (from 0.006° to 0.0126°) and is symmetrical. This phenomenon was also observed in previous cases such as those of biogenic crystals [90] and for crystals that contained amino acids incorporation. [93-95] The cause of the broadening after annealing has been discussed previously, but in short, it stems from the formation of new interfaces as the organics are burnt out.

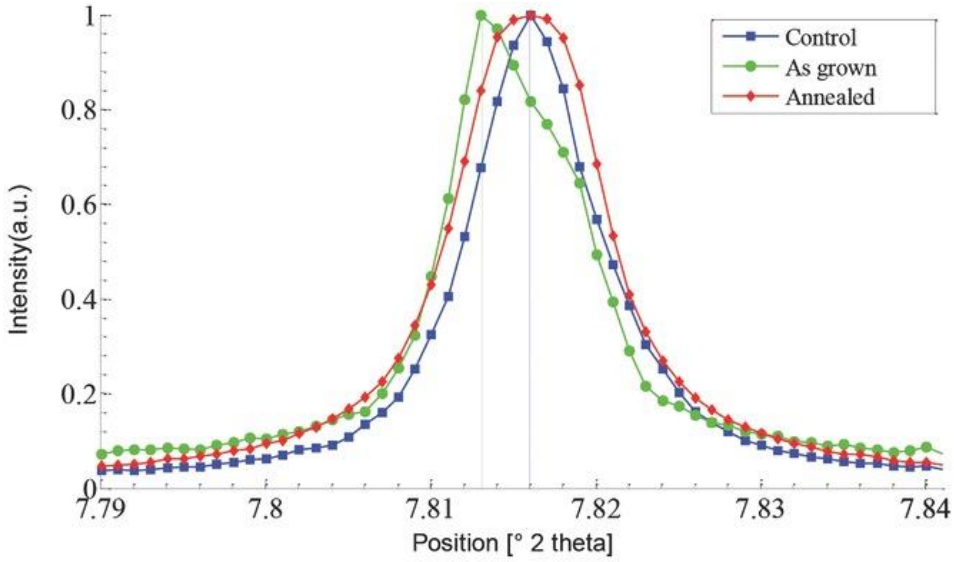

Figure 16. The (104) calcite diffraction peak for control calcite (blue), DOX/calcite hybrid crystals (green) and after thermal annealing (red).

Rietveld structure refinement analysis was applied to all diffraction spectra utilizing the GSAS software and the EXPGUI interface. [96] This analysis determined the lattice distortion, see Table 2. The strain along the *a,b* and *c* axes are almost equivalent (≈8 × 10^{-4}) and of positive sign (i.e., expansion) (Figure 17). The volume change due to the incorporation is 0.24%, which may imply that the level of DOX incorporation is about 0.24% in volume.

Table 2. Quantitative data of lattice parameters, lattice distortions, unit cell volume and goodness of fit parameters for the Rietveld refinement fit (χ^2)

DOX concentration in solution [m]	***a,b* parameters [Å]**	**Strain *a,b*-axis**	***C* parameter [Å]**	**Strain *c*-axis**	**Unit cell volume [Å^3]**	**χ^2**
–	4.990380	–	17.063950	–	368.03	4.334
5 × 10^{-2}	4.994405	8.066×10^{-4}	17.077791	8.111×10^{-4}	368.92	2.303
5×10^{-2} annealed	4.990319	−1.222×10^{-5}	17.064249	1.752×10^{-5}	368.02	3.754

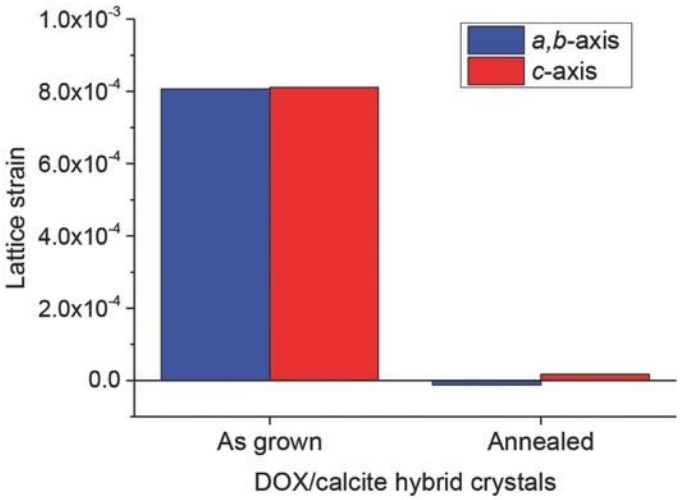

Figure 17. Lattice distortions before and after thermal annealing for DOX/calcite hybrids compared to calcite control.

We further performed line profile analysis on the diffraction spectra. This allowed extraction of microstructural parameters (coherence length and microstrain fluctuations). Single diffraction peaks were fitted to a Voigt function, which enabled independent evaluation of the contributions of the Lorentzian and Gaussian types, which correlate to the coherence length (crystallite size) and microstrain fluctuations, respectively. The profile fitting was performed using the Gnuplot 4.7 interface on the most intense calcite (104) peak (Figure 18). The results revealed noticeable reduction in crystallite size (threefold) upon annealing, which were accompanied by an increase in the averaged microstrain fluctuations, similar to biogenic and other biomimetic crystals in which intracrystalline organic molecules exist.

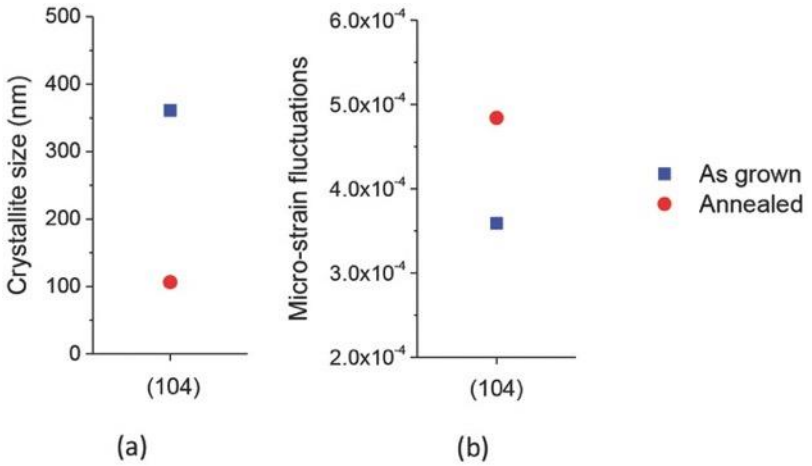

Figure 18. A) Crystallite size (nm) and B) microstrain fluctuations shown before (blue square) and after (red circle) thermal annealing at 250 °C for 120 min for the DOX/calcite hybrid crystals along the (104) crystallographic plane.

2.1.5.3.1 Quantification and Distribution of DOX in the DOX/Calcite Hybrid Crystals

An evaluation of the total amount of DOX adsorbed in the calcite crystal was carried out by combining UV–Vis spectroscopy, for the determination of DOX, and flame atomic absorption spectroscopy, for the determination of Ca^{2+}. A loading of 0.3 ± 0.1 wt% was determined.

The spatial distribution of DOX in calcite crystals was also evaluated by assessing the DOX fluorescence by confocal laser scanning microscopy. Figure 19 shows the fluorescence images obtained by a *z*-stacking of DOX containing crystals. All longitudinal sections of the crystal display a homogeneous fluorescence intensity indicating that DOX was uniformly embedded in the crystal and that the drug is not simply adsorbed on the crystal surface. No luminescence could be detected from the reference crystal grown in the absence of DOX.

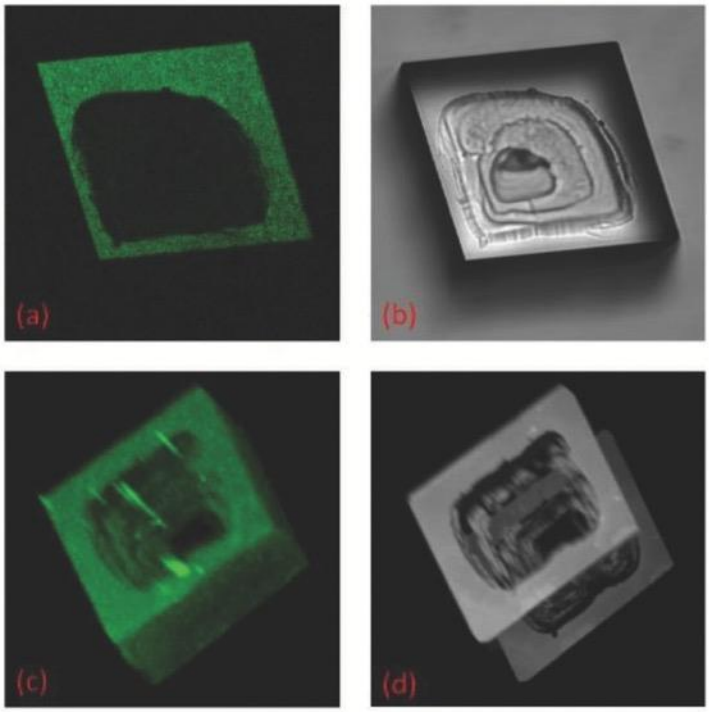

Figure 19. A,B) Single xy plane and C,D) 3D reconstruction of A,C) a z-stacking of a DOX/calcite crystal in fluorescence and B,D) reflection mode. The photodetector was set up in the wavelength range of the DOX emission and of the DOX excitation.

2.1.5.3.2 Targeted DOX Release

As expected, the drug carrier was pH-sensitive (Figure 20). The DOX release kinetics from DOX/calcite crystals was measured by UV–vis spectrophotometry in a citrate buffer at a pH of 5.6. The release of DOX was active for 72 h. The same measurements performed at a pH of 7.4 in PBS (phosphate buffered saline) did not show any detectable release of DOX. The drug release from the hybrid crystals is controlled by the dissolution rate of the $CaCO_3$ host crystals. [81] In PBS we do not observe significant calcite crystals dissolution (see Figure 20) and as a consequence no UV signal at 499 nm.

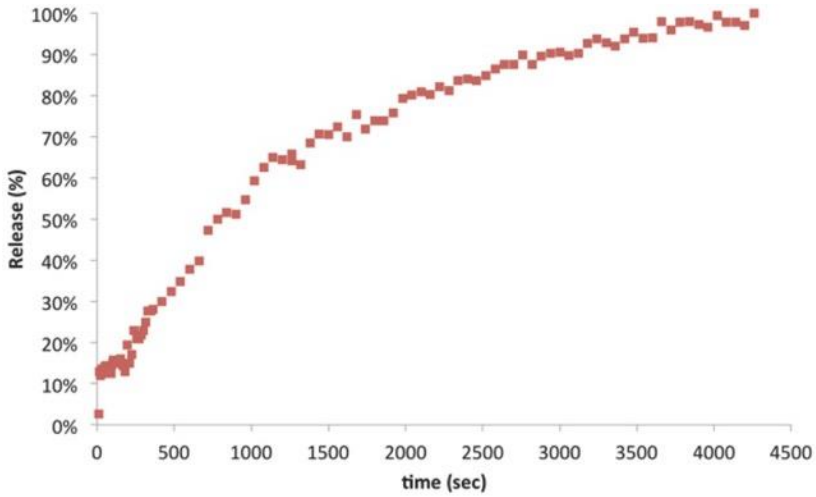

Figure 20. Kinetics of DOX release from DOX/calcite hybrid crystals in citrate buffer at pH 5.6.

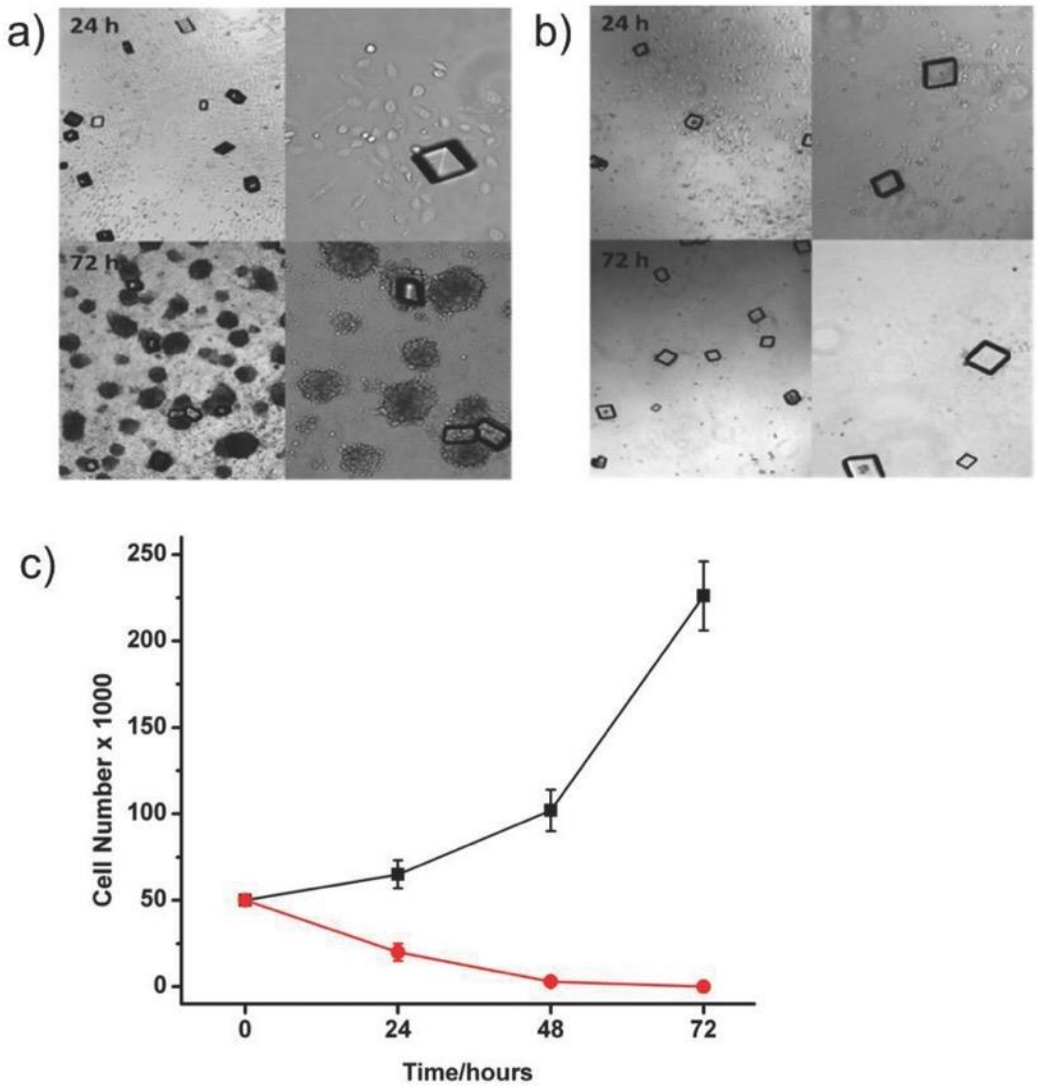

Figure 21. A) MCF10A RasV12 cells cultured with calcite crystals and B) DOX/calcite hybrid crystals. Acquisitions were carried out at 24 and 72 h. C) Growth curves of MCF10A RasV12 expressing cells in complete culture medium in the presence of calcite crystals (squared black) and of DOX/calcite hybrid crystals (circle red). Average values ± SD of (trypan blue negative) cell number from three independent experiments/time point.

2.1.5.3.3 In Vitro Test of the DOX/Calcite Hybrid Crystals

The pharmacological activity of DOX/calcite hybrid crystals was tested in vitro on cell cultures. The in vitro cancer model used is based on the activation of the Ras oncogenic pathway. Human nontumorigenic breast epithelial cells (MCF10A) were subjected to retroviral (pBabe vector) infection to express the oncogenic form of Ras. [97]

We cultured the transformed MCF10A cells in the medium in the presence of DOX/calcite hybrid crystals or calcite crystals as control. Cell growth was followed by cell counting. The contrast phase optical microscopy images at 24 and 72 h from plating are presented in Figure 21.

Pure calcite crystals revealed no toxic effect on MCF10A transformed cells. MCF10A cells in the presence of these crystals followed the same cell growth curve of the control cells. In contrast the DOX/calcite hybrid crystals demonstrated heavy toxic effects for the cells (Figure 21) and after 72 h the mortality reached 100%. This result suggests that the activity of DOX is retained in the crystal and that the DOX/calcite hybrid crystals are able to release the drug in proper concentrations. The MCF10A transformed cells induce specifically a drug release as a consequence of the cell metabolism, which decreases the local pH as a result of the increased lactate production.

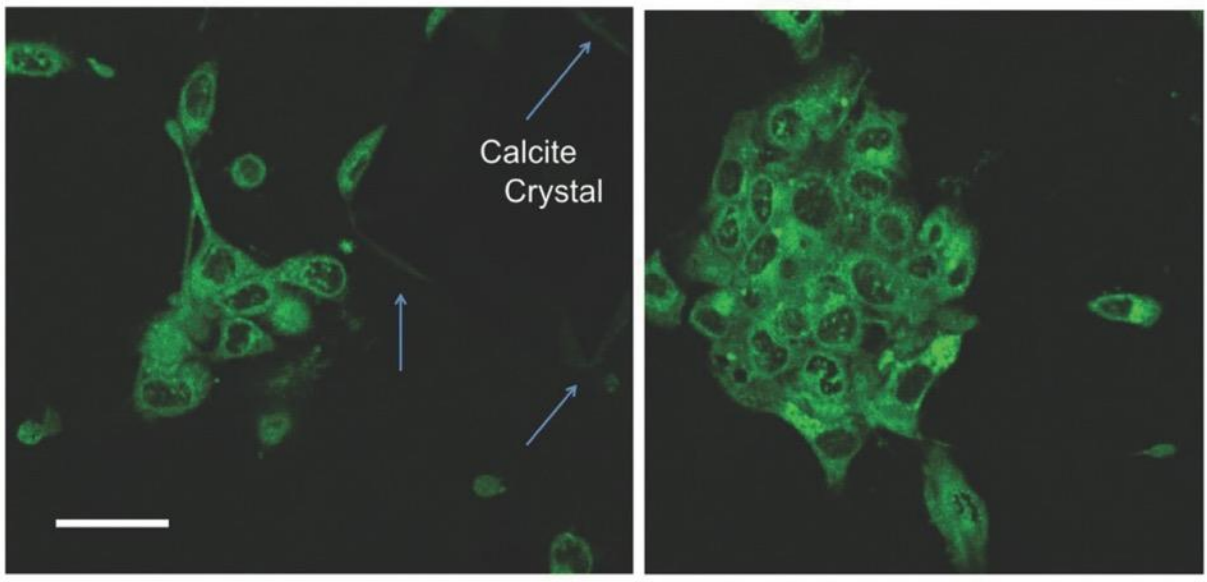

Figure 22. Uptake of DOX by cancer cells. The light blue arrows highlight the DOX release by the DOX/calcite crystal. The arrows indicate the periphery of the calcite crystals. In this figure DOX fluorescence is not visible in the DOX/calcite crystal, as compared to the fluorescence in Figure 19, because the DOX signal of the cells is much larger than that of the crystal due to the cellular uptake that increases the DOX local concentration and saturate the signal. Scale bar 50 µm.

The DOX uptake by MCF10A RasV12 cells from the DOX/calcite hybrid crystals was assessed by following DOX fluorescence signal, using confocal laser fluorescence microscopy (Figure 22). After 6 h of cell culturing in the presence of the crystals, the RasV12 MCF10A cell

fluorescence images clearly indicated that the DOX molecules were inside the cells. Confocal measurements on the cells growth on pure calcite do not show the typical fluorescence of DOX. The DOX signal was clear on the dissolving surfaces of the DOX/calcite crystals (see arrows in Figure 22). The molecular distribution in the cells is in accord with previous results for the same treatment time. [98]

2.1.5.4 Conclusion

In conclusion, this study presents a complete structural and biological characterization of DOX/$CaCO_3$ crystals as a system to specifically target drugs to particular cells or tissues. The pH sensitive $CaCO_3$ solubility can release entrapped molecules only when the dissolution of the crystals occurs and allows zero-leakage of drugs at the physiological pH. The main results can be summarized in the following points: (i) calcite is able to host DOX molecules efficiently; (ii) the entrapment occurs along specific crystallographic directions; (iii) the release of DOX is controlled by pH and occurs preferentially in proximity of the surface of cancer cells; (iv) the released drug molecules are uptaken by the cancer cells, killing them.

2.2 Aim of the project

As previously discussed, calcite single crystal composites cover a crucial role both for understanding biomineralization processes and to obtain functional materials.
The work described in this chapter addresses the double goal of clarifying the mechanism of embedding of additives into single crystals and exploiting this knowledge to prepare new advanced materials.
Pursuing this goal, multiple approaches have been adopted:

- Crystallization of calcium carbonate in the presence of small molecules, such as the fluorescent tag calcein and the anti-inflammatory drug oxytetracycline, both used to mark calcifying tissues growth, and the differentiation factor retinoic acid;
- Crystallization of calcite in the presence of nanoparticles. The use of core-shell nanoparticles, that is to say nanoparticles composed of a core surrounded by a shell of a different material, allows to include functionalities in the core while keeping constant the shell, optimizing the surface chemistry to enhance the entrapment. Both magnetic nanoparticles and silica nanoparticles carrying a variety of functional groups on the surface have been used;
- Precipitation of biogenic calcium carbonate from living organisms in the presence of nanoparticles in order to obtain “bionic crystals”. This approach takes advantage of the ability of living organisms to precisely control mineral deposition to deposit hybrid calcite crystals including functional nanoparticles, thus obtaining a higher control on morphology and polymorphism of the final material.

2.3 Small molecules entrapment within calcium carbonate

2.3.1 Introduction

Ions and small molecules can be entrapped into the lattice of inorganic crystals, acting as impurities that interact with the growing mineral phase. [99,100] This phenomenon is widespread in Nature and examples can be found in the inclusion of Mg^{2+} ions, amino acids and macromolecules into calcified skeletons and the entrapment of ions into minerals. The same principles can be exploited to include molecules into the crystalline lattice of calcium carbonate to draw conclusions on the mechanisms governing this process, such as the presence of particular charge distribution or functional groups in the additive, and to obtain new hybrid materials. The inclusion of small molecules into $CaCO_3$ single crystals is often approached using a trial and error method and little information relating the nature of the additive with its inclusion rate are available. Negatively charged groups such as carboxylated and sulphonated groups have been associated with a higher chance of inclusion since many of the macromolecules embedded into biomineralized skeletons are acidic and rich in aspartate and glutamate residues. [10,12,16] Borukhin et al. studied the entrapping of different amino acids into calcite single crystals using high resolution synchrotron radiation and they stated that parameters crucial for inclusion are whether the additives are acidic or basic, the relative pKa values of the carboxyl and amino terminal groups, their size, and their rigidity. [93] Many additives that can chelate calcium have been shown to become entrapped into the lattice and some of them have been used to mark the growth of calcified tissues. [101,102] In this chapter, the effect of calcein, a fluorescent molecule with two EDTA moieties, oxytetracycline, an anti-inflammatory drug, and retinoic acid, a differentiation factor for stem cells, on the crystalline habit and polymorphic distribution of calcite and aragonite has been investigated. The former gives new insights on the crystal growth process while the others produces a delivery system, exploiting the ability of $CaCO_3$ to dissolve in the acidic extracellular matrix, characteristics of inflamed and cancer tissues.

2.3.2 Results & discussion

2.3.2.1 Calcein

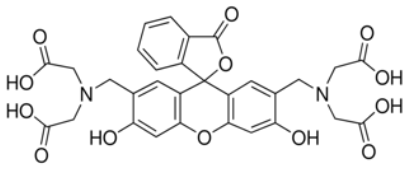

Figure 23. Calcein structure

Calcein (Figure 23), a derivative of fluorescein synthesized in the '50, has been widely use to selectively titrate calcium in solution, even in the presence of interfering ions such as Mg^{2+}.[103,104] It has been used since the early '90 to mark growing shells of various organisms, taking advantage of its fluorescence that can be easily detected with a fluorescence microscope, thus allowing to relate the mineral phase with the time at which it was deposited.[101,105-108] Despite that, no studies shedding light on the effect of this dye on $CaCO_3$ are readily available.

Crystals were prepared by using the vapor diffusion method, consisting in the diffusion of $NH_{3(g)}$ and $CO_{2(g)}$ obtained from the decomposition of $(NH_4)_2CO_{3(s)}$, into a Ca^{2+} solution containing the dye. This method is relevant for biomineralization process due to the slow increase of the concentration of CO_3^{2-} ions in the crystallization solution. It exploits carbonate speciation in water resembling the process suggested to occur in living systems, in which carbonic anhydrase the supply of carbonate to the calcification site. [109]

In our experimental setting, calcite precipitated when solely Ca^{2+} was present in the crystallization solution, while aragonite was the main polymorph obtained when Mg^{2+} is co-present with a Mg^{2+}/Ca^{2+} molar ratio equal to 4. [6,110]

While no detectable inhibition or promotion of precipitation due to the presence of calcein was observed, as evaluated by the measure of total Ca^{2+} deposited in each experiment, the presence of calcein promotes precipitation of magnesium calcite on the expense of aragonite and when 400 µM calcein is present in the crystallization solution only 4 wt.% of aragonite co-precipitate (Figure 24, Figure 25 and Table 3). This trend could be related to the higher complexation constant of calcein for Ca^{2+} than for Mg^{2+} that, increasing the concentration of free Mg^{2+} ions with respect to Ca^{2+}, affects $CaCO_3$ supersaturation of the precipitating solution and the thermodynamic stability of magnesium calcite and aragonite.

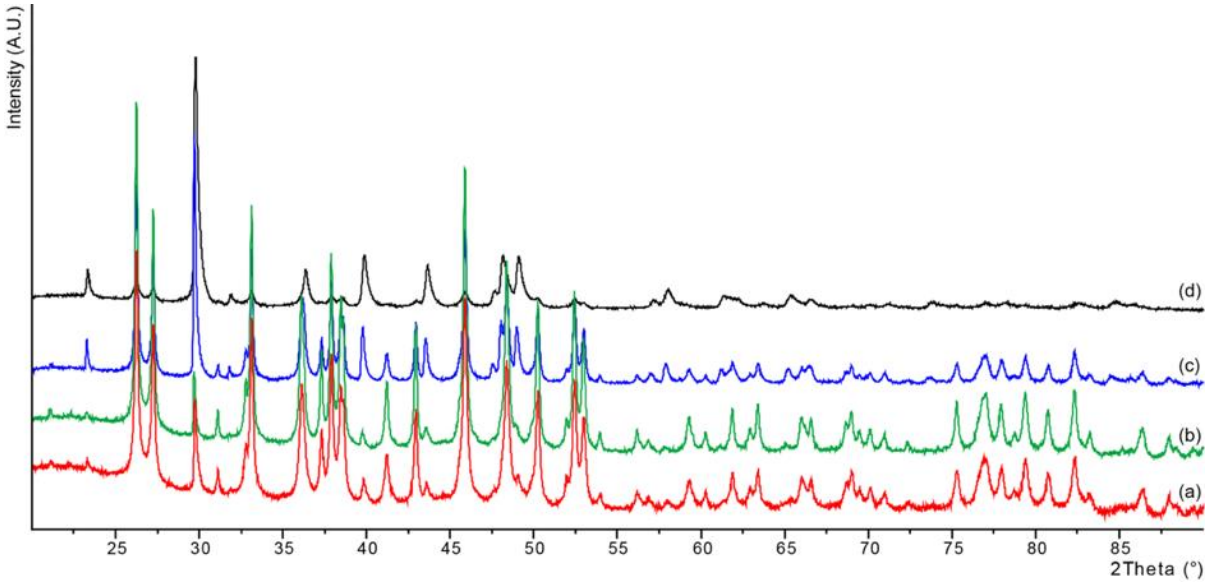

Figure 24. High resolution X-ray powder diffraction patterns of crystals grown from a solution containing 40 mM Mg^{2+} and 10 mM Ca^{2+} (a) without additives and in the presence of (b) 4 µM (c) 40 µM and (d) 400 µM calcein. Wavelength converted from 0.4959 Å to 1.5406 Å.

Table 3. Aragonite and Mg-calcite content of samples grown in the presence of 40 mM Mg^{2+} and 10 mM Ca^{2+} in the presence of different calcein concentrations.

Calcein / µM	Aragonite / wt.%	Mg-calcite / wt.%
blank	93	7
4	98	2
40	76	24
400	4	96

A similar effect can be observed in calcite samples, where in the presence of calcein pure calcite is obtained, while in the absence of the additive traces of aragonite and vaterite are present.

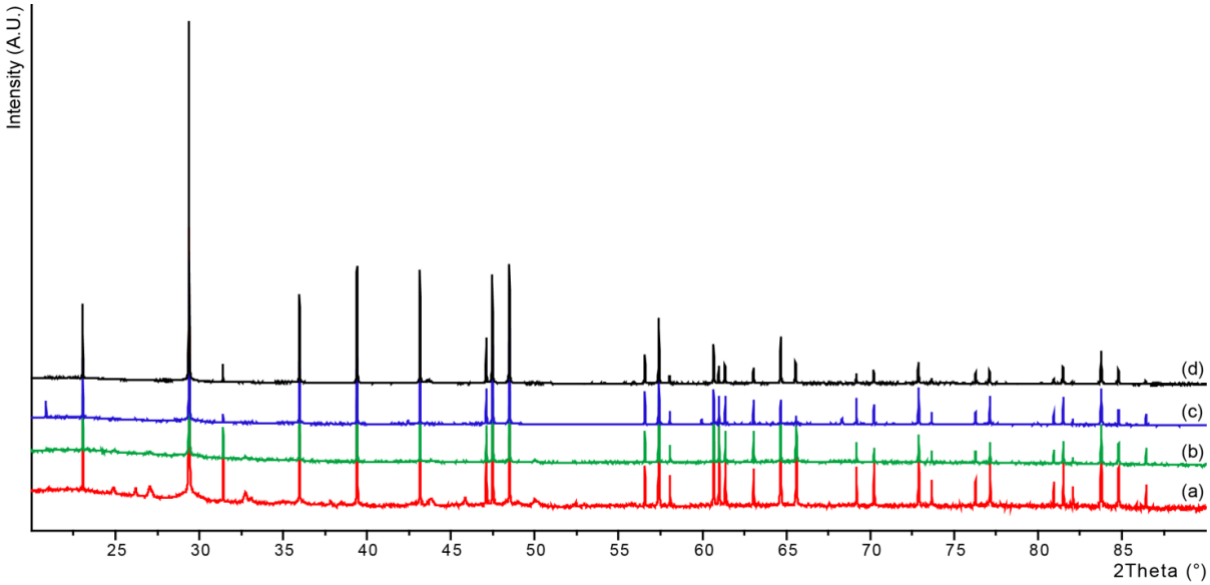

Figure 25. High resolution X-ray powder diffraction patterns of calcite crystals grown (a) without additives and in the presence of (b) 4 µM (c) 40 µM and (d) 400 µM calcein. Wavelength converted from 0.4959 Å to 1.5406 Å.

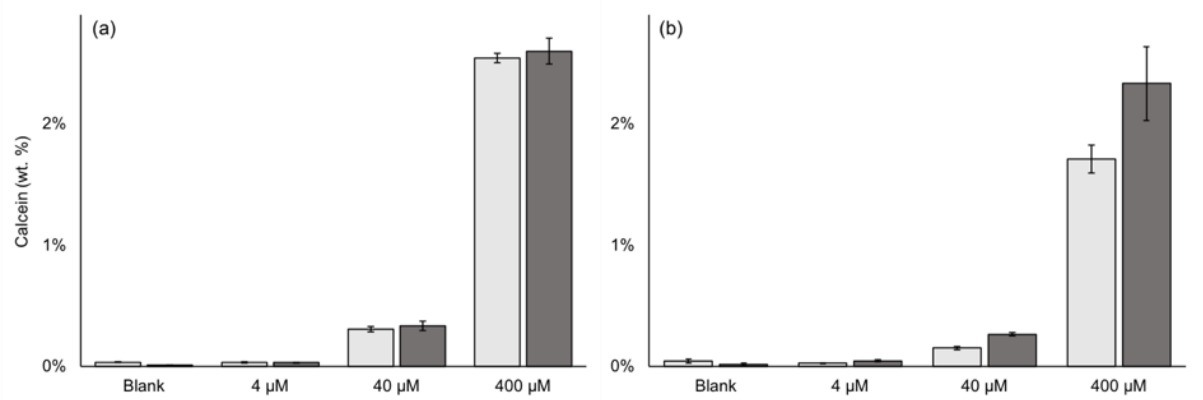

Figure 26. Calcein content (wt.%) measured in (a) calcite and (b) aragonite precipitated in the presence of the different dye concentration examined. The data on bleached samples are reported in light grey and those on untreated ones are reported in dark grey.

Calcein loading was calculated with respect to the calcium content measured on pristine precipitates and bleached ones. Calcite crystals entrap significantly higher quantity of calcein as compared to aragonite ones ($p \leq 0.05$, Figure 26). Interestingly, bleaching does not significantly change the content of calcein in calcite crystals ($p > 0.05$), while in aragonite crystals it significantly decreases after bleaching ($p \leq 0.05$), implying that the quantity of surface adsorbed dye is meaningful only for aragonite. Indeed, it has been reported that aragonite has a surface area almost ten times higher than that of calcite, justifying a higher adsorption efficiency for mass unit of $CaCO_3$. [111]

The experimental data indicate that the amount of dye entrapped within calcium carbonate increases increasing its concentration solution. On the other side, the percentage of dye removed from the solution during the crystallization process decreases with its concentration. This observation indicates that 40 µM, the concentration used in *in vivo* experiments, does not allow a maximum of loading into calcium carbonate in the experiments carried out *in vitro*. In fact, increasing the concentration to 400 µM results in the increase of the loading of almost ten times. Thus, if an organism accumulates calcein at the mineral growing sites, a higher entrapment can be achieved, with an enhancement of the fluorescence signal.

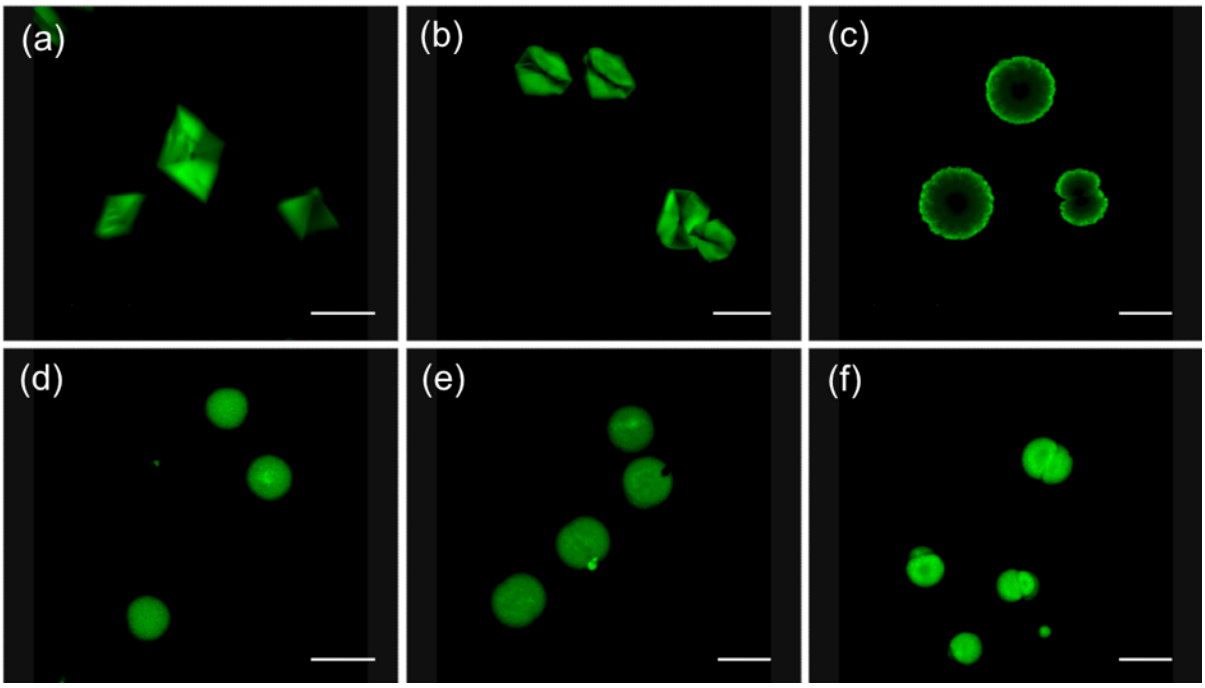

Figure 27. Confocal micrographs of calcite crystals grown in the presence of (a) 4 µM, (b) 40 µM and (c) 400 µM calcein and aragonite crystals grown in the presence of (d) 4 µM, (e) 40 µM and (f) 400 µM calcein. Scalebar is 50 µm.

The spatial distribution of calcein entrapped within the crystals was investigated by confocal microscopy. This analysis was carried out on the samples chemically bleached prior to the imaging to exclude any fluorescence contribute from the dye adsorbed onto crystal surfaces. Confocal images of calcite crystals grown in the presence of calcein (Figure 27a-c) show an inhomogeneous distribution of the dye within the crystals. The dye localizes preferentially on rhombohedral faces, which in the spherulitic calcite (Figure 27c) are more extended in the external layers. In addition to this, it cannot be excluded that the signal from the center of the spherulitic crystals is not detected, since the thickness of the sample and the geometry of the microscope do not allow the laser to reach the top layers. Confocal images of aragonite

crystals grown in the presence of calcein (Figure 27d-f) show a homogeneous distribution of the dye inside the crystals. Since aragonite particles, as well as those of magnesium calcite, are composed of packed acicular crystals, [112] it can be assumed that the dye is mainly entrapped among the crystalline domains, and only partly is embedded within the lattice. This observation is also confirmed by the results on dye loading, which show a significant reduction of loading after bleaching.

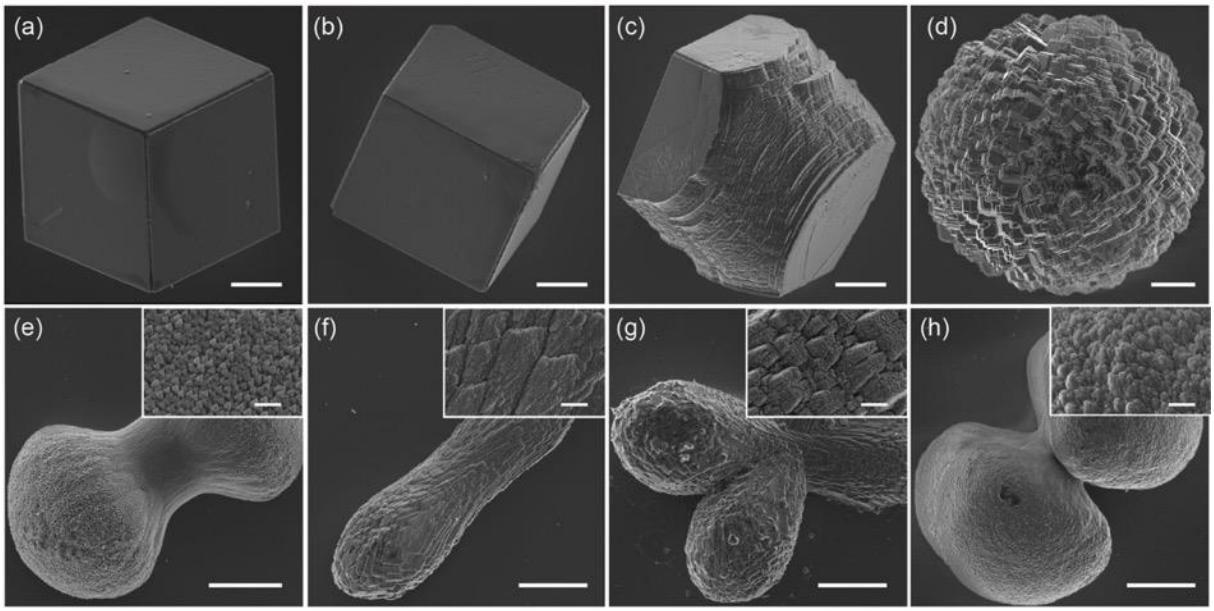

Figure 28. SEM images of crystals grown in the presence of 10 mM Ca^{2+} (a) without additives and in the presence of (b) 4 µM, (c) 40 µM and (d) 400 µM calcein and crystals grown in the presence of 10 mM Ca^{2+} and 40 mM Mg^{2+} (e) without additives and in the presence of (f) 4 µM, (g) 40 µM and (h) 400 µM. Scalebar is 10 µm in the main picture and 1 µm in the inset.

SEM images show that the dye modifies calcite crystal shape and morphology (Figure 28a-d). When grown in the presence of 4 or 40 µM calcein, the crystals show only {10.4} rhombohedral faces (Figure 28b) or demonstrate additional crystalline {hk.l} faces almost parallel to the c-axis, respectively. The presence of 400 µM calcein in the crystallization solution leads to the formation of spherulitic aggregates exposing small {10.4} faces. A similar trend in the evolution of the shape and morphology with the increase of the concentration of an additive has been observed in the presence of block copolymer poly(ethylene glycol)-block-poly(methacrylic acid), [113] which similarly to calcein contains carboxylate functional groups. Aragonite crystals precipitated in the absence of additives (Figure 28e) present a dumbbell shape, composed of needles with a triangular section. Crystals grown in the presence of 4 µM or 40 µM calcein (Figure 28f-g) appear elongated and show {hk0} faces, which dimensions decrease with the increase of the concentration of the additive. The mass ratio of magnesium calcite increases at higher calcein concentration and, when crystals are

grown in the presence of 400 µM calcein (Figure 28h), they are composed of small particles aggregated in a dumbbell shape in which the characteristic stepped {01.1} faces are observable. [114]

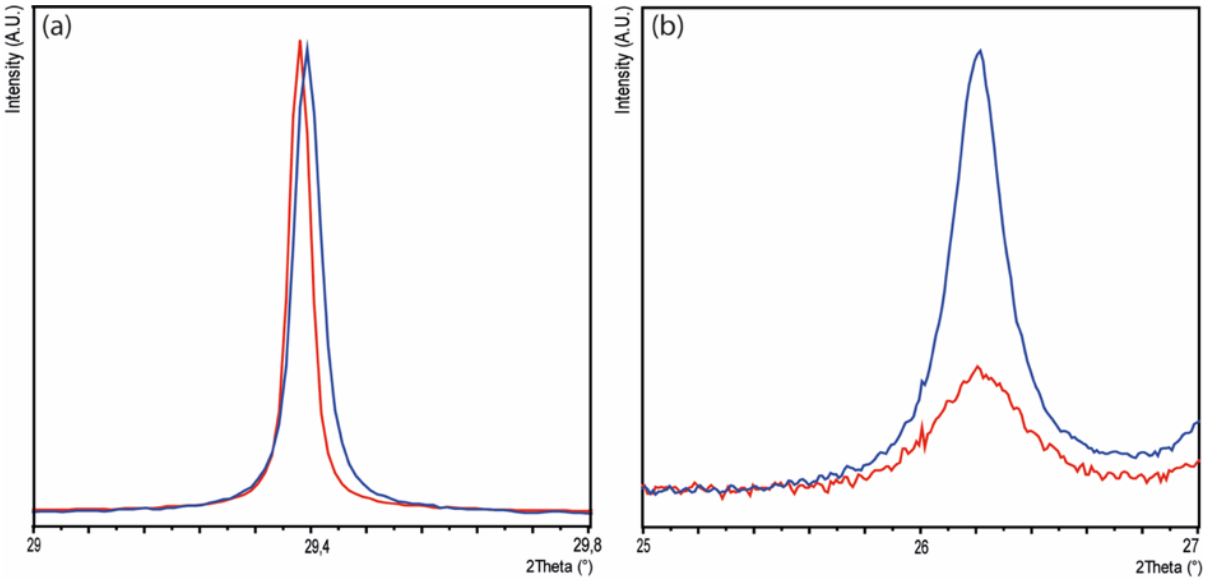

Figure 29. (a) The (104) calcite diffraction peak for control calcite (blue) and calcite grown with 400 µM calcein (red) and (b) the (111) aragonite diffraction peak for control aragonite (blue) and aragonite grown with 400 µM calcein (red). Wavelength converted from 0.4959 Å to 1.5406 Å.

Rietveld refinement applied to the high resolution X-ray powder diffraction data allowed quantifying the $CaCO_3$ polymorphic distribution and the lattice distortions induced by calcein interaction with calcium carbonate crystals. [115,88] The presence of calcein also induces a change in the lattice parameters of calcite (see Table 4). This change is visualized in Figure 29a where the (104) diffraction peak of calcite shifts to a lower 2θ value when it is grown in the presence of 400 µM of calcein. This is mainly related to an expansion of the c-axis associable to the entrapping of the additive. No significant shift of aragonite peaks is observed (Figure 29b), indicating that calcein is mainly localized among the crystalline units of aragonite, as suggested by the bleaching results and confocal microscopy experiments and the non-significant variation of the lattice parameters (Table 5). In the magnesium calcite crystals, the lattice distortions are due to a combined opposed effect of calcein and Mg^{2+} ions, with the former expanding the c-axis, as observed for calcite and the latter decreasing the a-axis (Figure 30 and Table 5).

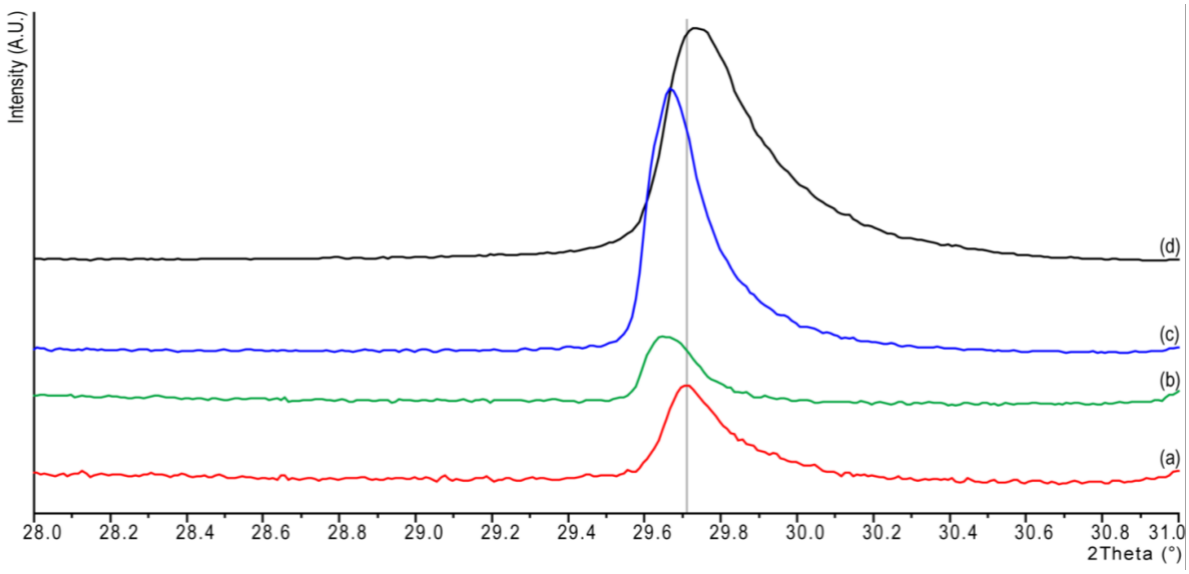

Figure 30. High resolution X-ray powder diffraction patterns in the 28 – 31 2θ(°) range of magnesium calcite crystals grown from a solution containing 40 mM Mg^{2+} and 10 mM Ca^{2+} (a) without additives and in the presence of (b) 4 µM (c) 40 µM and (d) 400 µM calcein. Wavelength converted from 0.4959 Å to 1.5406 Å.

Table 4. Cell parameters and distorsions of calcite crystals grown in the presence of different calcein concentrations.

	Blank	**4 µM**	**40 µM**	**400 µM**
a, Å	4.99053(5)	4.99059(4)	4.99066(6)	4.99048(2)
distortions, a		*1.0E-05*	*2.4E-05*	*-1.2E-05*
c, Å	17.06772(8)	17.06868(8)	17.0713(1)	17.07949(4)
distortions, c		*5.6E-05*	*2.1E-04*	*6.9E-04*

Table 5. Cell parameters and distorsions of aragonite and Mg-calcite crystals grown in the presence of different calcein concentrations.

	Blank		**4 µM**		**40 µM**		**400 µM**	
phase	**Aragonite**	**Mg-calcite**	**Aragonite**	**Mg-calcite**	**Aragonite**	**Mg-calcite**	**Aragonite**	**Mg-calcite**
a, Å	4.9626(1)	4.943(2)	4.96340(8)	4.9489(7)	4.9628(1)	4.9503(4)	4.9566(8)	4.937(5)
distortions, a			*1.6E-04*	*1.2E-03*	*4.0E-05*	*1.5E-03*	*-1.2E-03*	*-1.2E-03*
b, Å	7.9680(2)	4.943(2)	7.9687(1)	4.9489(7)	7.9683(2)	4.9503(4)	7.985(2)	4.937(5)
distortions, b			*8.8E-05*	*1.2E-03*	*-6.5E-04*	*1.5E-03*	*2.1E-03*	*-1.2E-03*
c, Å	5.7515(1)	16.851(3)	5.75352(8)	16.907(2)	5.7517(1)	16.8794(7)	5.7487(9)	17.14(13)
distortions, c			*3.5E-04*	*3.3E-03*	*3.5E-05*	*1.7E-03*	*-4.9E-04*	*1.7E-02*

In conclusion, we studied the effect of calcein, a dye commonly used to mark the growth of calcifying organisms, on the growth of calcite and aragonite crystals in vitro. These data reveal a strong influence of calcein on the precipitation of calcium carbonate, affecting both polymorphic distribution and crystal morphology. Calcein is loaded into the structure of both polymorphs, localizing within the lattice preferentially along (104) planes in calcite crystals and adsorbing among crystalline domains in aragonite. These in vitro observations do not find a documented correspondence in in vivo systems, for which no effect of calcein on the calcification process have been reported so far. Thus, it appears evident that the organisms' capability to control the deposition of the mineral phases can overcome the potential interference caused by calcein.

The work discussed in this paragraph has been published as G. Magnabosco, I. Polishchuk, J. Erez, S. Fermani, B. Pokroy and G. Falini, CrystEngComm, 2018, 20, 4221 DOI: 10.1039/C8CE00853A - Reproduced by permission of The Royal Society of Chemistry

2.3.2.2 Oxytetracycline

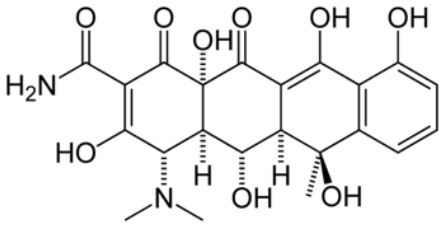

Figure 31. Oxytetracycline structure

Oxytetracycline (OXY) is a broad-spectrum antibiotic of the family of tetracycline (Figure 30). These drugs were found to localize in bone tissue and to retain their structure, that is to say their activity and fluorescence, even when entrapped within the inorganic matrix. [116,117] They adsorb on the surface of $CaCO_3$ crystals and their entrapped may be ascribed to the ability to interact with calcium ions.

As described above, $CaCO_3$ dissolves at low pH values and this feature makes it an ideal candidate as passive drug delivery host to treat diseases characterized by acidic extracellular matrix, such as inflammation and cancer. In this work, the entrapment of OXY into calcite and aragonite was studied in order to obtain a drug delivery system.

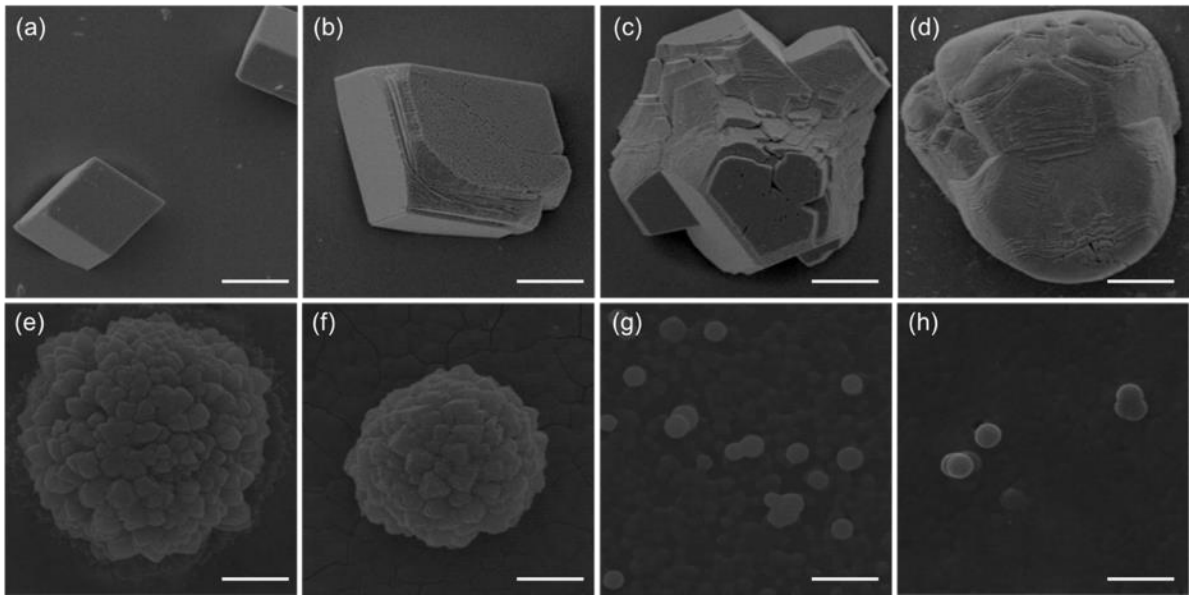

Figure 32. SEM images of crystals grown in the presence of 10 mM Ca^{2+} (a) without additives and in the presence of (b) 2 µM, (c) 50 µM and (d) 500 µM OXY and crystals grown in the presence of 10 mM Ca^{2+} and 40 mM Mg^{2+} (e) without additives and in the presence of (f) 2 µM, (g) 50 µM and (h) 500 µM OXY. Scalebar is 10 µm.

As discussed previously, the effect of an additive on crystalline habit gives preliminary information on the interaction of the additive with the growing crystal. As can be seen in Figure 32 a-d, oxytetracycline strongly affect the morphology of calcite crystals. In fact, even

when the concentration of OXY in the crystallization solution is as low as 50 µM, crystalline aggregates start to form and, when crystals are grown in the presence of 500 µM OXY, crystal faces can not be identified anymore and {hk0} faces forms as a consequence of the crystal/OXY interaction. The presence of OXY in the crystallization solution increases significantly the dimension of the crystals.

On the other hand, aragonite crystals (Figure 32 e-h) are smaller than calcite ones and their dimension decreases with the increase of OXY concentration. At higher OXY concentration, the typical acicular morphology of aragonite crystals disappears, and the surface of the particles becomes smooth. X-ray diffraction confirms that the crystalline phase of the particles is still aragonite.

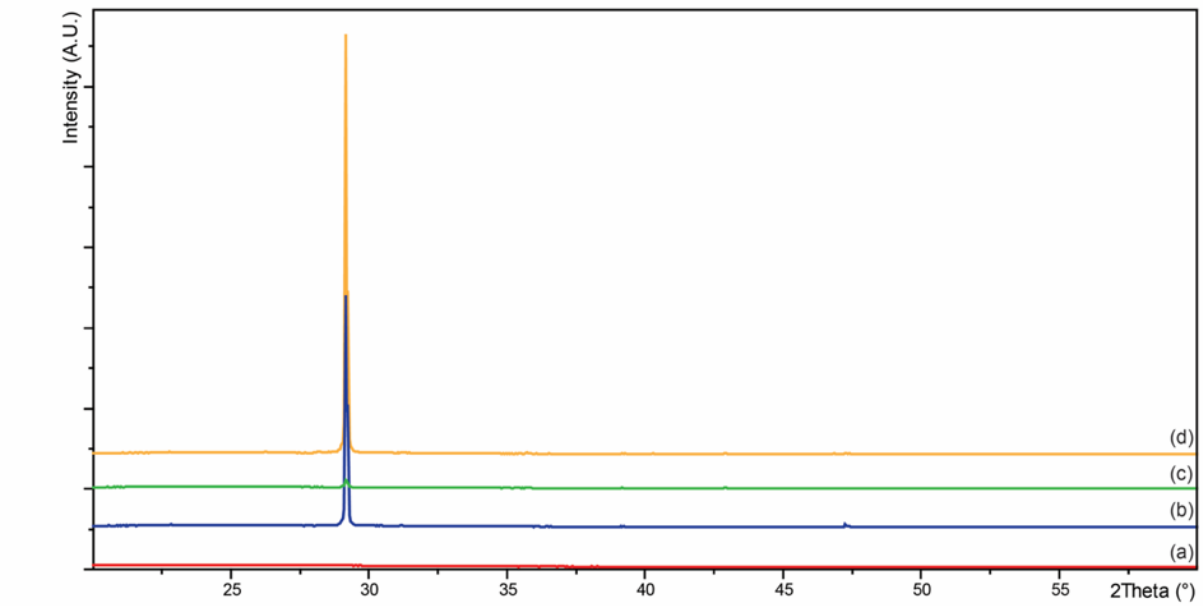

Figure 33. X-ray powder diffraction patterns of calcite crystals grown in the presence of (a) 500 µM (b) 50 µM and (c) 2 µM OXY and (d) without additives.

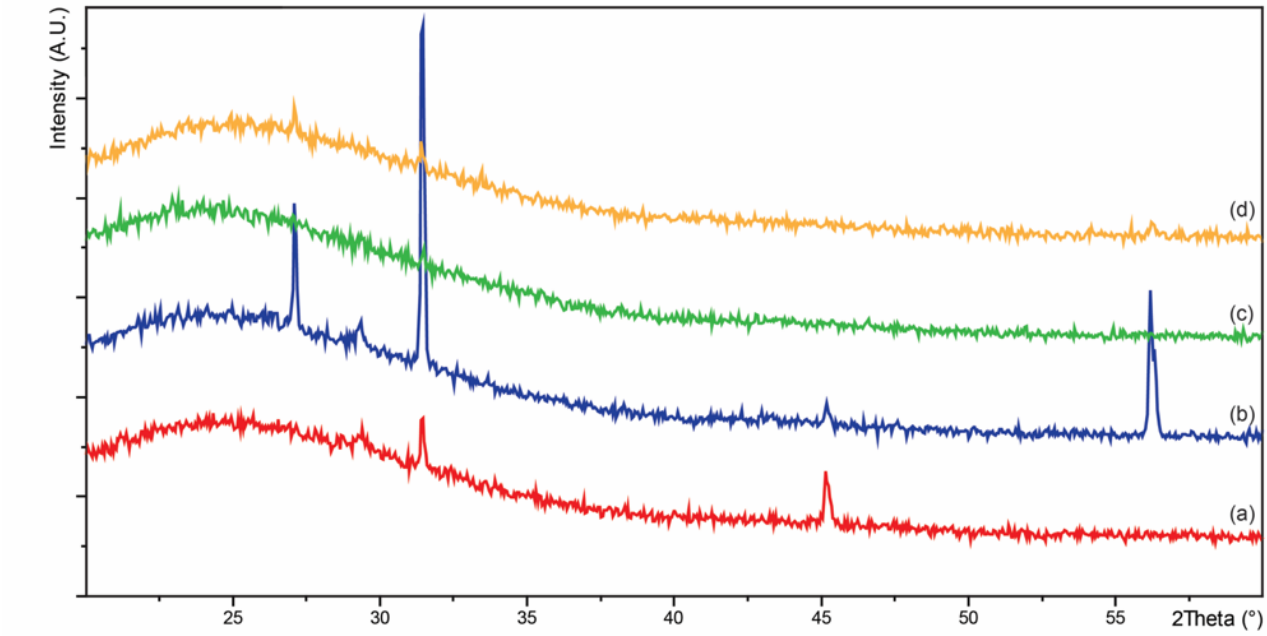

Figure 34. X-ray powder diffraction patterns of crystals grown from a solution containing 40 mM Mg^{2+} and 10 mM Ca^{2+} in the presence of (a) 500 µM (b) 50 µM and (c) 2 µM OXY and (d) without additives.

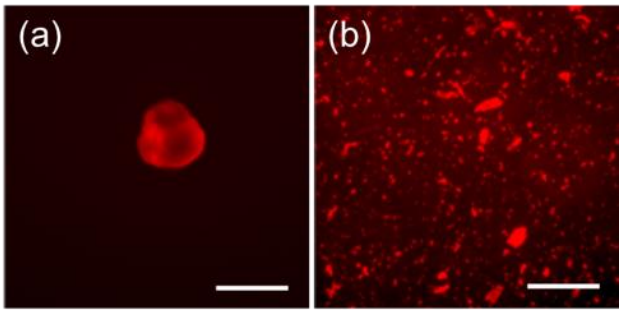

Figure 35. Fluorescence micrographs of (a) calcite and (b) aragonite crystals grown in the presence of 500 µM OXY. Scalebar is 50 µm.

Since OXY absorbs UV-light, its presence and distribution within the crystals can be determined with fluorescence microscopy. As can be seen in Figure 35, both polymorphic forms of $CaCO_3$ grown in the presence of 500 µM OXY show a strong fluorescence, that is higher in aragonite crystals. In the case of calcite, is interesting to notice that fluorescence is higher at the edge of crystalline faces, confirming the adsorption of the additive on the faces that are then expressed.

In conclusion, OXY can be entrapped within calcite and aragonite crystals, as confirmed by the fluorescence of the crystals and the effect on the morphology of the crystals. Aragonite crystals grown in the presence of 500 µM OXY are promising as drug delivery systems due to the small dimension of the final particles.

2.3.2.3 Retinoic acid/calcite micro-carriers into fibrin scaffolds modulate neuronal cell differentiation

The achievement of an efficient modulation of cell differentiation requires controlling and localizing the release of differentiating agents. This can be obtained by the embedding an active molecule in a slow release system localized within the scaffold hosting the cells. [118,119] Calcite, the thermodynamically most stable polymorph of calcium carbonate, can be used as a delivery system for active molecules due to the ability to (i) embed molecules within its crystalline lattice forming hybrid crystals and (ii) selectively release them only upon dissolution, which occurs at the acidic pHs as those typical of inflamed and cancer tissues. These hybrid crystals enable the modulation and the localization of the release and provide a sustained dosage of the entrapped agents over an extended time, reducing the initial burst release.

The capability of calcite to host various molecules and macromolecules within its crystalline lattice has been discovered in biominerals. Berman et al demonstrated that glycoproteins (about 0.3 wt.%) were entrapped within magnesium calcite single crystals that form sea urchin spine, increasing their resistance to breakage and cleavage. [120] Since that, the entrapment of macromolecules within crystalline lattice has been observed in almost every biomineral. [12,13,16]

In parallel, taking inspiration from nature, many efforts have been made toward the production of hybrid single crystals embedding various single molecules and molecular assemblies to obtain novel functional materials. [5,45,115,121] Among many cases of study, doxorubicin/calcite single crystals were synthesized and provided a controlled release system for cancer cell treatment. [19] Doxorubicin was uniformly embedded within the calcite crystals and slowly released only in the proximity of the targeting cancer cells. When there was a technological vision, intrinsically colorless and diamagnetic calcite single crystals were turned into colored and paramagnetic solids through incorporation of Au and Fe_3O_4 nanoparticles without significantly disrupting the crystalline lattice of calcite. [47,122] Sulfonated fluorescent dyes with different emission wavelength were successfully occluded within calcite lattice and white emission was obtained by precipitation in the presence of the right ratio of different dyes. [20] Other than obtaining a white emitting device, the inclusion of dyes in calcite lattice allows their easy localization and the study on mechanism of their interaction with the growing surface.

Perlucin, a recombinant biomineralization protein, fused to green fluorescent protein gets incorporated into the calcite structure and induces concentration-dependent anisotropic lattice distortions along the host's c-axis. [123] Bigger species such as micelles [22,46,124] and block co-polymer have been occluded within calcite single crystals and it was verified that the

formation of a single crystal composite enhances mechanical proprieties of the calcite host, similarly to what can be observed in nacre. [18]

Ascertained the remarkable ability of calcite to act as a host matrix for various water dispersed species, this paper: (*i*) describes for the first time the synthesis of calcite crystals entrapping retinoic acid (RA) and (*ii*) reports on the inclusion of these composite crystals into fabricated bioactive fibrin scaffolds to control the release of RA inducing the differentiation of the cells. [125]

The main advantage of using this system compared to a direct incorporation of the RA in the fibrin scaffold is that the calcitic micro-carriers avoid a single burst release owing to the slow pH dependent dissolution of the $CaCO_3$ crystals, which can be used for a fine tuning of the release towards cells.

The final system is completely biocompatible and biodegradable as $CaCO_3$ dissolves into calcium and carbonate ions, which can be easily eliminated by the organism. Furthermore, this system allows for an extended release in the case of an implanted device, avoiding the need of sequential drug administrations.

In order to verify the possibility of using single crystals of calcite as micro-carrier of molecules to regulate cell growth processes, the RA was used as a model of differentiation factor of stem cells and fibrin as bioactive scaffold. RA is a potent metabolite of vitamin A and it acts as a growth and differentiation factor in many tissues. [126,127] Fibrin is commonly used as a biological scaffold for stem or primary cells to regenerate adipose tissue, bone, cardiac tissue, cartilage, liver, nervous tissue, ocular tissue, skin, tendons and ligaments. [128-133] [134] In the present study, neuroectodermal stem cells (Ne4C) and human neuroblastoma cells (SH-SY5Y) were used, in minimal essential medium to test if the delivery of RA from the calcite carriers could induce their differentiation.

Calcite crystals have been grown in the presence of a 200 µM RA solution. In this condition solely calcite crystals formed. The SEM images reported in Figure 36 do not show relevant morphological differences between pure calcite crystals and ones grown in the presence of 200 µM RA. RA/calcite hybrid single crystals show the typical {104} faces and have a uniform size distribution of 5 µm along the c-axis. These crystals had a loading of 0.12 wt. % of RA.

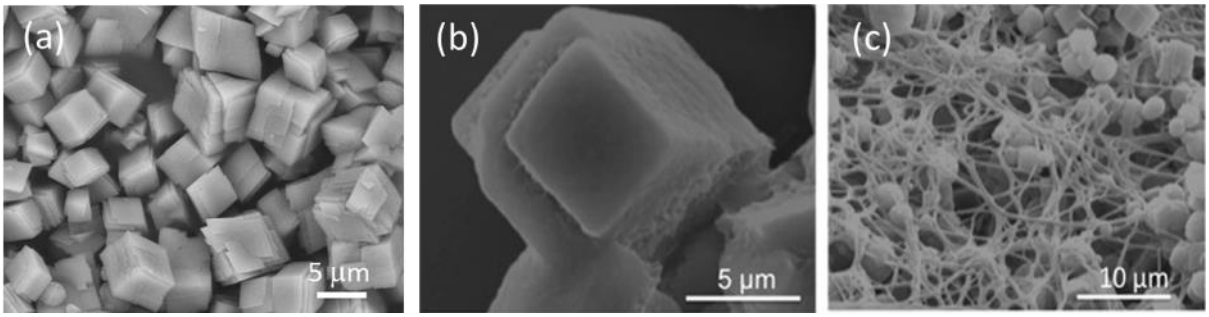

Figure 36. SEM images of a) calcite crystals, b) calcite crystals grown in the presence of 200 µM RA and c) the same crystals are occluded within the fibrin structure.

The incorporation of RA into calcite lattice has been investigated by high resolution synchrotron powder X-ray diffraction. Rietveld refinement of collected diffraction patterns shows that the inclusion of RA into calcite structure causes lattice strain of 7.62×10^{-5} along the c-axis and of 3.53×10^{-5} along the a-axis compared to pure calcite crystals. Not only this strain was removed after a thermal treatment at 250 °C for 180 min but we also observed broadening of the post-annealed diffraction peaks. We performed line profile analysis of the (104) diffraction peak collected from the crystals containing RA before and after annealing (Figure 37). As can be concluded from the analysis, after annealing the crystallite size decreases while microstrain fluctuations increase as compared to those prior heat treatments. This latter observation is common for the behavior of composite bio-crystals upon annealing [91] and demonstrates unequivocally that the RA is located within the crystalline lattice of the calcite.

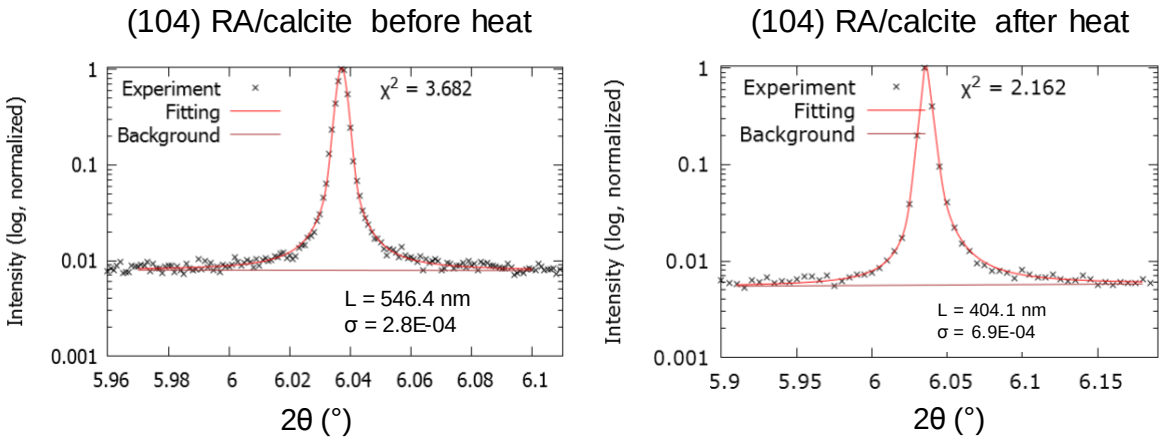

Figure 37. Line profile analysis of the (104) calcite diffraction peak collected on calcite crystals grown in the presence of 200 µM RA before (left) and after thermal treatment (right), where L is crystallite size, σ – microstrain fluctuations and χ^2 – goodness of fit parameter.

The combination of RA/calcite hybrid single crystals with fibrinogen and thrombin yielded to a gel slightly less transparent compared to that made of pure fibrin, due to the light scattered by the embedded particles (Figure 38). SEM microscope image (Figure 36c) illustrates the homogeneous inclusion of the micro-carriers within the fibrin fibrous matrix.

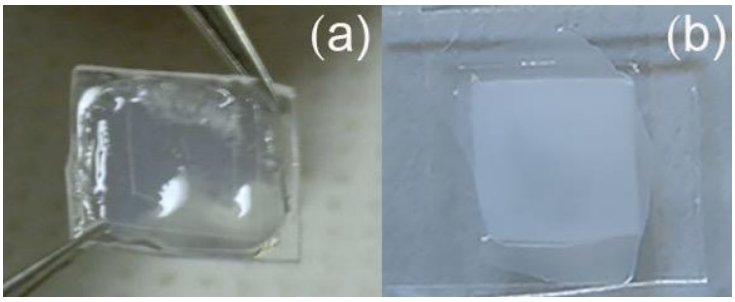

Figure 38. Fibrin. (a) without and (b) with RA/calcite hybrid single crystals.

The differentiation of NE-4C/SH-SY5Y cells into a densely interconnected neuronal network was first assessed seeding the cells in the presence of the RA/calcite hybrid single crystals and it is shown in the Figure 39a, b. This step demonstrates that the micro-carriers loaded with RA are able to induce the differentiation by locally releasing the active molecule to the cells. This effect is related by the slow etching of the crystals in the slightly acidic environment in the proximity of these cell lines. [135] When the same experiment was carried on pure calcite no differentiation took place and the crystals displayed almost no toxicity (Figure 39c, d).

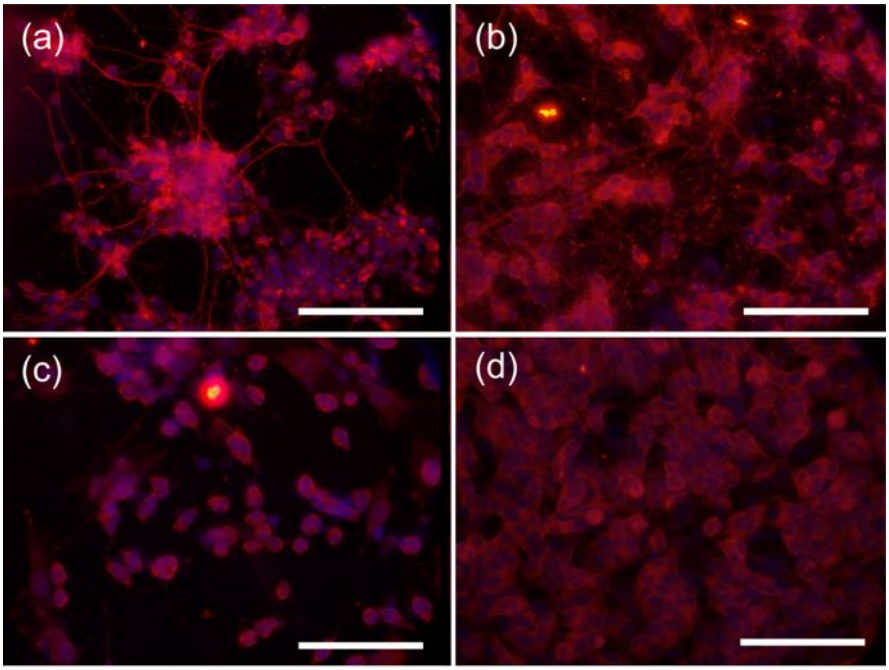

Figure 39. Immunofluorence images. (a and b) Cell differentiation day 8 through retinoic acid released from the calcite/RA hybrid single crystals; (a) shows the formation of the neuronal network of Ne4C in astrocytes, (b) shows the differentiation of SH-SY5Y cells into neurons. The blue color (DAPI) marks the nuclei of all the cells. The differentiation is visualized by the specific labelling of III β-tubulin, a typical marker of neuronal processes (red). (c and d) cells after 8 days of incubation without retinoic acid in the presence of calcite crystals; (c) Ne4C cells, (d) SH-SY5Y cells. The blue color (DAPI) marks the nuclei of all the cells. The red color (III β-tubulin) marker the microtubule and the neuronal filament. Scale bars 100µm

A progressive cell morphological change was observed during the differentiation process. After prolonged time of incubation (from day 5) neuronal processes become visible and the active areas are almost completely covered by a dense layer of mature neuronal cells. Figure 4a and b shows typical fluorescence microscopy results of the neuronal network at eight days upon induced differentiation (day 8) after co-staining with specific probes. This clearly demonstrates the differentiation of the majority of cells and the formation of a dense neuronal network with long and interconnected neuronal filaments. These images show that there is also a substantial growth of the network in presence of RA-loaded microcrystal.

The differentiation of the cells in the RA/calcite-fibrin composite was monitored following the same protocol. It is worth underlining that this is a 3D scaffold fully biodegradable and bioresorbable.

The images displayed in Figure 40 were obtained at the end of the differentiation, Ne4C cell successfully differentiated on the scaffold as supported by the immunofluorescence staining.

Optical and SEM micrographs revealed that the neurite processes are still attached to the area of the microcrystal, indicating that the calcium present both in the crystals and in the fibrin does not negatively affect the cell viability and the neuronal maturation.

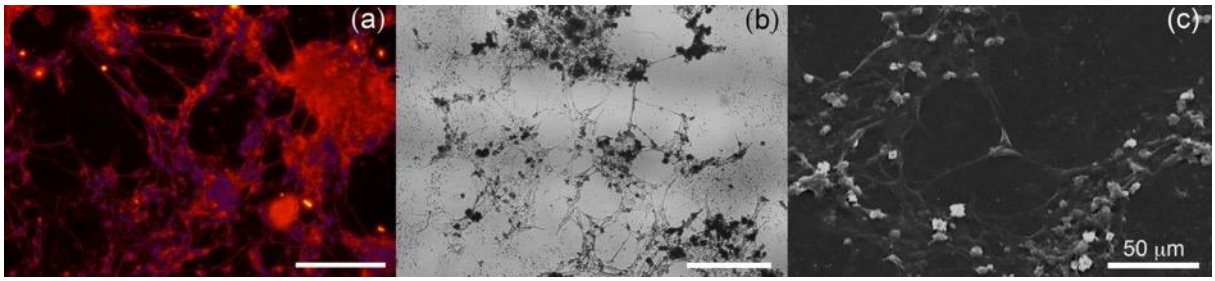

Figure 40. Ne4C cell differentiation day 8 through calcite/RA hybrid single crystals. Immunofluorence images: (a) optical images: (b) SEM images: (c) the formation of the neuronal network of Ne4C in astrocytes. Scale bars 100μm

To confirm the result obtained by the release of RA by means of the calcite crystals, we carried out control tests on pure calcite. FiguresFigure 41-Figure 43 show respectively the results obtained by differentiating the cells on a simple fibrin gel or on unloaded calcite crystals where the RA was supplied in solution (top).

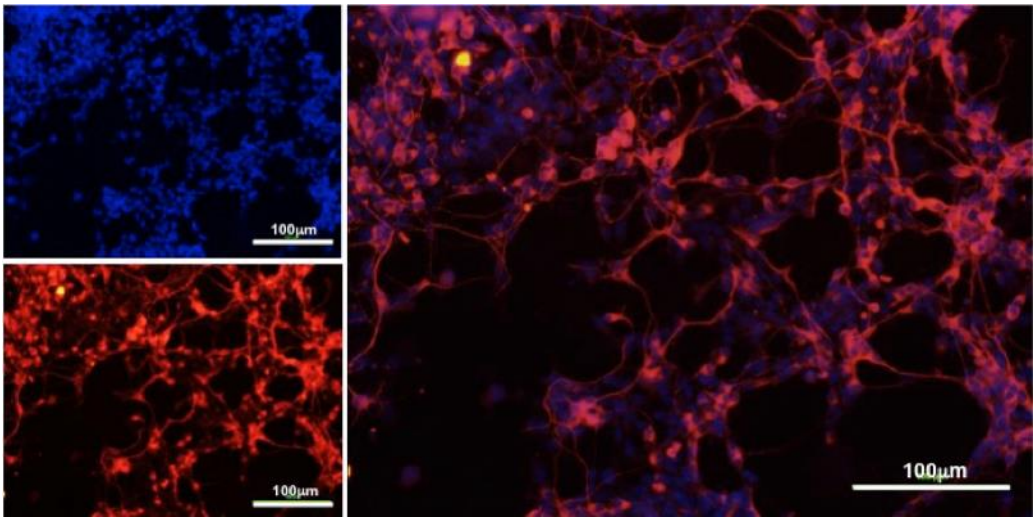

Figure 41. Immunofluorence images: cell differentiation on a fibrin gel at day 8 through the external supplying of 1μM retinoic acid. The images show the formation of the neuronal network of Ne4C in astrocytes.

There are not differences compared to the results obtained by incorporating RA in crystals, thus confirming the retention of the proprieties of RA even after the release from the crystals. In Figure 42 (c and d) and Figure 43 (c and d) it is shown that in the presence of crystals without RA both cell lines continue to proliferate as stem cells with no differentiation.

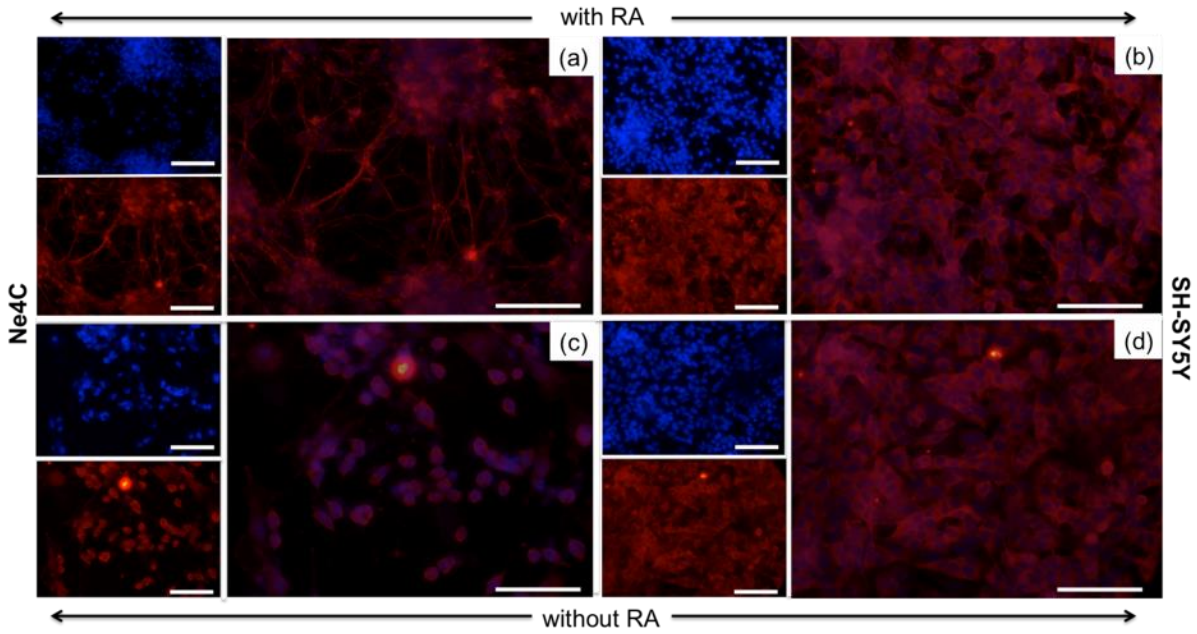

Figure 42. Immunofluorence images: cell differentiation at day 8 through externally supplied 1µM retinoic acid in solution in the presence of calcite crystals; (a) show the formation of the neuronal network of Ne4C in astrocytes, (b) show the differentiation of SH-SY5Y cells into neurons; (c) and (d) show the cells after 8 days of incubation without retinoic acid in the presence of calcite crystals.

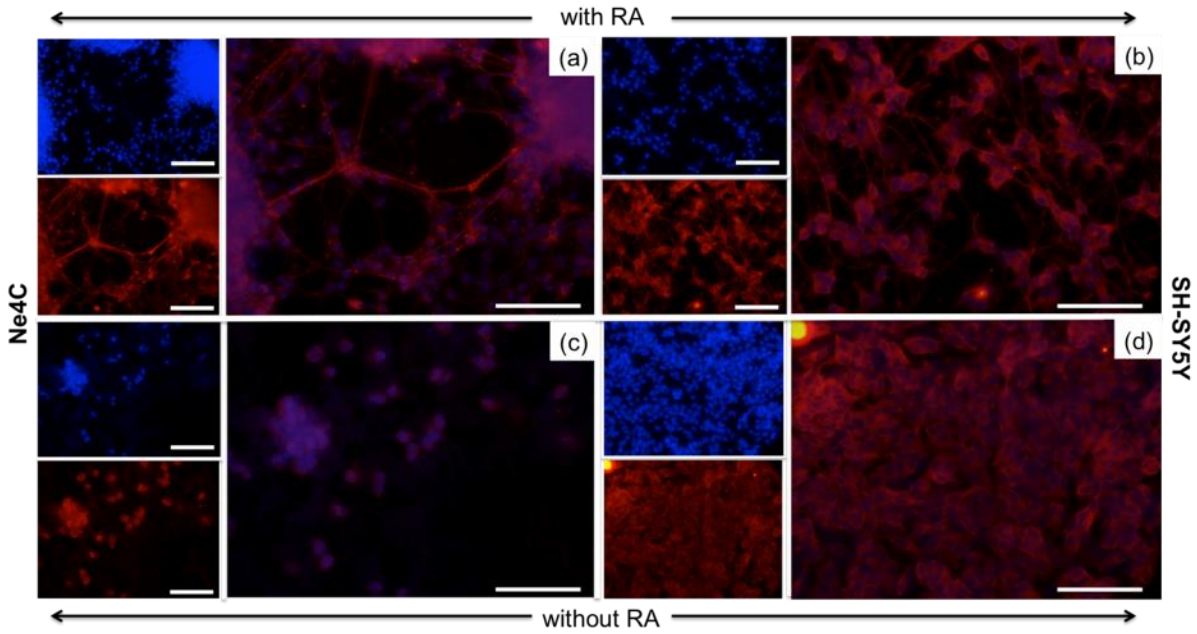

Figure 43. Immunofluorence images: cell differentiation at day 8 through externally supplied 1µM retinoic acid in solution in the presence of calcite crystals; (a) show the formation of the neuronal network of Ne4C in astrocytes, (b) show the differentiation of SH-SY5Y cells into neurons; (c) and (d) show the cells after 8 days of incubation without retinoic acid in the presence of calcite crystals.

These images, obtained at the end of the days of differentiation, reveal that the neurite processes are still attached to the area of the microcrystals, indicating that the presence of calcium does not negatively affect the cell viability and the neuronal maturation.

We developed a novel composite material able to host and induce proliferation and differentiation of stem cells based on the combination of fibrin gel and calcite micro-carriers. Fibrin acts as a fully bioresorbable 3D scaffold where cells adhere and migrate and whose degradation can be tuned using proper enzyme inhibitors. RA can be successfully incorporated within calcite crystals and released in an acidic environment, as the one in proximity of the chosen cell lines. Differentiation towards neuronal cells has been achieved and cells formed a three-dimensional neuronal network in the environment provided by the composite scaffold. Our results pose the bases for the fabrication of implantable scaffold for new active coating of implantable devices both to prevent nosocomial infections, [136] and to promote the integration in the hosting organism. [137]

2.3.3 Methods

2.3.3.1 Crystal growth

Synthesis of OXY or calcein/$CaCO_3$ hybrid crystals

Calcium chloride dehydrate was purchased from Fluka, magnesium chloride hexahydrate was purchased from Sigma Aldrich and anhydrous ammonium carbonate was purchased from Acros Organics. All reagents were ACS grade and used as purchased. Calcium carbonate crystals were prepared using the vapor diffusion technique, consisting in the diffusion of NH_3 and CO_2 vapor obtained from the decomposition of 3.5 g of $(NH_4)_2CO_3$ into 750 µL of 10 µM $CaCl_2$ solution contained in a 24-well multiwell dish containing glass coverslips and covered with aluminum foil with a hole of ø1 mm on each well in a closed desiccator. The appropriate amount of additive was added to each well. To obtain aragonite $MgCl_2$ was added to $CaCl_2$ to obtain a 4:1 Mg:Ca ratio. The precipitation process was allowed to proceed for 4 days, after which each well was washed 3 times with DI water and once with ethanol.

Synthesis of RA/calcite hybrid crystals

Calcite crystals were synthesized by dropwise addition of 2 ml of 500 mM Na_2CO_3 to a solution containing 2 ml of 500 mM $CaCl_2$ and 1 ml of 1 mM RA under vigorous stirring. After 24 hours the crystals were collected by filtration under vacuum using a RC 0.45 µm filter (Sartorius), thoroughly washed with distilled water and ethanol, and then air-dried. The solution in which the crystallization occurred was kept for quantification of the residual RA.

Calcite crystals for HRXRPD have been synthesized using the vapor diffusion method. Briefly, ammonia and CO_2 obtained from decomposition of solid $(NH_4)_2CO_3$ were allowed to diffuse in 750 µL of a solution containing 10 mM $CaCl_2$ and 200 µM RA in a closed desiccator. The crystallization process was allowed to proceed for 4 day, after which the crystals were washed 3 times with distilled water, once with ethanol and air-dried.

2.3.3.2 Characterization

Fluorescence microscopy

Confocal imaging A Leica TCS SL microscope was used to perform confocal microscopy, using the software “Leica confocal software”. Samples for confocal imaging were precipitated directly onto glass coverslip as described above and mounted on glass slides by using Canada balsam (Sigma Aldrich-C1795). Samples were irradiated with 488 nm laser and emission was observed in the 520 nm-700 nm range. Slices were collected in z-stack mode and stacked to obtain the presented images.

Calcein loading 750 µL of 0.1 M citrate buffer pH 4.5 were added to each well in order to dissolve the crystals. Dissolution was allowed to proceed for 4 hours on a rocking plane.

Absorbance spectra were collected using an Agilent Cary 300-Bio UV-Vis spectrophotometer and calcium content was measured with flame atomic absorption spectroscopy (Perkin-Elmer AAnalyst 100). The calcein content was computed by dividing the quantity of calcein obtained from the UV-Vis spectra by the calcium carbonate quantity computed by calcium measures with atomic absorption.

RA loading RA content in the produced crystals was evaluated by UV-Vis spectroscopy measuring the intensity of the RA absorption band at 290 nm. Briefly, the residual RA was quantified after the precipitation process and the RA wt.% was calculated as the ratio between RA and the calcium carbonate obtained during the synthesis. RA calibration curve was obtained using the standard addition method to consider the matrix effect due to the Ca^{2+} still present in the solution.

X-Ray diffraction

High resolution X-Ray diffraction High resolution X-Ray powder diffractogram were collected at European Synchrotron Radiation Facility (Grenoble, France), beamline ID22, using a wavelength of 0.4959 Å. Diffraction patterns were converted to Cu Kα wavelength (1.5406 Å) for easier understanding.

SEM imaging SEM images were collected using a HR-SEM (ULTRA Plus, Zeiss, Oberkochen, Germany) or a FEG-SEM (Hitachi S4000) after coating the samples with 3 nm of gold.

The composite material fibrin-microcrystals was characterized by scanning electron microscopy (SEM) imaging using a Hitachi S4000 FEG-SEM. Samples had to undergo a preparation typical of biological materials: 2.5% gluteraldehyde in phosphate buffered saline (PBS) buffer was added at 4 °C for 1 hour. Each sample was then rinsed three times in PBS for 5 minutes before being incubated for 1 hour with 1% osmium tetra-oxide (OsO_4). The samples were then rinsed 3 times with distilled water 10 minutes each time. A sequential dehydration in 50%, 75%, 95% and 99% ethanol was then performed before coating the sample surface with a 10 nm thick gold layer by sputtering.

Fabrication of micro-carriers with retinoic acid

The composite material was prepared by first combining fibrinogen (10 mg/ml) with thrombin (0.5 NIH unit corresponding to 0.065 µg/ml) to achieve the fibrin network formation, then the microcrystals were added to the reticulating fibrin to get a full incorporation.

For the experiments where only the micro-carriers were present, both calcite and vaterite microcrystals were drop casted onto glass slides where cell lines were then seeded.

β-Tubulin III Antibody Staining

Tubulins are the major components of cellular cytoskeleton, class III β-tubulin is a microtubule element expressed exclusively in neurons and is a popular marker specific for this kind of cells

and thus to assess a proper differentiation towards these lines. [138] The detailed steps of the staining protocol are: cultured cells are fixed with 4% paraformaldehyde in 1X PBS for 15-20 minutes at room temperature; they are then washed twice with 1X washing buffer. To permeabilize cells 0.1% Triton X-100 in 1X PBS is added for 1-5 minutes at room temperature and then washed twice with 1X washing buffer. Blocking solution (BSA) and primary antibody (Anti-β-Tubulin III) in blocking solution are applied for 30 minutes and 1 hour respectively at room temperature and then washed three times (5-10 minutes each) with 1X wash buffer. Secondary antibody (Alexa fluor 594) freshly diluted in 1X PBS is incubate for 30-60 minutes at room temperature and washed three times with 1X washing buffer. Following this washing step, nuclei counterstaining can be performed by incubating cells with DAPI (4',6-diamidino-2-phenylindole) for 1-5 minutes at room temperature, followed by washing cells three times (5-10 minutes each) with 1X washing buffer. Fluorescence images have then been collected with a fluorescence microscope Nikon Eclipse I80, equipped with appropriate fluorescence filters and a Nis-Elements F300 CCD camera.

Cell culture and differentiation

Two cell lines were used in this work: NE-4C and SH-SY5Y. 25,000 cells per cm^2 were seeded as required by the differentiation protocol; after 4 hours from sowing, the time required for cell adhesion, differentiation was induced by replacing the medium with differentiation medium composed of DMEM F-12 Ham (1:1), 1X insulin/transferrin/selenium (ITS), 4 mM glutamine, 40 μg ml^{-1} gentamicin and 2.5 μg ml^{-1} amphotericin (DM); 1μM all-trans retinoic acid (RA) was present only in the control experiments. After two days, the DM was replaced by DM containing 40 ng ml^{-1} neurothropic brain-derived factor (BDNF). Half of the DM was then changed every day by subsequent replacing it with DM, without any inducers until the end of the experiment. Cell-free reference devices were subjected to the same protocol without the initial cell seeding. As a control, the same differentiation protocol was applied in parallel also to cells seeded on glasses inserted in a 24-multiwell plate. After 8 days of differentiation, the samples were characterized using the protocol of immunofluorescence staining of β-tubulin III co-labeling the nuclei with DAPI as described in Cramer et al. [139]

2.3.4 Conclusions

The data shown in this paragraph show that $CaCO_3$ is a promising material to be used as host of molecules. As happens in the biominerals that can be found in nature, small molecules shape the inorganic phase and become entrapped within the crystalline lattice.

The work here described aims to satisfy the double goal of understanding the interaction process while preparing advanced materials that exploits both $CaCO_3$ and the additive proprieties.

Calcein, a molecule routinely used to mark shells growth, strongly affect crystalline morphology of both calcite and aragonite, becomes embedded within the crystalline lattice of calcite localizing along (104) planes and is entrapped between the crystalline domains of aragonite.

One of the most promising application of hybrid $CaCO_3$ composites is drug delivery. Here, we studied the interaction of OXY, an antibiotic, with $CaCO_3$. The drug becomes entrapped within the crystals and strongly decreases the dimension of aragonite crystals, making them appealing as a drug delivery system. Retinoic acid, a differentiation agent which promotes the differentiation of staminal cells into neuron and astrocytes, is efficiently embedded into calcite single crystals and an efficient cell differentiation scaffold is obtained by entrapping the RA/calcite hybrid crystals into a fibrin matrix.

2.4 Nanoparticles embedding within calcite crystals

2.4.1 Introduction

Recently inorganic nanocomposites have been widely investigated due to the possibility to modulate their composition and so to customize their proprieties, leading to their application in a wide range of fields, such as drug delivery [19,72], optics [47] and nanotechnology.[23,140,141] Nature shows how a wide range of objects can be embedded inside the mineral phase, modifying its precipitation pathway, final morphology, polymorphism and size [22,142] and enhancing its performances, [46,48] as can be seen comparing abiotic calcium carbonate ($CaCO_3$) and biogenic one, such as nacre. [9] Up to now, a wide range of molecules relevant for biomineralization [143,144] or of technological interest have been occluded inside calcium carbonate crystals leading to the formation of new materials. [46,115] Recently a lot of attention has been payed to the entrapment of nano-object inside the inorganic matrix. [21,46,124,145,146] Even if the inclusion of a bigger object can be difficult compared to the one of a single molecule, it has the great advantage to overcome the molecule-dependent incorporation and extend the type of object that can be included since the incorporation relays mostly on the particle surface groups, that can be tailored to have the desired grade of occlusion.

2.4.2 Results & discussion

2.4.2.1 Magnetic nanoparticles

Among the different types of nanoparticles available, superparamagnetic ones have attracted great attention since they allow the manipulation of the material they interact with and they are used for different application in which a physical separation by means of a magnetic field can be advantageous. [140,147-149] Particles possessing a magnetic core can be functionalized with different types of shells to improve their solubility in aqueous solvents and to improve their interaction with other additives or to perform reactions on their surface. Other molecules, such as dyes, can be included in the shell in order to easily detect and localize the particles. [150-152]

Calcite crystals were precipitated in the presence of fluorescent magnetic nanoparticles with different surface functionalization to identify which one of them allows their best distribution inside the inorganic matrix while preserving the single crystallinity. Superparamagnetic magnetite nanoparticles MAG/X with a diameter of 100 nm labelled with a fluorescent dye functionalized with i) Polyethylene glycol (2000 Da) having as a functional group phosphate sodium salt (MAG/PEG-P), ii) Polyethylene glycol (20000 Da) having amine as a functional group (MAG/PEG-am) and iii) dextran (MAG/DX) provided by Chemicell.

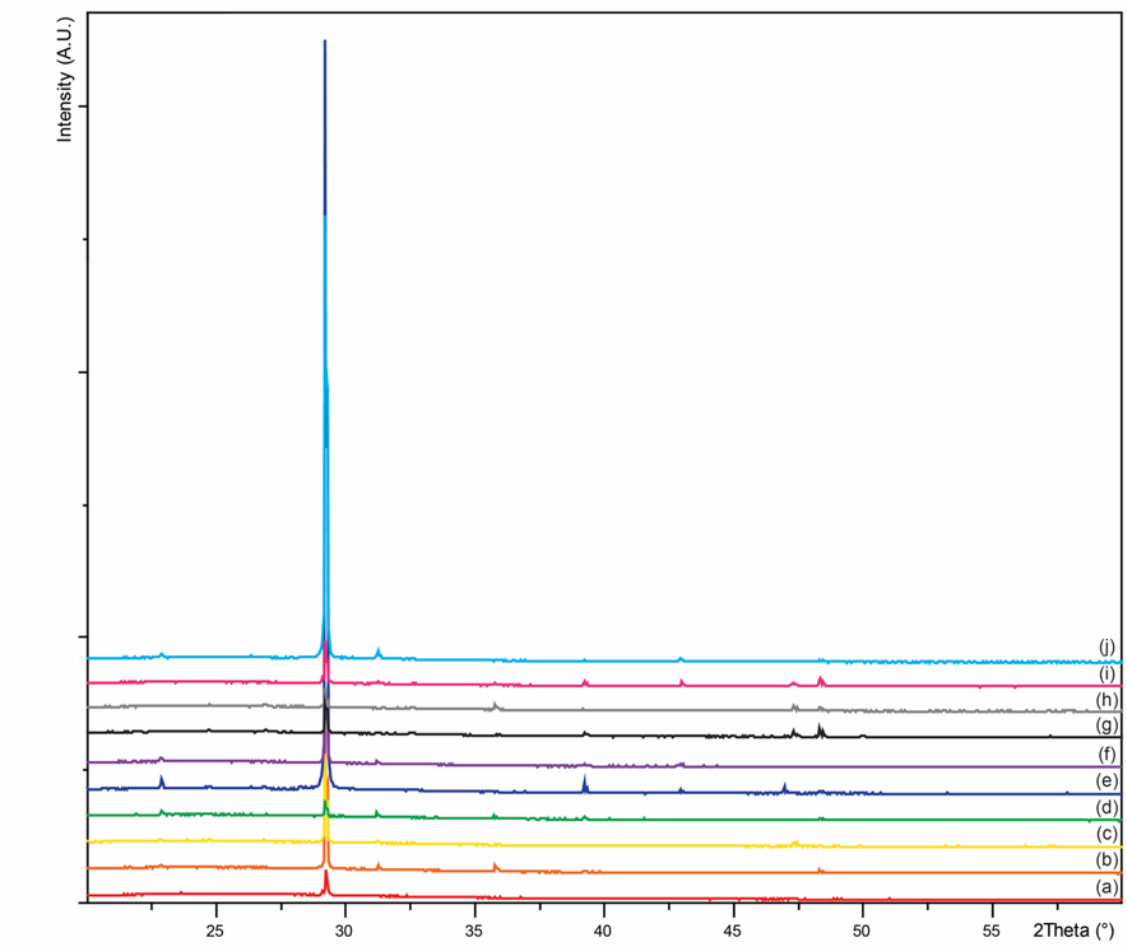

Figure 44. XRPD pattern of samples prepared (a)without additives and in the presence of (b) 0.001 mg/mL MAG/DX, (c) 0.01 mg/mL MAG/DX, (d) 0.1 mg/mL MAG/DX, (e) 0.001 mg/mL MAG/PEG-am, (f) 0.01 mg/mL MAG/PEG-am, (g) 0.1 mg/mL MAG/PEG-am, (h) 0.001 mg/mL MAG/PEG-P, (i) 0.01 mg/mL MAG/PEG-P and (j) 0.1 mg/mL MAG/PEG-P. Only calcite peaks are present.

X-ray diffractograms confirm that calcite is the only phase precipitated even in the presence of a high concentration of MAG/X.

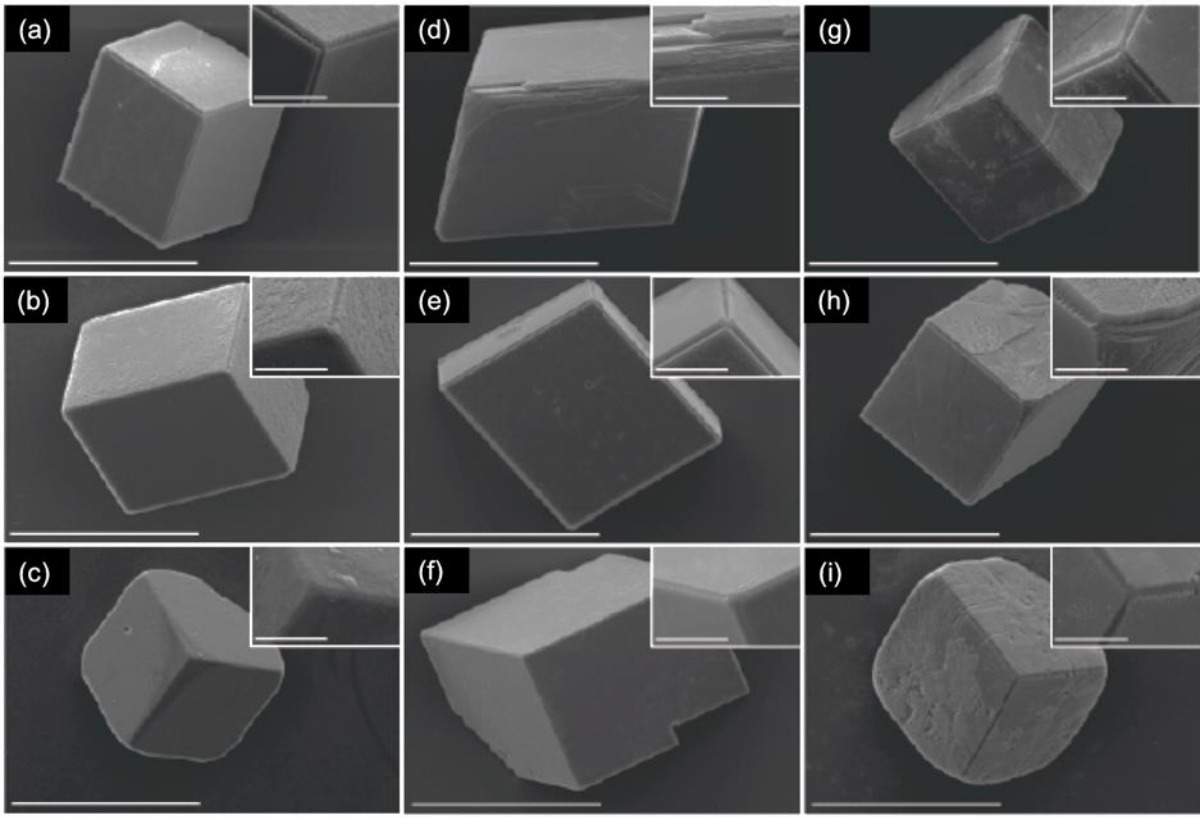

Figure 45. SEM images of samples prepared in the presence of (a) 0.1 mg/mL MAG/DX, (b) 0.01 mg/mL MAG/DX, (c) 0.001 mg/mL MAG/DX, (d) 0.1 mg/mL MAG/PEG-P, (e) 0.01 mg/mL MAG/PEG-P, (f) 0.001 mg/mL MAG/PEG-P, (g) 0.1 mg/mL MAG/PEG-am, (h) 0.01 mg/mL MAG/PEG-am and (i) 0.001 mg/mL MAG/PEG-am. Scalebar is 40 µm in the main image and 10 µm in the inset.

From low magnification SEM images of crystals grown in the presence of MAG/X is possible to notice that the crystals maintain the rhombohedral shape at every concentration examined, but at higher MAG/X concentration corners are rounder and less defined. From high magnification images it can be noticed that holes are present on the surface of the crystals. MAG/PEG-P cause the appearance of terraces near the edges of the crystals at the highest concentration studied (Figure 45 d), while they do not affect the morphology of the crystals at lower concentration. MAG/PEG-am modify the morphology of the crystals even when present at 0.001 mg/mL, causing the appearance of holes and terraces on {104} faces. MAG/DX do not modify the morphology of the crystals but significantly increase the roughness of the surface. Since no new faces are expressed, the interaction of MAG/DX with the growing crystals is face non-specific. Since MAG/DX expose hydroxyl groups, we hypothesize that they mildly interact with both positive and negative ions on the surface of the growing crystals, becoming passively incorporated within them while not stopping any growing step, thus preserving the rhombohedral morphology. For this reason, we decided to further characterize crystals grown in the presence of this kind of particles.

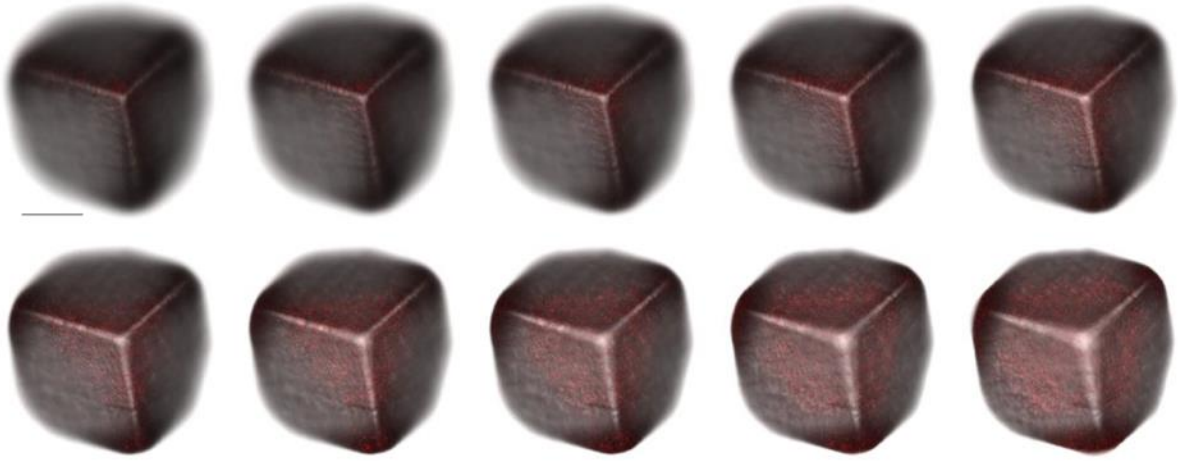

Figure 46. Confocal fluorescence microscopy images of sections of a calcite crystal grown in the presence of 0.1 mg/mL MAG/DX. Scalebar is 50 µm

Since the particles are labelled with a fluorescent dye, we used scanning confocal microscopy to verify the incorporation of MAG/DX into the crystals. As can be seen in Figure 46, the emission signal is homogeneous among all the sectioned planes and is preserved even if the crystal is bleached, confirming an embedding of the additive.

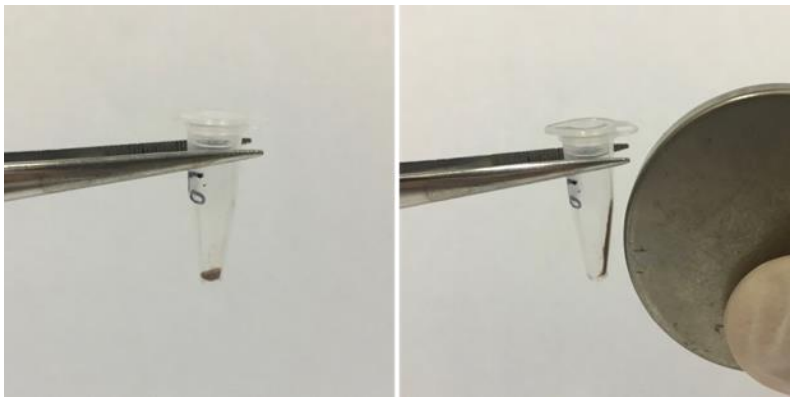

Figure 47. Crystals prepared in the presence of 0.1 mg/mL MAG/DX respond to an external magnetic field.

Finally, hybrid MAG/DX/calcite crystals show the superparamagnetic proprieties typical of MAG/DX themselves. In fact, despite the weight of the crystals, the embedded particles allow them to move inside a magnetic field, as can be seen in Figure 47.

In conclusion, in this paragraph we screened the inclusion efficiency of magnetic nanoparticles with different surface chemistry, we prepared and characterized a single crystal composite made of dextran coated magnetic nanoparticles and calcite which allow the final crystals to show the magnetic proprieties of the additive.

2.4.2.2 Silica nanoparticles

The mechanism of inclusion of different classes of molecules, ranging from amino acids [12,44,93,153,154] to drugs [19], and nanoparticles within calcite single crystals has been extensively studied. [46,47,146,155]However, at our knowledge so far, few information that relates the yield of additive occlusion to its complex surface chemistry has been reported. In fact, taking into consideration a small molecule, it is not possible to change just a functional group without affecting its charge distribution and, therefore, its electronic density. [156]

The use of bigger species, such as micelles and nanoparticles, overcomes this problem, but introduces further restrictions related to limited chemical and physical stability conditions. Micelle assisted silica nanoparticles are ideal to be used as additives since they are composed of a core that is not influenced by the environment and by a shell that can carry a great number of functional groups. [157] Furthermore, their chemistry is not influenced by the pH of the solution as strongly as it happens in micelles and block copolymers, allowing the investigation of a variety of crystal growth conditions in which other species would not be stable. [158]

In this work, we used silica nanoparticles functionalized with an ethylene glycol shell (PluS-X) carrying different functional groups (amine, carboxylated and hydroxylated) to investigate the effect of these surface functional groups on the inclusion of the additives within calcite single crystals. This approach offers an additional advantage of minimizing the effect of other proprieties of the additive by keeping constant the nanoparticle size and the number of functional groups per surface, allowing us to directly relate the effect of the nanoparticles on the calcite crystal to the functional group they are carrying.

PluS-X (Figure 48a) are 25 nm nanoparticles made of a 10 nm rigid silica core and a soft pluronic shell (PEGylated polymer) terminating with hydroxyl groups (PluS-OH), that can be easily modified to expose different functions. Fluorescent dyes, which allow a convenient quantification and localization of the particles, are chemically incorporated into the core and eventually protected from the environment by the silica core matrix and the shell, preventing any effect caused by the external environment on the absorption and emission of the dye. PluS-X were decorated using respectively carboxylic (PluS-COOH) and amine groups (PluS-

NH_2) to study the role of surface chemistry while keeping constant all the other parameters, namely core and shell dimensions (Figure 48b and c), core charge and emission.

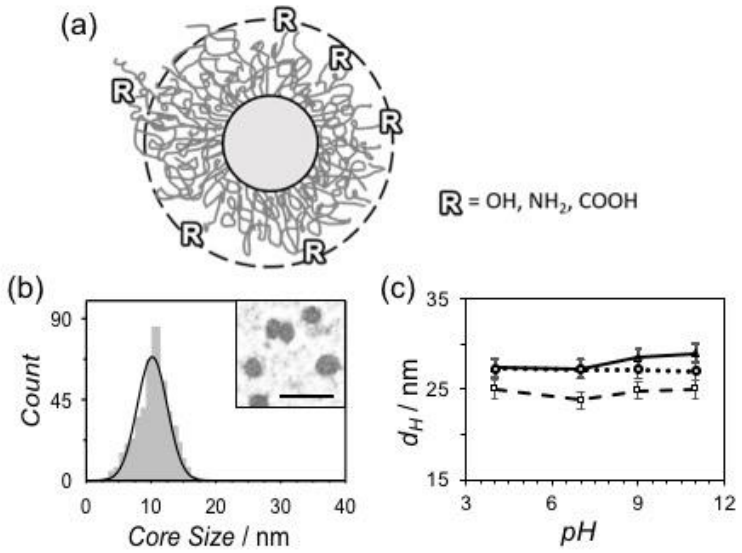

Figure 48. (a) Schematic illustration of PluS-X structure, (b) distribution of silica core diameter and transmission electron microscopy (TEM) image of PluS-X silica core (scale bar 20 nm). (c) trends of the hydrodynamic diameter of PluS-OH (dashed line), PluS-NH_2 (dotted line), PluS-COOH (solid line), at different pH ($CaCl_2$ 10 mM, [PluS-X]= 1 μM).

As mentioned above, calcite single crystals were grown in the presence of various concentrations of PluS-X using the vapor diffusion technique. Crystals were formed in all the examined conditions and no relevant change in the number of precipitated crystals was detected, meaning that the additives do not inhibit the nucleation phase. Furthermore, only single crystals were observed, except when the highest concentration of positively charged particles was used, indicating the absence of secondary nucleation events.

Exploiting the fluorescence of the PluS-X, it was possible to quantify their embedding in the crystalline lattice (see Figure 49). Each PluS-X has been functionalized with an average value of 10 Rhodamine B (RB) dyes yielding very bright nanoarchitectures (Photoluminescence quantum yield (PluS- ΦPL=0.24). The concentration of the PluS-X embedded in the crystal lattice has been measured by recording the fluorescence of the RB in solution upon the dissolution of the crystals, while the concentration of Ca^{2+} has been measured by atomic

absorption allowing the computation of PluS-X content as the ratio of the PluS-X divided by the Ca^{2+} concentration.

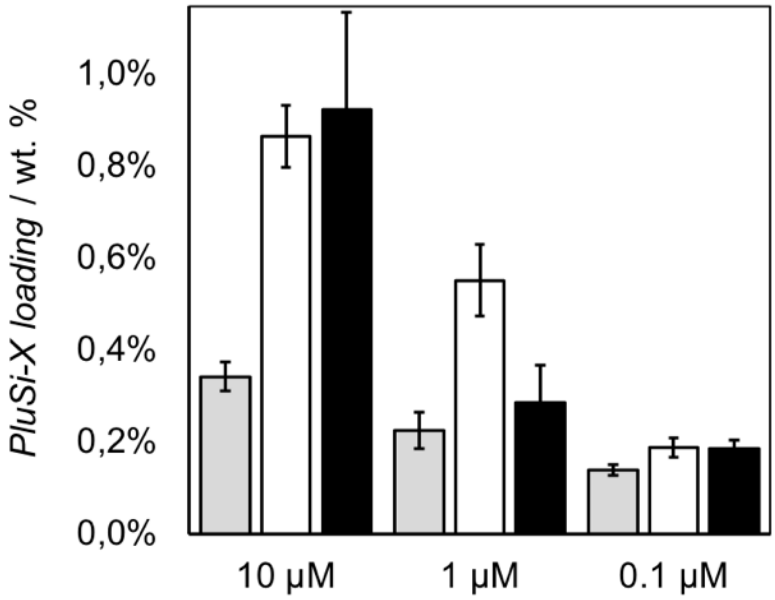

Figure 49. PluS-X loading (wt %) in calcite crystals grown with PluS-OH (white), PluS-NH_2 (black), PluS-COOH (gray).

At low concentration, PluS-X content is comparable for all the samples. At intermediate concentrations, we can observe that PluS-OH are more likely to be incorporated than PluS-NH_2 and PluS-COOH while at highest concentration the amount of PluS-NH_2 loaded is comparable to that of PluS-OH. The latter effect can be ascribed to the formation of polycrystalline aggregates when the crystallization process is carried out in the presence of 10 µM PluS-NH_2, making possible for the PluS-NH_2 to be entrapped between crystalline domains. Furthermore, since in the experimental conditions the growing calcite crystals have

a negatively charged surface, [159,160] it discourages the negatively charged PluS-COOH from adsorbing onto it.

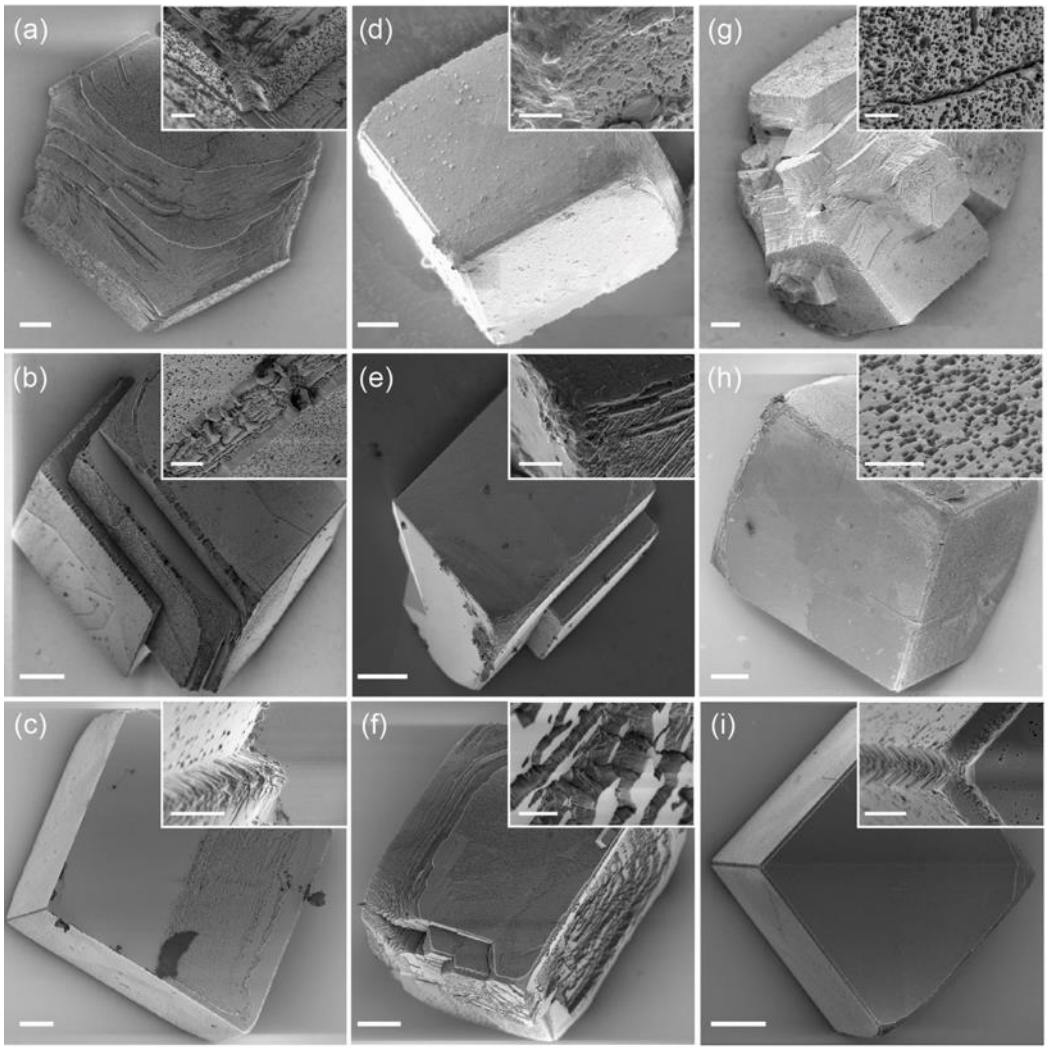

Figure 50. SEM micrographs of calcite crystals grown in the presence of (a) 10 µM, (b) 1 µM, (c) 0.1 µM PluS-COOH, (d) 10 µM, (e) 1 µM, (f) 0.1 µM PluS-OH, (g) 10 µM, (h) 1 µM, (i) 0.1 µM PluS-NH_2. Scalebar is 10 µm in the main image and 1 µm in the inset.

The change in morphology of the final crystals is related to the adsorption of the PluS-X on the crystalline faces, thus giving information on the mechanism of interaction.

Looking at scanning electron microscopy (SEM) pictures (Figure 50) of crystals grown in the presence of different concentrations of PluS-X, we can see that at low concentration of PluS-COOH and PluS-OH nanoparticles cause the crystal to develop a hopper-like morphology and all PluS-X form holes into the {104} faces. Increasing the concentration of nanoparticles in solution gives rise to epitaxial growth of crystals and appearance of {hk0} faces.

Regarding PluS-NH_2, a higher concentration is needed to observe a comparable change in morphology. In fact, at the lowest concentration studied, we observe only a limited quantity of defects on the surface of the crystals while, increasing the concentration of PluS-NH_2 to 1

µM, the number of holes increases as the morphology of the crystal remains unaffected. When crystals are grown in the presence of 10 µM PluS-NH_2, a strong modification of the morphology can be observed and polycrystalline aggregates, that can be ascribed to the secondary nucleation processes, form.

We hypothesize that PluS-OH are better entrapped within the crystal since they do interact with the crystal surface without preventing further growth, as confirmed by the rhombohedral shape of the crystal grown in the presence of 10 µM PluS-OH.

To verify the incorporation of the particles inside the crystals we took advantage of the fluorescent dyes linked to the core of the particles that allows us to localize them inside the crystals using confocal microscopy. As can be seen in Figure 51, all the particles are embedded inside the crystals rather than just adsorbed on the surface.

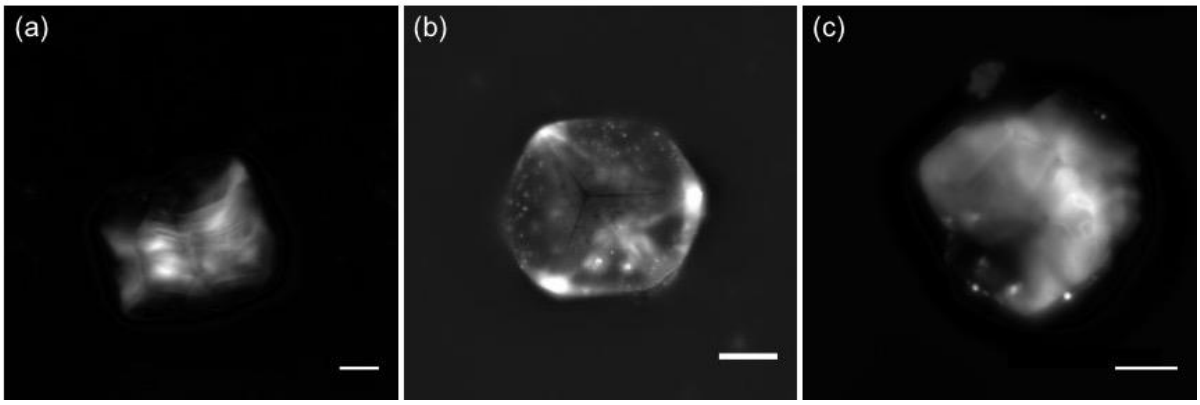

Figure 51. Z-stack confocal images of calcite crystals grown in the presence of 10 µM (a) PluS-COOH, (b) PluS-OH and (c) PluS-NH2. Scalebar is 100 µm.

According to the high resolution X-ray diffraction analysis, lattice parameters are not significantly affected by the presence of PluS-X.

To better understand the interaction of PluS-X with the growing calcite surface, we performed overgrowth experiment using pristine calcite crystals as seeds for the new inorganic phase. In these conditions, no secondary nucleation is observed for any of the samples.

We performed atomic scale analysis on the thin sections of the overgrowth crystals obtained in the presence of PluS-OH particles. Using scanning TEM (STEM) coupled to the high-angular annular dark field (HAADF) imaging mode and to an advanced energy dispersive X-ray (EDS) detector allowed measuring the location of PluS-X particles within the overgrown layer with atomic resolution. Our observations suggest that PluS-X localize at the interface between the core crystal and the overgrown layer (Figure 52 a, b and c). Images obtained in transmission electron microscopy (TEM) mode confirmed that the lattice of the overgrown calcite layer is not disrupted and its further growth is not affected by occluded PluS-X particles (Figure 52 d

and e). Fast Fourier transforms (FFT) applied to the lattice images acquired from the interface area demonstrate a single-crystalline nature of the crystal (Figure 52, inset).

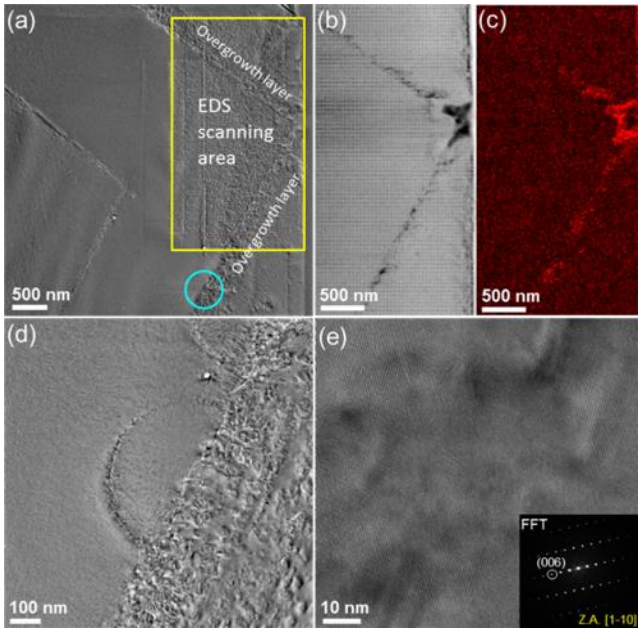

Figure 52. High resolution TEM analysis of the overgrowth crystals. (a) STEM image of the analyzed thin section. (b) STEM-HADAAF image of the area marked in yellow in (a). Dark spots correspond to the embedded PluS-X particles due to their lower Z-values as compared to that of the calcite surrounding matrix. (c) STEM-EDS map of the Si Kα peaks revealing localization of the PluS-X. (d) Low magnification TEM image of the area marked in blue in (a). (e) High magnification TEM image demonstrating not disrupted calcite lattice. Inset – FFT-generated diffraction pattern that can be well fitted to that of a single crystal of calcite.

In conclusion, we proved that surface chemistry is an important parameter affecting the inclusion of nanoparticles inside calcite single crystals. Our experiments showed that PluS-OH are the most efficiently embedded particles among the ones studied. This is due to the ability of the OH group to adsorb onto the growing surface while not carrying any charge that can cause repulsion in crystallization conditions. PluS-COOH are incorporated in lower quantity due to their negative charge, while PluS-NH_2 cause secondary nucleation processes and localize between crystalline domains. TEM analysis performed on the thin section of the overgrown crystal confirms that PluS-X adsorb on the growing calcite surface and do not prevent the growth of the inorganic single-crystalline phase. In addition, we observed that the nanoparticles inclusion does not induce a distortion of the crystal lattice.

These observations are relevant in material science and in biomineralization. Regarding the former, enhancing the inclusion of PluS-X into calcite single crystals exploiting the shell chemistry allows one to integrate non-native functions into the material, with the advantage of integrating multiple functionality, within the core of the particles with no effect on the inclusion rate. This possibility can find application in drug delivery, combining the passive delivery of PluS-X in the acidic tumor environment due to dissolution of $CaCO_3$ and the active

delivery that can be obtained functionalizing PluS-X with specific cancer targeting agents and anticancer drugs. In the latter the occlusion of nanoparticles into a crystalline framework is a widespread phenomenon, which often involves macromolecular ultra-structures containing polysaccharides and thus exposing hydroxyl groups, with minimal or no distortion of the crystal lattice.

2.4.3 Conclusions

Calcite crystals were grown *in vitro* in the presence of silica and magnetite nanoparticles with different types of surface chemistry in order to clarify the effect of functional groups on inclusion into the inorganic phase. The use of core-shell nPs instead of micelles or block copolymer permits the investigation of a wider range of conditions in which the latter are not stable and easy to characterize. In fact, core shell nPs allow to change the chemistry of the shell, exposing amine, hydroxyl or carboxyl terminal groups while exploiting the fluorescence of dyes conjugated with the core of the nanoparticles, allowing an easy and convenient localization of the nanoparticles even when they are embedded within the crystalline matrix. The possibility of including molecules into the core poses the basis for new strategies to embed non-native proprieties into the inorganic material.

Among the studied functional groups, hydroxyl groups allow higher entrapment with almost no influence on the macroscopic morphology of the crystals. This effect can be ascribed to the weak interaction between the particles and the growing crystals, allowing the adsorption of the particles on its surface without preventing further growth. This trend was verified for both classes of nPs examined, even though the shell is composed of different macromolecules, namely dextran and PEG.

These results shed light on the inclusion of objects bigger than molecules into calcite single crystals and poses new basis for the synthesis of functional single crystal composites.

2.4.4 Methods

2.4.4.1 Crystal growth

Calcium chloride dehydrate was purchased from Fluka, magnesium chloride hexahydrate from Sigma Aldrich and anhydrous ammonium carbonate from Acros Organics. All reagents were ACS grade and used as purchased. $CaCO_3$ crystals were grown by vapor diffusion method. Briefly, $(NH_4)_2CO_3$ vapor is allowed to diffuse into 750 µL of a 10 mM $CaCl_2$ solution containing the additives into a closed container for 4 days. The obtained crystals are then rinsed 3 times with water, once with ethanol and air-dried.

For overgrowth experiments, $CaCO_3$ crystals to be used as seeds were grown by vapor diffusion method in the absence of additives as described above. Calcite seeds were then put in a solution containing 750 µL of a 10 mM $CaCl_2$ solution containing the additives in a close container in the presence of $(NH_4)_2CO_3$. After 4 days, the crystals were washed 3 times with water, once with ethanol and air-dried.

2.4.4.2 Characterization

SEM images were collected using a Zeiss Gemini SEM Ultra Plus with an acceleration voltage of 1.00 KeV after coating the sample with 2 nm of PtPd.

In order to measure the PluS-X content, the samples were first treated with 5% v/v sodium hypochlorite to bleach the fluorescence of the PluS-X adsorbed on the surface, then dissolved in 0.8 mL 0.1 M citrate buffer at pH 4.5 and finally the emission spectra were collected using Fluoromax-4 Horiba equipped with 150 W Xenon lamp single monochromator for both excitation and emission (λ_{exc}=530 nm, slit width=8x8, scan from 550 nm to 750 nm). Calcium content was measured using flame atomic absorption spectroscopy (Perkin-Elmer AAnalyst 100). PluSi-X loading was calculated assuming that a PluSi-X particle weights 1M Da.

High resolution X-ray powder diffraction (HRPXRD) measurements were collected with a dedicated high-resolution powder diffraction synchrotron beamline (ID22 at the European Synchrotron Radiation Facility (ESRF), Grenoble, France) at a wavelength of 0.039 nm. Crystal lattice parameters were assessed by the Rietveld refinement method with GSAS software and the EXPGUI interface.

High resolution scanning transmission electron microscopy (HRTEM), high-angle annular dark-field scanning transmission electron microscopy (HAADF-STEM) images and electron dispersive spectroscopy (EDS) maps were acquired using a monochromated and double corrected Titan Themis G2 60-300 (FEI / Thermo Fisher) operated at 200KeV and equipped with a DualX detector (Bruker). The quantitative analysis of the EDS maps was done using the Velox software. Thin sections for TEM analysis were prepared using FEI Strata 400S FIB.

Confocal microscope images were collected using an Upright Zeiss LSM 710 equipped with a laser diode (561 nm) and analysed using the software imageJ, making a sum of the slides.

2.5 Synthesis of bionic crystals

2.5.1 Introduction

Living organisms are able to shape minerals into outstandingly complex morphology with exceptional control over location of the crystals, their polymorphism and habit which cannot be replicated synthetically. A good example of organism's control can be found in sea urchin spines, which are composed of pure Mg-calcite aligned along the c-axis with interconnected pores. [120,161] Another example is nacre, in which hexagonal aragonite tablets of controlled thickness of around 20 μm grow connected by mineral bridges and with the c-axis aligned perpendicular to the shell surface. [13]

Given that the control exerted by organisms cannot be replied synthetically, the use of calcifying systems as bioreactor is an appealing possibility to obtain $CaCO_3$ composites with controlled morphology and polymorphic distribution.

Up to now, no organisms producing $CaCO_3$ have been used to obtain functional composites. Despite that, a similar approach has been used with diatoms, algae producing a silica shell, which often shows photonic proprieties. By introducing organic dyes into the silica shell simply growing the organisms in a doped medium, Kucki *et al.* obtained photonic structures whose emission could be shifted by changing the dye. [162-164]

Calcifying organisms can entrap molecules in the growing shells, as demonstrated by the various staining techniques commonly use to mark their growth, which mainly rely on the detection of ions or fluorescent molecules delivered through the growth medium. A wide range of functional molecules can be entrapped within $CaCO_3$ crystals *in vitro*, thus making possible to hypothesize their inclusion within biogenic crystals. The presence of the organism can enhance or diminish the efficiency of entrapment since many parameters should be considered when evaluating the inclusion of molecules. First, the molecule should be internalized by the organism without causing side effects, then it should be transported to the site of mineralization and entrapped in the inorganic matrix.

As model organism we used foraminifera, unicellular calcifying algae whose calcification mechanism is well characterized. [37,165-167] The specie used in the following experiment is *Amphistrigina lessoni,* foraminifera of the radial group that grows by sequential addiction of single chambers to the shell. The deposition of the mineral phase takes place after the formation of a scaffold of organic matrix and a new chamber is formed every few days. Seawater is internalized using vacuoles, which are moved to the site of mineralization without involving transport through membranes (Figure 53). Carbonate and magnesium ions content is controlled by membrane pumps; magnesium is removed from the vacuoles in order to favor calcite precipitation while carbonate is transported into the vesicles in order to increase pH and allow mineralization.

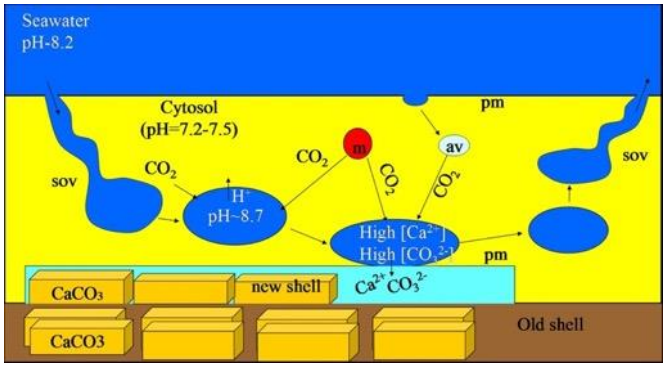

Figure 53. Schematic representation of shell formation in foraminifera. Reproduced from [166]

Even though the mineralization mechanisms of more complex species (e.g. corals) is not completely understood, [4,168] forams are the only organisms believed to exploit this technique and not involving the transport of ions through membranes. This pathway should allow the delivery of additives present in the water to the site of biomineralization without relying on their charge and dimension, allowing their inclusion into the newly formed skeleton.

A drawback of using these organisms is that they live in symbiosis with green algae containing chlorophyll, a molecule with a wide absorption spectrum that interfere with additive detection when using spectroscopic techniques, and need light to grow, thus causing photodamage to the additives.

Having demonstrated the possibility to entrap magnetic nanoparticles functionalized with dextran (MAG/DX) in synthetic crystals, we decided to use them to prepare bionic crystals, that is to say crystals precipitated by living organisms entrapping functional particles. This type of nanoparticles can be functionalized with different dyes, thus allowing to tune their absorption and emission to suit experimental need and can be detected by mapping iron distribution. For these reasons, MAG/DX are the ideal additive to be used for a proof-of-concept and the same idea can be extended to functional molecules such as drugs.

2.5.2 Results & discussion

Magnetic nanoparticles (MAG/X) functionalized with fluorescent dyes were chosen for this set of experiments to make easier to localize them during the treatment of the organisms by using their fluorescence and after the culture taking advantage of the presence of iron in the core of the MAG/X. The interaction of MAG/X with different surface chemistry and calcite crystals *in vitro* was studied in order to identify the type of particles influencing less the habit of the final crystal while allowing a significant inclusion rate. Among the examined MAG/X, MAG/DX, magnetic nanoparticles with a dextran shell, have a high inclusion rate and do not modify the macroscopic crystal habit (see 2.4.2.1). The latter characteristics makes them appealing as an additive for bionic crystals. Other than acting as an additive to be included in the inorganic matrix, delivering MAG/DX to the organisms can give further information on the biomineralization process, confirming the model illustrated above, since those particles are not able to passively pass nor are actively pumped across membranes.

Amphistrigina lessoni foraminifera were collected just before the treatment in Eilat (IL) and selected in order to have a set of samples with similar dimensions.

Since the biomineralization process is not continuous but the organism forms a new chamber every few days, *A. lessoni* specimens were grown in the presence of both MAG/DX and calcein, used to mark the newly formed chambers on each examined organism, thus working as internal reference. Looking at the living specimen during the treatment under the confocal microscope, it can be seen that the particles are running through the pseudopods to eventually enter into the organism (Figure 54).

Since the organisms live in symbiosis with green algae, it is difficult to observe the fluorescence of the particles once that they accumulate inside the cell since the absorption and emission of chlorophyll of the symbiotic green algae overlap with the one of the dyes.

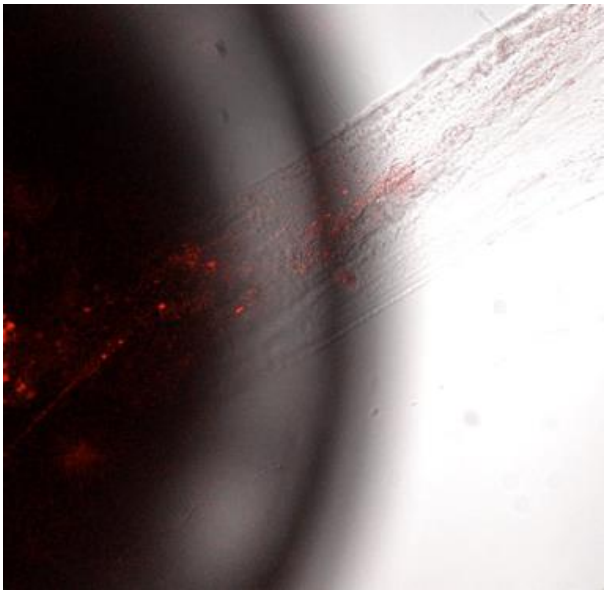

Figure 54. Confocal images which shows MAG/DX moving inside *A. lessoni* pseudopods

The specimen that formed new chambers were isolated and chemically bleached in order to eliminate the signal of adsorbed MAG/DX. Samples were then observed using an SEM coupled to an advanced energy dispersive X-ray (EDX) detector to reveal the location of MAG/DX.

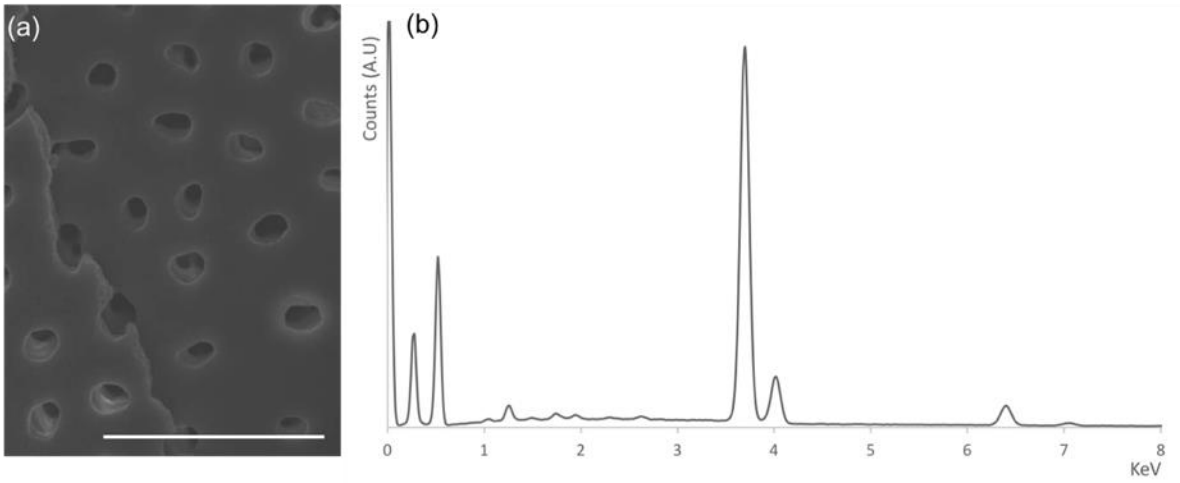

Figure 55. (a) detail of pore of the shell of a foram treated with MAG/DX and (b) EDX spectra acquired on (a). Scalebar is 3 µm

EDX analysis reveals the presence of iron, represented by the peaks at 6.404 and 7.058 KeV in the analyzed area (Figure 55).

Mapping the distribution of iron and calcium on the surface we can observe that the signal of iron is coming mainly from the pore, suggesting a higher concentration of iron inside the shell (Figure 56).

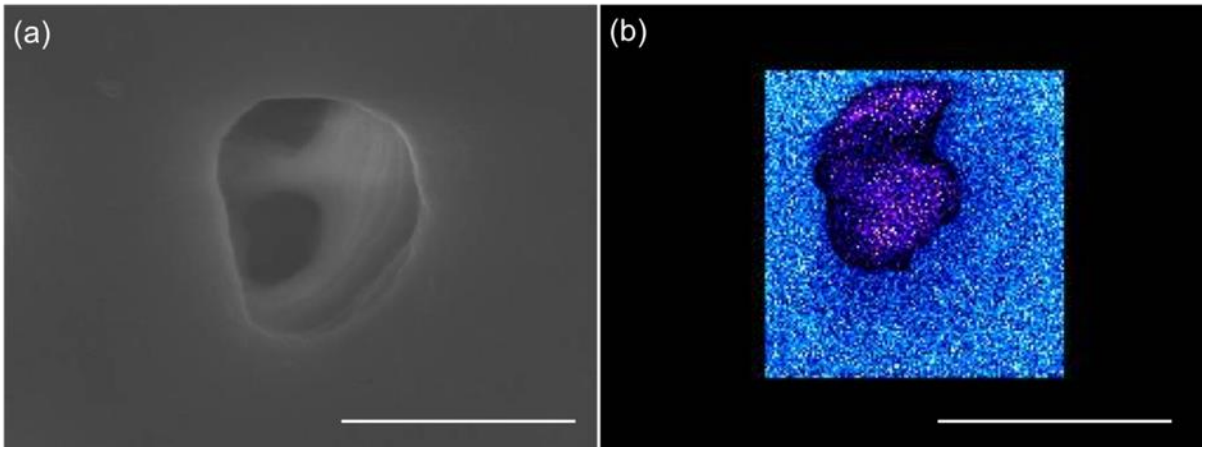

Figure 56. (a) detail of pore of the shell of a foram treated with MAG/DX and (b) EDX map acquired on (a), where Ca signal is reported in blue and Fe signal is reported in purple. Scalebar is 3 µm

Upon breaking of the skeleton to expose the inside layer it was possible to map the distribution of iron on the inner surface of the shell. It can be notice that clusters of MAG/DX are adsorbed on the inner layer of the skeleton, with no preferential location (Figure 57). Thus, we can confirm the inclusion of MAG/DX in the foram skeleton.

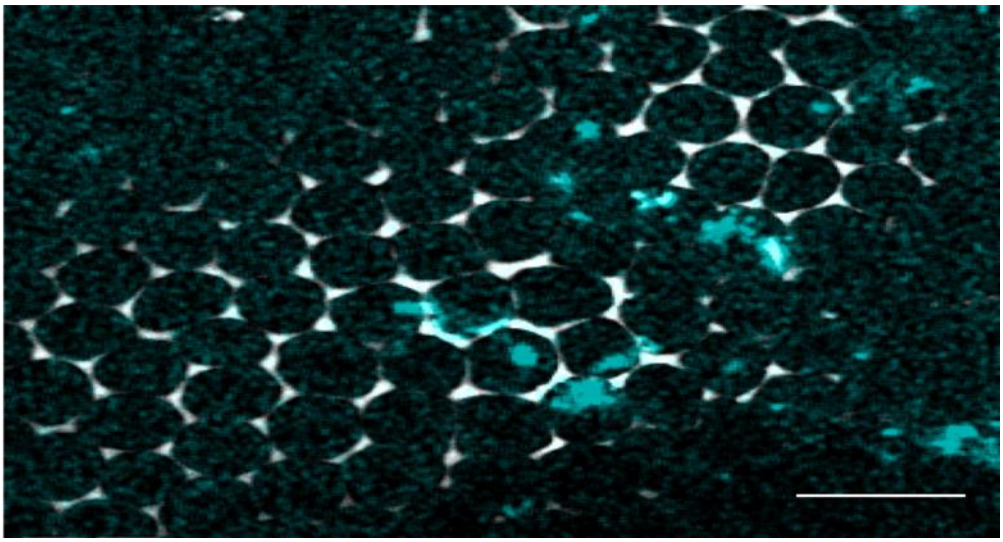

Figure 57.EDS image of foram inner side of the skeleton. Fe signal is reported in blue. Scalebar is 10 µm.

2.5.3 Conclusions

The work discussed in this chapter show a pioneering attempt of obtaining bionic crystals, that is to say a functional crystalline material produced by using a living organism as a bioreactor, thus taking advantage of its ability of controlling the polymorphism and morphology of the inorganic matrix.

A. lessoni specimens were cultured in the presence of MAG/DX particles, which can be entrapped within synthetic calcite crystals as discussed previously (see 2.4.2.1). The fluorescence of the particles allowed us to follow their internalization pathway and we demonstrated that they are successfully internalized by the organism through the pseudopods. MAG/DX are incorporated into the skeleton and are localized preferentially on the inner surface of the shell.

This discovery paves the way for the preparation of other composite materials through the use of foraminifers or other organisms using similar calcification processes. This potential will be even more exploitable when the research will be able to describe the biochemical processes that go from the uptake of the nano-particle dispersed in sea water to their deposition in the skeletal region. In this study, the process, described only from a phenomenological point of view, thanks to the traceability of the MAG/DX, allowed to ascertain how effectively the MAG/DX are sequestered by sea water and transported to the calcification sites. The preparation of bionic materials is an issue of increasing relevance, even if up now it has not involved processes of calcification in complex marine organisms.

In conclusion in this study for the first time we used foraminifera as bioreactor for the synthesis of the composite, exploiting the organism's natural ability to control the calcification process to easily obtain a new advanced functional material.

2.5.4 Methods

2.5.4.1 Organism culture

Foraminifera (collected in Eilat-Israel on 7/7/16) with dimension between 250 μm and 350 μm were selected using sieves and *A. lessoni* specimens were selected.

The dead control was prepared washing the forams 2 times with distilled water (DW) and 3 times with double distilled water (DDW), putting them in sodium hypoclorite (NaOCl) (prepared diluting the analytical grade one 1:5 NaOCl:DW) for at least 2 hours and drying them in the oven at 60°C.

The solutions were prepared diluting the dyes directly in seawater to obtain calcein 40 μM and MAG/DX 0,01 mg/mL.

40 specimens were put in a jar and the following experiment were performed:

	Calcein	**MAG/DX**	**Calcein/MAG/DX**
Living specimen	40 specimens in 50 mL	40 specimens in 50 mL	40 specimens in 50 mL
Dead control	10 specimens in 1 mL	10 specimens in 1 mL	10 specimens in 1 mL

The samples were kept under a lamp with a temperature of 23,5 °C.

After 2 days the samples treated with calcein were observed under a binocular and, since the last chamber of all the specimens was labelled, all the incubations were stopped.

2.5.4.2 Characterization

Confocal microscope images were collected using an upright Olympus microscope equipped with laser 488 nm and 561 nm lasers and a spectral detector and analysed using the software imageJ, making a sum of the slides.

SEM imaging and EDS analysis were performed using Zeiss LEO 1530 after coating the samples with carbon.

2.6 References

1 J. J. De Yoreo, J. J. De Yoreo and P. G. Vekilov, *Reviews in Mineralogy and Geochemistry*, 2003, **54**, 57–93.

2 J. J. De Yoreo, *MRS Bull.*, 2017, **42**, 525–536.

3 J. J. De Yoreo, P. U. P. A. Gilbert, N. A. J. M. Sommerdijk, R. L. Penn, S. Whitelam, D. Joester, H. Zhang, J. D. Rimer, A. Navrotsky, J. F. Banfield, A. F. Wallace, F. M. Michel, F. C. Meldrum, F. M. Michel, H. Cölfen and P. M. Dove, *Science*, 2015, **349**, 6760–6760.

4 S. Weiner and L. Addadi, *Annu. Rev. Mater. Res.*, 2011, **41**, 21–40.

5 F. C. Meldrum and H. Cölfen, *Chem. Rev.*, 2008, **108**, 4332–4432.

6 S. Mann, *Biomineralization: principles and concepts in bioinorganic materials chemistry*, Oxford University Press, 2001.

7 S. Weiner, *Reviews in Mineralogy and Geochemistry*, 2003, **54**, 1–29.

8 E. Zolotoyabko and B. Pokroy, *CrystEngComm*, 2007, **9**, 1156–1161.

9 L. Addadi, D. Joester, F. Nudelman and S. Weiner, *Chem. Eur. J.*, 2006, **12**, 980–987.

10 S. Weiner and L. Addadi, *Trends in Biochemical Sciences*, 1991, **16**, 252–256.

11 G. Falini, S. Fermani and S. Goffredo, *Seminars in Cell and Developmental Biology*, 2015, 1–10.

12 B.-A. Gotliv, N. Kessler, J. L. Sumerel, D. E. Morse, N. Tuross, L. Addadi and S. Weiner, *ChemBioChem*, 2005, **6**, 304–314.

13 F. Nudelman, B.-A. Gotliv, L. Addadi and S. Weiner, *Journal of Structural Biology*, 2006, **153**, 176–187.

14 R. A. Metzler, J. S. Evans, C. E. Killian, D. Zhou, T. H. Churchill, N. P. Appathurai, S. N. Coppersmith and P. U. P. A. Gilbert, *J. Am. Chem. Soc.*, 2010, **132**, 6329–6334.

15 I. C. Olson, A. Z. Blonsky, N. Tamura, M. Kunz, B. Pokroy, C. P. Romao, M. A. White and P. U. P. A. Gilbert, *Journal of Structural Biology*, 2013, **184**, 454–463.

16 R. A. Metzler, G. A. Tribello, M. Parrinello and P. U. P. A. Gilbert, *J. Am. Chem. Soc.*, 2010, **132**, 11585–11591.

17 L. Addadi and S. Weiner, *Proc Natl Acad Sci USA*, 1985, **82**, 4110–4114.

18 J. W. C. Dunlop and P. Fratzl, *Annu. Rev. Mater. Res.*, 2010, **40**, 1–24.

19 G. Magnabosco, M. D. Giosia, I. Polishchuk, E. Weber, S. Fermani, A. Bottoni, F. Zerbetto, P. G. Pelicci, B. Pokroy, S. Rapino, G. Falini and M. Calvaresi, *Adv. Healthcare Mater.*, 2015, **4**, 1510–1516.

20 D. C. Green, J. Ihli, P. D. Thornton, M. A. Holden, B. Marzec, Y.-Y. Kim, A. N. Kulak, M. A. Levenstein, C. Tang, C. Lynch, S. E. D. Webb, C. J. Tynan and F. C. Meldrum, *Nature Communications*, 2016, **7**, 13524.

21 Y. Ning, L. A. Fielding, L. P. D. Ratcliffe, Y.-W. Wang, F. C. Meldrum and S. P. Armes, *J. Am. Chem. Soc.*, 2016, **138**, 11734–11742.

22 Y.-Y. Kim, K. Ganesan, P. Yang, A. N. Kulak, S. Borukhin, S. Pechook, L. Ribeiro, R. Kröger, S. J. Eichhorn, S. P. Armes, B. Pokroy and F. C. Meldrum, *Nat Mater*, 2011, **10**, 890–896.

23 M. D. Giosia, I. Polishchuk, E. Weber, S. Fermani, L. Pasquini, N. M. Pugno, F. Zerbetto, M. Montalti, M. Calvaresi, G. Falini and B. Pokroy, *Adv. Funct. Mater.*, 2016, **26**, 5569–5575.

24 M. Calvaresi, G. Falini, S. Bonacchi, D. Genovese, S. Fermani, M. Montalti, L. Prodi and F. Zerbetto, *Chemical Communications*, 2011, **47**, 10662–3.

25 C. Lu, L. Qi, H. Cong, X. Wang, J. Yang, L. Yang, D. Zhang, J. Ma and W. Cao, *Chem. Mater.*, 2005, **17**, 5218–5224.

26 J. De Yoreo, *Nat Mater*, 2013, **12**, 284–285.

27 E. Saridakis and N. E. Chayen, *Trends in Biotechnology*, 2009, **27**, 99–106.

28 M. P. Andersson, S. Dobberschütz, K. K. Sand, D. J. Tobler, J. J. De Yoreo and S. L. S. Stipp, *Angew. Chem. Int. Ed. Engl.*, 2016, **55**, 11086–11090.

29 H. H. Teng, P. M. Dove and J. J. De Yoreo, *Geochimica et Cosmochimica Acta*, 2000, **64**, 2255–2266.

30 M. Niederberger and H. Cölfen, *Phys. Chem. Chem. Phys.*, 2006, **8**, 3271–3287.

31 H. Cölfen and M. Antonietti, *Angew. Chem. Int. Ed.*, 2005, **44**, 5576–5591.

32 Y.-Y. Kim, A. S. Schenk, J. Ihli, A. N. Kulak, N. B. J. Hetherington, C. C. Tang, W. W. Schmahl, E. Griesshaber, G. Hyett and F. C. Meldrum, *Nature Communications*, 2014, **5**, 4341–14.

33 Elena Sturm (née Rosseeva), Helmut Cölfen, *Crystals*, 2017, **7**, 207–17.

34 E. V. S. Rosseeva and H. Cölfen,, *Chemical Society Reviews*, 2016, **45**, 5821–5833.

35 T. Wang, H. Cölfen and M. Antonietti, *J. Am. Chem. Soc.*, 2005, **127**, 3246–3247.

36 S. Raz, P. C. Hamilton, F. H. Wilt, S. Weiner and L. Addadi, *Adv. Funct. Mater.*, 2003, **13**, 480–486.

37 G. M. Khalifa, D. Kirchenbuechler, N. Koifman, O. Kleinerman, Y. Talmon, M. Elbaum, L. Addadi, S. Weiner and J. Erez, *Journal of Structural Biology*, 2016, **196**, 155–163.

38 P. J. M. Smeets, A. R. Finney, W. J. E. M. Habraken, F. Nudelman, H. Friedrich, J. Laven, J. J. De Yoreo, P. M. Rodger and N. A. J. M. Sommerdijk, *Proc. Natl. Acad. Sci. U.S.A.*, 2017, **114**, E7882–E7890.

39 P. J. M. Smeets, K. R. Cho, N. A. J. M. Sommerdijk and J. J. De Yoreo, *Adv. Funct. Mater.*, 2017, **27**, 1701658–7.

40 G. Falini, S. Albeck, S. Weiner and L. Addadi, *Science*, 1996, **271**, 67–69.

41 A. Alabi, M. Chiesa, C. Garlisi and G. Palmisano, *Environmental Science: Water Research & Technology*, 2015, **1**, 408–425.

42 J. A. Wojtowicz, *Journal of the Swimming Pool and Spa Industry*, 2001, **4**, 54–59.

43 J. Ihli, P. Bots, A. Kulak, L. G. Benning and F. C. Meldrum, *Adv. Funct. Mater.*, 2012, **23**, 1965–1973.

44 L. Addadi, J. Moradian, E. Shay, N. G. Maroudas and S. Weiner, *Proc Natl Acad Sci USA*, 1987, **84**, 2732–2736.

45 F. Nudelman and N. A. J. M. Sommerdijk, *Angew. Chem. Int. Ed.*, 2012, **51**, 6582–6596.

46 Y.-Y. Kim, M. Semsarilar, J. D. Carloni, K. R. Cho, A. N. Kulak, I. Polishchuk, C. T. Hendley IV, P. J. M. Smeets, L. A. Fielding, B. Pokroy, C. C. Tang, L. A. Estroff, S. P. Baker, S. P. Armes and F. C. Meldrum, *Adv. Funct. Mater.*, 2016, **26**, 1382–1392.

47 A. N. Kulak, P. Yang, Y.-Y. Kim, S. P. Armes and F. C. Meldrum, *Chemical Communications*, 2014, **50**, 67–69.

48 Y.-Y. Kim, J. D. Carloni, B. Demarchi, D. Sparks, D. G. Reid, M. E. Kunitake, C. C. Tang, M. J. Duer, C. L. Freeman, B. Pokroy, K. Penkman, J. H. Harding, L. A. Estroff, S. P. Baker and F. C. Meldrum, *Nat Mater*, 2016, **15**, 903–910.

49 B. Marzec, D. Green, M. Holden, A. Cote, J. Ihli, A. Kulak, D. Walker, S. Khalid, C. Tang, D. Duffy, Y.-Y. Kim and F. Meldrum, *Angew. Chem.*, 2018, 1–7.

50 O. C. Farokhzad and R. Langer, *ACS Nano*, 2008, **3**, 16–20.

51 T. Sun, Y. S. Zhang, B. Pang, D. C. Hyun, M. Yang and Y. Xia, *Angew. Chem. Int. Ed. Engl.*, 2014, **53**, 12320–12364.

52 R. Langer, *Nature*, 1998, **392**, 5-10.

53 R. Liang, M. Wei, D. G. Evans and X. Duan, *Chemical Communications*, 2014, **50**, 14071–14081.

54 N. Qiu, H. Yin, B. Ji, N. Klauke, A. Glidle, Y. Zhang, H. Song, L. Cai, L. Ma, G. Wang, L. Chen and W. Wang, *Materials Science and Engineering: C*, 2012, **32**, 2634–2640.

55 J. Wang, J.-S. Chen, J.-Y. Zong, D. Zhao, F. Li, R.-X. Zhuo and S.-X. Cheng, *J. Phys. Chem. C*, 2010, **114**, 18940–18945.

56 H. Chen, G. Chen, F. Du, Q. Fu, Y. Zhao and Z. Tang, *RSC Adv.*, 2013, **3**, 16251.

57 C. Wang, C. He, Z. Tong, X. Liu, B. Ren and F. Zeng, *Int J Pharm*, 2006, **308**, 160–167.

58 Y. Ueno, H. Futagawa, Y. Takagi, A. Ueno and Y. Mizushima, *Journal of Controlled Release*, 2005, **103**, 93–98.

59 W. Cui, Y. Cui, J. Zhao and J. Li, *J. Mater. Chem. B*, 2013, **1**, 1326–1332.

60 Y. Guo, J. Zhang, L. Jiang, X. Shi, L. Yang, Q. Fang, H. Fang, K. Wang and K. Jiang, *Chemical Communications*, 2012, **48**, 10636–10638.

61 M. Ukrainczyk, M. Gredičak, I. Jerić and D. Kralj, *Journal of Colloid and Interface Science*, 2012, **365**, 296–307.

62 H. Peng, K. Li, T. Wang, J. Wang, J. Wang, R. Zhu, D. Sun and S. Wang, *Nanoscale Res Lett*, 2013, **8**, 321.

63 W. Wei, G.-H. Ma, G. Hu, D. Yu, T. Mcleish, Z.-G. Su and Z.-Y. Shen, *J. Am. Chem. Soc.*, 2008, **130**, 15808–15810.

64 B. V. Parakhonskiy, A. Haase and R. Antolini, *Angew. Chem. Int. Ed.*, 2011, **51**, 1195–1197.

65 D. Zhao, C.-J. Liu, R.-X. Zhuo and S.-X. Cheng, *Molecular Pharmaceutics*, 2012, **9**, 2887–2893.

66 J.-L. Wu, C.-Q. Wang, R.-X. Zhuo and S.-X. Cheng, *Colloids and Surfaces B: Biointerfaces*, 2014, **123**, 498–505.

67 S. Kamba, M. Ismail, S. Hussein-Al-Ali, T. Ibrahim and Z. Zakaria, *Molecules*, 2013, **18**, 10580–10598.

68 A. Shafiu Kamba, M. Ismail, T. A. Tengku Ibrahim and Z. A. B. Zakaria, *BioMed Research International*, 2013, **2013**, 587451–10.

69 P. Liang, C.-J. Liu, R.-X. Zhuo and S.-X. Cheng, *J. Mater. Chem. B*, 2013, **1**, 4243–4250.

70 D. Zhao, R.-X. Zhuo and S.-X. Cheng, *Molecular BioSystems*, 2012, **8**, 753–759.

71 D. Zhao, R.-X. Zhuo and S.-X. Cheng, *Molecular BioSystems*, 2012, **8**, 3288.

72 Y. Zhao, Y. Lu, Y. Hu, J.-P. Li, L. Dong, L.-N. Lin and S.-H. Yu, *Small*, 2010, **6**, 2436–2442.

73 Á. Hernández-Hernández, A. B. Rodríguez-Navarro, J. Gómez-Morales, C. Jiménez-Lopez, Y. Nys and J. M. Garcia-Ruiz, *Crystal Growth & Design*, 2008, **8**, 1495–1502.

74 L. Addadi, S. Raz and S. Weiner, *Adv. Mater.*, 2003, **15**, 959–970.

75 H. A. Lowenstam and S. Weiner, *On Biomineralization*, Oxford University Press, 1989.

76 K. E. Sapsford, W. R. Algar, L. Berti, K. B. Gemmill, B. J. Casey, E. Oh, M. H. Stewart and I. L. Medintz, *Chem. Rev.*, 2013, **113**, 1904–2074.

77 I. Schmidt, K. Lee, E. Zolotoyabko, P. Werner, T. S. Shim, Y.-K. Oh, P. Fratzl and W. Wagermaier, *ACS Nano*, 2014, **8**, 9233–9238.

78 D. V. Volodkin, N. I. Larionova and G. B. Sukhorukov, *Biomacromolecules*, 2004, **5**, 1962–1972.

79 S. Biradar, P. Ravichandran, R. Gopikrishnan, V. Goornavar, J. C. Hall, V. Ramesh, S. Baluchamy, R. B. Jeffers and G. T. Ramesh, *J. Nanosci. Nanotech.*, 2011, **11**, 6868–6874.

80 H. Cölfen and M. Antonietti, *Langmuir*, 1998, **14**, 582–589.

81 T. Ogino, T. Suzuki and K. Sawada, *Geochimica et Cosmochimica Acta*, 1987, **51**, 2757–2767.

82 I. F. Tannock and D. Rotin, *Cancer Res*, 1989, **49**, 4373–4384.

83 H.-L. Pu, W.-L. Chiang, B. Maiti, Z.-X. Liao, Y.-C. Ho, M. S. Shim, E.-Y. Chuang, Y. Xia and H.-W. Sung, *ACS Nano*, 2014, **8**, 1213–1221.

84 Y. Zhao, Z. Luo, M. Li, Q. Qu, X. Ma, S.-H. Yu and Y. Zhao, *Angew. Chem.*, 2015, **54**, 912–922.

85 O. Tacar and C. R. Dass, *Journal of Pharmacy and Pharmacology*, 2013, **65**, 1577–1589.

86 S. Amelinckx, *The London, Edinburgh, and Dublin Philosophical Magazine and Journal of Science*, 2010, **44**, 337–339.

87 J. S. Langer, *Reviews of Modern Physics*, 1980, **52**, 1–28.

88 B. Pokroy, J. P. Quintana, E. N. Caspi, A. Berner and E. Zolotoyabko, *Nat Mater*, 2004, **3**, 900–902.

89 B. Pokroy, A. N. Fitch, F. Marin, M. Kapon, N. Adir and E. Zolotoyabko, *Journal of Structural Biology*, **155**, 96–103.

90 B. Pokroy, A. N. Fitch, P. L. Lee, J. P. Quintana, E. N. Caspi and E. Zolotoyabko, *Journal of Structural Biology*, 2006, **153**, 145–150.

91 B. Pokroy, A. Fitch and E. Zolotoyabko, *Adv. Mater.*, 2006, **18**, 2363–2368.

92 B. Pokroy, A. N. Fitch and E. Zolotoyabko, *Crystal Growth & Design*, 2007, **7**, 1580–1583.

93 S. Borukhin, L. Bloch, T. Radlauer, A. H. Hill, A. N. Fitch and B. Pokroy, *Adv. Funct. Mater.*, **22**, 4216–4224.

94 A. Brif, G. Ankonina, C. Drathen and B. Pokroy, *Adv. Mater.*, 2014, **26**, 477–481.

95 A. Brif, L. Bloch and B. Pokroy, *CrystEngComm*, 2014, **16**, 3268–3273.

96 B. H. Toby, *Journal of Applied Crystallography*, 2001, **34**, 210–213.

97 H. Land, L. F. Parada and R. A. Weinberg, *Nature*, 1983, **304**, 596–602.

98 C. Wang, C. Wu, X. Zhou, T. Han, X. Xin, J. Wu, J. Zhang and S. Guo, *Sci. Rep.*, 2013, **3**, 1686.

99 C. A. Orme, A. Noy, A. Wierzbicki, M. T. McBride, M. Grantham, H. H. Teng, P. M. Dove and J. J. DeYoreo, *Nature*, 2001, **411**, 775–779.

100 L. C. Nielsen, J. J. De Yoreo and D. J. DePaolo, *Geochimica et Cosmochimica Acta*, 2013, **115**, 100–114.

101 É. Tambutté, S. Tambutté, N. Segonds, D. Zoccola, A. Venn, J. Erez and D. Allemand, *Proc. Biol. Sci.*, 2012, **279**, 19–27.

102 M. Holcomb, A. L. Cohen and D. C. McCorkle, *Journal of Experimental Marine Biology and Ecology*, 2010, **440**, 126–131.

103 R. Markuszewski, Structure, fluorescence, and chelating properties of Calcein, *Retrospective Theses and Dissertations*, 1976, 5755.

104 H. Diehl and J. L. Ellingboe, *Anal. Chem.*, 1956, **28**, 882–884.

105 A. L. Moran, *Marine Biology*, 2000, **137**, 893–898.

106 *Journal of Experimental Marine Biology and Ecology*, 2011, **399**, 1–7.
107 W. Sontag, *Metals in Bone*, Springer, Dordrecht, 1985, 29–37.
108 D. Dissard, G. Nehrke, G. J. Reichart, J. Nouet and J. Bijma, *Geochemistry, Geophysics, Geosystems*, 2009, **10**.
109 A. Moya, S. Tambutté, A. Bertucci, É. Tambutté, S. Lotto, D. Vullo, C. T. Supuran, D. Allemand and D. Zoccola, *J. Biol. Chem.*, 2008, **283**, 25475–25484.
110 G. Falini, S. Fermani, G. Tosi and E. Dinelli, *Crystal Growth & Design*, 2009, **9**, 2065–2072.
111 H. Rademaker and M. Launspach, *Beilstein J. Nanotechnol.*, 2011, **2**, 222–227.
112 S. Fermani, B. N. Džakula, M. Reggi, G. Falini and D. Kralj, *CrystEngComm*, 2017, **19**, 2451–2455.
113 S.-H. Yu, H. Cölfen and M. Antonietti, *J. Phys. Chem. B*, 2003, **107**, 7396–7405.
114 G. Falini, S. Fermani, M. Gazzano and A. Ripamonti, *J. Mater. Chem.*, 1998, **8**, 1061–1065.
115 E. Weber and B. Pokroy, *CrystEngComm*, 2015, **17**, 5873–5883.
116 R. A. MILCH, J. E. TOBIE and R. A. Robinson, *J. Histochem. Cytochem.*, 1961, **9**, 261–270.
117 G. A. M. Finerman and R. A. Milch, *Nature*, 1963, **198**, 486–487.
118 H. E. Davis and J. K. Leach, *Annals of Biomedical Engineering*, 2010, **39**, 1–13.
119 B. C. Thompson, S. E. Moulton, J. Ding, R. Richardson, A. Cameron, S. O'Leary, G. G. Wallace and G. M. Clark, *Journal of Controlled Release*, 2006, **116**, 285–294.
120 A. Berman, L. Addadi and S. Weiner, *Nature*, 1988, **331**, 546–548.
121 F. C. Meldrum, *International Materials Reviews*, 2003, **48**, 187–224.
122 Y.-Y. Kim, A. S. Schenk, D. Walsh, A. N. Kulak, O. Cespedes and F. C. Meldrum, *Nanoscale*, 2014, **6**, 852–859.
123 E. Weber, L. Bloch, C. Guth, A. N. Fitch, I. M. Weiss and B. Pokroy, *Chem. Mater.*, 2014, **26**, 4925–4932.
124 K. R. Cho, Y.-Y. Kim, P. Yang, W. Cai, H. Pan, A. N. Kulak, J. L. Lau, P. Kulshreshtha, S. P. Armes, F. C. Meldrum and J. J. De Yoreo, *Nature Communications*, 2016, **7**, 10187.
125 A. E. X. Brown, R. I. Litvinov, D. E. Discher, P. K. Purohit and J. W. Weisel, *Science*, 2009, **325**, 741–744.
126 M. B. Söderlund, A. Sjöberg, G. Svärd, G. Fex and P. Nilsson-Ehle, *Scand. J. Clin. Lab. Invest.*, 2002, **62**, 511–519.
127 L. Altucci and H. Gronemeyer, *TRENDS in Endocrinology Metabolism*, **12**, 460–468.
128 T. A. E. Ahmed, E. V. Dare and M. Hincke, *Tissue Eng Part B Rev*, 2008, **14**, 199–215.
129 D. M. Albala, *Cardiovasc Surg*, 2003, **11 Suppl 1**, 5–11.
130 T. Fattahi, M. Mohan and G. T. Caldwell, *J. Oral Maxillofac. Surg.*, 2004, **62**, 218–224.
131 M. R. Jackson, *Am. J. Surg.*, 2001, **182**, 1S–7S.

132 G. Pellegrini, P. Rama, F. Mavilio and M. De Luca, *J. Pathol.*, 2009, **217**, 217–228.
133 N. Laurens, P. Koolwijk and M. P. M. de Maat, *J. Thromb. Haemost.*, 2006, **4**, 932–939.
134 Q. Ye, G. Zünd, P. Benedikt, S. Jockenhoevel, S. P. Hoerstrup, S. Sakyama, J. A. Hubbell and M. Turina, *Eur J Cardiothorac Surg*, 2000, **17**, 587–591.
135 Y. Kato, S. Ozawa, C. Miyamoto, Y. Maehata, A. Suzuki, T. Maeda and Y. Baba, *Cancer Cell Int.*, 2013, **13**, 89.
136 E. M. Hetrick and M. H. Schoenfisch, *Chem. Soc. Rev.*, 2006, **35**, 780–789.
137 S. B. Goodman, Z. Yao, M. Keeney and F. Yang, *Biomaterials*, 2013, **34**, 3174–3183.
138 R. M. Zachariah, C. O. Olson, C. Ezeonwuka and M. Rastegar, *PLoS ONE*, 2012, **7**, 49763.
139 T. Cramer, B. Chelli, M. Murgia, M. Barbalinardo, E. Bystrenova, D. M. de Leeuw and F. Biscarini, *Phys. Chem. Chem. Phys.*, 2013, **15**, 3897–3905.
140 D. Walsh, Y.-Y. Kim, A. Miyamoto and F. C. Meldrum, *Small*, 2011, **7**, 2168–2172.
141 M. Calvaresi, G. Falini, L. Pasquini, M. Reggi, S. Fermani, G. C. Gazzadi, S. Frabboni and F. Zerbetto, *Nanoscale*, 2013, **5**, 6944–6949.
142 S. Weiner and L. Addadi, *J. Mater. Chem.*, 1997, **7**, 689–702.
143 M. Reggi, S. Fermani, C. Samorì, F. Gizzi, F. Prada, Z. Dubinsky, S. Goffredo and G. Falini, *CrystEngComm*, 2016, **18**, 8829–8833.
144 M. Reggi, S. Fermani, V. Landi, F. Sparla, E. Caroselli, F. Gizzi, Z. Dubinsky, O. Levy, J.-P. Cuif, Y. Dauphin, S. Goffredo and G. Falini, *Crystal Growth & Design*, 2014, **14**, 4310–4320.
145 Y. Ning, L. A. Fielding, K. E. B. Doncom, N. J. W. Penfold, A. N. Kulak, H. Matsuoka and S. P. Armes, *ACS Macro Lett.*, 2016, **5**, 311–315.
146 A. Hanisch, P. Yang, A. N. Kulak, L. A. Fielding, F. C. Meldrum and S. P. Armes, *Macromolecules*, 2016, **49**, 192–204.
147 A. N. Kulak, M. Semsarilar, Y.-Y. Kim, J. Ihli, L. A. Fielding, O. Cespedes, S. P. Armes and F. C. Meldrum, *Chem. Sci.*, 2014, **5**, 738–743.
148 M. Mihai, V. Socoliuc, F. Doroftei, E.-L. Ursu, M. Aflori, L. Vekas and B. C. Simionescu, *Crystal Growth & Design*, 2013, **13**, 3535–3545.
149 R. F. Fakhrullin, A. G. Bikmullin and D. K. Nurgaliev, *ACS Appl. Mater. Interfaces*, 2009, **1**, 1847–1851.
150 A.-H. Lu, E. L. Salabas and F. Schüth, *Angew. Chem. Int. Ed.*, 2007, **46**, 1222–1244.
151 R. Hao, R. Xing, Z. Xu, Y. Hou, S. Gao and S. Sun, *Adv. Mater.*, 2010, **22**, 2729–2742.
152 R. Ghosh Chaudhuri and S. Paria, *Chem. Rev.*, 2012, **112**, 2373–2433.
153 J. S. Evans, *Chem. Rev.*, 2008, **108**, 4455–4462.
154 J. Aizenberg, A. J. Black and G. M. Whitesides, *Nature*, 1999, **398**, 495–498.

155 Y.-Y. Kim, C. L. Freeman, X. Gong, M. A. Levenstein, Y. Wang, A. Kulak, C. Anduix-Canto, P. A. Lee, S. Li, L. Chen, H. K. Christenson and F. C. Meldrum, *Angew. Chem. Int. Ed. Engl.*, 2017, **56**, 11885–11890.

156 S. Elhadj, J. J. De Yoreo, J. R. Hoyer and P. M. Dove, *Proc Natl Acad Sci USA*, 2006, **103**, 19237–19242.

157 L. Zuccarello, E. Rampazzo, L. Petrizza, L. Prodi and C. Satriano, *RSC Advances*, 2016, **6**, 52674–52682.

158 M. Helle, E. Rampazzo, M. Monchanin, F. Marchal, F. Guillemin, S. Bonacchi, F. Salis, L. Prodi and L. Bezdetnaya, *ACS Nano*, 2013, **7**, 8645–8657.

159 S. L. S. Stipp, *Geochimica et Cosmochimica Acta*, 1999, **63**, 3121–3131.

160 D. Al Mahrouqi, J. Vinogradov and M. D. Jackson, *Advances in Colloid and Interface Science*, 2017, **240**, 60–76.

161 J. Aizenberg, J. Hanson and T. F. Koetzle, *J. Am. Chem. Soc.*, 1997, **119**, 881–886.

162 M. Kucki, S. Landwehr, H. Rühling, M. Maniak and T. Fuhrmann-Lieker, 2006, vol. 6182.

163 M. Kucki and T. Fuhrmann-Lieker, *Journal of The Royal Society Interface*, 2012, **9**, 727–733.

164 M. Grimann and T. Fuhrmann-Lieker, *J. Photochem. Photobiol. B, Biol.*, 2016, **163**, 105–109.

165 H. Elderfield, C. J. Bertram and J. Erez, *Earth and Planetary Science Letters*, 1996, **142**, 409–423.

166 S. Bentov, C. Brownlee and J. Erez, *Proc Natl Acad Sci USA*, 2009, **106**, 21500–21504.

167 D. Evans, W. Müller and J. Erez, *Geochimica et Cosmochimica Acta*, 2018.

168 S. Tambutté, M. Holcomb, C. Ferrier-Pagès, S. Reynaud, É. Tambutté, D. Zoccola and D. Allemand, *Journal of Experimental Marine Biology and Ecology*, 2011, **408**, 58–78.

3 Photonic structures for bio-catalysis

3.1 Introduction

Periodic structures interact with radiation generating a wide variety of physical phenomena. Scientist have been taking advantage of diffraction and scattering of high frequency radiation, such as X-Ray, to get information on the material structure and characterize its structure at the nanoscale before the advent of high-resolution microscopy. This phenomenon can be exploited even at different length scales to fabricate materials with interesting proprieties. A widely known example are semiconductors, materials in which electron cannot propagate along certain direction when their frequency fall between the valence and the conduction band. This propriety is due to the wave nature of particles, which allows them to propagate within the periodic structure without scattering if certain criteria are met.

Recently, great attention has been paid to photonic crystals (PC), that is to say medium with a refractive index that varies in space periodically in 1, 2 or 3 dimensions.

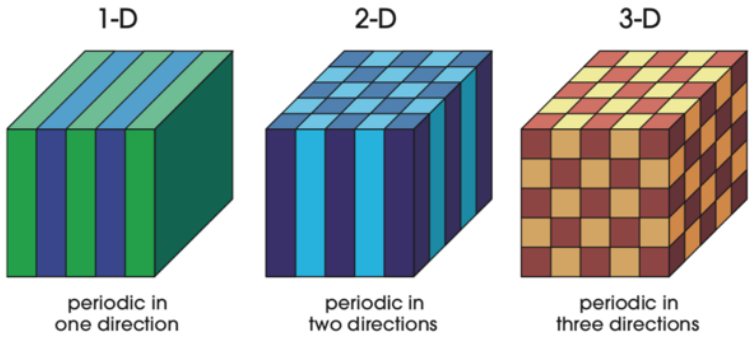

Figure 58. Schematic representation of 1, 2 and 3 dimensional photonic crystals. Reproduced from [1]

Such structures can interact with photons in the visible range and give rise to optical phenomena which can be used high performances mirrors, filters and waveguiding devices as well as more advanced devices, such as quantum computers and sensors.

This kind of nanostructures are difficult to fabricate, mainly because they need to combine a precise control over the nanostructure with a high coverage area to improve their performances. Self-assembly strategies are the most promising ones for fabricating these structures.

A great variety of photonic structures can be found in Nature. The incredible control that organisms exert over material deposition allow them to easily obtain such structures, often adding tunability or additional proprieties to them. [2-4]

The biomimicry of these structures with materials that are not readily available for living organisms, such as materials with high refractive indexes, can produce devices with astonishing performances. [5,6]

3.1.1 Photonic crystals proprieties

As mentioned above, photonic crystals are materials with a periodic variation in refractive index in 1, 2 or 3 dimensions. By controlling the PC structure and composition, it is possible to mold the flow of light and give rise to physical effects which can be exploited for technological applications. Reflection and refraction inside the material can cause a complete reflection of light that is seen as a coloration together with interesting phenomena described below.

3.1.1.1 Photonic band gap origin

To describe the origin of the photonic band gap, let's consider a 1D PC, in which the refractive index varies periodically along one dimension (z axis in Figure 59a). The physical behavior of this kind of structures is known since 1887, when lord Rayleigh published a pioneering analysis of light propagation in a multilayered stack. He stated that when a planar wave propagates in such a structure it is reflected and refracted by each interface it encounters. By considering a wave that propagates along the z, we can plot the light line ($\omega(k)$) for different PC. When the material is homogeneous (GaAs bulk in figure Figure 59b), the light is only slowed down due to the refractive index of the material, but all the frequencies can propagate inside the material. Considering a PC composed of alternating layers of GaAs and GaAlAs (refractive indexes are 13 and 12 respectively), we can see that a region where no frequencies can propagate, called photonic band gap, forms. The gap increases when a GaAs/Air multilayer (air refractive index is close to 1) is considered. To understand why the band gap forms, it is useful to consider the possible localization of the electric field just above and below the band gap. The band gap between n=1 and n=2 occurs when $k = \frac{\pi}{a}$ and the modes have a wavelength of 2a. Modes with this wavelength can be centered only as represented in Figure 59c for symmetry reasons, centering their maximum or in the high refractive index region or in the low refractive index one. This means that the energy density will be localized (i) in the high RI material for in the dielectric band (n=1) or (ii) in low RI material for in the air band (n=2).

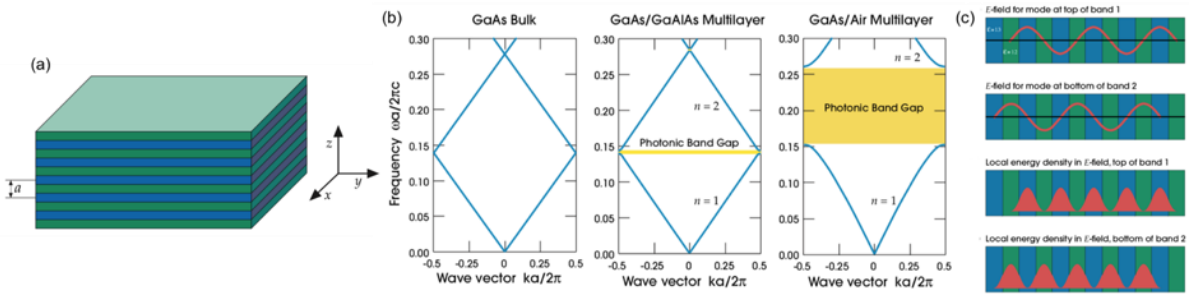

Figure 59. (a) Schematic representation of a 1D PC, (b) photonic band diagram for 1D PC made of materials with different RI and (c) possible electric field arrangement in the 1D PC and their energy densities. Reproduced from [1]

This brief section shows how the band gap is related to the presence of a periodic structure, without which no photonic effect would exist. The presence of the photonic band gap is the key point for the phenomena exploited in real PC applications.

3.1.1.2 Practical implication of the slow light effect

One of the most exploited effect produced by the photonic band gap is the slow light effect. The frequencies at the edge of the band gap can still propagate in the material due to defects and inhomogeneities in the crystalline structure. These frequencies will propagate at slower velocities than the permitted modes, thus being absorbed more efficiently by molecules or materials according to the Fermi's golden rule.

From an experimental point of view, we can relate the regions at the edge of the band gaps (underlined in red in Figure 60a) with the ones next to the peaks present in the reflectance spectrum of the PC (red boxes in Figure 60b). So, the characterization of the reflectance of the PC allows to collect information on the photonic band structure. By tailoring the morphology of the material, it is possible to tune the slow light region to match the desired wavelength.

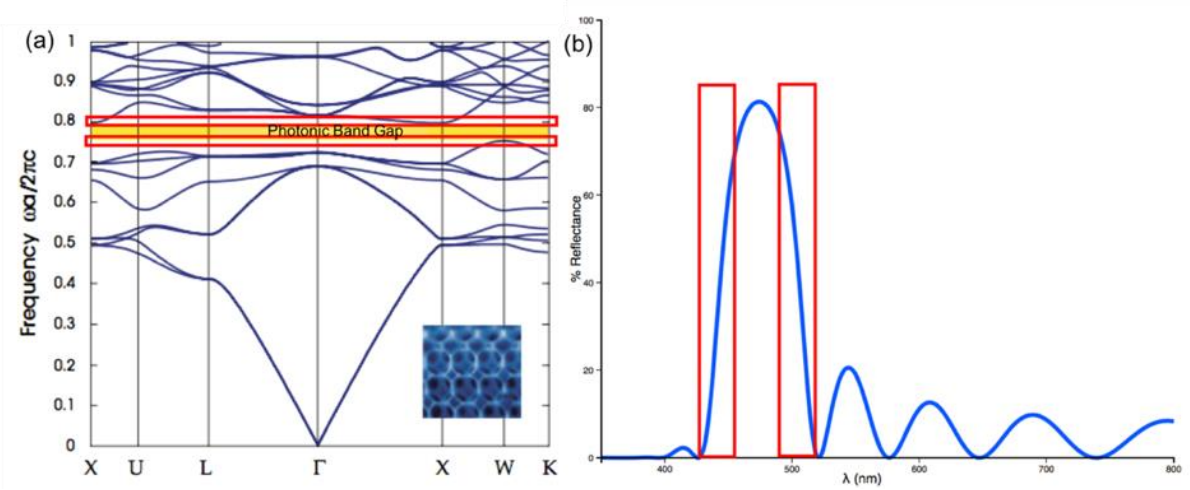

Figure 60.(a) Photonic band structure for a 3D PC and (b) typical reflectance spectrum of a 3D PC. The regions underlined in red in (a) correspond to the ones in (b). (a) is reproduced from [1].

This PC propriety has been widely employed, for example, in the enhancement of photocatalytic efficiency of organic dyes degradation by titania 3D PC, which is promoted by UV light, by slowing the light in this spectral region and increasing its absorption by the material. [7,8]

3.1.2 Photonic structures in Nature

Nanostructures are widespread in Nature and serve a variety of purposes. Well-known examples are the structures present on lotus leaves, which gives them anti-wetting and self-cleaning proprieties, and the ones on Gecko paws, which allows them to stick to flat vertical surfaces. Sometimes those structures produce structural color, a technique that organisms use to obtain brighter color that depend on angle and can be tuned by changing the composition or the morphology of the components. For example, butterfly wings are covered in nanostructures giving them anti-wettability and strong color at the same time and many beetles have photonic exoskeletons with good mechanical proprieties. [9-11] Even if photonic structures are widespread among different types of organisms, their role still needs to be clarified. [12] The most acknowledged hypothesis is that they are used to communicate with other organisms, especially for mating or defense purposes. The relation between the outcoming color, the typical wavelength in which it's found and the mechanism producing it is reported in Table 6. Then, examples of photonic structures which can be found in Nature are given.

Table 6. Correlation between the structural color produced, the mechanism generating it and the typical wavelength involved. [13]

structural color	**mechanism**	**wavelengths reflected**
simple metallic hues	multilayer reflector	discrete band of visible spectrum
silver or gold color	variable thickness broadband multilayer reflector	all visible
circularly polarized color	helically arranged multilayer reflector	yellow–green
spectral iridescence	diffraction grating	all visible, as ordered spectra
opal or diamond effects	three-dimensional photonic crystal	all visible
UV and white reflectance	Tyndall scattering	all visible, plus ultraviolet
most non-metallic blues	quasi-ordered array	typically blues and purples

3.1.2.1 Butterfly wings

Butterfly wings are one of the most outstanding and wide known examples of structural color. Wings of the butterflies of the *Morpho* phylum show a strong iridescent blue coloration that is not due to pigments embedded in the material but to the nanostructures present on their surface (Figure 61). SEM imaging of the scales composing the wings reveals the presence of chitinous Christmas-tree like structures who are responsible for light diffraction, scattering and interference. The most important feature is the distance between the ridges, which corresponds to half of the reflected wavelength. The presence of multiple ridges, their offset and their curvature are responsible for the angle independency of the color with respect to the viewer angle. [14]

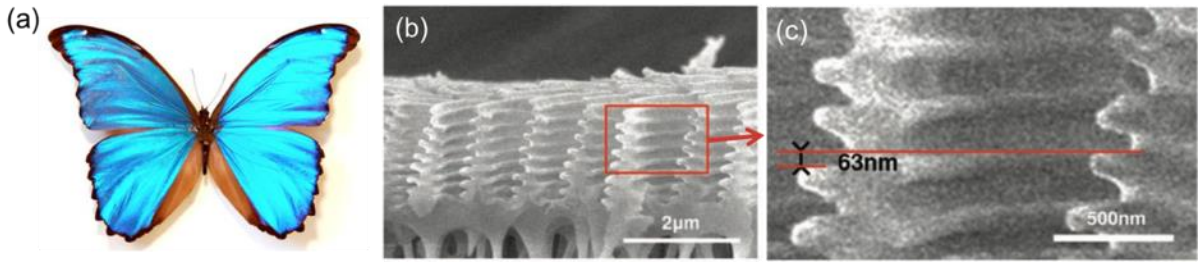

Figure 61.(a) Butterfly of the Morpho phylum. (b) Cross-sectional SEM image of the multilayered ridges on the dorsal ground scale of a Morpho Didius butterfly. The red rectangle indicates the region shown in more detail in (c). Reproduced from [14]

The butterfly *Callophrys rubi* is a great example of iridescence suppression. Its wings show a matt green color which is thought to exploit a camouflage function (Figure 62a).
The scales present on the wing are composed of domains of chitinous 3D single gyroid crystals with different orientations, which color ranges from blue to yellow-green when observed normal to the scale surface. When the scales are observed with a low magnification objective, thus meaning that both incident and reflected light are almost perpendicular to the surface due to the numerical aperture (NA) of the objective, domains with different coloration due to the interaction of the light with a single plane of the gyroid crystal can be distinguished. When the scale is observed at higher magnification and higher NA, the contribution of other crystalline planes becomes more significant, thus changing the coloration by merging the single signals. When the wing is observed from a greater distance, the different colored domains cannot be distinguished anymore due to their dimensions below the eye resolution limit, similarly to what happens for LCD screens. It was hypothesized that the presence of the blue component might be exploited in communication with organisms with a higher-resolution vision system, while the matt green coloration is used for camouflage from other species. [15]

In conclusion, butterfly wings are a good example showing how different photonic structures can be used to obtain opposite effects, such as strong iridescence and matte coloration, just by changing the arrangement of the material in the space.

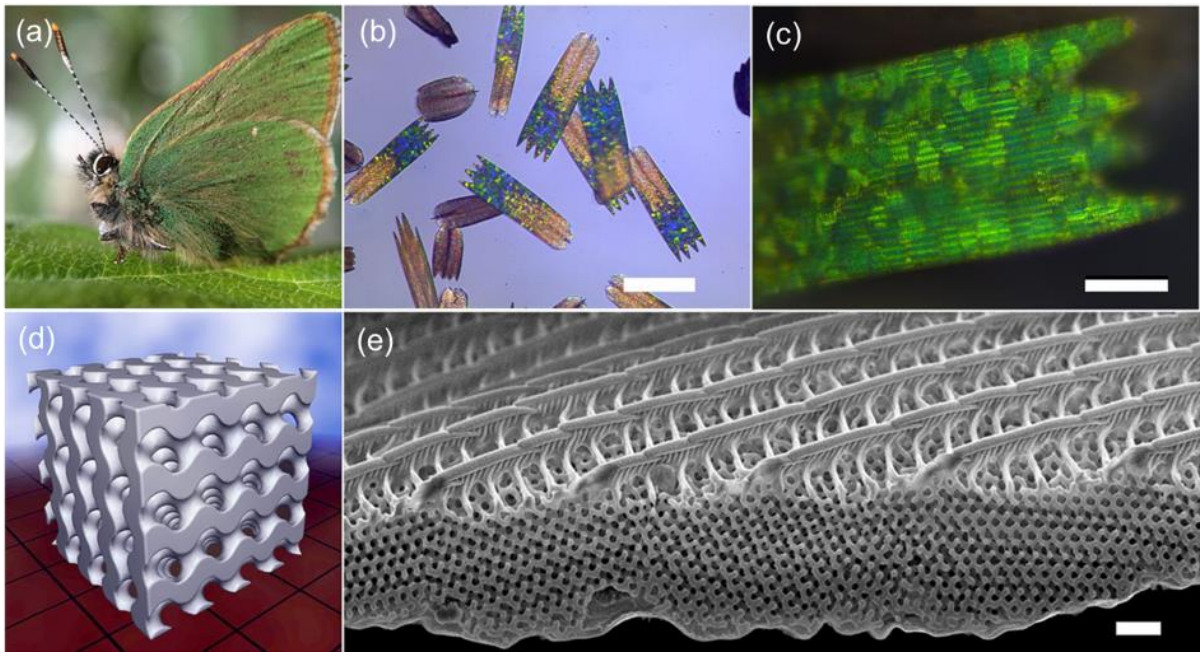

Figure 62. (a) *Callophrys rubi* (Linnaeus, 1758) also known as the green hairstreak; (b) optical microscope image of both colored and brown cover scales from *C. rubi* taken at low NA; (c) high NA (high magnification) optical micrograph of a colored wing scale showing that the characteristic green–yellow color arises from many individual photonic crystal domains. Note that the longitudinal ribs are also visible; (d) computer-generated single gyroid model—4x4x4 unit cells; (e) SEM image of a colored wing scale showing the ribbed upper surface, an undulating lower plate and five porous, single gyroid domains in different orientations. Note the continuous network spanning crystal grain boundaries suggestive of twinning planes, yet with some lattice defects such as dislocation planes and holes. Scale bars: (b, c and e) 100, 20 and 1 mm, respectively. Reproduced from [15]

3.1.2.2 *Chrysina resplendens* exoskeleton

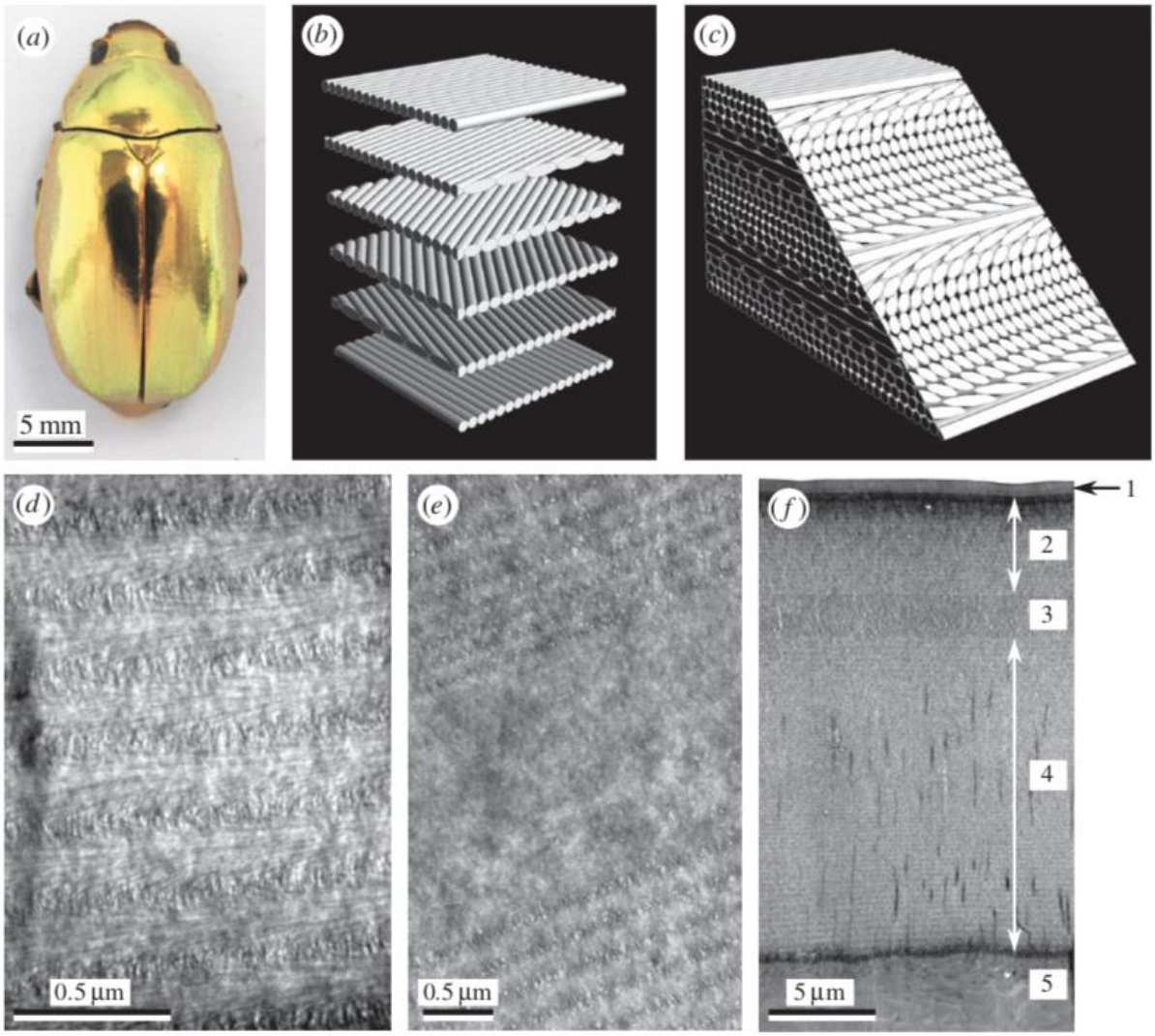

Figure 63. Helicoidal constructions and their exhibition in the scarab beetle *Chrysina resplendens*. (a) Dorsal view of C. resplendens photographed under unpolarized illumination. (b) An exploded view of a helicoidal set of filament planes. A left-handed helicoid is shown, in which successive planes further from the observer are rotated anticlockwise. (c) A view of a section of an assembled helicoidal stack. The oblique cut reveals Bouligand curves in the filament arrangement. A full helicoidal pitch is shown, comprising two lamellae as indicated by the Bouligand curves. (d) TEM showing detail of an oblique section of the elytron of *C. resplendens*. Helicoidal lamellae are identified by the Bouligand curves. (e) TEM showing detail of a normal section of the cuticle. The unidirectional layer or birefringent retarder is shown as the uniform band extending across the centre of the image. Helicoidal regions are disposed above and below. (f) TEM of a normal section through the outer part of the cuticle of *C. resplendens*, indicating its component regions: 1: epicuticle; 2: upper helicoid; 3: unidirectional layer; 4: lower helicoid; 5: endocuticle (portion). Regions 2–4 form the exocuticle. Reproduced from [16]

C. resplendens is a beetle that can be found in central America, known for its peculiar golden metallic appearance. Such a color cannot be obtained by using pigments as it involves a broad reflection over a wide angular range. *C. resplendens* exoskeleton is composed of chitin microfibers disposed on stacked planes, which give rise to a 2D photonic crystal. The filament

planes are disposed following an helicoidal arrangement along the stacking direction. Similar structures have been observed in many similar beetles and are associated with their metallic appearance. The main characteristic *of C. resplendens* is that its exoskeleton is composed of two layers of helicoidal filaments planes separated by a unidirectional layer that acts as a retarder, a component able to invert light polarization. Doing so, the organism can reflect both L-polarized and R-polarized light. The inhomogeneity in thickness over the filament plane and the chirping of the planes allows to diffract light over a broad band of the visible spectrum simultaneously, giving rise to a broadband reflector. The color of broad-band reflectors is also less directionally dependent, because the full range of wavelengths is reflected. The broader the range of bandwidths, the closer to pure gold (mirror-like) the cuticle appears. [16]

This organism is a good example of how different strategies can be combined in the same structure to obtain new proprieties.

3.1.2.3 *Entimus imperialis* exoskeleton

E. imperialis is a weevil endogenic of Brazil that has a black exoskeleton covered in spots which appear green when observed from a long distance (Figure 64a) and iridescent when observed close up (Figure 64b), thus serving at the same time for camouflage and communication. The color is generated by the great number of scales disposed inside pits on the weevil body, which are composed of big photonic domains (Figure 64c-d). Each photonic domain is composed of a chitinous single-network diamond 3D photonic crystal (Figure 64e-f). The photonic crystals inside the scales form a layer of fused photonic crystal domains. Since the refractive index contrast between air and chitin is low, the reflected spectrum is strongly dependent on crystal orientation. When a whole pit is illuminated, the reflection peak broadened, generating a scatterograms containing a few prominent reflection spots on a more or less angle-independent green-yellow background. This phenomenon can be ascribed to the angular orientation of the scales inside the pit, which sums the reflection from the single scale and causes the broadening of the peaks. The concentration of the scales in pits presumably serve three functions: protection from mechanical damage and accidental loss, intraspecific recognition of brilliant spots and camouflage in foliaceous environments by the integral green coloration. [17] In conclusion, the 3D photonic structures present on *E. imperialis* exoskeleton and their spatial arrangement are good example of multipurpose structural color.

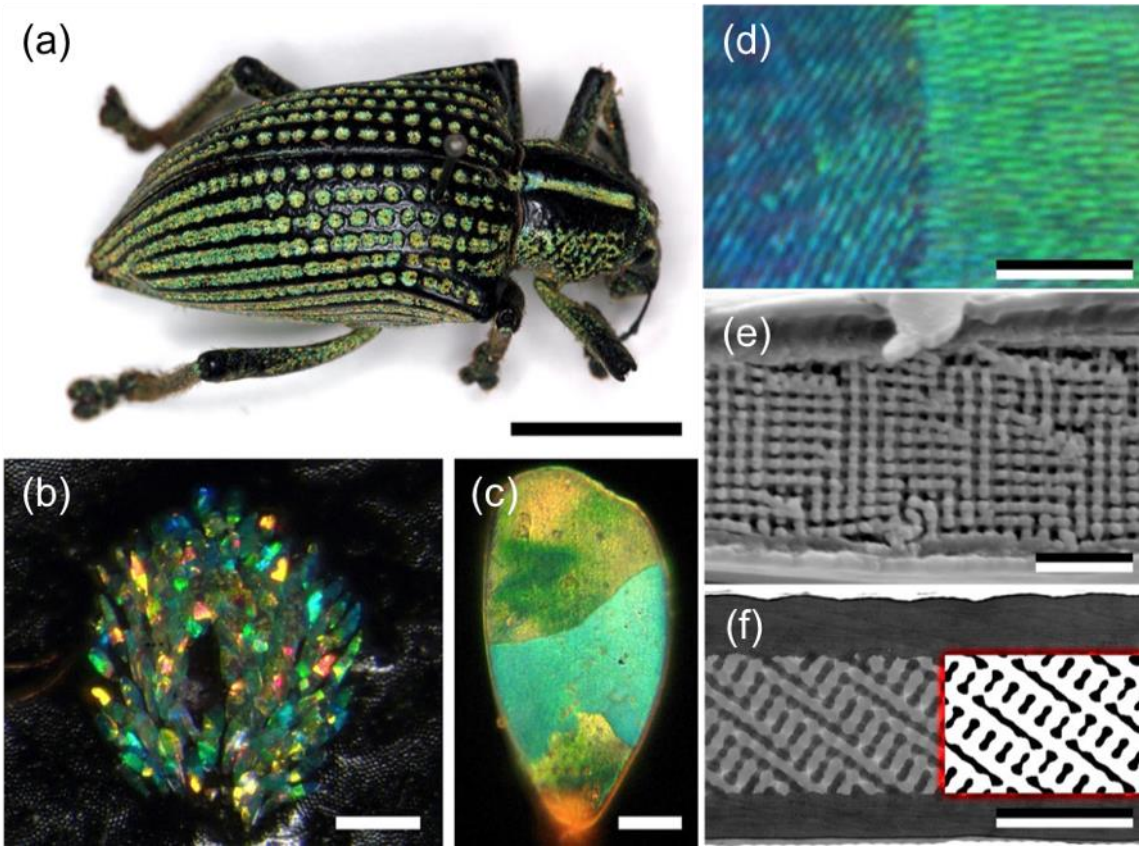

Figure 64. The diamond weevil, *Entimus imperialis*, and its scale organization. (a) The intact animal with the black elytra where numerous pits are studded with yellow-green scales. Scale bar, 1 cm. (b) A single pit as seen in an epi-illumination microscope, showing highly reflective scales of different colors. Scale bar, 200 mm. (c) A single scale with a few differently colored domains. Scale bar, 20 mm. Microstructure of the scales of *Entimus imperialis*. (d) Highly magnified image of a single scale at a zone boundary. Note the different lamellar arrangements in the two areas. Scale bar, 5 mm. (e) Scanning electron microscopy of a cross section of a fractured scale showing a highly organized interior of tilted sheets with square symmetry. Scale bar, 2 mm. (f) Transmission electron microscopy (TEM) image of the nanostructure of an *E. imperialis* scale. The red-bordered inset shows a simulated (3 2 12) TEM cross section of a level-set single-network diamond-type crystal. Scale bar, 2 mm. Reproduced from [17]

3.1.3 Synthetic photonic crystals and fabrication methods

To display photonic proprieties in the visible range, a nanostructure should possess features in the visible light length scale, thus requiring fabrication techniques with a resolution of ten nanometers. The recent advances in instrument technologies and performances opened up an unexplored range of possibility for photonic crystal fabrication for novel applications. A brief overview of the most commonly used strategies to produce 1, 2 or 3D inorganic photonic crystals is given below.

3.1.3.1 1D structures

1D photonic structures consist in alternate layers of materials with different refractive indexes and are commonly known as Bragg stack. Silica or titania 1D PC can be fabricated by spin coating of inorganic nanoparticles, easily obtained due the sol-gel chemistry involved in the materials synthesis, followed by thermal treatment to sinter them (Figure 65a-b). It is possible to obtain a good control on the materials porosity while it is tricky to control the thickness of the deposited layers. Overall, this method allows an economical and easy preparation of good quality 1D PC. [18-20]

A higher control over layer thickness can be reached by using chemical vapor deposition (CVD), a technique depositing a thin layer of inorganic material by reaction of precursor in vapor phase. Although this technique requires advanced instrumentation, it produces homogeneous high-quality crystalline materials with exceptional control over dimensions. [21]

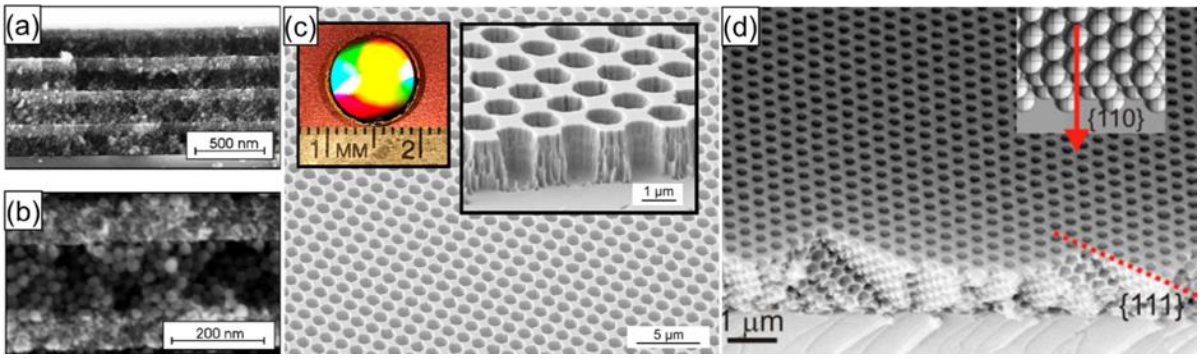

Figure 65. (a,b) FESEM images of the cross section of an eight-layer Bragg reflector made of silica and titania nanoparticles deposited alternately on the substrate using spin coating. The concentration employed in both suspensions is 5 wt %, and the rotational speed is set at 100 rps. Reproduced from [19] (c) Scanning electron micrograph of fabricated W PhC Sample (r = 0.55 µm, a = 1.40 µm, d = 1.60 µm) over a large area, showing excellent uniformity. Interference lithography and standard reactive ion-etching techniques are used to fabricate the samples. (Left Inset) Digital photo of the full 1-cm-diameter sample. (Right Inset) Magnified cross-sectional view of W PhC Sample II. Reproduced from [22] (d) fracture cross section of a crack-free I-SiO_2 film on a Si wafer, showing the h110i growth orientation, as illustrated by an fcc model (Inset). Reproduced from [23]

3.1.3.2 2D structures

2D PC fabrication usually involves the deposition of a layer of the substrate followed by its patterned etching. The deposition of the material can be done with CVD or a commercial

substrate can be used. The first, and most critical, step is the fabrication of a pattern to be used as a mask for etching on top of the substrate. If a resolution over 200 nm is required, photolithography is the ideal technique to use since it is fast and easy to perform. [22] If a higher resolution is required, electron beam technology can create patterns with features in the order of ten nanometers. Photolithography is a parallel technique, allowing to reproduce the whole pattern at once, while e-beam is a serial technique, which requires more time and expensive equipment. After the fabrication of the mask, chemical wet or dry etching can be used to obtain the 2D structure, paying attention to the diffusion of the etching substances if small features are present in the pattern.

3.1.3.3 3D structures

3D PC fabrication still poses challenges despite the research effort done for their production. Layer-by-layer deposition, holographic or lithographic techniques and self-assembly are the most diffused techniques employed. Layer-by-layer consist in the fabrication of 2D structures followed by their stacking, allowing a good control over the structure but reducing the thickness of the final material. It has been used to obtain complex structures, such as woodpile arrangements. [21] Lithographic techniques using 2 laser beams were successfully applied to create 3D PC, often followed by dissolution of the irradiated materials and the filling of that volume with an inorganic phase. Holographic techniques allow to irradiate all the substrate at the same time, increasing the velocity of the process.

Self-assembly is the fastest and easiest technique to up-scale. It consists in the assembly of colloidal particles over as substrate, as it naturally happens in opal gems. Synthetic opals consisting of polymeric particles can be easily formed by solvent evaporation or particles assembly on the surface of the liquid. Then, the resulting scaffold can be infiltrated with a matrix and a so-called inverse opal is obtained upon dissolution of the polymeric particles. [24,25] Among all the different fabrication protocols published, colloidal co-assembly is one of the most promising. This method consists in the assembly of the colloidal particles together with the matrix precursor on a vertical substrate by evaporation of the solvent, followed by a thermal treatment which simultaneously remove the templating particles and sinter the matrix components. [8,23,26-29]

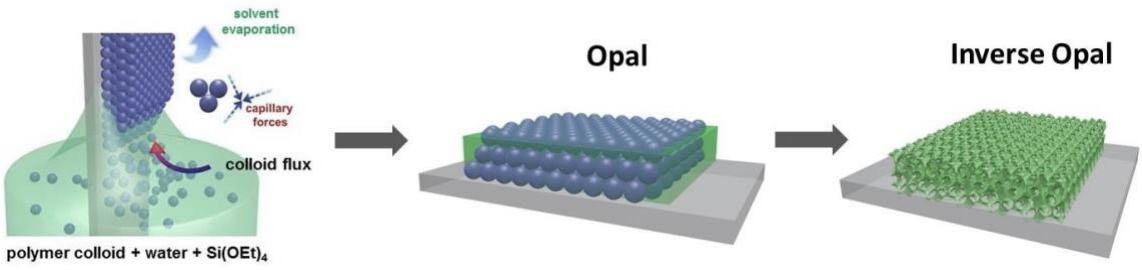

Figure 66. Schematic representation of colloidal co-assembly process to obtain IO

As shown above, a lot of progresses were done on photonic structure fabrication, but fabrication of complex and performing structures is still a challenging task.

3.1.4 Beyond color: PC applications

Beyond displaying structural color, PC physical proprieties might be used for functional application. Even in Nature these structures play a role in thermoregulation, friction reduction, water repellency, strengthening, photoprotection and vision enhancement. [12] The recent advancements in fabrication technology and the deeper knowledge acquired on their behavior allowed scientist to design new materials taking advantage of photonic structures to fabricate devices with a variety of functions. Representative examples are given.

3.1.4.1 Bragg stack for in situ cell monitoring

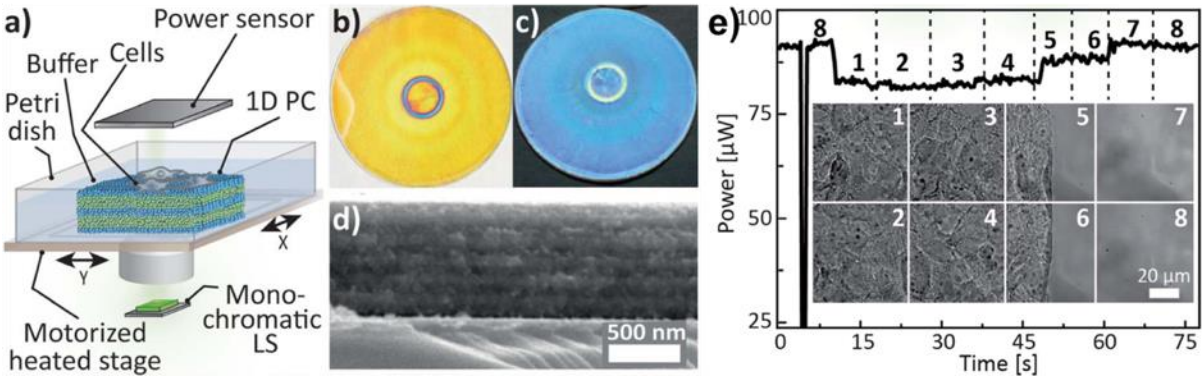

Figure 67. (a) Schematic illustration of the photonic-to-electronic plat- form for cellular sensing: a 1D PC is placed into a buffer solution in the Petri dish and covered with cells, and the modulated power of the monochromatic LS is recorded by the power sensor. The photographs of the employed 1D PC taken normally (b) and approximately at 45° (c) to the PC surface (the diameter of the round substrate is 5 cm); (d) cross-section SEM image of a 1D PC composed of 6 nanoparticle-based SiO_2 (≈90 nm)/TiO_2 (≈60 nm) bilayers. (e) laser power signal obtained during scanning the partially covered 1D PC with a HuH7 cell monolayer in the positions 1–8 with a microscope stage; the black dashed lines mark the time instants of the stage position change. Reproduced from [30]

Pavlichenko *et al.* [30] showed some powerful application of 1D PC coupled with different light sources and detectors. By coupling a monochromatic light source, a Bragg stack and a silicon power sensor (Figure 67a) they fabricated a novel device that can be used for *in situ* label-free, non-invasive monitoring of cells, with promising application in analysis of cell proliferation and differentiation, wound healing, cytotoxicity and drug screening. The core of the device is the 1D PC, prepared by sequential spin coating of silica and titania nPs layers followed by calcination. The number and thickness of the layer has been optimized to display a PBG around 532 nm, the wavelength emitted by the light source (Figure 67 b-d). By adding a motorized stage, they were able to scan the cell growth area and obtain a signal proportional to the confluency state of the cell layer (Figure 67e). This device represents a versatile example of transduction of a photonic signal into an electric one with application in the medical diagnosis field.

3.1.4.2 Stretchable photonic fibers for pressure determination

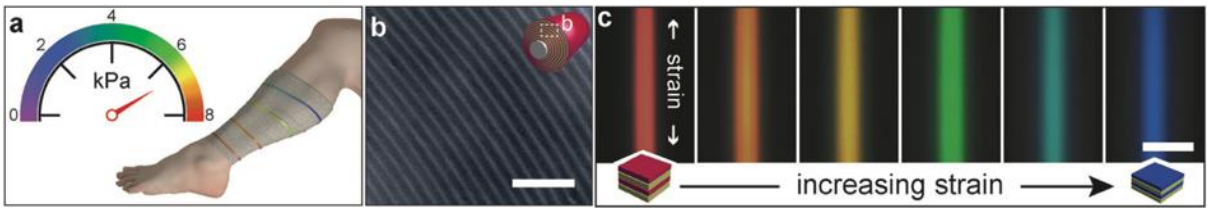

Figure 68. Concept for sensing bandage pressure. a) Depiction of the proposed use of fibers as colorimetric sub-bandage pressure indicators in compression therapy. b) Scanning electron microscopy image of a cross- section of a multilayer cladding, showing its distinct radial periodicity. Scale bar 2 µm. c) A series of optical micrographs showing the vivid, strain-dependent color of a fiber that is colored red when no strain is applied and changes to orange, yellow, green, and finally blue as the strain increases and the layer period decreases. The direction of applied strain is marked in the first image. Scale bar 100 µm. The color sequence is reversed from the conceptual sketch in (a). reproduced from [31]

Sandt *et al.* [31] prepared and tested highly elastic fibers with good mechanical proprieties coupled with photonic proprieties whose color is dependent on their stretching with application in compressive medical textiles (Figure 68a). The fibers are prepared by casting a layer of polydimethylsiloxane (PDMS, refractive index n ≈ 1.41) over a layer of polystyrene-polyisoprene triblock copolymer (PSPI, n ≈ 1.55) and wrapping them around a PDMS core fiber (Figure 68b). The layers composing the structure act as a Bragg stack and show a strong coloration due to the high number of layers with low refractive index contrast. At the same time, this choice of materials allows the fabrication of a fiber with good mechanical proprieties that is not subject to breakage over repeated stretching. The stretching of the fiber changes the thickness of the layers, causing a blueshift in their reflectance spectra and making them act as pressure sensors when wrapped around objects (Figure 68c). The fibers have been successfully integrated into compressive bandages and improved the easiness of usage by non-expert users.

This structure geometry can be replicated by changing the constituent materials and opens up the possibility of obtaining fibers responding to temperature, solvent vapors, magnetic field with a change in their coloration.

3.1.4.3 Wetting in color

Inverse opal pores, other than molding the flow of light, have different wettability rate depending on the geometry on the opal itself, in particular of the necks between pores, and on the surface tension of the wetting liquid. When the pores are filled with a medium with refractive index similar to the one of the slab, the iridescent coloration disappear. So, when using silica IO, which refractive index is around 1.4, the infiltration with most of the solvent will reduce or completely cancel the opal color.

By using silica IO with different number of layers, commonly obtained by using the colloidal co-assembly method, and functionalizing them with different alkylchlorosilanes and grading vertically the surface chemistry, Burgess *et al.* [29] were able to visually distinguish between different classes of liquids. The wettability of the functionalized IO decreases with depth, causing distinct infiltration patterns in different liquid, each penetrating a fixed depth. As the total thickness of the IO gradually vary across the sample, distinct depths of penetration are viewed as distinct rainbow patterns whose size and location in the chip is unique to the depth filled, given that the displayed color is related only to the number of empty pores left.

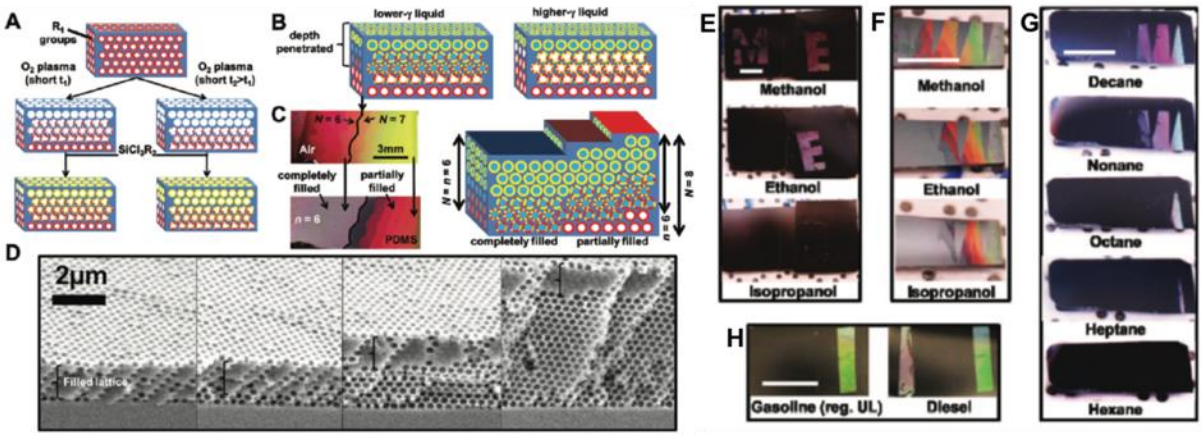

Figure 69. (A) Schematic depicting the use of short O_2 plasma exposure between successive silanizations to generate a vertical gradient of wettability. (B) Using vertical gradients where wettability decreases toward the bottom of the sample, liquids penetrate up to a fixed depth that increases with decreasing surface tension (decreasing θc). The blue circles represent pores that are filled with liquid in the schematics. (C) This depth translates into a distinct color pattern in IOFs having a naturally varying total number of layers (shown in schematic). Photographs show an IOF-functionalized DEC→13FS (45 s plasma exposure) in air (top) and after soaking in PDMS precursors (cured before imaging). The total thickness of this IOF is increasing from the left to the right of the image. The color completely disappears in the regions where the total thickness is less than the penetration depth (n = 6). The black line on the images indicates the boundary between regions with 6 and 7 total layers (N). (D) Scanning electron micrograph (SEM) cross-sections illustrating the fixed degree of layer penetration of the PDMS precursors (subsequently cured) over a wide range of film thicknesses. (E) Two IOFs, functionalized from evaporation of solutions containing 99:1 ("M") and 5:1 ("E") ratios of DEC- and 13FS-trichlorosilanes, are used to distinguish between alcohols. The backgrounds of the IOFs have been selectively oxidized to reveal "ME" in methanol, "E" in ethanol, and no color in isopropyl alcohol. (F,G) Photographs of IOFs

functionalized with a vertical gradient of wettability (DECf13FS) to distinguish between alcohols and alkanes. An array of teeth is oxidized (so that θc f ∼0 in these regions for all liquids) to make the patterns easier to visibly distinguish. (H) Photographs of an IOF regionally functionalized with 13FS (right stripe) and a vertical gradient of DECf13FS (left stripe) on an oxidized background that shows different patterns in samples of regular unleaded gasoline and diesel. Scale bars: 5 mm. reproduced from [29]

The gradient in surface chemistry of the pores has been obtained by functionalizing them with the first silane, which is then partially removed by short O_2 plasma treatment, followed by functionalization with the second silane (Figure 69a). Liquids with lower surface tension will infiltrate deeper into the IO (Figure 69b). Considering an IO with increasing number of layers, only the thinnest section will be completely filled, thus becoming colorless while the thicker part will remain colored (Figure 69 c-d).

By using different functionalization protocols and patterning the surface to increase the readability of the results, platforms able to distinguish between different alcohols (Figure 69e-f), alkanes (Figure 69g) and regular gasoline and diesel (Figure 69h) were prepared.

This innovative IO platform finds application in the recognition of unknown liquid mixtures by preparing an inexpensive and reliable device to be used as an indicator.

3.2 Aim of the project

Enzymatic reactions have high selectivity of the substrate, high control on the product and are often carried out at room temperature with no or few side products, thereof they are appealing from an industrial point of view as well as for therapeutic purposes. The ability of activating enzymes using light allow to control them remotely, with high special resolution and using a renewable resource. Up to now, all the protocols used to prepare light activated enzymes rely on the chemical modification of the enzyme near the active site [32,33] or the use of a photoactivated cofactor [34], thus making it necessary to tailor the procedure for every specific enzyme.

The aim of this project is to obtain laser driven remote and localized enhanced catalytic efficiency of enzymes by using a photonic structure coupled with plasmonic nanoparticles (nPs). To do so, we prepared inverse opals with tailored pore size and refractive indexes able to slow light at 532 nm. In order to take advantage of the slow light effect, plasmonic nPs able to absorb light around this wavelength were immobilized on the IO surface. The enhancement of the enzyme activity is obtained exploiting the heating of the plasmonic nPs and can be potentially applied to every enzyme by exploiting their increased activity at higher temperatures.

Titania inverse opals with 380 nm pore diameter were obtained using the colloidal co-assembly method and their ability to slow light around 520 nm was verified. Gold nPs seeds were immobilized on the inverse opal surface and grown by reduction of gold ions in situ and their heating was verified. Candida rugosa lipase was chosen as a model enzyme for its interest in industrial application and it was immobilized on the IO surface using electrostatic interactions. Enzyme efficiency was evaluated measuring diacetyl fluorescein conversion into fluorescein, an easy to monitor absorbing molecule, by the enzyme.

The results shown in this chapter describe the first steps toward a universal platform for enhanced catalytic activity of all the chemical reactions favored by heating using light as a trigger.

3.3 Results

The platform fabrication can be divided into 3 main parts: (i) IO fabrication, (ii) plasmonic nPs immobilization on the surface and (iii) enzyme immobilization on the surface.

3.3.1 Inverse opals fabrication and pore size tuning

Inverse opals were prepared using colloidal co-assembly. [26,35] Briefly, polymeric colloidal particles were assembled on a glass substrate in the presence of titania nanoparticles to obtain a titania matrix or tetraethylortosilane to obtain a silica matrix. The templating colloidal particle were then removed by thermal treatment to obtain an inorganic matrix with interconnected pores of the size of the colloids (see 3.1.3).

Silica and titania were chosen as matrix components for their refractive indexes of 1.4 and 2.5 at 532 nm, respectively. Since the photonic band gap is dependent on the refractive index contrast between the matrix and the pore, materials with different refractive index have different band gap wavelength. The high refractive index gap between titania and water (n=1.33) makes it appealing for wet application, while it can be easily predicted that silica IO won't have a strong photonic behavior due to its low refractive index. Thus, titania IO were chosen for obtaining a photonic platform, while silica IO were used as a reference.

SEM imaging of silica and titania IO (Figure 70) reveals that inverse opal with few cracks and high order domains are obtained.

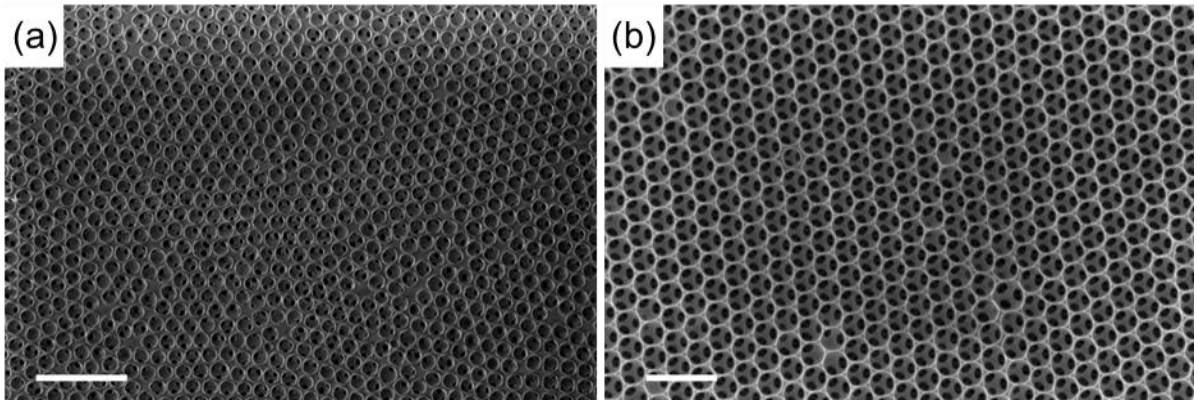

Figure 70. SEM images of (a) SiO2 inverse opal and (b) TiO2 inverse opal.

The photonic proprieties of the IO were studied both in air and water, whose refractive indexes are 1 and 1.33 respectively. Silica IO show a high reflection peak around 480 nm when dry, but once wetted they lose any photonic behavior (Figure 71 a, b, e). This effect is due to the low refractive index contrast between water and silica. Titania IO show a lower intensity reflectance compared to the silica ones when dry but they reflect light around 550 nm when wet(Figure 71 c, d, f). As previously discussed, light is slowed at the edge of the band gap, making titania IO with 380 nm pore size ideal for slowing light around 532 nm.

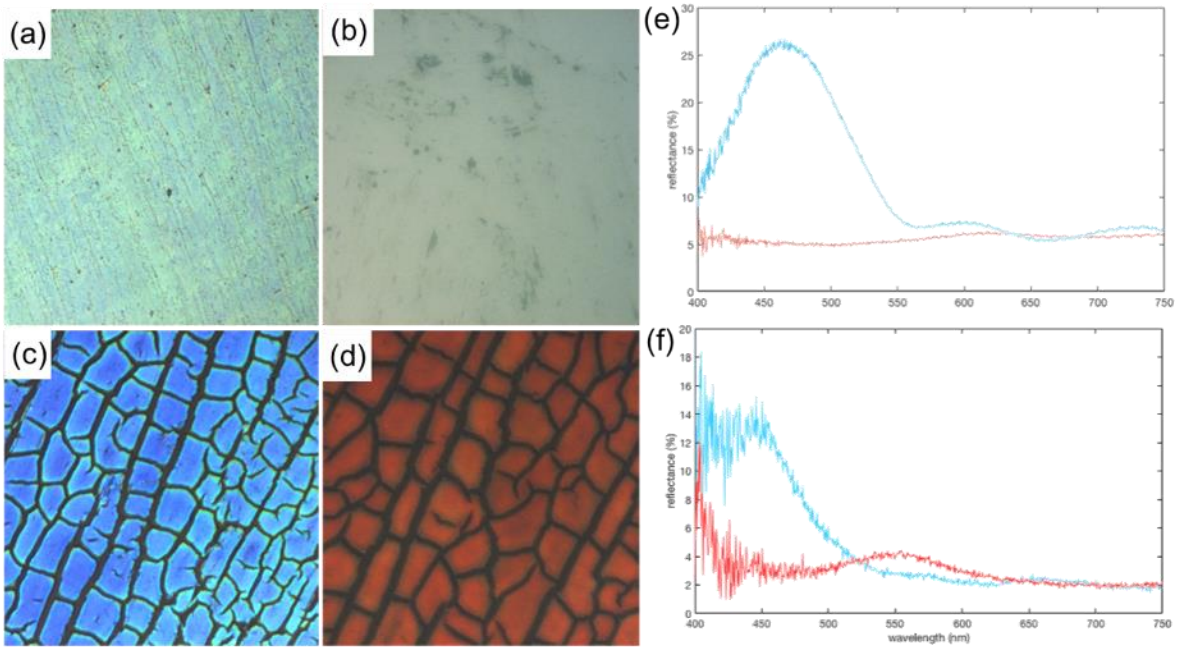

Figure 71. (a) dry and (b) wet optical images of silica IO and (c) dry and (d) wet optical images of titania IO. (e) silica and (f) titania IO reflectance spectrum for dry (blue) and wet (red) samples.

3.3.2 Plasmonic nanoparticles immobilization on IO surface

Gold nanoparticles were chosen as plasmonic nPs for this study for their ability to convert visible light into heating, their well-known chemistry and their availability. Three different approaches for immobilization were used: (i) gold sputtering, (ii) gold nPs seedling and growth and (iii) gold nPs adsorption.

Gold sputtering on the surface followed by thermal treatment is a fast and convenient method to obtain gold islands on a flat surface since it does not require sample preparation (Figure 72). Despite that, it is not ideal for 3D structures since gold can not reach the inside of the pores and the particle size distribution is wide. The resulting gold island can heat up by almost 15°C when irradiated with a 110 mW 532 nm laser.

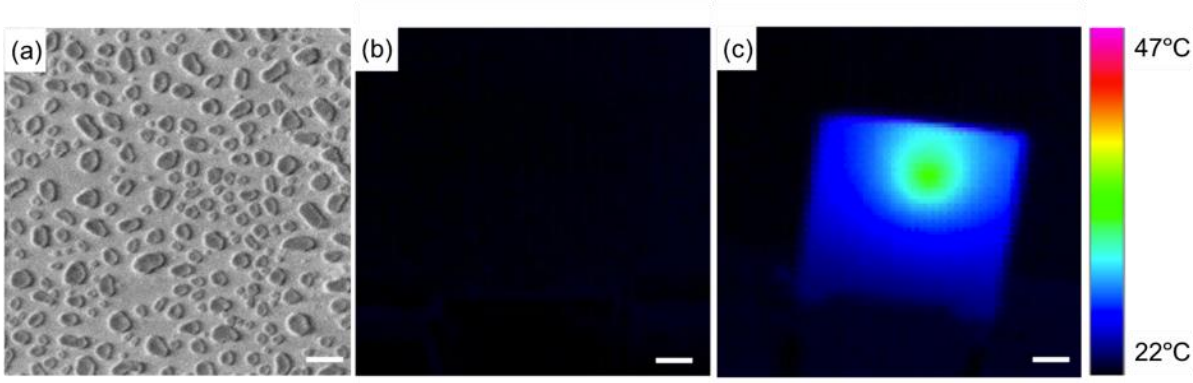

Figure 72.(a) SEM image of gold islands obtained by gold sputtering and calcination, scalebar is 20 nm. Thermal images of flat substrates (b) without and (c) with gold island. Scalebar is 2 mm.

Pre-formed gold nPs adsorption on the surface has the advantage of controlling accurately the dimension of the gold nPs, thus optimizing their heating rate. Despite that, the surface needs to be functionalized to increase the adsorption rate and functionalized nPs are required. Citrate capped gold nPs were adsorbed on the IO surface previously functionalized with APTMS. With this method no significant heating can be detected even using a high laser power (Figure 73).

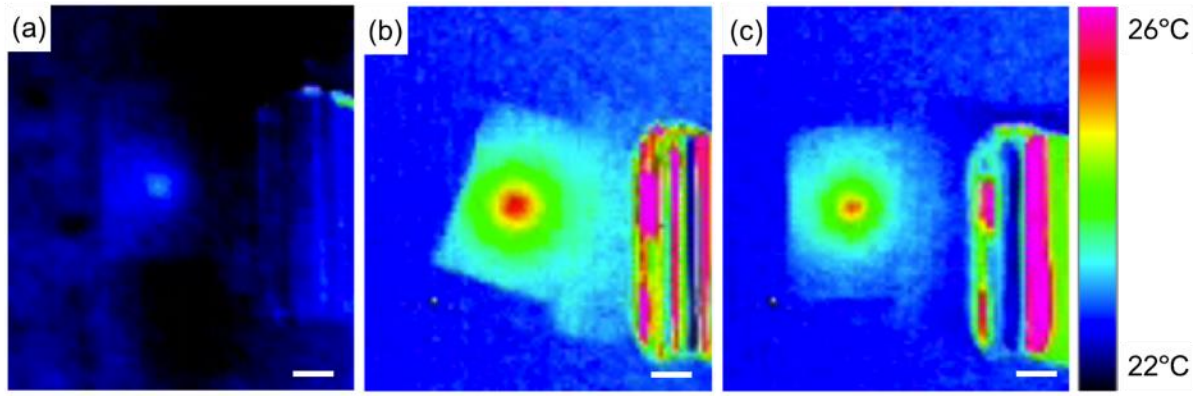

Figure 73. Thermal images of substrates on which were adsorbed (a) 5 nm, (b) 15 nm and (c) 20 nm gold nanoparticles. Scalebar is 2 mm.

Gold nPs seedling and sequential growth by reduction on gold atoms is the most efficient methodology to adsorb nPs on IO surface. In fact, using 2 nm gold nPs as seeds is possible to prevent clogging at the pore necks and easy diffusion into the inner layers. Seeds appear homogeneously distributed on the IO surface, as shown in Figure 74a. Gold nPs size can be increase by in situ reduction of gold ions, controlling the size of the particles by modifying the reaction time. This process gives rise to gold nPs with inhomogeneous size distribution and shape (Figure 74b), which can be improved by thermal treatment (Figure 74c). IOs with gold nPs immobilized on their surface can heat up by almost 30°C and the heating is localized only on the area irradiated by the laser beam (Figure 74d-e).

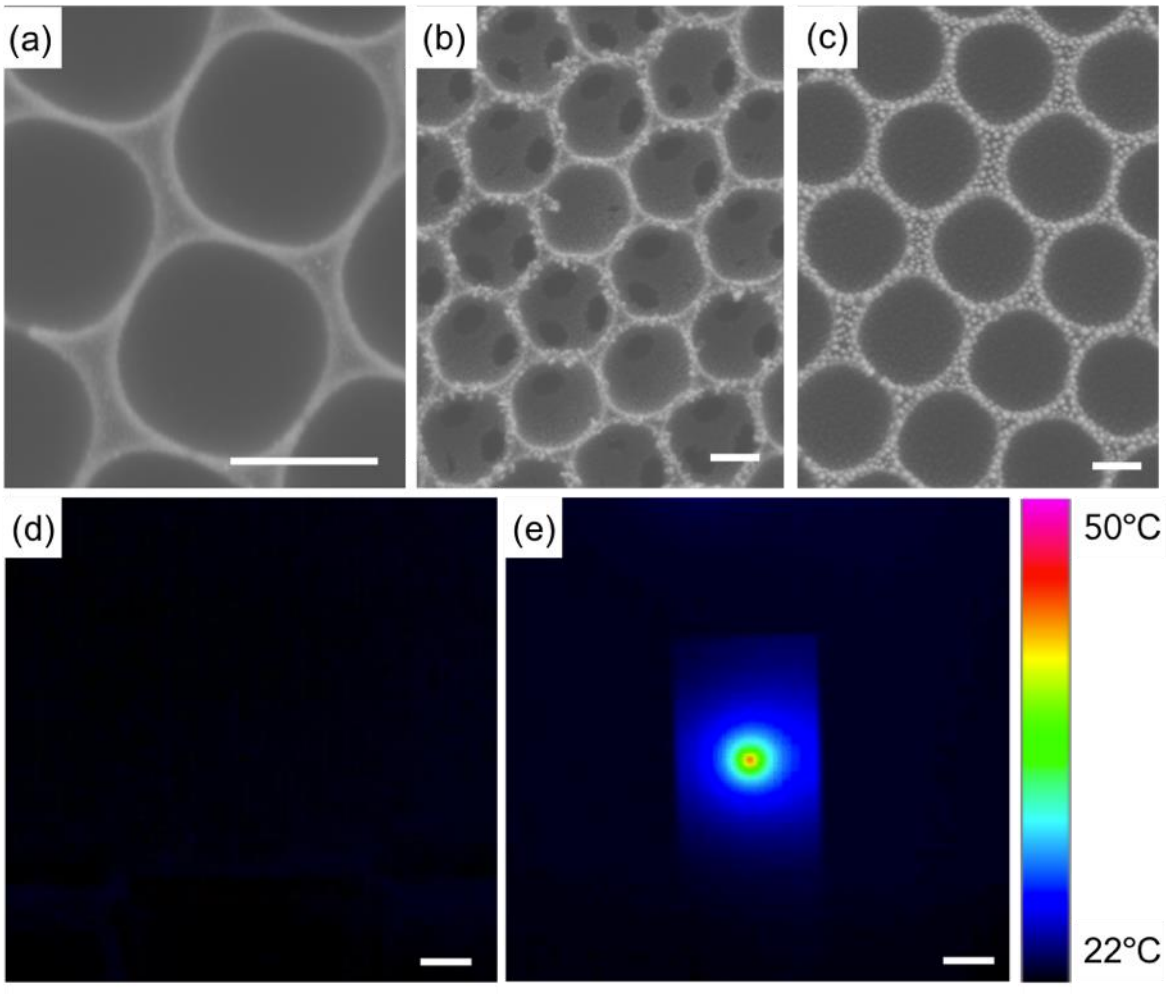

Figure 74 SEM images of IO (a) with gold seeds, (b) after nPs growth by gold reduction and (c) after calcination. Scalebar is 200 µm. Thermal images of IO (b) without and (c) with gold nPs. Scalebar is 2 mm.

3.3.3 Functionalization with enzyme

Lipase by *Candida rugosa* was used as a model enzyme for this study for its well characterized chemistry and the relevance it covers in industrial processes. It is an enzyme present in living organisms for digestion and it catalyzes the hydrolysis of fats. Its optimal working temperature is 60°C.

The most efficient immobilization protocol consists in simply adsorbing lipase onto the APTMS functionalized surface taking advantage of electrostatic interactions. The process has been followed using a quartz crystal microbalance (QCM), an instrument that measures a mass variation per unit area by measuring the change in frequency of a quartz crystal resonator with low detection limit. First, the silica surface is activated using O_2 plasma cleaning to create hydroxyl groups. 64 ng/cm^2 of APTMS can covalently bond to the surface and expose amine groups. Since the adsorption reaction is conducted in DI water, amine groups are positively charged. Finally, when the substrate is immerged into a lipase water solution, 350 ng/cm^2 of enzyme can be immobilized on the surface. Interestingly, no desorption is observed when rinsing the substrate with DI water.

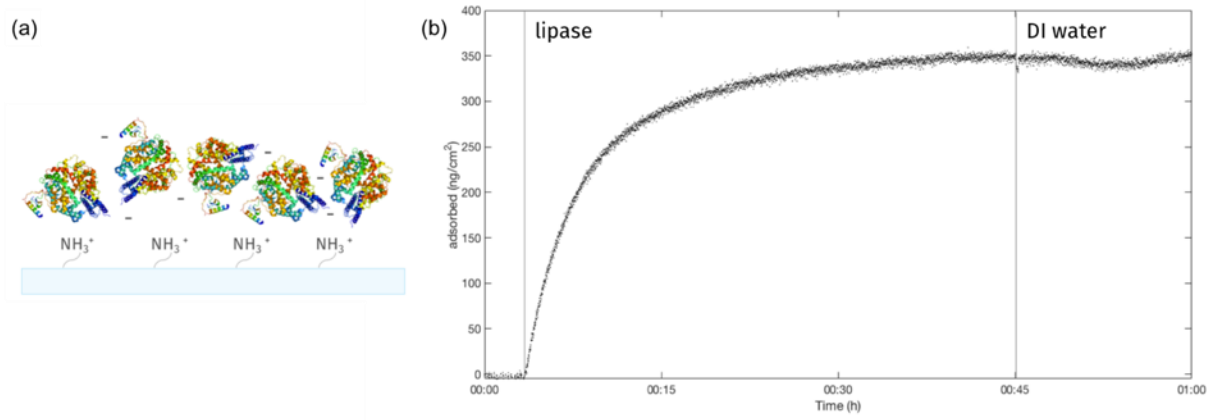

Figure 75. (a) schematic of enzyme adsorption protocol and (b) QCM measurement to quantify the amount of immobilized enzyme.

This simple method is more convenient that other techniques such as layer-by-layer deposition and covalent bonding since (i) it reduces the number of reagents involved, making the final platform greener and easier to recover, (ii) doesn't involve the use of polymers, whose diffusion inside the pores is complicated by aggregation processes and (iii) is fast and convenient.

3.3.4 Platform testing

The final platform is obtained as following (Figure 76):

1. IO fabrication;
2. IO surface activation by O_2 plasma and APTMS functionalization;
3. Gold nPs adsorption and growth;
4. 3 nm layer SiO_2 deposition by atomic layer deposition;
5. Activation by O_2 plasma and APTMS functionalization;
6. Lipase adsorption.

The thin SiO_2 layer seal the gold nanoparticles acting as a new surface on which APTMS functionalization can be performed and prevents catalytic effects by the titania IO surface.

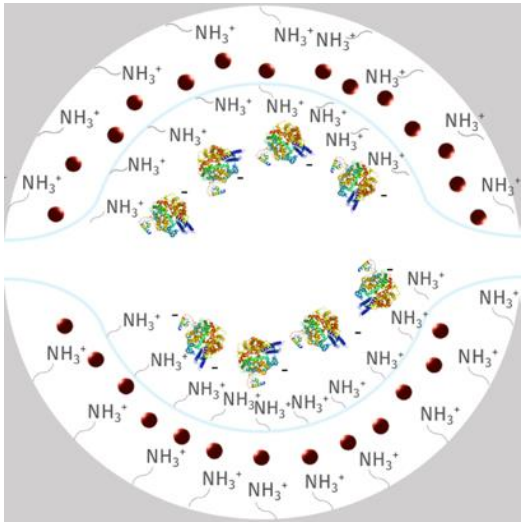

Figure 76. Schematic representation of the IO functionalization

Lipase efficiency is measured in activity units, where 1 enzyme unit (U) produces 1 µmol of product per hour. To follow the activity of the enzyme we took advantage of diacetylfluorescein conversion into fluorescein (Figure 77), a strongly absorbing and emitting molecule convenient to monitor.

Figure 77. Schematic reaction of hydrolysis of diacetyl fluorescein into fluorescein by lipase

Since fluorescein absorption profile is strongly dependent (i) on pH due to three different protonation states each giving rise to a peak in the absorption spectra and (ii) on time since there is a kinetically controlled conversion towards the most stable protonated specie, measurements were carried out buffering the solution at pH 9 to avoid changes in the relative intensity of the peaks. Absorption was chosen instead of emission to monitor the reaction

since allows to check the molecule protonation state and is not affected by the presence of the 532 nm laser used to activate the platform.

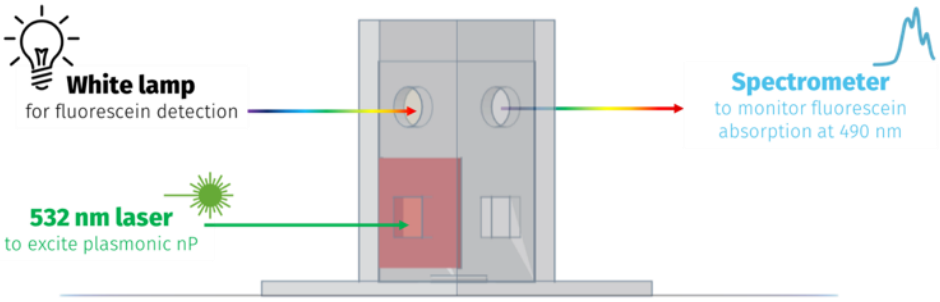

Figure 78. Schematic illustrating the setup for activity measurement

A customized cuvette holder (see Figure 78) was 3D printed to allow (i) stirring, (ii) substrate irradiation using a 532 nm laser (iii) white lamp irradiation and (iv) spectroscopic detection for fluorescein quantification.

Titania and silica IO with the same pore size were tested using the latter as a reference to account for functionalization and diffusion contributes. Laser off-on cycles were performed and the activity measured in the presence of the laser was normalized on the one in absence of the laser to take into consideration the possible difference in the quantity of enzyme adsorbed.

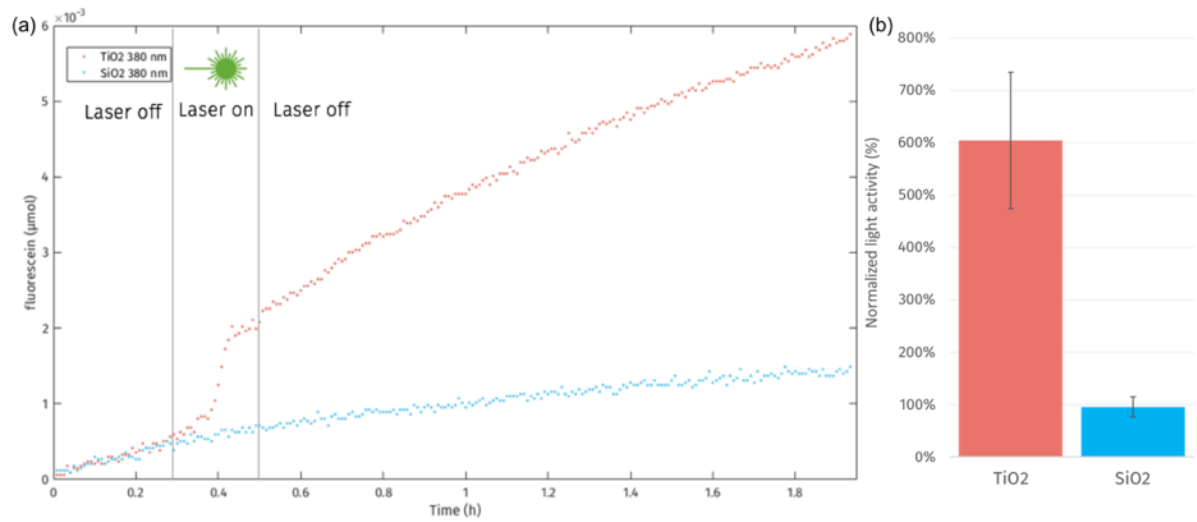

Figure 79. (a) fluorescein production in time upon on/off laser cycle. Titania IO is reported in red and silica IO in blue. (b) Enzyme activity during laser irradiation normalized on activity without laser irradiation.

In the case of silica substrates, no enhancement in the catalytic efficiency was detected upon laser irradiation. On the other hand, titania substrates increase the enzyme efficiency by almost 6 times when a 110 mW laser light is shined onto the substrate, as shown in Figure 79, thus confirming the efficacy of the platform.

3.4 Methods

3.4.1 Inverse opals fabrication

Inverse opals were prepared using colloidal co-assembly. [26,35]

Briefly, colloidal polymeric particles were assembled on a substrate in the presence of the precursor for the matrix.

Polystyrene nPs (PS nPs) synthesis PS nPs with diameter ranging from 200 nm to 600 nm were prepared by polymerization of styrene in water emulsion promoted by potassium peruslphate, controlling the size by changing the temperature and reaction time. In a typical experiment, 12 grams of styrene were added to 100 mL of water in a round bottom flask under vigorous stirring. 500 mg of potassium persulphate were added to the solution and the polymerization was initiated by increasing the temperature until reflux. The reaction was allowed to proceed for 6 hours and the aqueous phase was separated from the organic one.

Size was determined by DLS measurements and nPs content by gravimetric techniques.

Inverse opals preparation Glass substrates were cleaned with O_2 Plasma for 5 minutes and piranha solution (1 part H_2O_2, 3 parts HNO_3) for 30 min at 50°C, then rinsed with water and ethanol and dried with N_2.

TEOS solution was prepared by mixing 1.5 mL EtOH, 1 mL TEOS and 1 mL 0.1 M HCl and stirred for 1 h.

In a glass vial were put 12 mL of water 0.1 wt% colloids and 75 µL of TEOS solution or 500 µL of TiO_2 nanocrystals solution. Glass slide were immerged in the solution avoiding touching the walls (holding it with a binder clip) and were put in the oven at 65°C for 2 days. Samples were calcined to sinter the matrix and eliminate the colloidal particles with the following cycle: 5 h 25°C→500°C, 2h at 500°C, 3 h 500°C→25°C.

SEM images were collected using a Zeiss UltraPlus SEM, reflectance spectra using ThorLabs optical fibers and OceanOptics spectrometer coupled with an optical microscope.

3.4.2 Gold nanoparticles growth on surface

Gold island fabrication Glass slides were prepared by washing slides with alcolnox, rinsing with water 5 times, and 5 times with ethanol. Glass slides are activated over O_2 atmosphere in plasma cleaner for 5 minutes, immerged in 2% v/v APTMS in acetone for 3 hours, wash with acetone and ethanol and dried under air flow.

Functionalized glass slides are stick to a big glass slide with tape and placed onto a stub. The stub is placed into a sputter coater and coated with gold (current= 18 mA, time= 3 min), glass slides are detached from the tape and then calcinated (2 hours to 500 °C, 2 hours at 500 °C, 2 hours to 25 °C).

Gold nPs adsorption Glass slides were prepared by washing slides with alcolnox, rinsing with water 5 times, and 5 times with ethanol. Glass slides are activated over O_2 atmosphere in plasma cleaner for 5 minutes, immerged in 2% v/v APTMS in acetone for 3 hours, wash with acetone and ethanol, dried under air flow and put in oven at 130 ◦C for 15 minutes.
Glass slides were immerged in gold nP for 2 hours and then rinsed with DI water.

Gold nPs seedling and growth Glass slides were activated over O_2 atmosphere in plasma cleaner for 5 minutes. Glass slides were immerged in 10% v/v APTMS in acetone for 30 minutes at room temperature, then washed with acetone and with absolute ethanol, dried under air flow and put in oven at 130 °C for 15 minutes. Substrates were put in gold seeds (1 wt.% concentrate solution diluted 1:4 with water) for 2 hours, transferred in water with gentle stirring and the solution was changed after 1 hour and once the next day. Stir for 24 hours.
A solution was prepared with 190 mL of water, 48 mg of K_2CO_3 and 33 mg of HAuCl previously dissolved in 50 µL of water and let sit for 24 hours (color should change from yellow to transparent). 4 mL of reduced Au solution and 1 mL of formaldehyde (200 µL/h for Au solution) were added with a syringe pump to 100 mL of water containing the substrate under gentle stirring injecting the solutions near the magnetic bar by using tubing. The substrates were washed by dipping them in water and then letting them in water for 30 min under gentle stirring and then dried under N_2 flow. Samples were calcined using the following cycle: 5 h 25°C→500°C, 2h at 500°C, 3 h 500°C→25°C.

3.4.3 Functionalization with enzyme

After gold nPs deposition and before enzyme deposition, the substrate was coated with 2.5 nm of SiO_2 (ALD, 26 repetition, 0.95 Å each cycle). *Candida rugosa* lipase was obtained from Sigma Aldrich and used as received. Substrates were activated over O_2 atmosphere in plasma cleaner for 5 minutes, immerged in 2% v/v APTMS in acetone for 30 minutes at room temperature, washed with acetone and absolute ethanol, dry under air flow and put in oven at 130 °C for 15 minutes. The substrates were then immerged in in lipase 0.02 wt. % solution under gentle stirring for 30 minutes, rinsed with DI water and kept at 4°C until measured.
Quartz crystal microbalance SiO_2 covered sensors (Biolin Scientific) were cleaned putting sensor in O_2 cleaner for 15 minutes, cleaning with SDS for 30 minutes, rinsing with water, drying with N_2 and putting sensor in O_2 cleaner for 10 minutes. The background signal was then measured by running water for 10 minutes (100 µL/min). The 13° frequency was chosen as a reference.
Sensor were functionalized with APTMS outside the QCM. Sensor were activated over O_2 atmosphere in plasma cleaner for 5 minutes, immerged in 2% v/v APTMS in acetone for 1

hour at room temperature, wash with acetone and absolute ethanol, dried under air flow and put in oven at 130 ◦C for 15 minutes. QCM signal was then measured to evaluate the quantity of APTMS adsorbed. The measurements were performing by running water (100 µL/min) until a flat baseline was reached, running 0.02 wt.% lipase (10 µL/min) for 45 minutes and running water (100 µL/min) for 15 minutes.

3.4.4 Device testing

To evaluate the activity of lipase, the conversion of diacetyl fluorescein (DAF) into fluorescein by the enzyme was monitored. Fluorescein production in solution was quantified using UV-Vis spectroscopy. The resulting plot reporting µmol of fluorescein produced vs. time expressed in minutes can be fit with a Michaelis-Menten kinetic curve, where fit the first section of the curve can be fit with a linear curve which slope corresponds to the activity of the enzyme.

A 100 µM DAF mother solution in DMSO was prepared and diluted 1:9 DAF/DMSO:PBS before each test. PBS buffer pH was adjusted to 9 using NaOH.

A customized cuvette holder was 3D printed and painted in black to minimize diffusion from the surfaces. The white light source was Ocean Optics LS-1, optical fibers from Thorlabs and Ocean Optics and an Ocean Optics Maya 2000 Pro spectrometer was used. The diode 532 nm laser source was Thor Labs ITC4005 with power ranging from 1 to 110 mW. Integration time was 15 ms, 5 scans to average.

3.5 Conclusions

The work presented in this chapter describes the fabrication of a platform for laser driven remote and localized activation of enzymes based on the slow light effect showed by photonic structures. The photonic structures used in this work are titania inverse opals with 380 nm pore size able to slow light around 532 nm, which is then absorbed by gold nPs adsorbed on the IO inner surface. Among the different methods tried for gold nPs immobilization, gold nPs seedling and growth was the most performing process. Lipase was immobilized on the platform surface by using electrostatic interaction, reaching 360 ng/cm^2 adsorption, as measured with QCM.

The platform was then tested by measuring fluorescein production by lipase and it was shown that titania IO increased the catalytic efficiency of lipase by almost 6 times when irradiated with 532 nm 110 mW compared to the same samples in the absence of light. Comparing these results with the one obtained using silica IO with the same pore size that do not show a photonic band gap, we can state that the catalytic efficiency enhancement is due to the slow light effect.

3.6 References

1 J. D. Joannopoulos, S. G. Johnson, J. N. Winn and R. D. Meade, *Photonic crystals: molding the flow of light*, 2011.

2 S. M. Doucet and M. G. Meadows, *Journal of The Royal Society Interface*, 2009, **6**, S115–S132.

3 P. Vukusic and J. R. Sambles, *Nature*, 2003, **424**, 852–855.

4 J. P. Vigneron and P. Simonis, *Physica B: Physics of Condensed Matter*, 2012, **407**, 4032–4036.

5 A. R. Parker and H. E. Townley, *Nature Nanotech*, 2007, **2**, 347–353.

6 M. Kolle, P. M. Salgard-Cunha, M. R. J. Scherer, F. Huang, P. Vukusic, S. Mahajan, J. J. Baumberg and U. Steiner, *Nature Nanotech*, 2010, **5**, 511–515.

7 M. Curti, J. Schneider, D. W. Bahnemann and C. B. Mendive, *J. Phys. Chem. Lett.*, 2015, **6**, 3903–3910.

8 E. Shirman, T. Shirman, A. V. Shneidman, A. Grinthal, K. R. Phillips, H. Whelan, E. Bulger, M. Abramovitch, J. Patil, R. Nevarez and J. Aizenberg, *Adv. Funct. Mater.*, 2017, **189**, 1704559–20.

9 C. Pouya, J. T. B. Overvelde, M. Kolle, J. Aizenberg, K. Bertoldi, J. C. Weaver and P. Vukusic, *Advanced Optical Materials*, 2015, **4**, 99–105.

10 P. Vukusic, J. R. Sambles and C. R. Lawrence, *Nature*, 2000, **404**, 457–457.

11 H. Ghiradella, *Applied Optics*, 1991, **30**, 3492–3500.

12 S. M. Doucet and M. G. Meadows, *Journal of The Royal Society Interface*, 2009, **6**, S115–S132.

13 A. E. Seago, P. Brady, J. P. Vigneron and T. D. Schultz, *Journal of The Royal Society Interface*, 2009, **6**, S165–S184.

14 K. Chung, S. Yu, C. J. Heo, J. W. Shim, S. M. Yang, M. G. Han, H. S. Lee, Y. Jin, S. Y. Lee, N. Park and J. H. Shin, *Adv. Mater.*, 2012, **24**, 2375–2379.

15 R. W. Corkery and E. C. Tyrode, *Interface Focus*, 2017, **7**, 20160154–16.

16 E. D. Finlayson, L. T. McDonald and P. Vukusic, *Journal of The Royal Society Interface*, 2017, **14**, 20170129–9.

17 B. D. Wilts, K. Michielsen, H. De Raedt and D. G. Stavenga, *Journal of The Royal Society Interface*, 2012, **9**, 1609–1614.

18 M. E. Calvo, S. Colodrero, N. Hidalgo, G. Lozano, C. López-López, O. Sánchez-Sobrado and H. Míguez, *Energy Environ. Sci.*, 2011, **4**, 4800–4812.

19 S. Colodrero, M. Ocaña and H. Míguez, *Langmuir*, 2008, **24**, 4430–4434.

20 C. López-López, S. Colodrero, S. R. Raga, H. Lindström, F. Fabregat-Santiago, J. Bisquert and H. Míguez, *J. Mater. Chem.*, 2012, **22**, 1751–1757.

21 H. Shen, Z. Wang, Y. Wu and B. Yang, *RSC Adv.*, 2016, **6**, 4505–4520.

22 Y. X. Yeng, M. Ghebrebrhan, P. Bermel, W. R. Chan, J. D. Joannopoulos, M. Soljačić and I. Celanovic, *Proc. Natl. Acad. Sci. U.S.A.*, 2012, **109**, 2280–2285.

23 B. Hatton, L. Mishchenko, S. Davis, K. H. Sandhage and J. Aizenberg, *Proc. Natl. Acad. Sci. U.S.*A., 2010, **107**, 10354–10359.

24 M. Schaffner, G. England, M. Kolle, J. Aizenberg and N. Vogel, *Small*, 2015, **11**, 4334–4340.

25 Y. Takeoka, *J. Mater. Chem. C*, 2013, **1**, 6059–17.

26 K. R. Phillips, T. Shirman, E. Shirman, A. V. Shneidman, T. M. Kay and J. Aizenberg, *Adv. Mater.*, 2018, **23**, 1706329–7.

27 T. A. Singleton, I. B. Burgess, B. A. Nerger, A. Goulet-Hanssens, N. Koay, C. J. Barrett and J. Aizenberg, *Soft Matter*, 2014, **10**, 1325–1328.

28 G. T. England and J. Aizenberg, *Rep. Prog. Phys.*, 2017, **81**, 016402–12.

29 I. B. Burgess, N. Koay, K. P. Raymond, M. Kolle, M. Lončar and J. Aizenberg, *ACS Nano*, 2012, **6**, 1427–1437.

30 I. Pavlichenko, E. Broda, Y. Fukuda, K. Szendrei, A. K. Hatz, G. Scarpa, P. Lugli, C. Bräuchle and B. V. Lotsch, *Materials Horizons*, 2015, **2**, 299–308.

31 J. D. Sandt, M. Moudio, J. K. Clark, J. Hardin, C. Argenti, M. Carty, J. A. Lewis and M. Kolle, *Adv. Healthcare Mater.*, 2018, **166**, 1800293–7.

32 H. -D. Gao, P. Thanasekaran, C.-W. Chiang, J.-L. Hong, Y.-C. Liu, Y.-H. Chang and H.-M. Lee, *ACS Nano*, 2015, **9**, 7041–7051.

33 B. Schierling, A.-J. Noël, W. Wende, L. T. Hien, E. Volkov, E. Kubareva, T. Oretskaya, M. Kokkinidis, A. Römpp, B. Spengler and A. Pingoud, *Proc. Natl. Acad. Sci. U.S.A.*, 2010, **107**, 1361–1366.

34 C. P. Salerno, D. Magde and A. P. Patron, *Journal of Organic Chemistry*, 2000, **65**, 3971–3981.

35 K. R. Phillips, G. T. England, S. Sunny, E. Shirman, T. Shirman, N. Vogel and J. Aizenberg, *Chemical Society Reviews*, 2015, **45**, 1–42.

4 Bio-templated multi-scale porosity scaffolds

4.1 Introduction

4.1.1 Bio-templated materials

The fabrication of nanostructured materials with complex morphologies often requires sophisticated equipment [1-3] or the exploitation physical processes such as self-assembly. [4,5] An alternative approach emerging for the bottom-up synthesis of nanostructured materials is the use of biological-based templates, which take advantage of structures generated by living organisms. [6]

Biotemplating takes advantage of the structural specificity of biological systems to fabricate new nanostructured functional materials. [7-10] After the selection of a biological structure meeting the required criteria and its deep characterization, a variety of wet or dry deposition techniques can be used to replicate the biological template, which then needs to be removed to obtain the final complementary structure.

Biotemplating is a promising tool in organizing nanomaterials into well-defined architectures and thus biological substrates with interesting morphological characteristics, such as diatoms, [11,12] butterfly wing scales [9,13] and viruses [14-16], have recently been exploited for the synthesis of new materials.

Among the characteristics found in those structures, porosity is one of the most investigated as it leads to high surface materials which find applications in catalysis. Sea urchin spines are an ideal template as they present interconnected pores which can be filled with the material of choice to obtain an exact replica of the starting structure. [17,18] Examples of the applicability of this strategy are given below.

4.1.2 Sea urchin spine morphology and characteristics

Sea urchins (class *Echinoidea*) are calcifying organisms producing calcite stereom, also known as spines, which attracted the attention of scientist both for their interesting morphology and their mechanical proprieties. In fact, despite showing a porous structure (see Figure 80) they diffract as a calcite single crystal with the c-axis aligned along the spine direction. [19-22] The formation of the spines in sea urchin larvae happens in the syncytium, a multicellular vesicle, and involves first the synthesis of a single calcite crystal followed by growth by means of an amorphous phase, which then crystallizes due to secondary nucleation events. Even though the spine diffracts as a single crystal, the coherence length is lower than that of geogenic calcite, confirming the amorphous mediated growth mechanism.

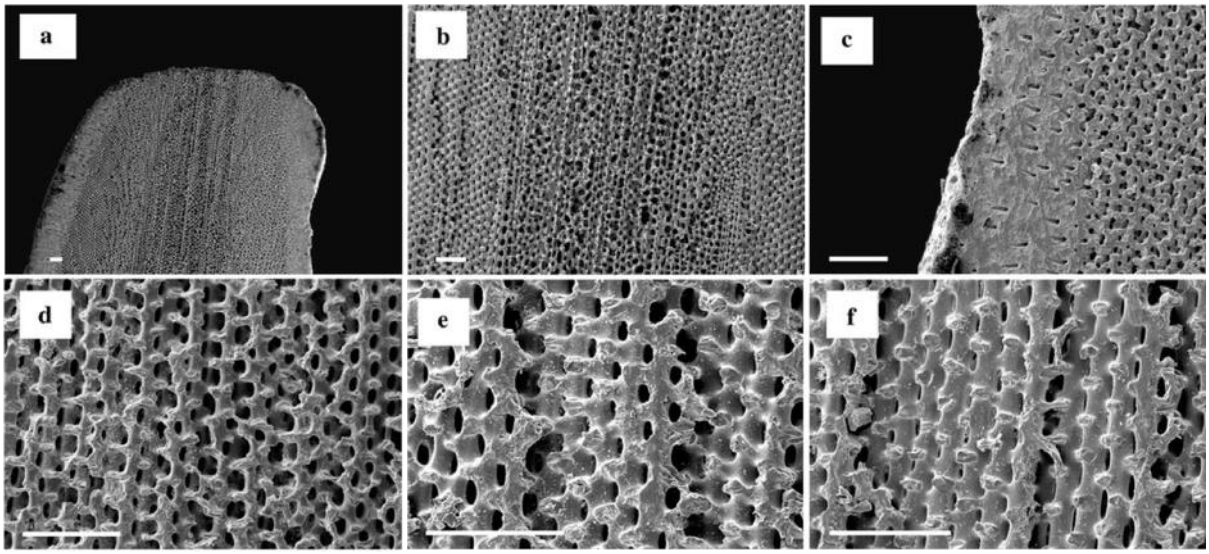

Figure 80. *Phyllacanthus imperialis* spine in longitudinal direction: (a) tip including medulla, radiating layer and cortex; (b) medulla followed by the radiating layer; (c) microperforate cortex; (d) radiating layer; (e) radiating layer near the base; (f) radiating layer in the middle of the shaft (scale bars 100 µm). Reproduced from [17]

The low percentage of organic matrix present in the spine together with the low fraction of the amorphous component give rise to the spine's outstanding mechanical proprieties coupled with light weight. In fact, despite being composed of calcite which is known for being brittle, the spine has high resistance to fracture and breaks as a glassy material generating a conchoidal fracture profile. The stereom presents interconnected pores with size ranging from 10 to 30 µm which can be arranged as follow to form (i) a labyrinthic stereom characterized by disorganized arrangement of pores and struts; (ii) laminar stereom present as a layered structure; (iii) galleried stereom with long parallel galleries with regular connections. The stereom gives resistance to breakage since the cracks are distributed between the bridges connecting the pores other than propagating, thus allowing high energy absorption before a fatal failure. [23-25] Many functional applications have been envisioned to exploit the interconnected porosity, light weight and mechanical resistance of the stereom.

4.1.3 Sea urchin spine templated materials

4.1.3.1 Sea urchin spine as a template for a variety of materials

Templating of the sea urchin skeletal plates has proven to be an extremely versatile technique for producing a wide range of macroporous solids with unique bicontinuous structures, which find application in catalysis, cell immobilization and filtration. Although a variety of methods to fabricate macroporous structures has been developed, the use of a biological template enables synthesis of morphologies not accessible by any other route.

As the calcium carbonate and porous fractions of the plate possess identical sizes and shapes, filling of the pores with a solid and subsequent dissolution the calcium carbonate generates a porous solid with identical structure to the original template.

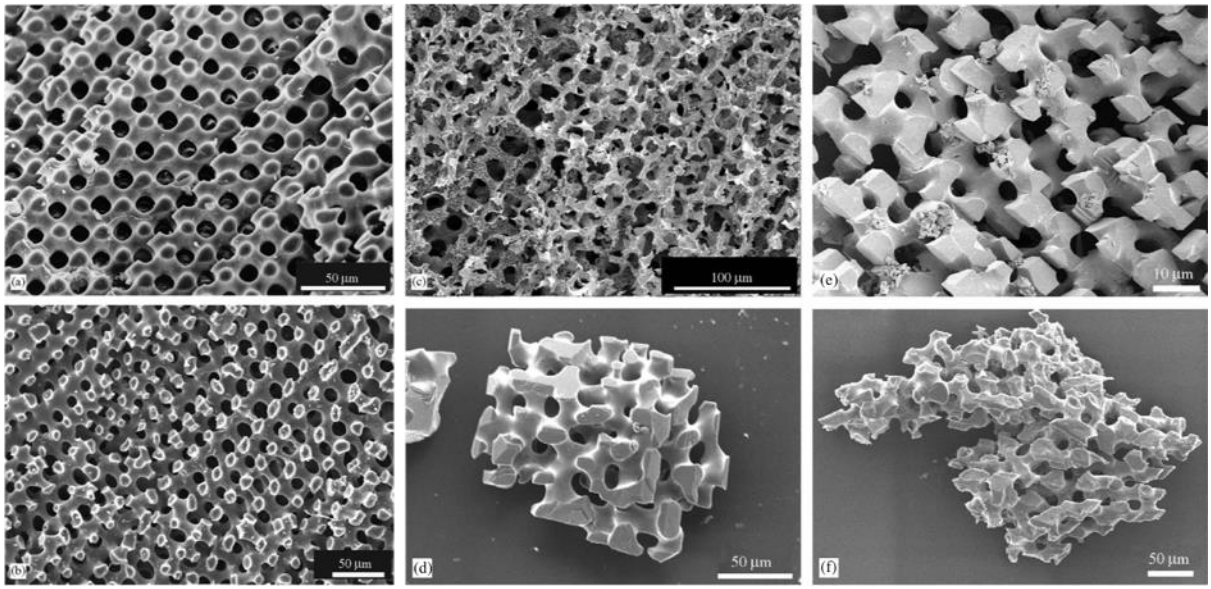

Figure 81. a) Cross-section through a sea urchin skeletal plate showing the bicontinuous structure and pores of diameter 10–15mm. (b) Polymer replica of sea urchin plate. (c) Macroporous nickel produced via electroless deposition showing a skeletal structure. Templated crystals of (d) $CaCO_3$ produced from 0.02 M reagents after 24 h, and (e) $SrSO_4$ produced from 0.05 M reagents after 24 h, all of which were synthesised using a double-diffusion technique. (f) Templated macroporous $CuSO_4 \bullet 5H_2O$ crystal precipitated from a supersaturated solution using an evaporation technique. Reproduced from [26]

By using polymer replica or the plate itself as a scaffold (Figure 81a-b), Yue et al. successfully prepared single crystals, amorphous and polycrystalline solids with unique, highly ordered bicontinuous structures using sea urchin plates as a template (Figure 81c-f). [26]

The quantity of material deposited within the template, together with the interaction of the deposited solid with the template surface, govern the morphology of the final structure producing (i) a perfect casts of the plate when the pores are completely filled, (ii) a double-sided surface when only the surface of the pore is covered or (iii) a skeletal structure with pores larger than in the original template when the pores are partially filled.

Overall, this methodology poses the bases for the fabrication of interconnected porous structures made of a wide range of materials.

4.1.3.2 Scaffolds for bone defect repair

Open-scaffold materials have recently attracted attention as scaffold for bone tissue regeneration due to their resistance and the possibility for cell and the regenerating bone tissue to diffuse in the pores. Thus, sea urchin spines are the ideal starting material for bone regeneration scaffolds. Cao et al. fabricated β-tricalcium phosphate scaffold by hydrothermal conversion of sea urchin plates keeping their habit unchanged. After machining, they tested the scaffold as implant in damaged femur and as joint fixation. The implants showed great biocompatibility, bone regenerating proprieties and underwent osseointegration, while untreated bones did not significantly promote bone regeneration. Furthermore, joint fixation produced using β-tricalcium phosphate structures can be biodegraded as opposed to hydroxyapatite ones. The unique structures of sea urchin spines with open-cell structures and thin struts are key to facilitating scaffold degradation and new bone formation.

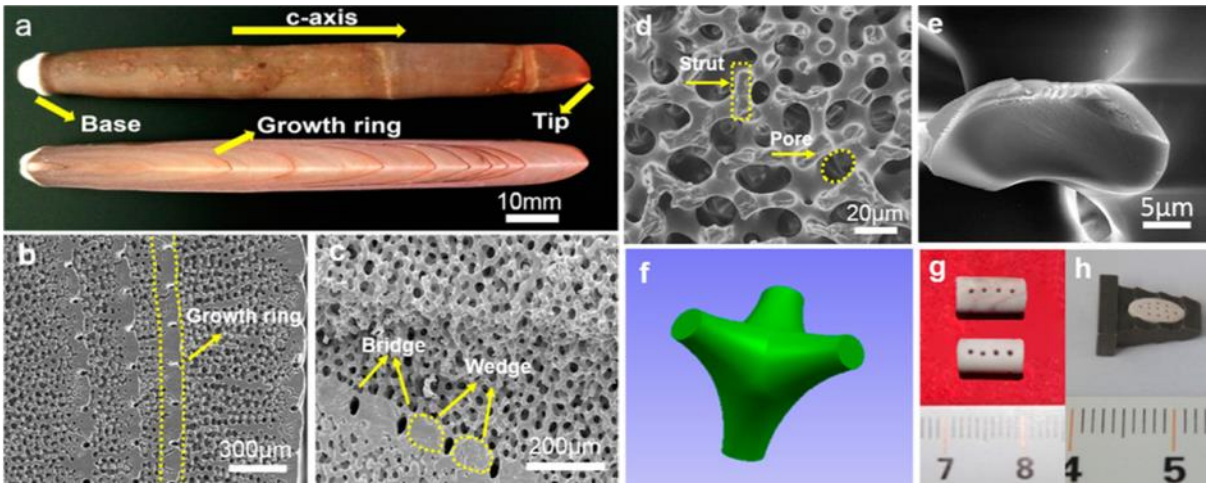

Figure 82. Section view of original sea urchin spines (H. mammillatus) (a), SEM micrographs of inner structures of sea urchin spines (b–e), and configuration of a truncated conical shell for a strut in the sea urchin spine (f) and machined sea urchin spine samples as bone implants (g and h). Reproduced from [27]

These findings may provide new insights to design of bioinspired functional materials particularly with open-cell structures and thin struts, possibly fabricated using advanced 3D printing techniques to obtain superior mechanical strength as well as a great match between scaffold degradation and new bone formation.

4.1.4 Aim of the project

This work focuses on the fabrication of inorganic scaffolds made of titania and silica with interconnected multiscale pores obtained using sea urchin spines together with colloidal assembly of nanoparticles as a template. The envisioned application is the degradation of organic pollutants made possible by the titania catalytic proprieties. The high surface volume ratio of sea urchin plates is enhanced by the addition of smaller pores created using colloidal particles assembled on the inner pore surface.

Depending on the casted material, the resulting scaffold can be applied to all the fields in which a high surface to volume ratio is desirable, as in cell regeneration and separation of adsorbing substances.

4.2 Results

4.2.1 Colloidal particles assembly

Polystyrene nanoparticles (PS nPs) with 220 nm diameter were assembled on the urchin pore surface by slow evaporation of a solution containing the colloids. As can be seen in Figure 83, the PS nPs adsorb on the urchin surface and, interestingly, are disposed in an ordered manner when the pore axis is perpendicular to the plate slice surface. This effect can be ascribed to the capillary effect during the evaporation of the liquid inside such a small channel, similarly to what happens in the colloidal co-assembly process previously described, where the solvent evaporation front drives the particles during their adsorption on the surface. The small size of the particles allows them to easily diffuse inside the pore channels without clogging the neck between consecutive pores and permits their distribution even in the inner surfaces.

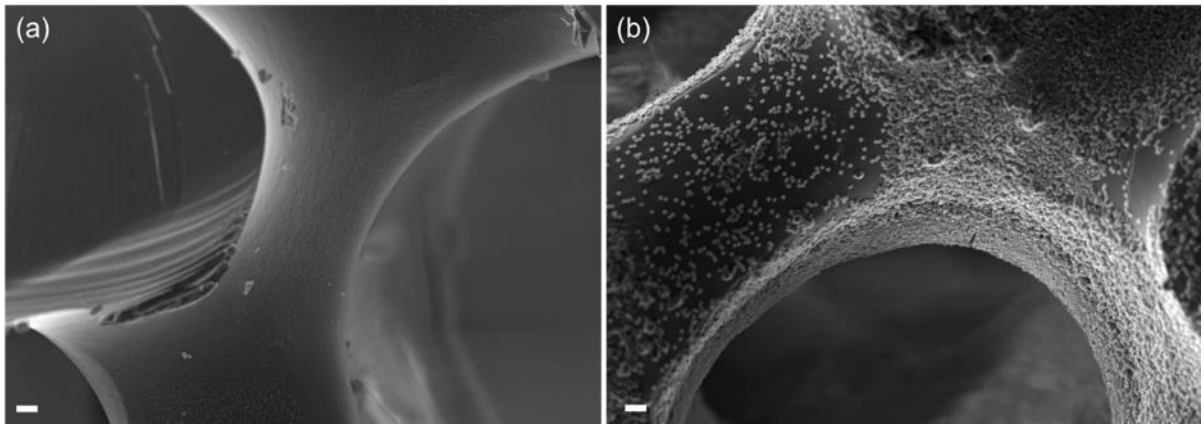

Figure 83. (a) pristine sea urchin spine and (b) sea urchin spine with colloids assembled on the surface. Scalebar is 1 µm.

The successful adsorption of colloids on the urchin surface increases the surface area of the scaffold, thus making it appealing for applications in which reactions are happening on the surface. Other than that, since the main fraction of the pore is still empty, we can hypothesize that the presence of the colloid will not have a negative impact on the scaffold filling.

4.2.2 Silica/titania replica

Sea urchin spine templates have been filled with SiO_2, TiO_2 or combination of both to obtain an inorganic based replica of the scaffold. To meet the requirements of the envisioned application, first a functional TiO_2 layer was deposited, followed by filling of the scaffold with SiO_2, which improves the stability and mechanical resistance of the replica. As can be seen in Figure 84a-b, the sea urchin spine template and the final replica show identical morphology, as previously shown in the literature. [7,26] In contrast with the previous studies present in the literature where only small fragments of the replica structure were obtained[7,26], a macroscopic replica of the template can be obtained by dissolution of the latter in a mildly acidic buffer after thermal treatment, thus improving the recoverability of the replica after its usage as a catalyst or filter.

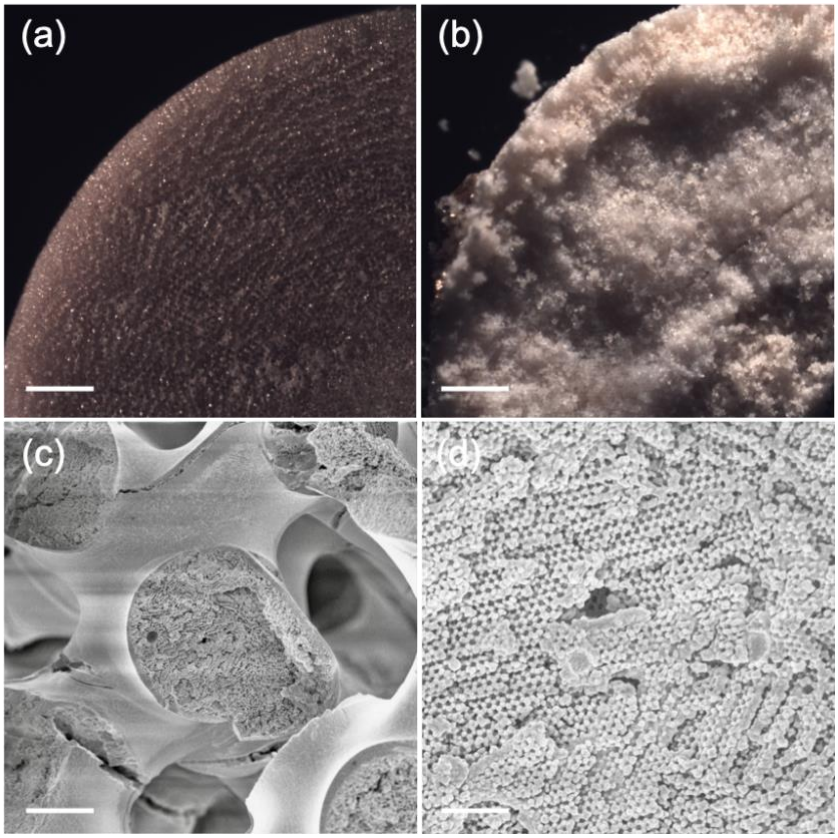

Figure 84. Optical image of (a) sea urchin spine and (b) SiO_2/TiO_2 replica. Scalebar is 2 mm. (c-d) SEM images of SiO_2/TiO_2 replica. Scalebar is (c) 2 µm and (d) 750 nm.

SEM images of the replica (Figure 84c) show that there pores where completely filled with the SiO_2/TiO_2 matrix. Looking at higher magnification images (Figure 84d) it is possible to observe the nano-porosity due to the templating effect of the colloids adsorbed on the spine. Although it is reasonable to think that the porosity is mainly localized on the surface, it is homogeneously distributed into the core of the structure, probably due to rearrangement and crystallization of the inorganic materials during the thermal treatment used to remove the polymeric colloidal scaffold. Exposing the inside of the scaffold a great number of

interconnected pores with ordered domains can be observed (Figure 85) which increased the surface area of 850 times compared to a pristine spine (determined by BET measurements).

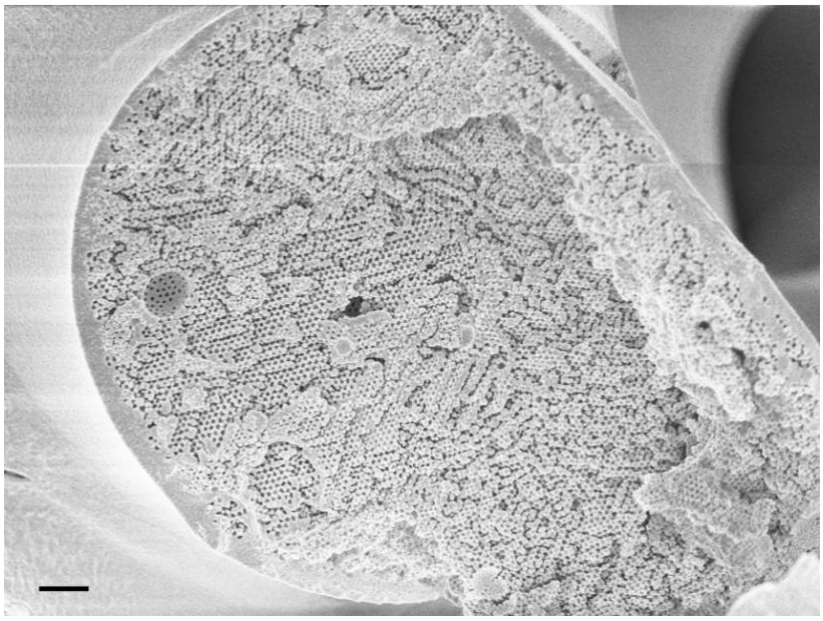

Figure 85. Cracked region exposing the inside of the scaffold. Interconnected pores can be observed. Scalebar is 1 µm.

4.3 Methods

Sea urchin spine preparation *Phyllicantus imperialis* spines were lapped to remove the external layer and sliced. The slices were then treated with 5% v/v sodium hypochlorite for 24 hours, thoroughly rinsed with water and air dried.

Colloidal particles synthesis PS nPs with diameter ranging from 90 nm to 200 nm were prepared by polymerization of styrene in water emulsion promoted by potassium peruslphate, controlling the size by changing the temperature and reaction time. In a typical experiment, 12 grams of styrene were added to 100 mL of water in a round bottom flask under vigorous stirring. 500 mg of potassium persulphate were added to the solution and the polymerization was initiated by increasing the temperature until reflux. The reaction was allowed to proceed for 6 hours and the aqueous phase was separated from the organic one. [28] Size was determined by DLS measurements (Malvern Nano ZS instrument equipped with a 633 nm laser diode).

Colloidal particles assembly Sea urchin spine slices were immerged in 750 µL of as-synthesized colloidal particles solution in a 24-well multiwell dish, put under vacuum several times to easy the wetting of the inner pores and put in the oven at 65°C until completely dry. The process was repeated 2 times.

Silica and titania synthesis Silica was obtained using tetraethyl orthosilicate (TEOS) as a precursor. 1 part of TEOS was mixed with 1 part of 0.1 M HCl and 1.5 parts of EtOH and stirred for 1 hour. Then, the TEOS solution was diluted 1:1 with ethanol and poured over the template. The sample was put under vacuum several times to easy the wetting of the inner pores and put in the oven at 65°C until completely dry. The process was repeated 4 times.

Titania was obtained using titanium isopropoxide (TTIP) as a precursor. Briefly, TTIP was diluted 1:10 with EtOH and poured over the template. The sample was put under vacuum several times to easy the wetting of the inner pores and put in a closed desiccator with water for 2 days. Then, the sample was transferred in an oven at 65°C until completely dry. The process was repeated 2 times.

Combination of silica and titania were prepared by sequentially following the same protocols. All the samples were calcined at 500°C for 5 hours to remove the PS nPs and sinter the inorganic matrix.

Removal of the template The $CaCO_3$ template was removed by immerging the calcined sample in pH 4.5 0.1 M acetate buffer for 14 days. The sample was than rinsed and freeze dried to remove the water. Samples were further calcinated at 650°C to improve their mechanical resistance.

Characterization SEM images were collected using a HR-SEM (ULTRA Plus, Zeiss, Oberkochen, Germany) or a Philips 545 SEM after coating the samples with 3 nm of gold.

4.4 Conclusions

Sea urchin spines show a complex microstructure made of interconnected pores while maintaining astonishing fracture resistance proprieties. For this reason, they are an attractive scaffold to obtain lightweight, porous and strong replica. The already high surface of sea urchin spines can be increased by adsorption of colloidal particles on the surface. When the axis of the pore is perpendicular to the liquid interface, an ordered assembly of the colloid on the surface is observed. Filling with SiO_2/TiO_2 matrix, followed by thermal treatment and template dissolution using wet chemistry, leads to a replica of the spine structure with an additional nano-porosity due to the presence of colloidal particles during the replica process and an increase of the surface area of 850 times compared to a pristine spine.

The possibility of obtaining a multiscale-porous material by the use of an implemented bio-template, together with the possibility of tailor the composition of the replica and embed functional molecules in it, opens up a wide variety of possibility in fields in which a high surface/volume ratio is crucial, such as filtration and catalysis as well as in applications requiring porous materials, such as tissue scaffolds and implants.

4.5 References

1 S. C. Han, J. W. Lee and K. Kang, *Adv. Mater.*, 2015, **27**, 5506–5511.

2 M. Khorasaninejad, W. T. Chen, R. C. Devlin, J. Oh, A. Y. Zhu and F. Capasso, *Science*, 2016, **352**, 1190–1194.

3 G. England, M. Kolle, P. Kim, M. Khan, P. Munoz, E. Mazur, J. Aizenberg and J. Aizenberg, *Proc Natl Acad Sci USA*, 2014, **111**, 15630–15634.

4 G. M. Whitesides and B. Grzybowski, *Science*, 2002, **295**, 2418–2421.

5 K. R. Phillips, G. T. England, S. Sunny, E. Shirman, T. Shirman, N. Vogel and J. Aizenberg, *Chemical Society Reviews*, 2016, **45**, 281–322.

6 S. Sotiropoulou, Y. Sierra-Sastre, S. S. Mark and C. A. Batt, *Chem. Mater.*, 2008, **20**, 821–834.

7 R. Seshadri and F. C. Meldrum, *Adv. Mater.*, 2000, **12**, 1149–1151.

8 Y. Xia, W. Zhang, Z. Xiao, H. Huang, H. Zeng, X. Chen, F. Chen, Y. Gan and X. Tao, *J. Mater. Chem.*, 2012, **22**, 9209–7.

9 R. E. Rodríguez, S. P. Agarwal, S. An, E. Kazyak, D. Das, W. Shang, R. Skye, T. Deng and N. P. Dasgupta, *ACS Appl. Mater. Interfaces*, 2018, **10**, 4614–4621.

10 J. W. Galusha, M. R. Jorgensen and M. H. Bartl, *Adv. Mater.*, 2010, **22**, 107–110.

11 M. Pérez-Cabero, V. Puchol, D. Beltrán and P. Amorós, *Carbon*, 2008, **46**, 297–304.

12 E. Van Eynde, T. Tytgat, M. Smits, S. W. Verbruggen, B. Hauchecorne and S. Lenaerts, *Photochem. Photobiol. Sci.*, 2013, **12**, 690–695.

13 W. Peng, S. Zhu, W. Wang, W. Zhang, J. Gu, X. Hu, D. Zhang and Z. Chen, *Adv. Funct. Mater.*, 2012, **22**, 2072–2080.

14 C. Radloff, R. A. Vaia, J. Brunton, G. T. Bouwer and V. K. Ward, *Nano Lett.*, 2005, **5**, 1187–1191.

15 M. Knez, A. M. Bittner, F. Boes, C. Wege, H. Jeske, E. Maiβ and K. Kern, *Nano Lett.*, 2003, **3**, 1079–1082.

16 H. Zhou, T. Fan and D. Zhang, *Microporous and Mesoporous Materials*, 2007, **100**, 322–327.

17 J. N. Grossmann and J. H. Nebelsick, *Zoomorphology*, 2013, **132**, 301–315.

18 Y. H. Ha, R. A. Vaia, W. F. Lynn, J. P. Costantino, J. Shin, A. B. Smith, P. T. Matsudaira and E. L. Thomas, *Adv. Mater.*, 2004, **16**, 1091–1094.

19 G. Donnay and D. L. Pawson, *Science*, 1969, **166**, 1147–1150.

20 S. Weiner and L. Addadi, *Annu. Rev. Mater. Res.*, 2011, **41**, 21–40.

21 Y. Politi, T. Arad, E. Klein, S. Weiner and L. Addadi, *Science*, 2004, **306**, 1161–1164.

22 E. Beniash, L. Addadi and S. Weiner, *Journal of Structural Biology*, 1999, **125**, 50–62.

23 C. Moureaux, A. Pérez-Huerta, P. Compère, W. Zhu, T. Leloup, M. Cusack and P. Dubois, *Journal of Structural Biology*, 2010, **170**, 41–49.

24 V. Presser, S. Schultheiß, C. Berthold and K. G. Nickel, *Journal of Bionic Engineering*, 2009, **6**, 203–213.

25 V. Presser, C. Kohler, Z. Živcová, C. Berthold, K. G. Nickel, S. Schultheiß, E. Gregorová and W. Pabst, *Journal of Bionic Engineering*, 2009, **6**, 357–364.

26 W. Yue, R. J. Park, A. N. Kulak and F. C. Meldrum, *Journal of Crystal Growth*, 2006, **294**, 69–77.

27 L. Cao, X. Li, X. Zhou, Y. Li, K. S. Vecchio, L. Yang, W. Cui, R. Yang, Y. Zhu, Z. Guo and X. Zhang, *ACS Appl. Mater. Interfaces*, 2017, **9**, 9862–9870.

28 R. H. Ottewill and J. N. Shaw, *Kolloid-Zeitschrift und Zeitschrift für Polymere*, 1967, **218**, 34–40.

5 Conclusion and future work

5.1 Summary

Nature offers outstanding examples of structures and composite materials which exploit a variety of functions, often combining two or more needs. The strategies found in Nature can be exploited to create new materials, optimizing both the fabrication processes and the material performances. In this thesis, I describe the fabrication of new inorganic materials with functional applications, ranging from drug delivery to bio-catalysis.

Calcite single crystal composites are commonly found in biomineralized shells, in which small molecules such as amino acids and macromolecules such as protein are embedded within the inorganic matrix and modify the habit and proprieties of the material. In the work described in chapter 2, we exploited the ability of calcite crystals to entrap molecules and nano-objects to obtain functional materials, with particular focus on drug delivery. In fact, calcium carbonate dissolves at acidic pHs that are typical of cancer and inflamed tissues, making it an ideal carrier for passive drug delivery systems. At the same time, the study of the additive entrapment and precipitation conditions gives insights on the crystallization mechanism, shedding light on biomineralization processes. Furthermore, the possibility of using living calcifying organisms as bioreactor to produce hybrid crystals has been explored. By culturing foraminifera in the presence of magnetic nanoparticles, whose entrapment into the crystalline lattice has been previously verified *in vitro*, a skeleton including the magnetic particles has been obtained.

Crystalline order on a bigger length scale gives rise to interesting optical proprieties when materials with appropriate dielectric constant are used, as it happens in inverse opals (IO), structures consisting in a periodic array of void spaces in a bulk matrix. In chapter 3, titania and silica inverse opals structures coupled with plasmonic nanoparticles have been successfully used to obtain laser driven remote and localize enhancement of the activity of the model enzyme lipase. In fact, tailoring IO features and composition it is possible to give rise to the slow light effect, which will increase the rate of light absorption by plasmonic particles according to the Fermi's golden rule, and eventually cause an increase of the local temperature of the platform. The heat can be then exploited to enhance the activity of lipase, increasing its activity of almost 6 times. Since most of the catalytic reactions increase their rate by increasing the temperature, such a system can be used as a universal platform for enhanced catalytic efficiency.

As stated previously, biominerals present such complex morphologies that is not possible to replicate them *in vitro*. Sea urchin spines are composed of an interconnected network of pores with controlled dimensions and arrangement that give rise to a structure with a high

surface area/volume ratio. In chapter 4, it is shown how those structures can conveniently be used as a template for the synthesis other materials with different proprieties. Colloidal nanoparticles were successfully assembled onto the sea urchin spine surface obtaining an ordered array. The different length scale porosity colloid/spine structure can be used as a mold for other inorganic materials, such as silica or titania. Titania is particularly interesting since it can catalyze the photodegradation of small organic molecules when irradiated with UV light. A hybrid silica/titania scaffold replicating the urchin spine was obtained after dissolution of the $CaCO_3$ and polymers template.

In conclusion, this thesis shows a selection of functional inorganic materials synthesized using design strategies found in Nature or exploiting natural occurring complex structures as templates, taking advantage of the possibility of using constituents that are not available to biological organisms.

5.2 Outlook

Despite all the efforts and outstanding results reached in the field of biomimicry and bioinspired materials, plenty of possibilities are still open due to the never-ending inspiration sources that Nature has to offer.

Regarding the preparation of hybrid $CaCO_3$ crystals, we aim to improve our knowledge on the impact of the chemical and physical behavior of the additive on the inclusion within the crystals, focusing in particular on understanding the size threshold from which an additive act as a nucleation surface. Other than that, we plan to embed additional functionalities in the nPs to obtain multifunctional materials. We plan to verify the possibility of obtaining bionic crystals using more complex organisms, such as bivalves and corals.

The concept developed in chapter 3 can be extended to incorporate multiple types of photonic structures and plasmonic NPs to perform different reactions in sequence or in parallel. We foresee the application of the demonstrated approach to dispersible particles for application in homogeneous systems and *in vivo*.

The platform developed in chapter 4 can be applied in a variety of fields in which surface area is a crucial parameter, ranging from catalysis to tissue regeneration, by changing the material used as a matrix. The same strategy can be used with different materials as template, thus being able to tune pore size and density. The final scaffold can be functionalized after the fabrication to give it additional features.

6 Acknowledgements

My PhD journey wouldn't have been possible without all the people I met along my way.
I am indebted to my supervisor Prof. Giuseppe Falini for his endless support, patience and trust in guiding me in the right direction while letting me free of following my interests. My scientific and personal growth wouldn't have been the same without joining his group.
I want to thank Prof. Joanna Aizenberg for welcoming me in her group and giving me the opportunity to blend in a completely different environment, expanding my knowledge of the world and significantly improving my self-confidence.
The work presented in this thesis was possible thanks to collaboration with excellent researchers. My first and most deep thanks goes to Prof. Boaz Pokroy and Dr. Iryna Polishchuk for their willingness to discuss results and future research, other than to the fun time we spent together while they always made me feel as a part of their team.
I want to thank Prof. Jonathan Erez for hosting me in his lab and teaching me how to culture foraminifera, Dr. Meganne Christian, Franco Corticelli and Dr. Vittorio Morandi for invaluable expertise in SEM imaging, Dr. Francesco Valle and Dr. Marianna Barbalinardo for useful discussion and collaboration over and incredible wide range of research topics, Dr. Francesco Palomba and Prof. Luca Prodi for collaboration in the nPs project, Dr. Elijah Shirman to teach me so much about photonics and make me experiment as much as I wanted in the lab while focusing on "drawing conclusions".
I want to thank the reviewer of my thesis for making the time to give their precious suggestions and evaluation on the work I did so far.
My time in Bologna and in Boston would not have been the same without all the people with whom I shared my time during the last 3 years.
Dr. Matteo Calvaresi and Dr. Stefania Rapino, who guided me during my early-stage research and made me think that (almost) everything is possible, supporting me during good and hard times.
Devis to be my lab-mate during the last five years, without limiting our support to work-related problems and experiencing so many things together. Matteo for our shared path in Bologna and endless beers talking about science as well as non-scientific issues. Michela, to be a good example of one should behave properly despite our differences. A special thanks goes to Anna for all the time we spent together, the teaching, support and inspiration who made my time in the Aizenberg lab invaluable. I thank the Aizenberg lab for the feeling of being a group they taught me and the fun time together.
My dear friends Enrico and Riccardo for sharing so much and giving useful advices even though we are spread all over Europe. Daniela, for standing my never-ending complain on

everything and keeping me up and running even from far away. All my friends for all the support, especially when they were not understanding what I was talking about.
My final thank goes to my family for the constant support throughout my pathway. To my mom and dad to let me free to follow my dreams and to my uncle to always feed my scientific curiosity. Hope I gave back all I got making you proud of me.
Thanks!

7 Side projects

7.1 Synthesis of calcium carbonate in trace water environments

Reproduced from G. Magnabosco, I. Polishchuk, B. Pokroy, R. Rosenberg, H. Cölfen and G. Falini, *Chem. Commun.*, 2017, **53**, 4811 **DOI:** 10.1039/C7CC01342F with permission from The Royal Society of Chemistry.

The study of the $CaCO_3$ precipitation process is a key point for many different fields, from material science[1-3] to biomineralization.[4-6] The processes happening *in vivo* are of great significance even for developing new methodologies that can be applied *in vitro*.[7, 8] Although it is well known that organic molecules,[9-14] supersaturation, pH, template and temperature[15-18] play a fundamental role in the control of polymorphism, morphology and dimension of the crystals, even the hydration sphere of the involved ions is of crucial importance.[19, 20] In fact, water molecules influence strongly the reactions taking place during the $CaCO_3$ precipitation,[21] in particular the ones involved in the carbonate speciation. Few works have been done to investigate the role of the solvent during $CaCO_3$ crystallization, principally because of the difficulties in finding an appropriate solvent in which to perform the precipitation process. The ideal solvent must be able to dissolve salts and easily stay anhydrous. Among organic solvents, alcohols meet these requirements and, moreover, ethanol is the most common used in the studies present in the literature.[22-26]

When ethanol is present as an additive in an aqueous solution during a $CaCO_3$ precipitation process, it stabilizes vaterite and prevents its conversion to calcite.[26-28] In addition Sand *et al.*[29] showed how different alcohols, their concentration and the experimental parameters affect the stability, morphology and polymorphism of $CaCO_3$ in binary alcohol-water system, developing a model that is able to predict the outcome of the reaction based on the conditions used. When ethanol acts as a solvent, amorphous calcium carbonate (ACC) is the predominant polymorph obtained with the diffusion of ammonium carbonate into a solution of calcium chloride,[19] while using calcium hydroxide as starting material, a mixture of calcite, vaterite and aragonite is obtained.[24] In these reactions the formation of carbonate ions from diffusing gasses (i.e. NH_3 and CO_2) implies the presence of water. To the best of our knowledge, no reports describing direct mixing of calcium and carbonate ions in an almost water free environment are present in the literature.

In this communication we describe a new simple method to precipitate calcium carbonate from alcohol solutions of anhydrous calcium chloride and ammonium carbonate. In this system the low quantity of water diminishes the rate of carbonate speciation, favoring the precipitation of only two products, $CaCO_3$ and ammonium chloride (NH_4Cl).

The effect of different molecular weight (MW) alcohols, their volume ratio and the concentration of calcium and carbonate ions (as reported in Table 7) was investigated.

Table 7. Table containing the concentrations and solvents examined in this work. The solvents used were methanol (MeOH), ethanol (EtOH), 1-propanol (1-PropOH) and 1-butanol (1-ButOH). Samples prepared using 1-PropOH and 10 mM salts precipitated after 5 days (Table SI1). The samples indicated in grey show precipitates while the white ones are stable dispersions.

Solvent Conc.	MeOH	EtOH	1-PropOH	1-BuOH
33 mM	66% EtOH 33% MeOH	100% EtOH	66% EtOH 33% 1-PropOH	66% EtOH 33% 1-BuOH
20 mM	40% EtOH 60% MeOH	100% EtOH	40% EtOH 60% 1-PropOH	40% EtOH 60% 1-BuOH
10 mM	20% EtOH 80% MeOH	100% EtOH	20% EtOH 80% 1-PropOH	20% EtOH 80% 1-BuOH
5 mM	10% EtOH 90% MeOH	100% EtOH	10% EtOH 90% 1-PropOH	10% EtOH 90% 1-BuOH

Anhydrous calcium chloride and ammonium carbonate were dissolved in absolute ethanol, then the solutions were added to absolute ethanol, or other alcohols, using syringe pumps under continuous magnetic stirring until reaching the desired concentration (see 7.1.1).

Table 8. Measurements of particles (nm) present in the solution still stable after a centrifugation at 4500 g for 10 minutes obtained using DLS. For the sample prepared using 5 mM salts in MeOH, it was not possible to measure particles since their concentration was too low.

Solvent Conc.	MeOH	EtOH	1-PropOH	1-BuOH
20 mM	120.9 ± 0.73	---	---	---
10 mM	74.7 ± 0.1	65.7 ± 0.31	---	---
5 mM	---$	35.7 ± 0.1	117.1 ± 0.32	22.0 ± 0.3

$ no measurable

After 3 hours from the beginning of the reaction, only some samples produced $CaCO_3$ particles that could be separated by centrifugation at 4500 g (highlighted in grey in Table 7). The other solutions presented a suspension of $CaCO_3$.

No other reaction times were analyzed, since the goal of this communication was to investigate the precipitation of $CaCO_3$ in the absence of water in diverse organic solvents, after a time when different behaviors were detectable. Shorter reaction time resulted in a general formation of suspensions and longer ones in the general formation of precipitates. In a further research the time-evolution of the $CaCO_3$ formation will be carried out.

The suspensions, which did not show a macroscopic precipitate were investigated by dynamic light scattering (DLS) and Analytical Ultracentrifugation (AUC). At 5 mM $CaCO_3$ concentration, nanoscopic species were detected by DLS for all solvents (exception methanol), at 10 mM only for methanol and ethanol and at 20 mM only for methanol (Table 8). These data indicate that with increasing solvent polarity, nanoparticles can be stabilized against precipitation and that with decreasing $CaCO_3$ concentration, the particle size decreases. For 5 mM and 10 mM $CaCO_3$ in ethanol and 5 mM in 1-butanol, the particle size distributions could be determined by AUC, which were in good agreement with the DLS data and showed that the 5 mM samples were rather monodisperse (Figure 86).

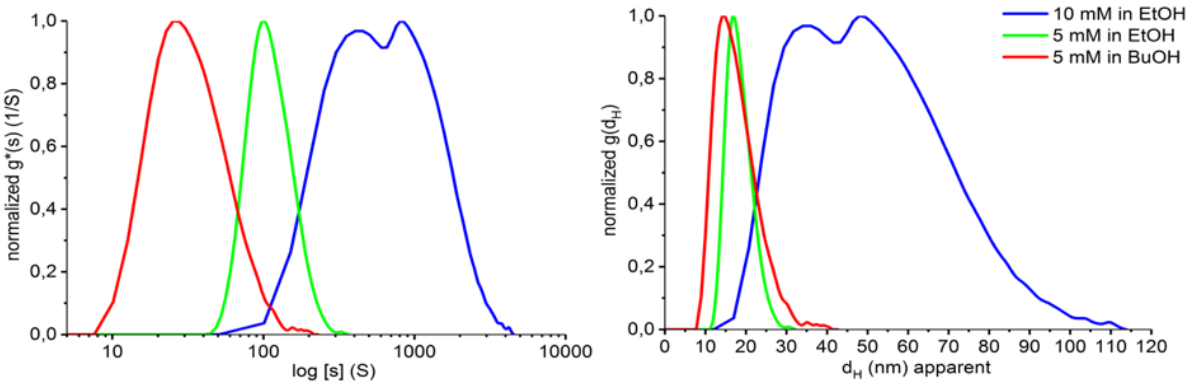

Figure 86. Sedimentation coefficient distribution of different salt concentrations in organic solvents from AUC and the corresponding particle size distribution calculated on basis of a density of ACC = 1.48 g/ml and using the densities and viscosities of the pure solvents.

However, the 5 mM and 20 mM $CaCO_3$ samples in methanol and 5 mM and 10 mM in ethanol as well as the 5 mM sample in 1-propanol contained very small species. Their sedimentation coefficients are shown in Figure 87. The sedimentation coefficients are in the order of 0.1 – 0.3 S which is typical for ions / ion pairs with the exception of the 1-propanol sample.[30] A larger species is also detected with sedimentation coefficients of around 1S, which falls into the range of prenucleation clusters with the exception of the 1-propanol sample.[30] Partly, even larger species with sedimentation coefficients around 3 S are observed (Figure 87).

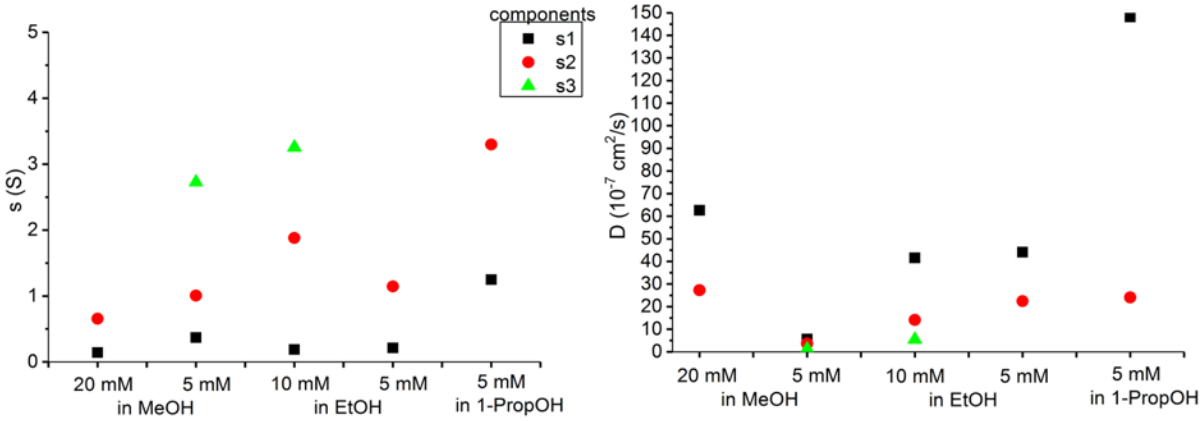

Figure 87. Sedimentation coefficients (left) and diffusion coefficients (right) of different $CaCO_3$ concentrations in organic solvents from AUC Non-Interacting Discrete Species Model. Up to three independent species are detected and marked with colours (black = species 1, red = species 2 and green = species 3)

What these species are cannot be determined from these data. Therefore, we employed the diffusion coefficients, which can at least qualitatively be determined via fitting of the sedimentation data to the Lamm equation (Figure 87). Using the Stokes-Einstein equation, the particle diameters (d) could be calculated.

With a modified Svedberg (equation 1), the density of the species can be estimated from the size and sedimentation coefficient as shown in Table 3.

$$\rho_i = \rho_0 + \frac{180\,\eta_0\,s}{d^2} \quad \text{equation 1.}$$

ρ_i (in g/ml) is the density of the sedimenting particle, ρ_0 and η_0 (in Poise) are the density and the viscosity of solvent, s (in Svedberg) is the sedimentation coefficient and d (in nm) is the particle size (Stockes-equivalent sphere diameter)

Table 9. Particle diameters in nm and densities in g/ml of small species detected via AUC

	d_1 / ρ_1	d_2 / ρ_2	d_3 / ρ_3
MeOH 20 mM	1.3 / 0.88	2.9 / 0.86	
EtOH 10 mM	1.0 / 1.18	2.9 / 1.24	7.4 / 0.91
EtOH 5 mM	0.9 / 1.29	1.8 / 1.48	

kes-equivalent sphere diameter)

Table 9, it can be seen that at least for methanol and ethanol, very small species could be detected with sizes around 1 nm for the smallest species 1, 2 – 3 nm for species 2 and 7.5 nm for species 3. The density of the species in methanol is markedly smaller than that in ethanol although the density of the solvents is almost equal (0.79 g/ml). This indicates a higher degree of solvation of the ionic calcium and carbonate species for the more polar methanol as compared to ethanol. The smallest detected species with a size of 0.9 nm - 1.3 nm could potentially be related to a solvated $CaCO_3$ ion pair (r Ca^{2+} = 0.10 nm, r CO_3^{2-} = 0.18 nm), while the larger species already must already contain dozens of ions with a size similarity to

prenucleation clusters for the water case.[30] The solubility of $CaCO_3$ in alcohol decreases with the increase of the alcohol MW, resulting in a higher $CaCO_3$ precipitation yield in high MW solvents even at lower starting salt concentration. The precipitates were characterized as collected after centrifugation and drying at 60 °C. No water washing was carried out to avoid any dissolution, and eventually, a re-precipitation process. The solid products were analyzed by Fourier transform infrared (FTIR) spectroscopy, scanning electron microscopy (SEM) and synchrotron high resolution powder X-ray diffraction (HRPXRD). The FTIR and HRPXRD data showed that $CaCO_3$ co-precipitated with NH_4Cl, as a side product. The bands in the FTIR spectra 1475 cm^{-1}, at 876 cm^{-1} and 746 cm^{-1} (Figure 90), correspond to v_3, v_2 and v_4, respectively, vibration modes of vaterite. The bands at 1420 cm^{-1} at 712 cm^{-1} indicate the presence of calcite traces in some precipitates, while the one at 1403 cm^{-1} indicates NH_4Cl. The presence of vaterite, NH_4Cl and trace of calcite was also confirmed by the Rietveld analysis of the HRPXRD data (Figure 88 and Table 10). This data confirmed the co-presence of NH_4Cl, which sublimates after thermal treatment at 300 °C (Figure 89).

Table 10. Unit cell parameters of calcite and vaterite obtained by the Rietveld analysis of the diffraction patterns of the samples investigated by synchrotron high resolution powder X-ray diffraction. The weight fraction of the detected mineral phases is also reported. The samples coded with heated were heated for 2 hours at 300 °C and then analysed at room temperature.

Sample	Calcite			Vaterite			NH_4Cl
	a,b (Å)	c (Å)	Weight fraction (wt%)	a,b (Å)	C (Å)	Weight fraction (wt%)	Weight fraction (wt%)
MeOH_33	4.986(1)	17.101(2)	35	4.1285(5)	8.4778(8)	65	
MeOH_33 heated	4.985(2)	17.087(4)	39	4.1287(8)	8.474(1)	61	
EtOH_33	4.9879(5)	17.0999(9)	6	4.1290(3)	8.4742(4)	80	14
EtOH_33 heated	4.9906(8)	17.075(2)	7	4.1294(3)	8.4713(4)	93	
PropOH_33	4.9849(3)	17.1040(3)	0.1	4.1260(6)	8.495(1)	74.9	25
PropOH_33 heated	5.00(5)	17.0(1)	0.7	4.1274(5)	8.479(1)	99.3	
BuOH_33	4.987(1)	17.097(2)	3	4.1291(3)	8.4808(6)	84	13
BuOH_33 heated	4.990(1)	17.078(2)	5	4.12966(2)	8.4707(4)	95	

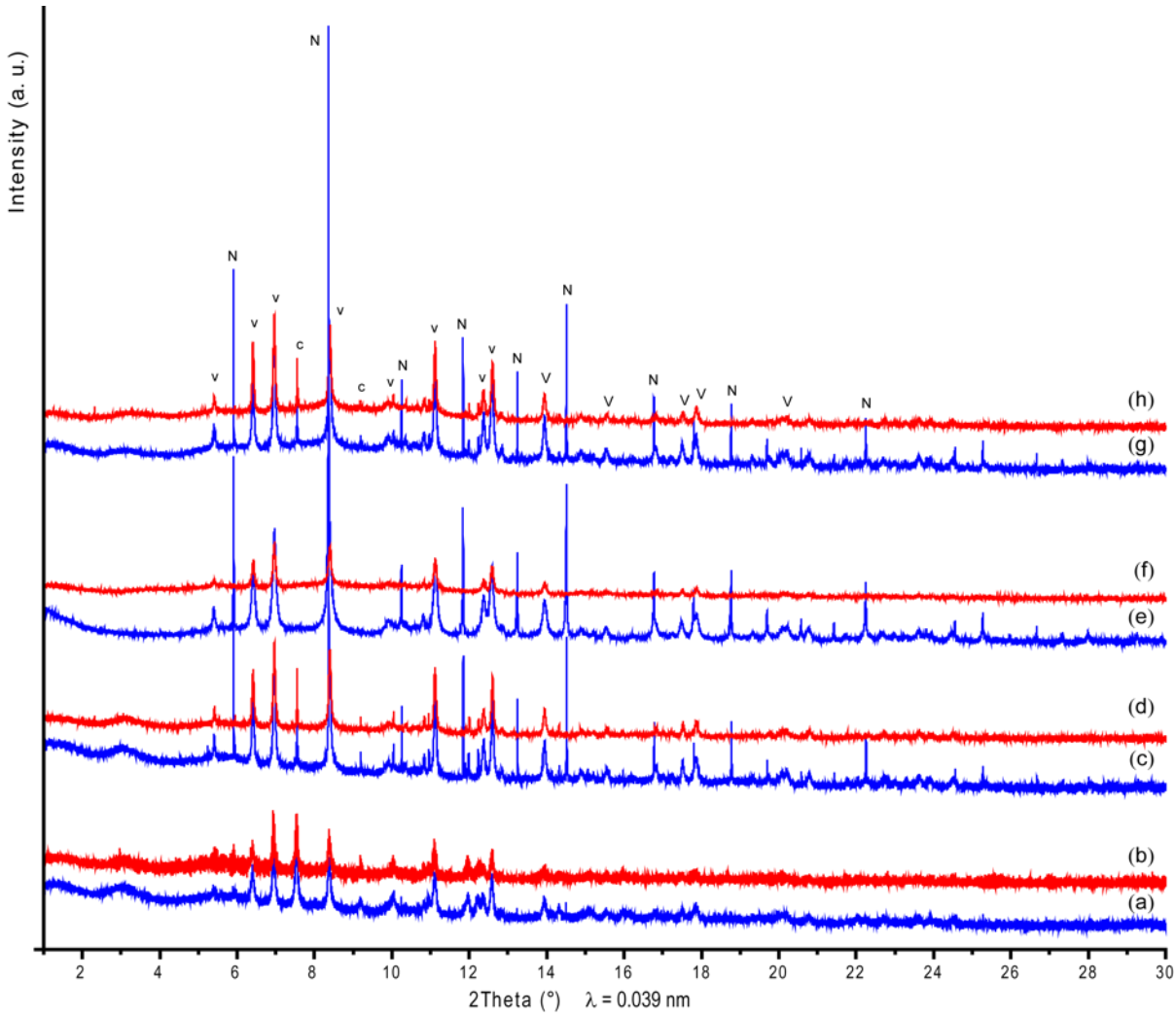

Figure 88. High resolution powder X-ray powder patterns of samples obtained using MeOH and 33 mM salts (a) before and (b) after heating at 300 ◦C, EtOH and 33 mM salts (c) before and (d) after heating at 300 ◦, PropOH and 33 mM salts (e) before and (f) after heating at 300 ◦C and BuOH and 33 mM salts (g) before and (h) after heating at 300 ◦C. Peaks marked with N correspond to NH_4Cl, the ones marked with V correspond to vaterite and the ones marked with C correspond to calcite.

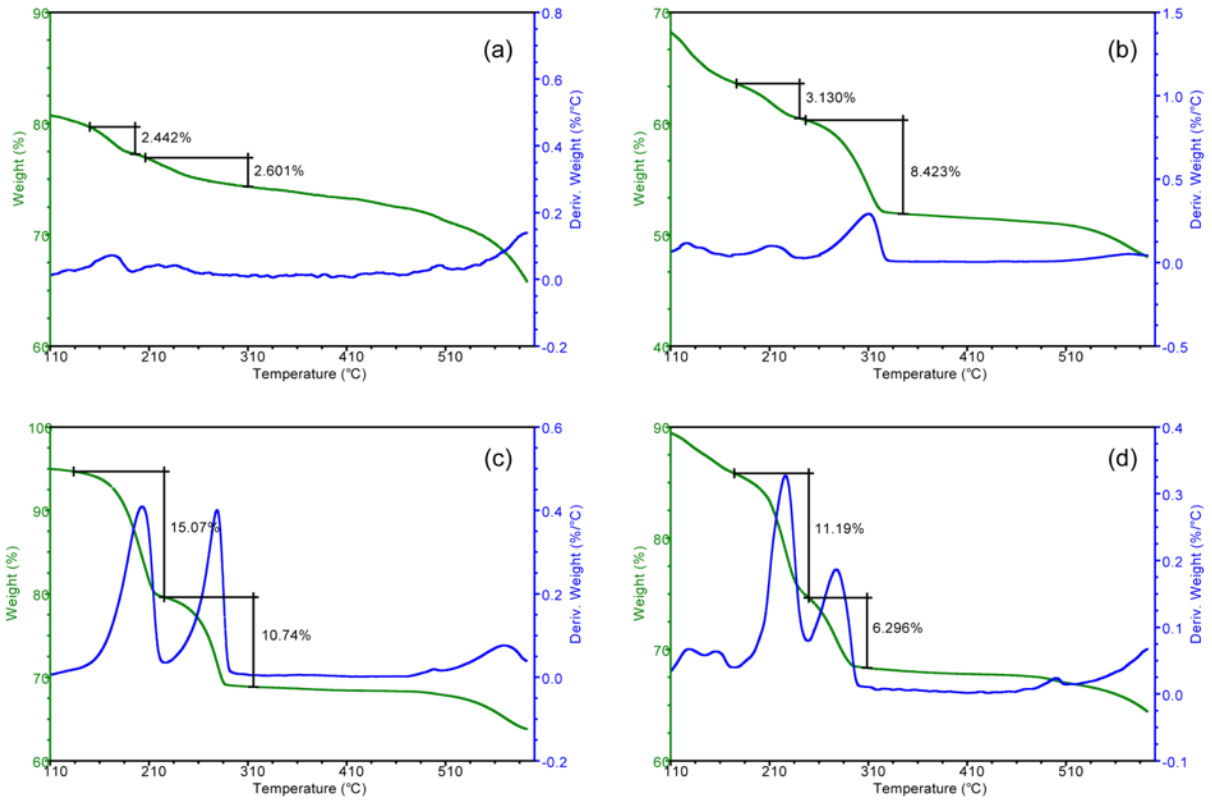

Figure 89. TGA profiles of samples obtained using (a) MeOH and 33 mM salts, (b) EtOH and 33 mM salts, (c) PropOH and 33 mM salts and (d) BuOH and 33 mM salts. The weight lost at about 200 °C is associated to a water lost, while that at about 280 °C to the sublimation of NH_4Cl.

The intensities of the band at 3000 cm^{-1} suggest a contribution of water to the ammonium absorption bands (Figure 90). This indication is confirmed by the thermogravimetric analysis (Figure 89), from which an amount of about 3-15 wt.% of linked water was detected in the precipitates, according to intensity of the absorption band at 1628 cm^{-1}.

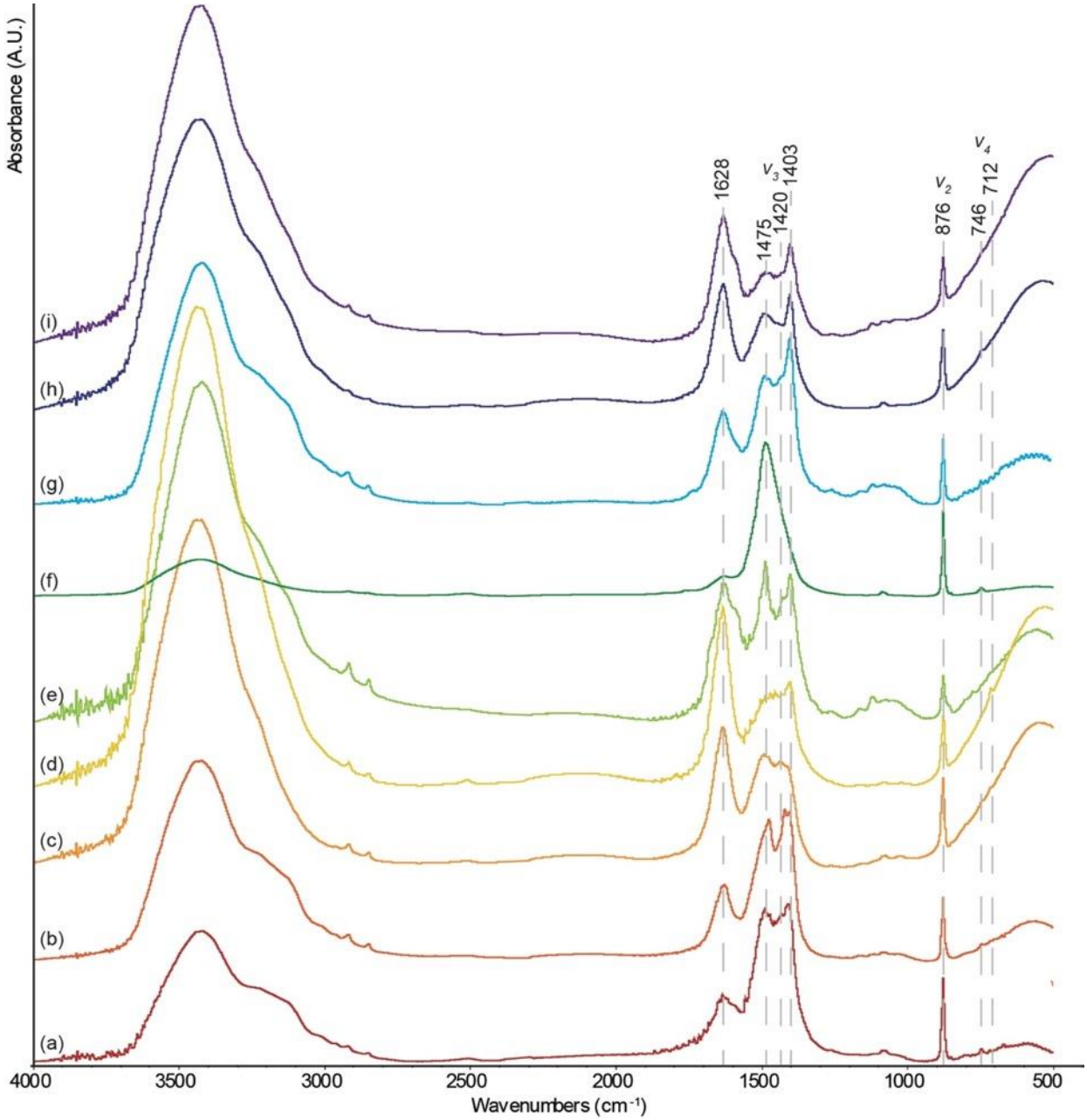

Figure 90. FTIR spectra of samples obtained using (a) MeOH and 33 mM salts, (b) EtOH and 33 mM salts, (c) EtOH and 20 mM salts, (d) PropOH and 33 mM salts, (e) PropOH and 20 mM salts, (f) PropOH and 10 mM salts, (g) BuOH and 33 mM salts, (h) BuOH and 20 mM salts and (i) BuOH and 10 mM salts. Collected with an FT-IR Bruker Alpha System spectrometer (64 scans).

Since after the precipitation process the quantity of water in the solution is lower than 0.5% (v/v), we can hypothesize that this water is collected from the environment due to its high affinity to the $CaCO_3$ surface and entrapped between the crystalline domains. Comparing all the samples prepared using 33 mM salt solutions it is possible to notice that the intensity of the band at 1628 cm^{-1} increases with the MW of the selected alcohol. The lower solubility of water in alcohols with longer chain may promote the entrapping of water in the precipitate.

SEM imaging (Figure 91) reveals the presence of $CaCO_3$ particles with different morphologies together with an unstructured thin layer, probably of NH_4Cl or amorphous calcium carbonate (not evident from HRPXRD and FTIR data) that covers the underlying material. The sample precipitated in the presence of methanol shows particles around 150 nm that assemble to form 3 µm aggregates with irregular shape. When the precipitation process is carried out using pure ethanol as solvent, particles with a more regular shape are present in the samples. Using 33 mM salt concentration, pillars with hexagonal section can be observed while, reducing the salt concentration to 20 mM, some elongated grain-like particles form. 1-propanol and 1-butanol precipitated samples seem to be influenced stronger by the concentration of the salts rather than by the nature of the solvent. In fact, for both samples prepared with 33 mM salts, it is not possible to recognize any regular shape. When decreasing the salt concentration to 20 mM and 10 mM, some spherical particles become visible due to the reduction of the covering layer. These particles are smaller than 1 µm and have an irregular surface (Figure 91).

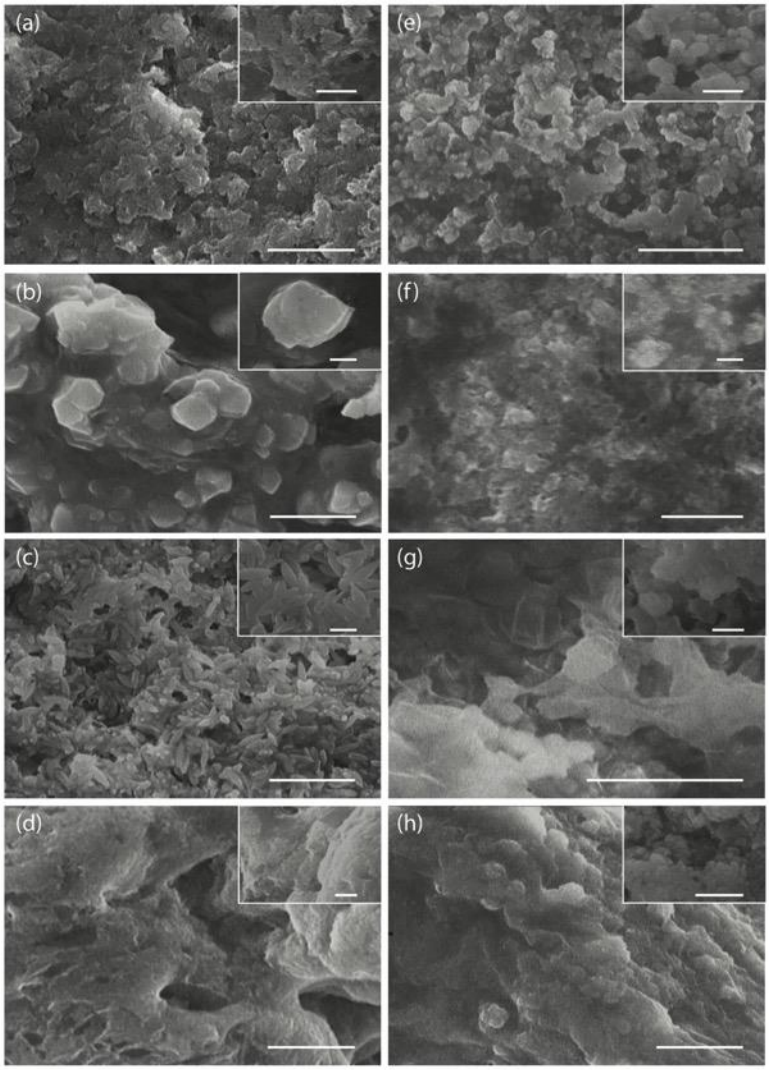

Figure 91. SEM images of samples obtained using (a) MeOH and 33 mM salts, (b) EtOH and 33 mM salts, (c) EtOH and 20 mM salts, (d) 1-PropOH and 33 mM salts, (e) 1-PropOH and 20 mM salts, (f) 1-BuOH and 33 mM salts, (g) 1-BuOH and 20 mM salts and (h) 1-BuOH and 10 mM salts. Scale bar is 5 µm in the main picture and 1 µm in the inset.

These results confirm that the solvent plays a fundamental role in the crystallization of $CaCO_3$ and add new information showing that the use of different alcohols stabilizes vaterite reducing its conversion to calcite, in agreement with previously published data.[30] The crystallization process in alcohol is slower than the one in water and, after 3 hours from ion addition, vaterite is the main component of the precipitate, while in pure water the same experimental conditions produce only pure rhombohedral calcite (Figure 91 and Figure 92). However, in similarity to the prenucleation clusters observed in water,[30] we could also detect several very small species in methanol and ethanol, which are likely solvated ions or their clusters.

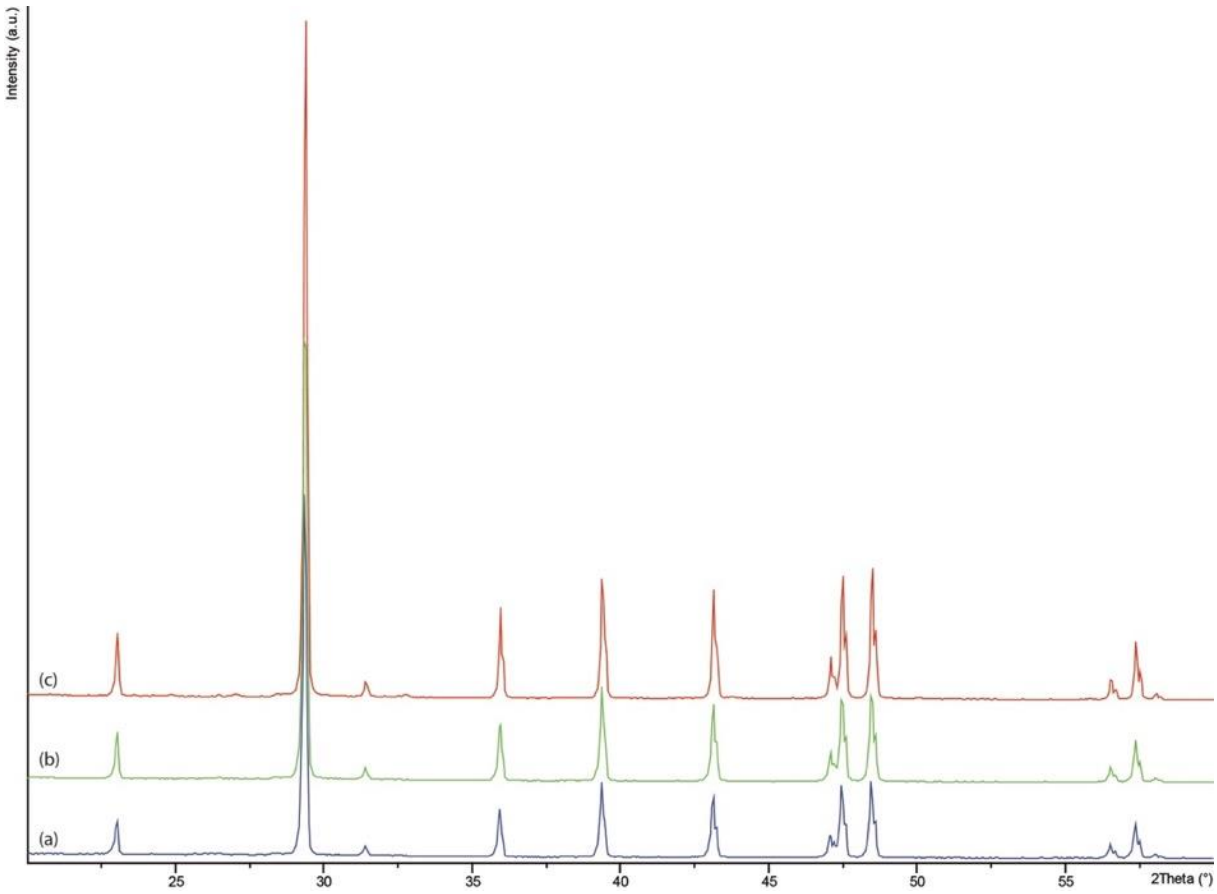

Figure 92. X-ray powder diffraction patterns of samples obtained in water with (a) 33 mM salts, with (b) 20 mM salts and (c) 10 mM salts using the same conditions used for the experiments with organic solvents. Only calcite peaks are present.

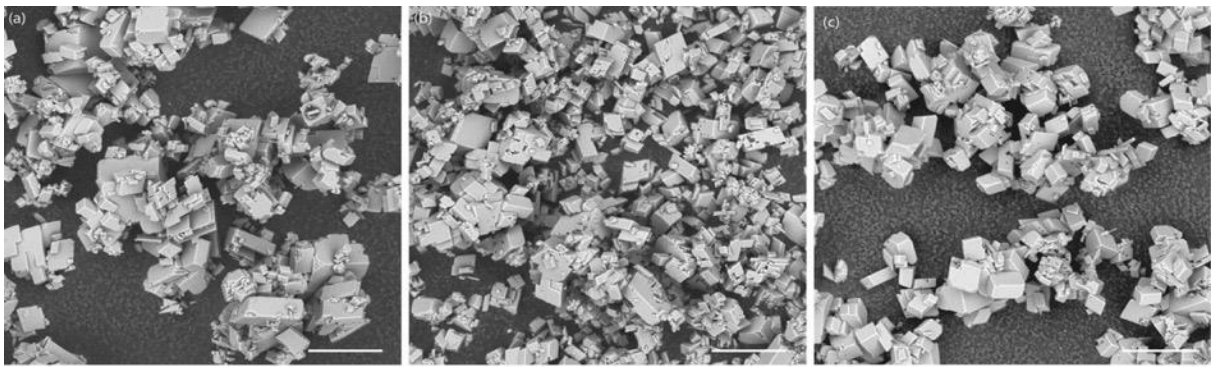

Figure 93. Scanning electron microscopy (SEM) of samples obtained in water with (a) 33 mM salts, with (b) 20 mM salts and (c) 10 mM salts using the same conditions used for the experiments with organic solvents. Only calcite rhombohedra are present. Scalebar is 10 µm.

In conclusion, this simple methodology can allow the study of the interaction between $CaCO_3$ and molecules that are not soluble in water, without the use of additional reactants, giving rise to new possible synthetic paths. Finally, the data show that the use of a different solvents significantly affects the $CaCO_3$ crystallization pathway, which will be the object of future further investigations.

7.1.1 Materials and methods

Experimental section Crushed anhydrous $CaCl_2$ (Sigma-Aldrich, granular, ≥93.0%) and anhydrous $(NH_4)_2CO_3$ (Acros organics, for analysis ACS) were put in a desiccator with P_2O_5 for several days in order to dry them completely. After this, they were stored in a closed desiccator with P_2O_5 until usage.

0.1 M solutions of $CaCl_2$ and $(NH_4)_2CO_3$ in absolute ethanol (sigma Aldrich, ≥98.0%) were prepared stirring the previously dried salts overnight. The solutions were filtered with 0.2 µm filters before use. Then, both solutions were injected with syringe pumps (rate 7.5 mL/h, era pump system inc.) in a volume of alcohol to reach the desired concentration, as reported in Table S1.

After 3 hours from the end of addition, the solutions were centrifuged at 4500 g for 10 minutes (ALC PK121). It was possible to separate the sample prepared using 10 mM salts in 1-PropOH only after 5 days (highlighted in patterned grey in Table S1). The samples were not washed with any solvent since the synthesis produced a very small amount of powder that would be almost totally lost with further processing. It was possible to separate a precipitate only from the samples highlighted in grey. After the centrifugation, the precipitate was collected and dried at 60 °C.

Characterization Fourier transform infrared (FTIR) spectra of samples in KBr pellet were collected at room temperature by using a FT-IR Bruker Alpha System spectrometer working in the range of wavenumbers 4000–400 cm^{-1} at a resolution of 1 cm^{-1} with 64 scans. High resolution X-ray powder diffraction (HRPXRD) measurements were collected with a dedicated high- resolution powder diffraction synchrotron beamline (ID22 at the European Synchrotron Radiation Facility (ESRF), Grenoble, France) using as wavelength 0.039 nm.

X-ray powder diffraction (XRPD) measurements reported in Figure SI 4 were carried out using a PanAnalytical X'Pert Pro diffractometer equipped with X'Celerator detector with Cu Kα radiation (range 20°-60°, step size 0.05°, time per step 120 s).

Scanning electron microscopy (SEM) images were collected with a Phenom G2 Pure microscope (FEI) for uncoated samples (reported in figure SI 3) and a Hitachi FEG 6400 microscope for samples after coating with 5 nm of gold (Figure 2).

Thermogravimetric analysis (TGA) was performed using an SDT Q600 instrument (TA Instruments).

Dynamic light scattering (DLS) was performed using a Malvern Zetasizer Nano ZS. Analytical Ultracentrifugation (AUC) measurements were performed on an Optima XL-I analytical ultracentrifuge (Beckman-Coulter, Palo Alto, CA, United States) using Rayleigh Interference optics and 12 mm double-sector titanium centerpieces (Nanolytics, Potsdam,

Germany). Samples were investigated at 25 °C and 5 000 rpm, 16 000 rpm and 60 000 rpm. 320 µl of the prepared salt solutions were used for the measurements. 350 µl of the corresponding organic solvent was used as reference solution.

The sedimentation velocity experiments at 5 000 rpm and 16 000 rpm were evaluated with the ls-g*(s) model using the SEDFIT software version 14.4d by Peter Schuck (http://www.analyticalultracentrifugation.com/default.htm). The measurement data at 60 000 rpm were evaluated with numerical fitting of the Lamm equation using a noninteracting species model yielding sedimentation and diffusion coefficient s resp. D as well as species concentration in fringe units using the same SEDFIT software.

7.1.2 Notes and references

1 L. A. Estroff and A. D. Hamilton, *Chem. Mater*., 2001, **13**, 3227–3235.

2 D. B. Trushina, T. V. Bukreeva and M. N. Antipina, *Crystal Growth & Design*, 2016, **16**, 1311–1319.

3 F. Nudelman and N. A. J. M. Sommerdijk, *Angew. Chem. Int. Ed.*, 2012, **51**, 6582–6596.

4 L. Addadi, A. Gal, D. Faivre, A. Scheffel and S. Weiner, *Israel Journal of Chemistry*, 2015, **56**, 227–241.

5 J. J. De Yoreo, P. U. P. A. Gilbert, N. A. J. M. Sommerdijk, R. L. Penn, S. Whitelam, D. Joester, H. Zhang, J. D. Rimer, A. Navrotsky, J. F. Banfield, A. F. Wallace, F. M. Michel, F. C. Meldrum, H. Cölfen and P. M. Dove, *Science*, 2015, **349**, 6760–6760.

6 S. Weiner and L. Addadi, *Annu. Rev. Mater. Res*., 2011, **41**, 21–40.

7 N. A. J. M. Sommerdijk and G. de With, *Chem. Rev*., 2008, **108**, 4499–4550.

8 F. C. Meldrum and H. Cölfen, *Chem. Rev.*, 2008, **108**, 4332–4432.

9 S. Weiner and L. Addadi, *Trends Biochem. Sci*., 1991, **16**, 252–256.

10 M. Reggi, S. Fermani, V. Landi, F. Sparla, E. Caroselli, F. Gizzi, Z. Dubinsky, O. Levy, J.-P. Cuif, Y. Dauphin, S. Goffredo and G. Falini, *Crystal Growth & Design*, 2014, **14**, 4310–4320.

11 D. Ren, Q. Feng and X. Bourrat, *Micron*, 2011, **42**, 228–245.

12 G. Falini, S. Albeck, S. Weiner and L. Addadi, *Science*, 1996, **271**, 67–69.

13 S. Weiner and L. Addadi, *J. Mater. Chem*., 1997, **7**, 689–702.

14 L. Kabalah-Amitai, B. Mayzel, Y. Kauffmann, A. N. Fitch, L. Bloch, P.U.P.A. Gilbert and B. Pokroy, *Science*, 2013, **340**, 454-457.

15 B. Pokroy and E. Zolotoyabko, *Chem. Commun*., 2005, **0**, 2140–2142

16 B. Njegić-Džakula, G. Falini, L. Brečević, Ž. Skoko and D. Kralj, J. Coll. *Inter. Sci.*, 2010, **343**, 553–563.

17 J. J. De Yoreo and P. G. Vekilov, *Rev. Mineral. Geochem.,* 2003, **54**, 57–93.

18 A. Navrotsky, *Proc. Natl. Acad. Sci. USA*, 2004, **101**, 12096–12101.

19 S.-F. Chen, H. Cölfen, M. Antonietti and S.-H. Yu, *Chem. Comm*., 2013, **49**, 9564–9566.
20 M. Sancho-Tomás, S. Fermani, M. Reggi, J. M. García-Ruiz, J. Gómez-Morales and G. Falini, *CrystEngComm*, 2016, **18**, 3265–3272.
21 F. Sebastiani, S. L. P. Wolf, B. Born, T. Q. Luong, H. Cölfen, D. Gebauer and M. Havenith, *Angew. Chemie I. E.*, 2017, **56**, 490–495.
22 G. Yan, L. Wang and J. Huang, *Powder Tech*., 2009, **192**, 58–64.
23 K. K. Sand, M. Yang, E. Makovicky, D. J. Cooke, T. Hassenkam, K. Bechgaard and S. L. S. Stipp, *Langmuir*, 2010, **26**, 15239–15247.
24 K. S. Seo, C. Han, J. H. Wee, J. K. Park and J. W. Ahn, *J. Crystal Growth*, 2005, **276**, 680–687.
25 M. Ryu, H. Kim, J. Ahn, K. You and S. Goto, *J. Ceram. Soc. Japan,* 2009, **117**, 106–110.
26 Z. Zhang, B. Yang, H. Tang, X. Chen and B. Wang, *J. Mater. Sci.*, 2015, **50**, 5540–5548.
27 L. Zhang, L.-H. Yue, F. Wang and Q. Wang, *J. Phys. Chem. B*, 2008, **112**, 10668–10674.
28 F. Manoli and E. Dalas, *J. Crystal Growth*, 2000, **218**, 359–364.
29 K. K. Sand, J. D. Rodriguez-Blanco, E. Makovicky, L. G. Benning and S. L. S. Stipp, *Crystal Growth & Design*, 2012, **12**, 842–853.
30 D. Gebauer, A. Völkel and H. Cölfen, *Science*, 2008, **322**, 1819–22.

7.2 Synthesis and adsorbing properties of thin plate-like {001} calcite crystals

Reproduced from Matijaković, N.; Magnabosco, G.; Scarpino, F.; Fermani, S.; Falini, G.; Kralj, D. Synthesis and Adsorbing Properties of Tabular {001} Calcite Crystals. Crystals 2018, 9, 16 DOI: 10.3390/cryst9010016. Supporting information available online.

7.2.1 Abstract

One of the most common crystal habits of the thermodynamically stable polymorph of calcium carbonate, calcite, is the rhombohedral one, which exposes {10.4} faces. When calcite is precipitated in the presence of Li^+ ions, dominantly {00.1} faces appear together with the {10.4}, thus generating truncated rhombohedrons. This well-known phenomenon is explored in this work, with the aim of obtaining calcite crystals with smooth {00.1} faces. In order to achieve this objective, the formation of calcite was examined in precipitation systems with different $c(Ca^{2+})/c(Li^+)$ ratios and by performing an initial high-power sonication. At the optimal conditions, a precipitate consisting of thin, tabular {001} calcite crystals and very low content of incorporated Li^+ has been obtained. The adsorption properties of the tabular crystals, in which the energetically unstable {00.1} faces represent almost all of the exposed surface, were tested with model dye molecules, calcein and crystal violet, and compared to predominantly rhombohedral crystals. It was found that the {00.1} crystals showed a lower adsorption capability when compared to the {10.4} crystals for calcein, while the adsorption of crystal violet was similar for both crystal morphologies. The obtained results open new routes for the usage of calcite as adsorbing substrates and are relevant for the understanding of biomineralization processes in which the {00.1} faces often interact with organic macromolecules.

7.2.2 Introduction

Investigation of precipitation mechanisms of calcium carbonates ($CaCO_3$) and their interactions with additives and surface chemistry, has attracted growing interest, due to promising technological applications [1–3] and the crucial role of this mineral in biomineralization [4–6]. Among $CaCO_3$ polymorphs, calcite is the most frequently studied, since it is in a thermodynamically-favored phase at ambient conditions and in the absence of additives. Calcite is an important product in the pharmaceutical, chemical, paper, and glass industries, and is also used as a sorbent for exhaust gasses and for the determination of the quality of drinking water [7–9]. Moreover, several organisms possess tissues mineralized with calcite that perform vital functions, like skeletal protection and support, light perception, or storage of calcium ions [10–13].

The morphology of calcite crystals produced in vitro is largely controlled by experimental conditions, such as pH, temperature, and supersaturation, as well as by the presence of impurities or additives that typically exert significant influence on the crystallization process [7,14–17]. The addition of inorganic additives such as Mg^{2+} and Li^+ causes selective stabilization of calcite crystals with different morphologies [18,19]. Thus, when precipitated in the presence of a Li^+-containing solution undersaturated with respect to Li_2CO_3, calcite shows {00.1} faces in addition to the {10.4} ones, which are typically obtained without additives. The extension of {00.1} faces depends on the $c(Ca^{2+})/c(Li^+)$ ratio [19–28]. In silico experiments on the calcite surface energy have shown that the rhombohedral {10.4} faces are the most stable, while the {00.1} faces have lower stability in the absence of additives [29]. The substitution of the surface Ca^{2+} with Li^+ destabilizes {10.4} faces, making the {00.1} ones the most stable and causing the formation of tabular crystals with {00.1} basal and {10.4} side faces [23,29].

Calcite has been used in experimental and theoretical studies as a model substrate for the investigation of the interactions occurring at organic-inorganic interfaces. Different classes of compounds have been tested, ranging from those with small molecular mass, such as water [30,31], alcohols [32], carboxylic [33,34] or amino acids [35,36], to bigger ones, such as polypeptides [37–39], proteins [40], or polysaccharides [41]. Most of these studies focus on the interaction of molecules on the calcite {10.4} surface, as this face is typically exposed by synthetic crystals, while the investigations of adsorption processes on other faces are relatively unexplored. Indeed, the structure of the monoatomic growing step on the {10.4} surface corresponds to {00.1} faces. Therefore, the study of the adsorption process on the well exposed and dominant {00.1} faces is also relevant. because the diffusion of additives along the {10.4} steps of calcite crystals occurs on them. Furthermore, this is a position of strong interfacial interactions with non-constituent molecules and organic matrix in biomineralization.

This study reports an optimized procedure for the preparation of size-uniform, thin, tabular calcite crystals with well-developed {00.1} faces ({00.1} calcite). In addition, the adsorption of model organic molecules, calcein and crystal violet, on {00.1} calcite is examined and compared to their adsorption on stable {10.4} faces. Besides the basic understanding of the specific {00.1} interactions with organic molecules, the knowledge gained from this research may be relevant to technology in which the presence of different crystal faces may tune the adsorbing capacities of a substrate. In addition, these data can contribute to the understanding of the processes of biomineralization, since the mineral interactions with intra-mineral macromolecules often occur exactly at {00.1} faces.

7.2.3 Materials and Methods

The reactant solutions were prepared by using the analytical grade chemicals, $CaCl_2 \cdot 2H_2O$, LiCl, and $NaHCO_3$ and deionized water (conductivity <0.055 $\mu S \cdot cm^{-1}$). Calcium carbonate precipitation was initiated by mixing equal volumes (200 cm^3) of $CaCl_2$/LiCl solution with $NaHCO_3$ solution. All solutions were freshly prepared and the initial concentrations of $CaCl_2$ and $NaHCO_3$ were identical, c = 0.1 mol dm^{-3}, while the concentration of LiCl varied in the range from 0 to 1.0 mol dm^{-3}. The initial supersaturation, expressed with respect to calcite, was $S_c \approx 23$. Calcite supersaturation, S, was defined as a square root of the activity product quotient, $S = [(a_{Ca} \times a_{CO3})/K_{sp}]^{1/2}$, where a indicates the species activity and the K_{sp} is the calcite solubility product. The reference experiments were performed in the absence of LiCl (reference system).

The sonication was initiated in $NaHCO_3$ solution before mixing with $CaCl_2$/LiCl solution. The systems were sonicated for 10 min and the pH was continuously measured. After that period, the mixture was left without stirring for 5 days. The ultrasonic irradiation was performed by using the Branson Sonifier 250 (20 kHz frequency). The ultrasound power output used in the experiments and set at 20% was 40 W. In order to avoid overheating the system, the pulsed mode was applied (60 cycles per minute, t = 0.2 s). The horn diameter was 5 mm and it was immersed in the center of the reaction vessel, 5 cm above the bottom. The crystal samples were collected by filtering 10 cm^3 of suspension through a 0.22 µm membrane filter. The precipitates were washed with small portions of water and dried at 90 °C for 2 h.

The polymorphic composition of the dried samples was determined by FT-IR spectroscopy (FT-IR TENSOR II, Bruker, Billerica, MA, USA), using the KBr pellets technique. X-ray powder diffraction, XRD (Philips X'Celerator diffractometer, Philips, Amsterdam, The Netherlands) was made in the angular range $20° \leq 2\vartheta \leq 70°$, setting a step size $2\vartheta = 0.05°$ and measuring time of 120 s per step. The crystal morphology was determined by scanning electron microscopy (FEG SEM Hitachi 6400 (Hitachi, Tokyo, Japan), JEOL JSM-7000F (JEOL, Tokyo, Japan) and Phenom model G2, (Phenom-World BV, Eindhoven, The Netherlands)),

operating in low-voltage mode. The SEM samples were placed on carbon tape without any coating. The calcium and Li^+ ion content in the crystals was determined by an ion chromatography system (ICS-1100, Dionex, Sunnyvale, CA, USA) fitted with a SC16 Analytical Column and using 30 mM MSA eluent. The specific surface area was determined by the multiple BET method (Micromeritics, Gemini), using liquid nitrogen.

For adsorption measurements the solutions of respective dye (c = 10 μmol dm^{-3}) were diluted in HEPES buffer (c = 0.1 mol dm^{-3}, pH 8.0). The buffer was pre-saturated with excess of rhombohedral calcite crystals, by mixing the suspension for 1 h and filtering by means of 0.2 μm membrane filter. Exactly 4 mg of calcite crystals (tabular or rhombohedral) were suspended in 2 mL of dye solution and stirred for 24 h, after which the crystals were separated by centrifugation. The quantity of residual dye in the solution was determined by UV-Vis spectroscopy (Cary UV-Vis 300Bio, Agilent Technologies, Santa Clara, CA, USA), measuring the absorbance at λ = 495 nm (calcein) and λ = 594 nm (crystal violet). The kinetics of adsorption was determined by the same protocol, by sampling at predetermined time intervals.

7.2.4 Results and Discussion

7.2.4.1 Synthesis and Characterization of Thin Tabular {00.1} Calcite Crystals

The first objective of this research was to identify the optimal conditions for the preparation of thin tabular calcite crystals, exposing predominantly the {00.1}, over the {10.4} faces. A series of $CaCO_3$ precipitation systems having high initial supersaturation, $c_i(CaCl_2)$ = $c_i(NaHCO_3)$ = 0.1 mol dm^{-3}; $S_c \approx 23$, and different $c(Li^+)$, were initially irradiated by high-power ultrasound for 10 minutes and the precipitates were left to age in the mother solutions without stirring for 5 days (Table 11).

The precipitates were sampled and characterized immediately after the sonication process, continuously during the aging of precipitate, and finally after the equilibrating of the process, which typically lasted for 5 days. The addition of Li^+ was supposed to stabilize {00.1} calcite crystals, while the ultrasound irradiation was applied in order to influence the nucleation and crystal growth processes, which may cause the changes of polymorphic composition, the morphology, or the size distribution of the precipitate. Indeed, in order to test a critical role of high-power ultrasound irradiation in the synthesis of {00.1} calcite, different types of stirring of the solutions during the nucleation period have been applied. Thus, either a mechanical propeller, Teflon-coated magnetic stirrer, or ultrasonic irradiation has been used during the first 10 minutes of the precipitation process. In Figure SI7, typical progress curves, pH vs time, of the systems ($c_i(CaCl_2)$ = $c_i(NaHCO_3)$ = 0.1 mol dm^{-3}; $c(Li^+)$ = 0.3 mol dm^{-3}, or $c(Li^+)$ = 0), stirred by different devices, are shown. Since the initial supersaturation was relatively high in all systems, precipitation started immediately after mixing the reactants (pH drops from 8.3 to 7.3, not shown). However, a shortening of the

induction time for vaterite formation, caused by applying more intensive agitation and seen as a pH drop, can be observed (ultrasonic < magnetic < mechanical). At that, the most likely mechanism of the promotion of nucleation in the case of sonication is a collapse of cavitation bubbles, which caused localized high pressure and temperature spots, while the literature data indicated that the energetic collisions among particles may enhance the transition of metastable vaterite to calcite as well [42–45]. In addition, the SEMs of the respective samples isolated after 5 days of aging showed significantly different morphologies of calcite crystals. Thus, only a partial truncation of {10.4} calcite faces occurred when magnetic or mechanical stirring were applied, while in the case of ultrasonication, relatively uniform, thin, and hexagonal tabular crystals could be observed. Consequently, it can be concluded that in this particular system, the morphology of calcite can be assigned to the both parameters, initial mode of mixing and the LiCl addition.

The results of analysis of the polymorphic distribution of the precipitates from the different systems are reported in Table 11 and showed in Figure 94.

Table 11. Properties of the precipitate and the calcite crystal obtained after initial sonication and 5 days of aging in mother solutions, containing different concentrations of Li^+ ions. In the system with $c(Li^+)$ = 1.0 mol dm^{-3}, about 2 wt % of vaterite has been obtained as well ($d \approx 3$ µm). * Two values indicate two different population of crystals. * The aspect ratio indicates the ratio between the longest axis of (00.1) planes and the thickness of the crystals: values of two different populations are shown.

$c(Li^+)$/ mol dm^{-3}	**w(calcite)/ wt %**	**Particle Size */ µm**	**Aspect Ratio #**	**$I_{(10.4)}/I_{(00.1)}$**	**w(Li)/ wt %**
0	100	9	-	68	0
0.1	100	11/27	11:1 27:1	39	0.004 ± 0.00017
0.3	100	12/32	12:1 32:1	25	0.008 ± 0.00011
0.5	100	23/43	23:1 43:1	30	0.012 ± 0.00015
0.7	100	23/40	23:1 40:1	23	0.015 ± 0.00023
1.0	98 ± 0.055	30/48	30:1 48:1	21	0.049 ± 0.00037

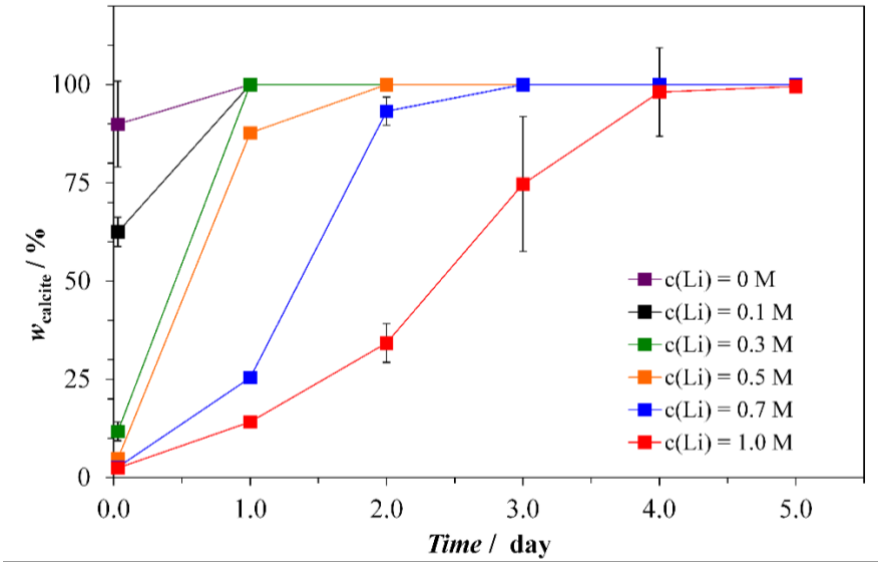

Figure 94. Content of calcite in a mixture with vaterite during the transformation process in the precipitation systems, $c_i(CaCl_2) = c_i(NaHCO_3) = 0.1$ mol dm^{-3}, with different initial concentrations of Li^+. In the reference system, $c(Li^+) = 0$. The initial concentrations of Li^+ are indicated.

It can be seen that during the early stages of the precipitation process, vaterite always co-precipitates with calcite, and its relative amount increases by increasing the $c(Li^+)$ in solution. Since vaterite is thermodynamically metastable, it converts into calcite during the time, with a transition time proportional to the $c(Li^+)$. Indeed, after 5 days of aging, vaterite completely transformed into calcite at all examined conditions, with differences obtained in the system of the highest $c(Li^+)$ applied, in which just 1.89 wt % of vaterite still persists. Aquilano et al. [27] showed that Li^+ is sporadically adsorbed on growing calcite crystals and that Li^+ is not homogeneously distributed in the crystals. On the other hand, no data reporting Li^+ distribution into the vaterite crystals are available, to the best of our knowledge. Therefore, we hypothesize that in the systems with higher Li^+ content, the increasing adsorption onto the vaterite surface cause its slower dissolution and kinetic stabilization, which consequently postpone the formation of calcite, as already reported for organic molecules [46]. However, the adsorption of Li^+ onto the calcite can also inhibit its growth, which influences the overall course of transformation.

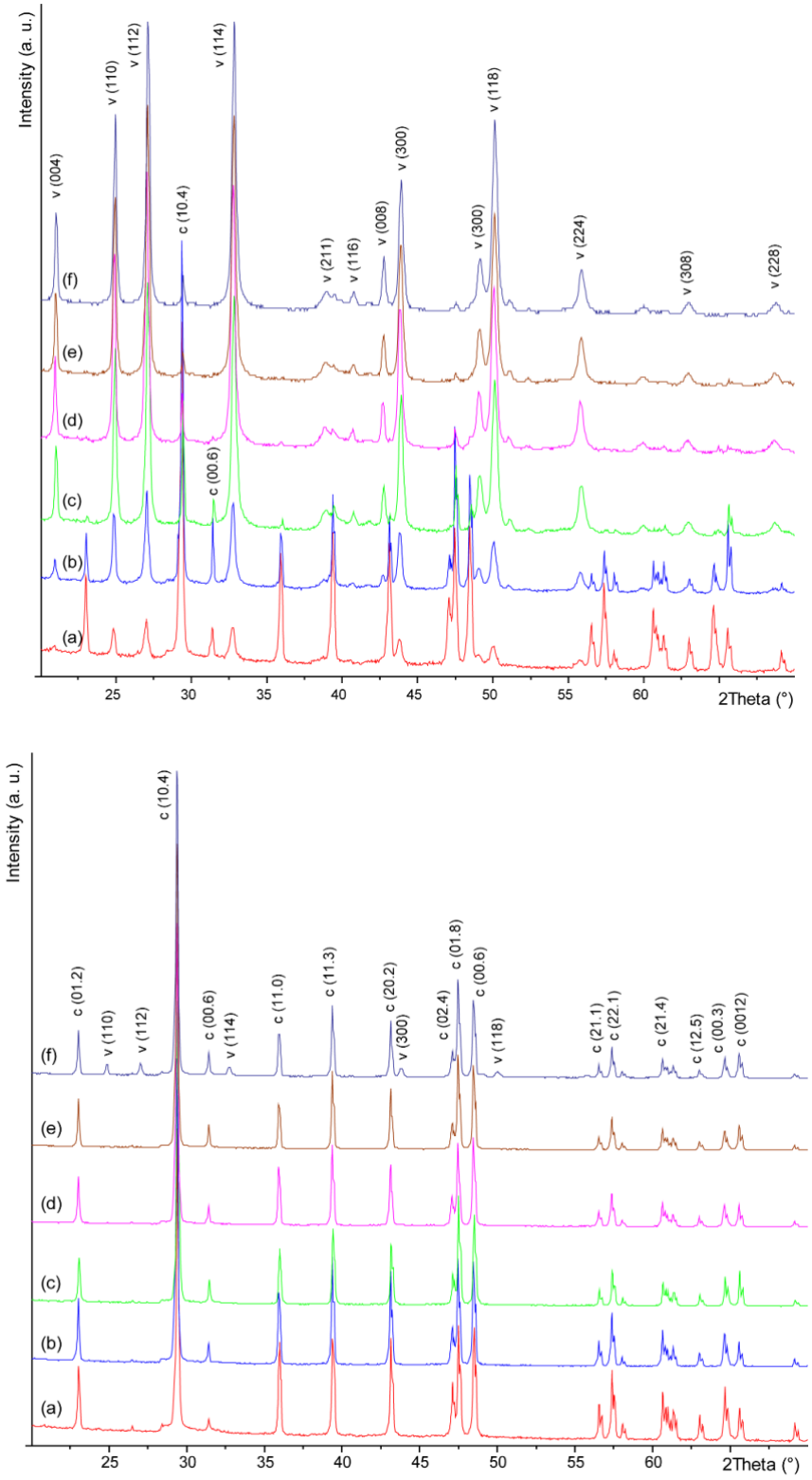

Figure 95. X-ray powder diffraction patterns of the precipitates obtained in the precipitation systems, ci(CaCl2) = ci(NaHCO3) = 0.1 mol dm–3, after 10 min (top) and 5 days of aging (bottom), in the presence of Li+ at the concentration of (a) 0.0 mol dm–3, (b) 0.1 mol dm–3, (c) 0.3 mol dm–3, (d) 0.5 mol dm–3, (e) 0.7 mol dm–3 or (f) 1.0 mol dm–3. The diffraction patterns were indexed accordingly to the PDF 00-005-0586 for calcite and PDF 00-033-0268 for vaterite PDF. In all systems only calcite and vaterite have been detected.

The analysis of X-ray powder diffraction (XRPD) patterns during the transformation process in all systems showed only diffraction peaks of vaterite and calcite (Figure 95), indicating that the formation of Li_2CO_3 does not occur at conditions studied in this work. On the contrary, in the systems described in the literature, which were supersaturated with respect to Li_2CO_3, the precipitation of this phase has been detected on calcite surface [25].

Shape and morphology of crystals were monitored during the progress of precipitation (Figure 96) and the obtained morphometric data are reported in Table 11. Thus, in the absence of Li^+, a mixture of hollow spherical vaterite and rhombohedral calcite crystals was obtained after 10 min of ultrasonic irradiation. The comparison of higher-magnification SEM of the vaterite samples, prepared in the presence (0.3 mol dm^{-3}) or in the absence of Li^+, indicates that the lithium ions do not significantly change the morphology of spherulites. However, after 5 days, only calcite crystals were detected, homogeneous in size and with surface pits, truncations, and ragged edges (Figure 96a), which can be attributed to the etching caused by the atmospheric CO_2 dissolved in the mother solution during the aging [47,48].

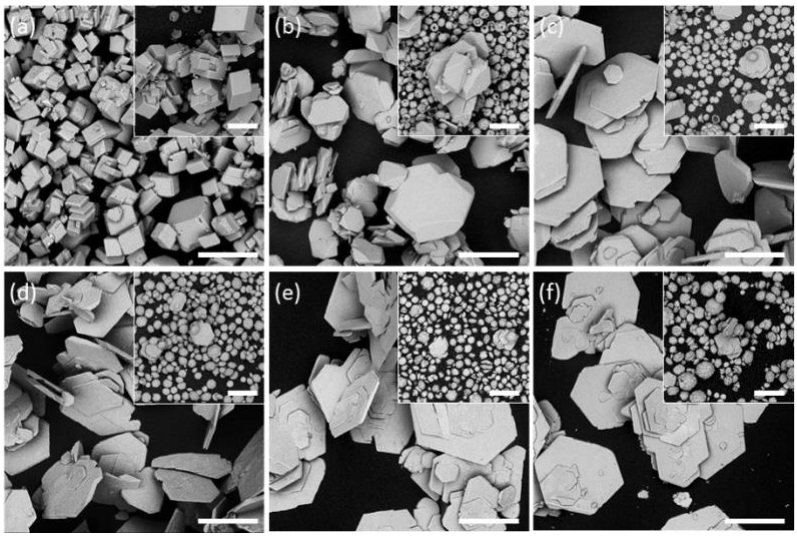

Figure 96. Scanning electron images of calcium carbonate samples obtained after 5 days of aging in the reference system, c(Li+) = 0 (a) and in the systems with c(Li+) = 0.1 mol dm–3 (b), c(Li+) = 0.3 mol dm–3 (c), c(Li+) = 0.5 mol dm–3 (d), c(Li+) = 0.7 mol dm–3 (e) and c(Li+) = 1.0 mol dm–3 (f). The inset shows the precipitates obtained after 10 min of ultrasonic irradiation at P = 40 W and at room temperature. Scale bars: 20 µm.

In the system with $c(Li^+)$ = 0.1 mol dm^{-3}, after 10 min of sonication, hollow spherulitic vaterite and rhombohedral calcite were observed as well. However, after 5 days the calcite crystals exhibited triangular faces, intergrowth, and crystal aggregation (Figure 96b). In addition, the smooth {10.4} crystal faces were truncated with {001} faces. Rajam and Mann [19] showed that calcite crystals truncation depends on Li^+/Ca^{2+} molar ratio, and that at low ratios the truncations are triangular, owing to growth of {00.1} and partial truncation of three {10.4} faces.

The system with $c(Li^+)$ = 0.3 mol dm^{-3}, after 10 min of ultrasonic irradiation contained mainly spherical vaterite particles agglomerated into 3 μm structures, as well as tabular calcite crystals and calcite crystals with triangular truncations (Figure 96c). After 5 days of aging, only thin hexagonal tabular calcite crystals, with well-developed basal {00.1} faces and {10.4} side faces, were obtained (Figure 96c). The hexagonal crystal truncations, formed by partial truncation of all six {10.4} calcite faces, are promoted by the adsorption of Li^+ and followed by absorption of Li_2CO_3 into growing calcite crystals, as showed by Aquilano [27].

At the highest Li^+ concentrations applied, $c(Li^+)$ = 0.5 mol dm^{-3} and 1.0 mol dm^{-3}, and after 10 min of ultrasonic irradiation a mixture of vaterite particles, together with small amounts of tabular calcite with well-developed {00.1} faces (Figure 96d–f insets), was obtained. The vaterite particles were aggregated in structures larger than those in the systems containing lower content of Li^+ (6–10 μm). At the end of the process, the remained vaterite particles converted into hollow particles (Figure 96f inset). Tabular hexagonal crystals obtained in the same systems, contained macro-steps on the {00.1} faces, which were not observed at lower $c(Li^+)$ (Figure 96d–f).

The aspect ratios of the calcite crystal were evaluated by analyzing the respective SEM images of the samples prepared in the systems with different Li^+ concentrations and isolated after 5 days of aging. At the same time, the ratios of relative intensities, $I_{10.4}/I_{00.1}$, were estimated from the XRPD patterns. The data shown in the Table 11 indicates that the aspect ratio increased with increasing the Li^+ content for each crystal population obtained in the respective system. Also, the ratios of relative intensities, $I_{10.4}$ / $I_{00.1}$, decrease with increasing Li^+ content. Indeed, the aspect ratio values of two classes of the crystals obtained in the final precipitate pointed to two nucleation events, which imply that the conditions in the solutions during these two events (S, Li/Ca) were not completely identical. However, these findings are consistent with SEM observations (Figure 96) which showed that in the system containing $c(Li^+)$ = 0.3 mol dm^{-3}, crystals were plate-like with well-developed {001} faces and without macro-steps. On other hand, in the systems with higher $c(Li^+)$, the crystals were larger, but contained macro-steps with expressed {104} side faces.

The content of Li^+ incorporated into the $CaCO_3$ samples prepared in different chemical environments (different additions of Li^+) and isolated during the aging of precipitate was determined by ion chromatography. Thus, Figure 97 shows that the Li^+ content in the precipitate continuously decreased during the progress of transformation in each precipitation system.

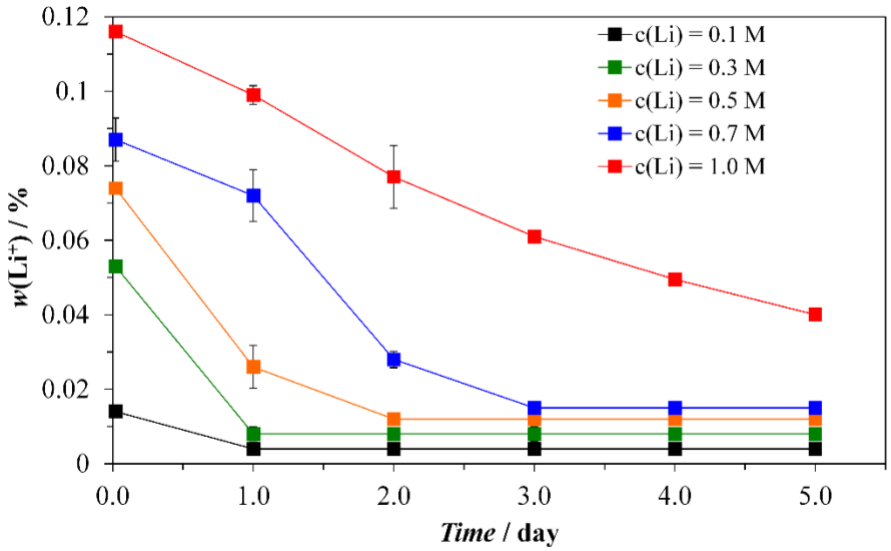

Figure 97. The content of Li+ incorporated into the crystals during the transformation process in the precipitation systems, ci(CaCl2) = ci(NaHCO3) = 0.1 mol dm−3, with different initial concentration of Li+. The initial concentrations of Li+ in solution are indicated.

The highest incorporation determined immediately after 10 minutes of sonication (t = 0 days) was found in the system with $c(Li^+)$ = 1.0 mol dm^{-3} ($w(Li^+)$ = 0.116 wt %), while in the systems with lower initial Li^+ concentrations, the content was in the range from 0.087 to 0.014 wt %. The amount of Li^+ incorporated into the precipitate and determined at the end of the aging process was found to vary in the very narrow range between 0.004 and 0.04 wt %. Again, the Li^+ incorporation increased almost linearly with increasing the initial Li^+ up to the c = 0.7 mol dm^{-3}, so the obtained values may be considered as typical for distribution between solution and tabular calcite crystals with dominant expression of {00.1} crystal planes. On the other hand, in the systems in which vaterite was still present, the measured incorporation of Li^+ was significantly higher, which implicate different mechanisms of Li^+ uptake. Thus, it can be concluded that, besides the adsorption, the calcite incorporates the Li^+ in the crystal structure, while vaterite particles can additionally entrap the Li-containing solution into the pores. Indeed, at the applied supersaturation level, vaterite spherulites are most probably formed by fast spherulitic growth, which is characterized exactly by the increased trapping of dissolved impurities, like Li^+ in this particular case [45,49,50].

The results of structural, morphological, and chemical analyses of calcium carbonate precipitate formed in the Li^+ containing solutions pointed out that the calcite crystals obtained in the system with $c(Li^+)$ = 0.3 mol dm^{-3} are appropriate for use in adsorption experiments, in which the {00.1} crystal faces should be investigated. Namely, the prepared crystals are relatively uniform in size, without expressed macro-steps and {10.4} faces, as well as the content of incorporated Li^+, is relatively low.

7.2.4.2 Adsorption of Model Molecules

The adsorption proprieties of {00.1} calcite prepared in the system $c(Li^+)$ = 0.3 mol dm^{-3} were compared with the {104} calcite obtained by the same procedure but in the absence of Li^+. The specific surface area of the {00.1} calcite used for the adsorption experiments was, s = 0.38 $m^2\ g^{-2}$, while of the {10.4} calcite was, s = 0.34 $m^2\ g^{-2}$. At that, calcein and crystal violet (CV) have been selected as representative organic molecules, due to their different chemical properties and strong molar extinction coefficients. Calcein possess 4 carboxyl groups are negatively charged at pH 8.0 and can chelate Ca^{2+}, while CV possesses terminal amine groups, which are positively charged at pH 8.0.

The actual adsorption of the selected dye molecules on the surface of the calcite crystals with different dominant crystal faces has been visualized by confocal microscopy. Figure 98 shows typical microphotographs of the plate-like and rhombohedral calcite crystals labeled with calcein. It can be seen that, within the limits of the resolution of the technique, calcein only partially covers the {00.1} faces, while a more intense fluorescence is observed on the {10.4} planes.

The adsorption properties of the calcite crystals of different morphologies have been determined by equilibrating them in solutions containing respective dye molecules for 24 h and by measuring the residual concentration after the crystals have been separated. No further adsorption was observed after 24 h. The kinetics of the adsorption have been determined as well and it could be seen that the concentration of adsorbed CV is much higher in comparison to calcein and for both crystal morphologies. In order to additionally understand a mode of specific molecule/surface interactions, the experiments designed in a different way will be performed. The equilibrium concentration of dye adsorbed on the surfaces of different calcite crystals is presented in Figure 99, which shows stronger interactions of CV with both morphologies, while the adsorption of calcein on {10.4} faces is about twice as strong as the adsorption on {00.1} faces.

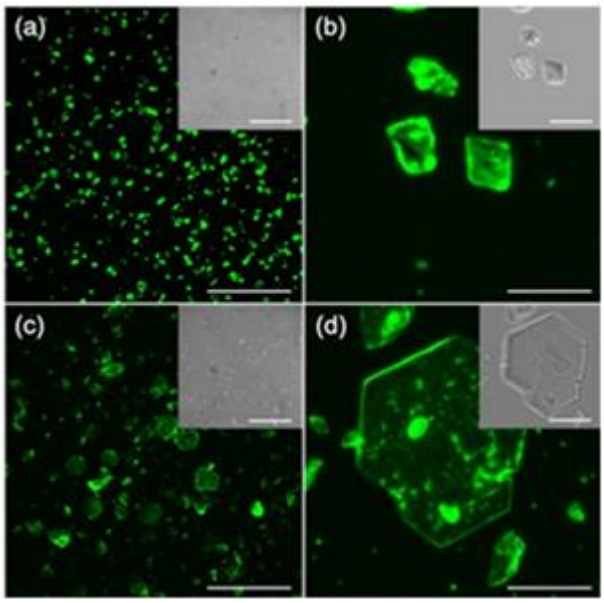

Figure 98. Confocal microscopy images of calcite crystals with adsorbed calcein. (a,b) {10.4} calcite, (c,d) {00.1} calcite. The insets show the corresponding transmission optical microscopy images. The scale bars are 50 µm (a,c) and 10 µm (b,d).

The obtained results and different abilities for adsorption can be ascribed either to the different structure of the crystal planes, or to the chemical nature of the adsorbate molecule. {00.1} calcite exposes alternating planes of Ca^{2+} and CO_3^{2-} ions, with a preference for the latter [27], while the {10.4} face exposes both ions. The different chemical structure, and the net charge which exists at the conditions applied, are responsible for the observed different adsorption properties. Thus, positively charged CV is more likely to adsorb on calcite crystals, which typically possesses a net negative charge at wide range of solution composition and pH, as determined previously by the zeta potential measurements [15]. The interactions of calcein are significantly stronger with the {10.4} than with the {00.1} calcite surfaces, which is consistent with previous studies in which a Langmuir isotherm was proposed to describe the process [51]. On the other hand, it is known that the surface of {00.1} faces exposes the incorporated Li^+ in the form of lithium carbonate islands [25,26], so the surface complexation of calcein molecules, which interact by their carboxylate groups with Ca^{2+}, is limited or even suppressed. It follows that on the tabular {00.1} faces, the interaction with the calcein can predominantly happen on the steps and kinks exposed by the {00.1} faces. The interaction between the CV and the surface of calcite crystals is purely electrostatic, unlike calcein which requires the complexion of Ca^{2+}, and is therefore less selective with regards to the structure and coordination of surfaces. Indeed, as shown in the Figure 99, the amount of adsorbed CV was similar for both calcite morphologies.

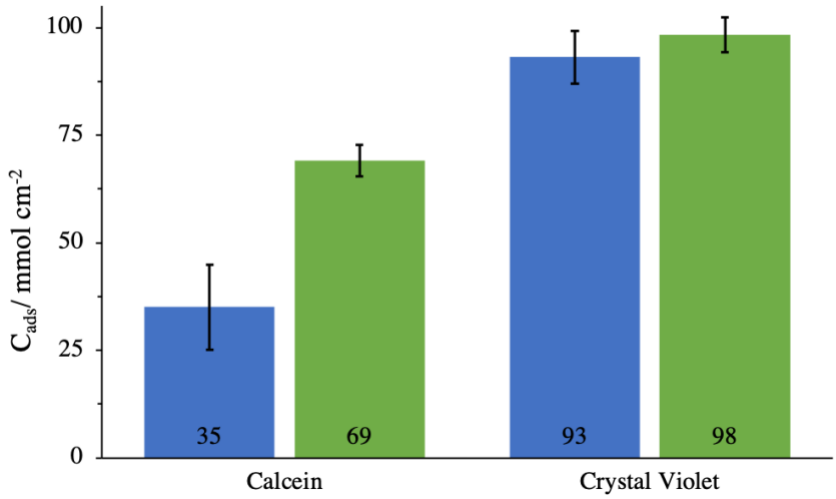

Figure 99. The concentration of respective dye molecules adsorbed after 24 h at the surface of {00.1} (blue) or {104} (green) calcite crystals.

7.2.5 Conclusions

A procedure for the preparation of uniform and thin tabular {001} calcite was proposed. Tabular calcite, which exhibited triangular and hexagonal faces, was precipitated from the Li^+-doped systems. In addition, the kinetics of formation of calcite crystals with a specific tabular morphology were demonstrated during the solution-mediated transformation process, in which predominantly vaterite initially appeared. With that, it was shown that higher Li^+ concentrations caused a slower conversion to calcite. The tabular {001} calcite, optimal for investigation of adsorption, was obtained at moderate Li^+ concentration, $c(Li^+) = 0.3$ mol dm^{-3}: the crystals were relatively uniform in size and {00.1} predominated over the other faces.

The adsorption properties of the tabular {001} calcite was investigated by using two model organic dye molecules. The results of adsorption of calcein and crystal violet were compared to their adsorption on more common {10.4} calcite morphologies, in order to understand their interfacial dynamic and reactivity. It was found that the adsorption capability of the tabular {001} calcite is lower than the capability of pure {104} faced crystals and that the adsorption of the selected organic molecules depends on their functional groups and charge.

Since it is known that dissolved organic molecules play an important role in the regulation of crystal growth during the biomineralization process, which is a consequence of their adsorption and absorption on/in crystal face, this research contributes to understanding a mode and extent of interfacial interactions at different crystal planes.

7.2.6 Author contribution

Conceptualization, D.K. and G.F.; investigation, N.M., G.M., F.S. and S.F.; formal analysis, N.M., G.M., F.S. and S.F.; writing–original draft preparation, G.F. and D.K.; writing–review and editing, D.K. and G.F.

7.2.7 References

1 G. Magnabosco, M. Di Giosia, I. Polishchuk, E. Weber, S. Fermani, A. Bottoni, F. Zerbetto, P. G. Pelicci, B. Pokroy, S. Rapino, G. Falini and M. Calvaresi, *Adv. Healthc. Mater.*, 2015, **4**, 1510–1516.

2 F. Nudelman and N. A. J. M. Sommerdijk, *Angew. Chemie - Int. Ed.*, 2012, **51**, 6582–6596.

3 D. C. Green, J. Ihli, P. D. Thornton, M. A. Holden, B. Marzec, Y. Y. Kim, A. N. Kulak, M. A. Levenstein, C. Tang, C. Lynch, S. E. D. Webb, C. J. Tynan and F. C. Meldrum, *Nat. Commun.*, 2016, **7**, 13524.

4 S. Weiner and L. Addadi, *Annu. Rev. od Mater. Res.*, 2011, **41**, 21–40.

5 L. Addadi and S. Weiner, *Proc. Natl. Acad. Sci.*, 1985, **82**, 4110–4114.

6 G. Magnabosco, I. Polishchuk, J. Erez, S. Fermani, B. Pokroy and G. Falini, *CrystEngComm*, 2018, **20**, 4221–4224.

7 M. Ukrainczyk, J. Stelling, M. Vučak and T. Neumann, *J. Cryst. Growth*, 2013, **369**, 21–31.

8 L. Wang, E. Ruiz-Agudo, C. V. Putnis and A. Putnis, *CrystEngComm*, 2011, **13**, 3962–3966.

9 B. Njegić-Džakula, G. Falini, L. Brečević, Ž. Skoko and D. Kralj, *J. Colloid Interface Sci.*, 2010, **343**, 553–563.

10 H. A. Lowenstam and S. Weiner, *On Biomineralization*, Oxford University Press, 1989.

11 G. Falini, S. Fermani and S. Goffredo, *Semin. Cell Dev. Biol.*, 2015, **46**, 17–26.

12 J. Aizenberg, A. Tkachenko, S. Weiner, L. Addadi and G. Hendler, *Nature*, 2001, **412**, 819–822.

13 L. Addadi, S. Raz and S. Weiner, *Adv. Mater.*, 2003, **15**, 959–970.

14 M. Ukrainczyk, J. Kontrec and D. Kralj, *J. Colloid Interface Sci.*, 2009, **329**, 89–96.

15 B. Njegić-Džakula, L. Brečević, G. Falini and D. Kralj, *Cryst. Growth Des.*, 2009, **9**, 2425–2434.

16 B. Njegić-Džakula, L. Brečević, G. Falini and D. Kralj, *Croat. Chem. Acta*, 2011, **84**, 301–314.

17 G. Magnabosco, I. Polishchuk, B. Pokroy, R. Rosenberg, H. Cölfen and G. Falini, *Chem. Commun.*, 2017, **53**, 4811–4814.

18 K. J. Davis, P. M. Dove, L. E. Wasylenki and J. J. De Yoreo, *Am. Mineral.*, 2004, **89**, 714–720.

19 S. Rajam and S. Mann, *J. Chem. Soc. Chem. Commun.*, 1990, **0**, 1789–1791.

20 R. Q. Song and H. Cölfen, *CrystEngComm*, 2011, **13**, 1249–1276.

21 J. O. Titiloye, S. C. Parker, D. J. Osguthorpe and S. Mann, *J. Chem. Soc. Chem. Commun.*, 1991, **0**, 1494–1496.

22 Y. Kitano, *Bull. Chem. Soc. Jpn.*, 1962, **35**, 1973–1980.

23 M. Bruno, F. R. Massaro, M. Prencipe and D. Aquilano, *CrystEngComm*, 2010, **12**, 3626–3633.

24 L. Pastero, E. Costa, M. Bruno, M. Rubbo, G. Sgualdino and D. Aquilano, *Cryst. Growth Des.*, 2004, **4**, 485–490.

25 L. Pastero and D. Aquilano, *Cryst. Growth Des.*, 2008, **8**, 3451–3460.

26 F. R. Massaro, L. Pastero, E. Costa, G. Sgualdino and D. Aquilano, *Cryst. Growth Des.*, 2008, **8**, 2041–2046.

27 D. Aquilano and L. Pastero, *Cryst. Res. Technol.*, 2013, **48**, 819–839.

28 L. Pastero, D. Aquilano, E. Costa and M. Rubbo, *J. Cryst. Growth*, 2005, **275**, 1625–1630.

29 J. O. Titiloye, S. C. Parker and S. Mann, *J. Cryst. Growth*, 1993, **131**, 533–545.

30 J. Bohr, R. A. Wogelius, P. M. Morris and S. L. S. Stipp, *Geochim. Cosmochim. Acta*, 2010, **74**, 5985–5999.

31 K. K. Sand, M. Yang, E. Makovicky, D. J. Cooke, T. Hassenkam, K. Bechgaard and S. L. S. Stipp, *Langmuir*, 2010, **26**, 15239–15247.

32 N. Bovet, M. Yang, M. S. Javadi and S. L. S. Stipp, *Phys. Chem. Chem. Phys.*, 2015, **17**, 3490–3496.

33 U. Aschauer, D. Spagnoli, P. Bowen and S. C. Parker, *J. Colloid Interface Sci.*, 2010, **346**, 226–231.

34 L. Mureşan, P. Sinha, P. Maroni and M. Borkovec, *Colloids Surfaces A Physicochem. Eng. Asp.*, 2011, **390**, 225–230.

35 R. M. Hazen, T. R. Filley and G. A. Goodfriend, *Proc. Natl. Acad. Sci.*, 2001, **98**, 5487–5490.

36 C. A. Orme, A. Noy, A. Wierzbicki, M. T. Mcbride, M. Grantham, H. H. Teng, P. M. Dove and J. J. Deyoreo, *Nature*, 2001, **411**, 775–779.

37 A. Wierzbicki, C. S. Sikes, J. D. Madura and B. Drake, *Calcif. Tissue Int.*, 1994, **54**, 133–141.

38 L. Sonnenberg, Y. Luo, H. Schlaad, M. Seitz, H. Cölfen and H. E. Gaub, *J. Am. Chem. Soc.*, 2007, **129**, 15364–15371.

39 M. Yang, P. Mark Rodger, J. H. Harding and S. L. S. Stipp, *Mol. Simul.*, 2009, **35**, 547–553.

40 C. L. Freeman, J. H. Harding, D. Quigley and P. M. Rodger, *J. Phys. Chem. C*, 2011, **115**, 8175–8183.

41 M. Yang, S. L. S. Stipp and J. Harding, *Cryst. Growth Des.*, 2008, **8**, 4066–4074.

42 E. Dalas, *J. Cryst. Growth*, 2001, **222**, 287–292.

43 I. Nishida, *Ultrason. Sonochem.*, 2004, **11**, 423–428.

44 S. S. Berdonosov, I. V. Znamenskaya and I. V. Melikhov, *Inorg. Mater.*, 2005, **41**, 1308–1312.

45 B. N. Džakula, J. Kontrec, M. Ukrainczyk, S. Sviben and D. Kralj, *Crystal Research and Technology*, 2014, **49**, 244–256.

46 W. Li and C. Gao, *Langmuir*, 2007, **23**, 4575–4582.

47 J. Luo, F. Kong and X. Ma, *Cryst. Growth Des.*, 2016, **16**, 728–736.

48 R. S. Arvidson, I. E. Ertan, J. E. Amonette and A. Luttge, *Geochim. Cosmochim. Acta*, 2003, **67**, 1623–1634.

49 G. De Giudici, *Am. Mineral.*, 2002, **87**, 1279–1285.

50 K. Sangwal, *Additives and crystallization processes: from fundamentals to applications*, John Wiley & Sons Ltd, West Sussex, England, 2007.

51 G. Atun and E. T. Acar, *Sep. Sci. Technol.*, 2010, **45**, 1471–1481.